IMPACT MODIFIED POLYSTYRENE BASED NANOCOMPOSITES

A THESIS SUBMITTED TO
THE GRADUATE SCHOOL OF NATURAL AND APPLIED SCIENCES
OF
MIDDLE EAST TECHNICAL UNIVERSITY

BY

CANAN ESMA YENİOVA

IN PARTIAL FULFILLMENT OF THE REQUIREMENTS
FOR
THE DEGREE OF MASTER OF SCIENCE
IN
CHEMICAL ENGINEERING

JANUARY 2009

Approval of the thesis:

IMPACT MODIFIED POLYSTYRENE BASED NANOCOMPOSITES

submitted by **CANAN ESMA YENİOVA** in partial fulfillment of the requirements for the degree of **Master of Science in Chemical Engineering Department, Middle East Technical University** by,

Prof. Dr. Canan Özgen
Dean, Graduate School of **Natural and Applied Sciences**   _____

Prof. Dr. Gürkan Karakaş
Head of Department, **Chemical Engineering**   _____

Prof. Dr. Ülkü Yılmazer
Supervisor, **Chemical Engineering Dept., METU**   _____

Prof. Dr. Erdal Bayramlı
Co-Supervisor, **Chemistry Dept., METU**   _____

Examining Committee Members:

Prof. Dr. Zuhal Küçükyavuz
Chemistry Dept., METU   _____

Prof. Dr. Ülkü Yılmazer
Chemical Engineering Dept., METU   _____

Prof. Dr. Leyla Aras
Chemistry Dept., METU   _____

Prof. Dr. Teoman Tinçer
Chemistry Dept., METU   _____

Assoc. Prof. Dr. Göknur Bayram
Chemical Engineering Dept., METU   _____

20.01.2009
Date: _____

I hereby declare that all information in this document has been obtained and presented in accordance with academic rules and ethical conduct. I also declare that, as required by these rules and conduct, I have fully cited and referenced all material and results that are not original to this work.

Name, Last name: Canan E. Yeniova

Signature:

ABSTRACT

IMPACT MODIFIED POLYSTYRENE BASED NANOCOMPOSITES

Yeniova, Canan E.

M.S. Department of Chemical Engineering

Supervisor: Prof. Dr. Ülkü Yılmazer

Co-supervisor: Prof. Dr. Erdal Bayramlı

January 2009, 201 Pages

Polystyrene, PS, is a preferable polymer in industry, but, its brittle characteristic restricts its utilization. The aim of this study is to improve the impact strength of PS by the help of elastomeric materials SEBS-g-MA and E-BA-GMA. In order to prevent the reduction in the tensile strength of the materials, three different types of organic montmorillonites, MMT, (Cloisite® 30B, 25A and 15A) were used as fillers. Nanocomposite preparation was performed in a co-rotating twin screw extruder.

Initially elastomer and organoclay contents were kept at 5wt% and 1-2wt% respectively. Well dispersed silicate layers were obtained for the nanocomposite containing SEBS-g-MA and Cloisite® 25A owing to the high viscosity of SEBS-g-MA and the solubility of polystyrene end block of SEBS with PS matrix. Owing to higher hydrophobicity of Cloisite® 15A a better dispersion was expected compared to Cloisite® 25A, but, it was concluded that two long aliphatic tails of Cloisite® 15A limited the access of polymer chains to the clay surface. The desired impact strength values could not be achieved by using 5wt% elastomeric materials; therefore, it was decided to increase the SEBS-g-MA content up to 15, 20, 30 and 40wt%.

With increasing elastomer content, increasing average elastomer domain size was obtained. Also, it was observed that with the addition of organoclay, the elastomeric domain size increases since the clay particles reside in the elastomer phase and at the interphase between elastomer and PS. The mechanical test results showed that the nanocomposites containing 15 and 20wt% SEBS-g-MA have the optimum average domain size that results in better impact strength values without deteriorating tensile properties.

Key words: Polystyrene, Impact modifier, Nanocomposite, Organoclay, Extrusion

ÖZ

DARBE DAYANIMI İYİLEŞTİRİLMİŞ POLİSİTİREN BAZLI NANOKOMPOZİTLER

Yeniova, Canan E.

Yüksek Lisans, Kimya Mühendisliği

Tez Yöneticisi: Prof. Dr. Ülkü Yılmazer

Ortak Tez Yöneticisi: Prof. Dr. Erdal Bayramlı

Ocak 2009, 201 Sayfa

Polisitiren, PS, endüstride tercih edilen bir polimer olmasına rağmen kırılgan yapısı kullanım alanlarını kısıtlamaktadır. Bu çalışmada amaç, SEBS-g-MA ve E-BA-GMA elastomerik malzemelerinin yardımıyla PS'nin darbe dayanımını arttırmaktır. Malzemenin gerilme dayanımındaki düşüşü engellemek amacıyla üç farklı çeşit organik montmorillonit, MMT, (Cloisite$^®$ 30B, 15A, 25A) dolgu malzemesi olarak kullanılmıştır. Nanokompozit malzemeler vidaları aynı yönde dönen ve iç içe geçmiş çift vidalı ekstrüder kullanılarak hazırlanmıştır.

Çalışmanın başında elastomer ve organik kil içerikleri sırasıyla ağırlıkça %5 ve %1-2'de sabit tutulmuştur. SEBS-g-MA'nın yüksek viskozitesi ve uç bloklarındaki polisitirenin ana PS matrisi içerisinde çözülmesine bağlı olarak silika tabakalarındaki en iyi dağılım SEBS-g-MA ve Cloisite$^®$ 25A içeren nanokompozitlerde elde edilmiştir. Cloisite® 25A ile karşılaştırıldığında yüksek hidrofobisitesine bağlı olarak Cloisite® 15A'nın daha iyi bir dağılım göstermesi beklenmiştir, ancak, sahip olduğu iki uzun alifatik kuyruğun polimer zincirlerinin kil yüzeyine erişmesini engellediği sonucuna varılmıştır. İstenilen darbe dayanımı değerleri %5 elastomer kullanılarak elde edilememiş, bu sebeple SEBS-g-MA içeriğinin %15, 20, 30 ve 40'a kadar arttırılmasına karar verilmiştir.

Artan elastomer içeriği ile birlikte ortalama elastomer faz boyutunda artış elde edilmiştir. Ayrıca, organik killerin eklenmesiyle de faz boyutunun arttığı gözlenmiştir, buna sebep olarak da kil parçacıklarının elastomer faz içerisinde ve elastomer ile PS matrisin ara yüzeyine yerleşmiş olmaları gösterilmiştir. Mekanik testlerin sonuçları %15-20 SEBS-g-MA içeren nanokompozitlerin optimum elastomer faz boyutuna sahip olduğunu ve gerilme özelliklerine zarar verilmeden en iyi darbe dayanımının elde edildiğini göstermiştir.

Anahtar Kelimeler: Polisitiren, Darbe dayanımı iyileştirici, Nanokompozit Organik kil, Ekstrüzyon

To my family

ACKNOWLEDGEMENTS

I am forever grateful for the love and support of my parents, Meral and Hasip Yeniova and my brother Özgür Yeniova. I could not achieve any of these without their support and belief in me. I am blessed to have them as my family.

Last, but not the least; I thank to Tarhan Göksu for being my best friend and sharing my life with all his love, patience and understanding. I owe him a lot for his endless encouragement during my undergraduate and graduate studies.

TABLE OF CONTENTS

APPENDICES

LIST OF FIGURES

xiv

LIST OF TABLES

NOMENCLATURE

A_i	Area of a domain in SEM analysis, μm^2
A_0	Initial cross sectional area, mm^2
d	Interlayer spacing, Å
d_{av}	Average domain size, nm
D	Distance between grips of tensile test specimen, mm
D	Extruder barrel diameter, mm
E	Young's Modulus, MPa
F	Instantaneous load, N
L	Extruder barrel length, mm
L	Total length of impact test specimen, mm
L	Overall length of tensile test specimen, mm
L_c	Capillary tube length, mm
L_0	Initial gauge length, mm
n	Order of diffraction peak
n	Rabinowitsch correction factor
n_i	Number of domains analyzed in SEM analysis
Q	Volumetric flow rate, $mm^3.s^{-1}$
R_c	Inside capillary tube radius, mm
T	Thickness of tensile and impact test specimen, mm
T_g	Glass Transition Temperature, ºC
T_m	Melting Temperature, ºC
T_c	Crystallization Temperature, ºC
W	Width of narrow section of tensile test specimen, mm

Greek Letters

σ	Engineering stress, MPa
σ_m	Tensile strength, MPa
ε	Engineering strain, mm/mm
θ	Scattering angle, º
λ	Wavelength, nm

η_i	Melt viscosity of component i, Pa.s
Φ_i	Volume fraction of component i
η_{hv}	Melt viscosity of high viscosity component i, Pa.s
Φ_{hv}	Volume fraction of high viscosity component i
η_{lv}	Melt viscosity of low viscosity component, Pa.s
Φ_{lv}	Volume fraction of low viscosity component i
Γ	Apparent shear rate, s^{-1}
γ	True shear rate, s^{-1}
μ	Viscosity of Newtonian fluids, Pa.s
τ_{wall}	Shear stress at tube wall, Pa
ΔP	Pressure drop across capillary tube, Pa

Abbreviations

CEC	Cation Exchange Capacity
DSC	Differential Scanning Calorimetry
DTA	Differential Thermal Analysis
E-BA-GMA	Ethylene-b-Butyl Acrylate-b-Glycidyl Methacrylate
GMA	Glycidyl Methacrylate
ISO	International Organization for Standardization
MA	Maleic Anhydride
MFI	Melt Flow Index
MMT	Montmorillonite
MT2EtOH	Methyl, tallow, bis-2-hydroxyethyl quaternary ammonium
OH	Hydroxyl
OPS	Poly (styrene-co-vinyloxazolin)
PA12	Polyamide 12
PA66	Polyamide 66
PMMA	Poly (methyl methacrylate)
PS	Polystyrene
SAXS	Small Angle X-Ray Scattering
SEBS-g-MA	MA grafted Styrene-b-(Ethylene-co-Butylene)-b-Styrene
SEM	Scanning Electron Microscopy

TEM	Transmission Electron Microscopy
TG	Thermogravimetry
WAXS	Wide Angle X-Ray Scattering
XRD	X-Ray Diffraction
15A	Cloisite® 15A
25A	Cloisite® 25A
30B	Cloisite® 30B
2MHTL8	Di-methyl, hydrogenated tallow, 2-ethylhexyl quaternary ammonium
2M2HT	Di-methyl, di-hydrogenated tallow quaternary ammonium

CHAPTER 1

INTRODUCTION

Composites are materials that consist of two different phases; continuous matrix phase and continuous or discontinuous reinforcement phase, combined in such a way to act together and identified physically [1]. They are used in many applications due to their better creep and fatigue resistance compared to separate phases, and their flexible structure has the ability of carrying combinations of shear and axial forces [2]. In addition, they are preferred in industry due to their long life and low cost.

Among the composite materials, the most preferred type is the one which is based on a polymer matrix. Owing to easy processing, this type of material is a growing research area. The most important advantage of polymer composites is their lightweight because of their lower density than ceramic and metallic composites. However, their mechanical properties are relatively low. Thus, they require improvement in their mechanical properties [3]. Polymer matrix can be either linear or branched with no chemical linking between them or can be a crosslinked network; these types of materials are called thermoplastics and thermosets respectively. When they are exposed to heat, thermoplastic materials take a new shape and then return to their original shape upon cooling. But, the case is different for thermosets; with further heating they undergo curing reactions that prevent reshaping of the material [4].

Polymer-clay nanocomposites are particulate-filled composites in which the reinforcement material is in the form of sheets and have a high aspect ratio with a thickness of one to few nanometers and length of hundreds to thousands of nanometers. Nanocomposites posses highly enhanced thermal and mechanical properties when compared with the pristine polymer due to their structural

properties [5]. Montmorillonite, which is a 2:1 layered clay mineral, is a widely used type of filler in polymer-clay nanocomposites. They consist of a 1nm thick layer composed of a central alumina sheet sandwiched between two silica tetrahedral sheets. Between these layers van der Waals gaps are formed and called interlayer spacing or gallery.

An excess negative charge called as "cation exchange capacity" is created by isomorphic substitution within the silicate layers [6]. These negative charges are balanced by alkali or alkaline earth cations and the presence of these cations increases the basal spacing of the clay crystal, but it also makes the clay crystal hydrophilic. This hydrophilic clay is turned into organophilic by imparting alkylammonium or alkylphosphonium ions within the clay structure replacing the cations [7]. The alkylammonium and alkylphosphonium cations provide functional groups that can react with the polymer or initiate polymerization of monomers [8].

The preparation of nanocomposites can be accomplished via different methods, such as melt intercalation, in-situ polymerization, and solution polymerization. Melt intercalation is a broadly used method due to its easy processing and environmentally friendly state. In this method, above the glass transition temperature of the polymer matrix, the molten polymer chains diffuse into the clay galleries leading to three types of structures [9]. If the clay platelets remain as large stacks and no polymer chains get inserted between the layers, the material is called "conventional composite". The polymer chains may be inserted between the clay layers without deteriorating the well ordered structure of the particles and this type of composites are mentioned as "intercalated" nanocomposites. In "exfoliated" nanocomposites, the clay particles are completely dispersed in the polymer matrix [10, 11]. The degree of exfoliation significantly depends on residence time, level of shear, selection of polymer grade, organoclay choice and level of reinforcement.

PS is a brittle material that can not endure high stresses. To solve this problem it is inevitable to use a third material, generally rubbery materials. In industry high impact polystyrene is obtained by the polymerization of styrene monomer in the presence of polybutadiene. However, polymerization is a difficult process to achieve. Thus, in this study melt intercalation method was used to prepare composite materials. In this study, the main aim is to improve the toughness of the

2

PS matrix by melt intercalation method without deteriorating the other mechanical properties like tensile strength or modulus. In order to do that, organoclay was used to get stiffer materials, and impact modifier was incorporated into the polymer matrix, to increase the toughening mechanism and also to provide the compatibilization between the polymer and the organoclay.

During the preparation of nanocomposites, effects of three different types of organoclays, Cloisite® 30B, 15A and 25A, and two different types of elastomers, poly[styrene-b-(ethylene-co-butylene)-b-styrene (SEBS-g-MA) and poly(ethylene-b-butyl acrylate-b-glycidyl methacrylate) (E-BA-GMA) on the morphological, rheological, mechanical and thermal properties were investigated.

To observe the dispersion of clay particles in the polymer matrix XRD and TEM analyses were performed, whereas the dispersion of elastomeric materials in the matrix and effect of organoclay on the phase domains were examined with SEM analysis. Melt flow index (MFI) test was applied to observe the flow characteristics, and with the capillary viscometry analysis the viscosity of the raw materials were observed at different shear rates. Mechanical properties of the specimens were evaluated according to the tensile and impact tests. Finally, the glass transition temperatures of the samples were measured by using differential scanning calorimetry.

CHAPTER 2

BACKGROUND

2.1 Composite Materials

The definition of composite materials is; combination of two or more materials in which the constituents retain their identities. Those constituents do not dissolve or merge completely in each other, however, they can be physically identified and act together [1]. For superior properties, such as lighter weight and higher strength, compared to those of the individual components, they are dispersed in a controlled way, which means relative amounts, the geometry of the dispersed phase, particle size, distribution and orientation affect the properties of composites [3].

Composites usually consist of two different phases; the first one is the continuous part which is called the matrix. This phase acts as a binder, which holds the components together, and the main load-bearing constituent, so it governs the mechanical properties of the materials. The second one is the reinforcement which is dispersed in the continuous phase. The main advantage of this phase is its strength, stiffness and hardness relative to the matrix phase [12]. Reinforcement phase can be in the form of either continuous (long fibers, sheets) or discontinuous (particles, short fibers, etc.). Particle-reinforced composite group includes single-layer and multi-layer composites that are composed of laminates (sheet constructions in a specified sequence), hybrids (construction with mixed fibers in a ply or layer by layer) and sandwich panels (structural composites with two outer sheets separated by a layer of less dense material) [13].

Another parameter that affects the properties of composites is the existence of the matrix and reinforcement interface, i.e. interphase. Failure mechanism, fracture toughness and overall stress-strain behavior of the material are generally

determined by this separate phase [14]. Wettability, surface roughness and bonding are the factors that the interphase depends on. These three factors are mainly related to one another. For instance, surface roughness has a prominent effect on wettability since it can reduce the bonded area and lead to void formation or stress concentrations [13]. There are different types of interfacial bonding mechanisms at the interphase. Mechanical bonding is one of these interfacial bonding types, it is efficient in load transfer when the force is applied parallel to the interface. However, pure mechanical bonding has low strength compared to chemical bonding, which includes bonding by direct reactions, coupling agents, molecular chain entanglement and inter-diffusion, at the interface. In addition, physical bonding is another important type of bonding mechanism. Physical bonding involves weak, secondary, van der Waals forces, dipolar interactions and hydrogen bonding; like mechanical bonding it is not enough for most of the cases owing to its effectiveness over small distances [15].

Composite structures can be classified according to the matrix material that they are made up of. The matrix can be metal, ceramic, polymer, etc. In composites with metal matrix, reinforcement improves specific stiffness, strength, abrasion resistance, creep resistance, thermal conductivity and dimensional stability. Also, their resistance to degradation, non-flammability and operating temperatures can be enhanced by organic fluids. For ceramic matrix composites, fibers are incorporated into them to preserve the high processing temperature and they have inherent resilience to oxidation and deterioration [3].

2.1.1 Polymer Matrix Composites

One of the most widely used types of composite structure is polymer matrix composites. They are mixtures of polymers with inorganic and organic additives having certain geometries, such as fibers, flakes, spheres and particulates. Polymers have many advantages over other types of materials, since processing polymers does not require high pressure and high temperatures, and the processing cost is low. Also, they have low density and have many useful characteristics, such as tensile strength, modulus, elongation and impact strength [16].

Polymers can be categorized into two main groups: thermoplastics and thermosets. Thermoplastics are linear or branched structure materials with no chemical linking between them. By the application of heat and pressure, weak secondary forces such as van der Waals and hydrogen forces are broken temporarily and material takes a new shape. Upon cooling, the secondary forces are restored resulting in a new solid shape. On the other hand, thermoset polymers are crosslinked networks. When they are heated, they undergo curing reactions, so they could be made to flow under stress only once. If further heating is applied degradation occurs and no softening or flow can be seen [4]. In uncured state, thermoset polymers have low viscosities compared to thermoplastic materials; this facilitates the wetting out of the reinforcement. However, their hard processing and long production rates make them less preferable compared to thermoplastics.

2.2 Nanocomposites

Polymers are filled with particles in order to improve the stiffness and the toughness of the materials, to increase their barrier properties, to enhance their resistance to fire and ignition or simply to reduce cost. Nanocomposites are a new class of polymer composites. International Union of Pure and Applied Chemistry specification defines them as "composite materials in which at least one of the phases has at least one dimension of the order of nanometers" [17]. They are mostly used in automotive, aerospace, telecommunication, housing, coating, electronic and packing industries due to their transparency, low density, reduced flammability, low permeability, and enhanced thermal and mechanical properties [18].

In nanocomposites, relatively low filler content, less than 6 %, is used to achieve optimal properties. Nevertheless, this is not valid for traditional polymer nanocomposites containing larger particles such as talc or short fibers (glass, carbon, aramid). The major differences between conventional composites and nanocomposites result from the fact that the latter have much larger interfacial area per unit volume leading to unique phase morphology [19].

One can distinguish three types of nanocomposites, depending on how many dimensions of the dispersed particles are in the nanometer range.

6

- *Isodimensional nanoparticles:* When the three dimensions are in the order of nanometers, we are dealing with isodimensional nanoparticles, such as spherical silica nanoparticles obtained by in situ sol–gel methods or by polymerization promoted directly from their surface, but also can include semiconductor nanoclusters and others [20-22].

- *Two–dimensional nanoparticles:* When two dimensions are in the nanometer scale and the third is larger, it forms an elongated structure, such as nanotubes or whiskers. For example, carbon nanotubes or cellulose whiskers, which are extensively studied as reinforcing nanofillers, yield materials with exceptional properties [23, 24].

- *One–dimensional nanoparticles:* The third type of nanocomposites is characterized by only one dimension in the nanometer range. In this case the filler is present in the form of sheets of one to a few nanometer thick to hundreds to thousands nanometers long. This family of composites can be gathered under the name of polymer-layered crystal nanocomposites, and they will be the main object of this study. These materials are almost exclusively obtained by the intercalation of the polymer (or a monomer subsequently polymerized) inside the galleries of layered host crystals. Table 2.1 presents a list of possible layered host crystals [25].

Table 2.1 Examples of layered host crystals [25]

Chemical Nature	Examples
Metal Chalcogenides	$(PbS)_{1.18}(TiS_2)_2$, MoS_2
Carbon Oxides	Graphite Oxide
Metal Phosphates	$Zr(HPO_4)$
Clays and Layered Silicates	Montmorillonite, hectorite, saponite, fluoromica, fluorohectorite, vermiculite, kaolinite, magadiite, etc.
Layered Double Hydroxides	$M_6Al_2(OH)_{16}CO_3.nH_2O$; M=Mg, Zn

2.2.1 Polymer – Layered Silicate Nanocomposites

Among all the potential nanocomposites discussed above, those based on clay and layered silicates have been more widely investigated probably because the starting clay materials are easily available and their intercalation chemistry has been studied for a long time [26, 27].

Polymer–layered silicate nanocomposites have several advantages owing to the nanometer-size particles obtained by dispersion. They are lighter in weight compared to conventional composites and they exhibit outstanding diffusional barrier properties without requiring a multipolymer layered design. Also their mechanical properties are potentially superior to unidirectional fiber reinforced polymers, because reinforcement from the inorganic layers will occur in two rather than in one dimension [28]. Another important point that makes polymer–layered silicate nanocomposites preferable is that their fabrication techniques are much easier and cheaper than the fabrication of conventional composites since they can attain the composite properties with low volume fraction of reinforcement.

2.2.2 Structure of Layered Silicates

As mentioned previously, fillers are added into polymer matrix to enhance physical properties such as mechanical, thermal, flame retardancy, processing characteristics, and barrier properties or to lower the cost. In order to improve the mechanical properties of polymer matrix composites, high aspect ratio (glass fibers, mica, clay minerals, and carbon nanotubes) and low aspect ratio (talc, kaolin, $CaCO_3$, glass spheres, and wood flour) fillers can be used.

Clay minerals are hydrous aluminum silicates and are generally classified as phyllosilicates, or layered silicates. Layered silicates that are used in the preparation of polymer–layered silicate nanocomposites belong to the 2:1 phyllosilicates family and they are among the large number of inorganic layered materials that have the capability of intercalation [29]. Their crystal lattices are generated by a combination of tetrahedral and octahedral sheets. In order to form 2:1 layered silicates, a natural stacking of those tetrahedral and octahedral sheets

occurs in the specific ratios and modes. Silica is the main component of a tetrahedral sheet, while octahedral sheet comprises diverse elements such as Al, Mg, and Fe. Those sheets are arranged as 1 nm thin layers, with an octahedral sheet sandwiched between two tetrahedral silica sheets. These layers organize themselves to form stacks with a regular van der Waals gap between them, which is called the interlayer, gallery or basal spacing.

This distance between the sheets of silicate layers can be determined by X-Ray Diffraction patterns which will be discussed later. It gives two categories of information; the first one is the basal 001 reflection that gives the distance between equivalent layers of basal oxygens or hydroxyl-oxygens and the second one is the two-dimensional hk diffraction bonds, which are independent from the basal spacing and are the same in all smectite types.

The phyllosilicate 2:1 layer clays include mica, smectite, vermiculite, and chlorite. Smectite group can be further divided into montmorillonite (MMT), saponite and hectorite species   [30]. Their chemical formulas are shown in Table 2.2 and chemical structures are given in Figure 2.1 [25].

Table 2.2 Chemical formulas of commonly used smectite type layered silicates

Layered Silicate	General Formula*
Montmorillonite	$M_x(Al_{4-x}Mg_x)Si_8O_{20}(OH)_4$
Saponite	$M_xMg_6(Si_{8-x}Al_x)O_{20}(OH)_4$
Hectorite	$M_x(Mg_{6-x}Li_x)Si_8O_{20}(OH)_4$

*M = monovalent cation; x = degree of isomorphous substitution.
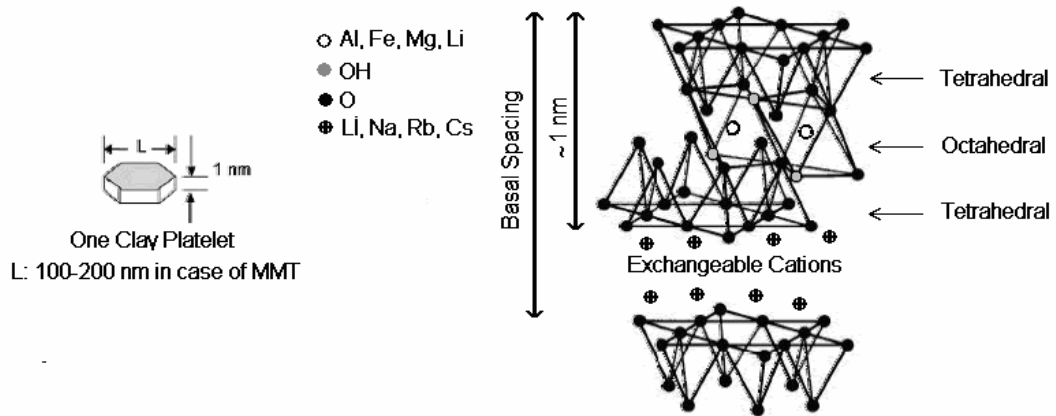
Figure 2.1 Chemical structure of commonly used smectite type layered silicates [25]

2.2.3 Montmorillonite

Between the various kinds of layered silicates, MMT is particularly attractive as reinforcement for the polymer–clay nanocomposites because it is environmentally friendly, readily available in large quantities with relatively low cost and its intercalation chemistry is well understood. It is a naturally occurring 2:1 phyllosilicate, which has the same layered and crystal structure as talc and mica but a different layer charge.

Montmorillonite has a high surface area about 750 m^2/g and its crystal lattice is composed of two silica tetrahedral sheets (SiO_4) and an octahedral alumina sheet ($AlO_4(OH)_4$) between tetrahedrons.

2.2.4 Organic Modification of Silicate Layers

Isomorphic substitution within the silicate layers, such as Al^{+3} replaced by Mg^{+2} or by Fe^{+2}, or Mg^{+2} replaced by Li^+, generates negative charges. These negative charges are balanced by alkali or alkaline earth cations (Na^+, Li^+ or Ca^{+2}) positioned in the gallery between the layers and these negative charges are usually quantified as the cation-exchange capacity (CEC meq/100g) [6]. The

gallery height of pristine clay is determined by the type of cations positioned in the gallery and the degree of hydration.

The presence of cations on the surface of the silica sheets generally increases the basal spacing of the clay crystal, but it also makes the clay crystal hydrophilic and thus incompatible with many hydrophobic engineering polymers. So the layered silicates are not easily dispersed in most polymers [31]. In order to make these hydrophilic phyllosilicates more hydrophobic, the hydrated cations of the interlayer can be exchanged with cationic surfactants such as alkylammonium or alkylphosphonium ions [29]. The interlayer spacing is usually larger for modified layered silicates because organic cations are bulkier than hydrated inorganic cations. The modified layered silicates are more compatible with organic polymers because of the lower surface energy. In addition, the organic cations may provide various functional groups that can react with the polymer chain to increase adhesion between the inorganic filler and the organic polymer matrix [28, 32]. The cation-exchange process between the alkylammonium ions and the exchangeable cations of layered silicate is shown in Figure 2.2.
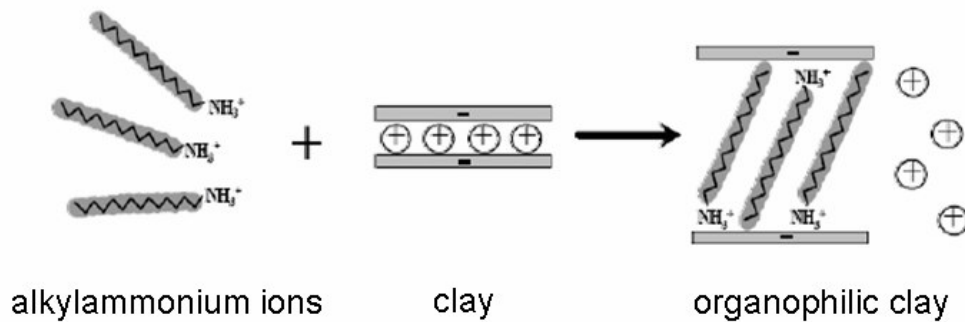
Figure 2.2 Cation exchange process between alkylammonium ions and exchangeable cations of layered silicate [33]

It should be noted that, as the negative charge originates in the silicate layer, the cationic head group of the alkylammonium molecule preferentially resides at the

11

layer surface, leaving the organic tail radiating away from the surface. In a given temperature range, two parameters then define the equilibrium layer spacing: the cation exchange capacity of the layered silicate, driving the packing of the chains, and the chain length of organic tail(s). So, depending on these parameters different arrangements of the onium ions are possible. The organic chains may lie either parallel to the silicate layer, forming mono or bilayers, depending on the packing density and the chain length, or radiate away from the surface, forming mono or even bimolecular tilted `paraffinic' arrangement [34, 35] as shown in Figure 2.3.
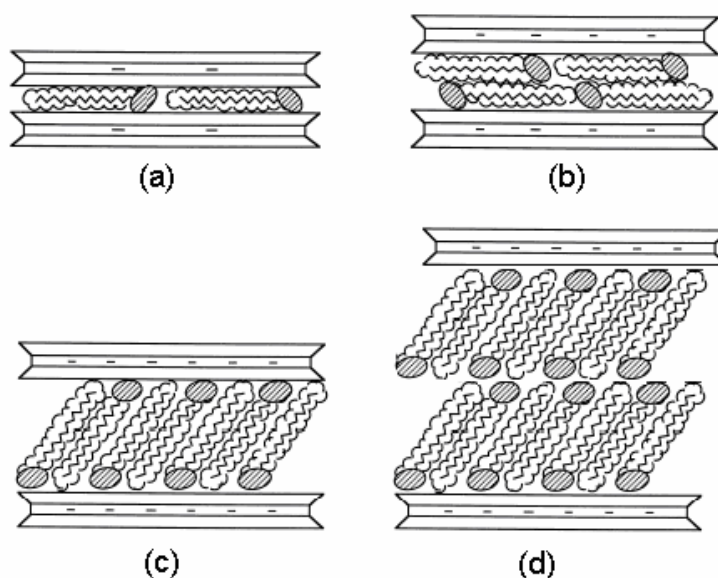
Figure 2.3 Orientation of alkyl chain in layered silicates: (a) lateral monolayer; (b) lateral bilayer; (c) paraffin-type monolayer and (d) paraffin-type bilayer [36]

2.2.5 Nanocomposite Structure Types

Nature of the components used, synthesizing methods, strength of the interfacial interactions and the clay loading directly affect the structure of the polymer–layered silicate nanocomposite. It is not always possible to end with a nanocomposite when the organoclay is mixed with a polymer, the dispersion of the clay platelets

should be in nanometer range. Nanocomposites have much higher surface area for polymer filler interaction compared to conventional composites [7, 37].

Depending on the structure of dispersed clay platelets in the polymer matrix, the composites can be categorized into three main groups; phase separated composites (conventional composite), intercalated nanocomposites, and exfoliated nanocomposites. Figure 2.4 shows the types of nanocomposites structures.
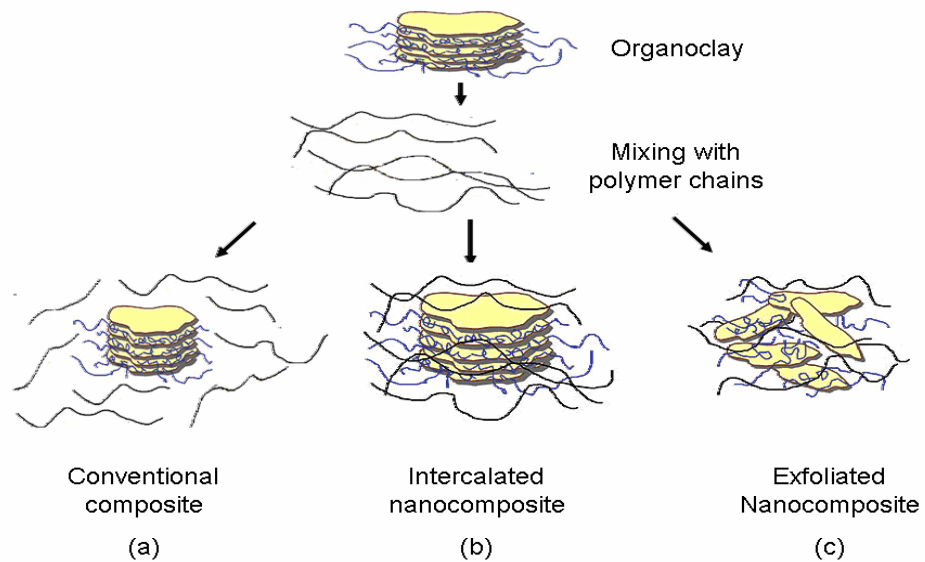
Figure 2.4 Types of nanocomposites structures [11]

If the polymer and clay are incompatible, the clay platelets remain as large stacks and no polymer chains get inserted between the layers. In this type of structures the clays are called tactoid and the properties of the composite stay in the same range as traditional conventional composites with poor properties (Figure 2.4.a).

Intercalated structures (Figures 2.4.b) are formed when polymer chains are inserted between the silicate layers, while the stacking order remains the same as

in microcomposites. This leads to an expansion of the interlayer spacing by less than 20-30 Å.

When the clay layers are completely pushed apart to create a disordered array and they are uniformly dispersed in continuous polymer matrix, the composite is considered to be exfoliated or delaminated. As a result of this delamination, the silicate sheets lose their geometry leading to a larger surface area with improved properties. However, fully exfoliated structure is rarely seen in practice. Instead, partially exfoliated and partially intercalated structures can be seen more often [10, 11].

2.2.6 Nanocomposite Preparation

Several methods have been considered to prepare polymer-layered silicate nanocomposites. They include three main processes; In-situ intercalative polymerization, solution intercalation and melt intercalation methods.

2.2.6.1 In-Situ Intercalative Polymerization Method

In this technique, the insertion of a suitable monomer into the clay galleries is followed by polymerization (Figure 2.5). Polymerization process requires an initiator and this initiator can be heat or radiation, diffusion of a suitable initiator or an organic initiator or a catalyst fixed through cation exchange inside the interlayer [18].

The polarity of monomer molecules is the driving force for in-situ intercalative method. Polar monomer molecules are attracted to the clay surface due to high energy surface, thus they can diffuse between the clay layers. Then, polymerization reaction starts by the attraction between the monomer and the curing agent. Finally, the organic molecules delaminate the clay layers [38].

Remarkably improved properties can be achieved by this nanocomposite preparation method. However, it is limited to small size reactors. Also, the presence of additives in the system results in complicated reactions, which makes

14

the materials complicated in large scales. Thus, bulk production of the nanocomposites by this method is very unlikely in industry.
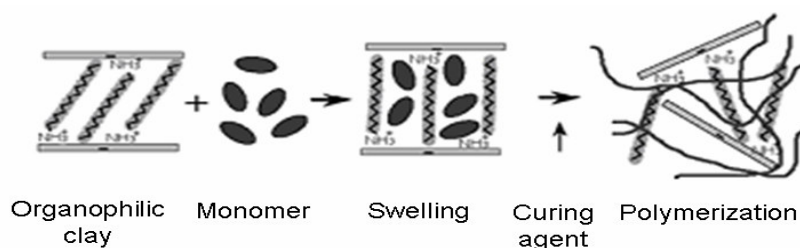
Figure 2.5 In-situ intercalative polymerization method [38]

2.2.6.2 Solution Intercalation Method

This nanocomposite preparation technique is based on a solvent system, the polymer is first dissolved in a solvent and then the modified layered silicate is added to the system. Clay platelets can be easily dispersed in an adequate solvent owing to the weak van der Waals forces that hold the clay platelets together. After the adsorption of polymer onto the delaminated sheets, the solvent is evaporated. The layers of the clay do not collapse back and they reassemble, sandwiching the polymer to form an ordered multilayer structure (Figure 2.6).

The entropy, which is gained by desertion of the solvent molecules, is the driving force of this method. The decrease in conformational entropy of the intercalated polymer chains is compensated with the entropy gained by desorption of the solvent molecules. For that reason, large number of solvent molecules must be desorbed from the clay to accommodate the incoming polymer chains [38].

This method is suitable for the polymers with little or no polarity. However, the use of large amounts of inorganic solvents that is environmentally unfriendly and economically prohibitive is one of the major drawbacks [37].
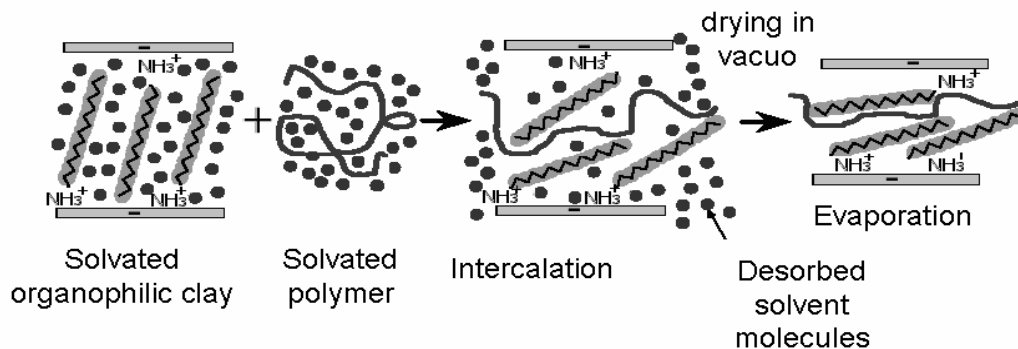
Figure 2.6 Solution intercalation method [38]

2.2.6.3 Melt Intercalation Method

Melt intercalation is a broadly applicable method to many commodity and engineering polymers, from non-polar polystyrene, polyolefin, weakly polar PET to strongly polar polyamide. It is a versatile process to prepare the clay–polymer nanocomposites which can be obtained by direct polymer melt intercalation, where molten polymer chains diffuse into the space between the clay layers or galleries [9, 39, 40]. The process is accomplished above the glass transition temperature of the polymer matrix in either static or flow conditions to complete the diffusion of macromolecules into the galleries (Figure 2.7). This solvent-free technique requires the polymer to be compatible with the clays, and the filler agglomerates are dispersed when the hydrodynamic separating forces applied by the matrix exceed the cohesive forces. When the processing conditions are optimized, the polymer can be inserted between interlayer spacing and form either an intercalated or an exfoliated nanocomposite [41].

The main difference between melt processing and other preparation methods is that strong shear forces act on the system, and these forces affect the dispersion of clay platelets. Besides the shear forces, matrix viscosity and the mean residence time also affect degree of the dispersion [10].

Interaction between the polymer matrix and silicate creates an enthalpic contribution and this contribution drives the melt intercalation process. Although an entropy loss occurs due to melt confinement, it is compensated by the entropy gain associated with layer separation, resulting in a net entropy change near to zero. Thus, the outcome of nanocomposite formation by melt intercalation depends primarily on energetic factors, which may be determined from the surface energies of polymer and organically modified layered silicates [37].
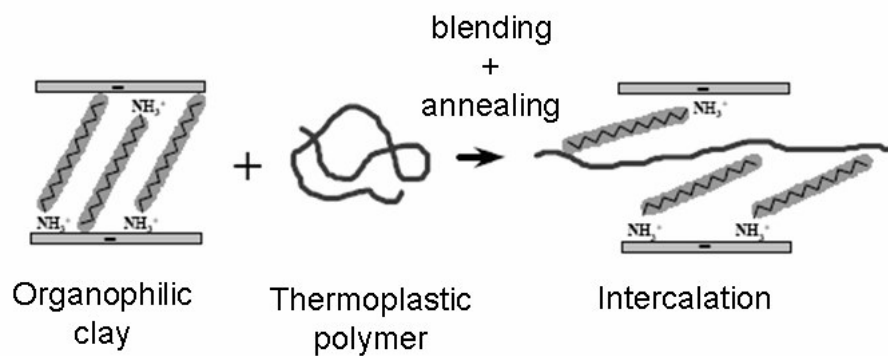
Figure 2.7 Melt intercalation method [38]

2.3 Polystyrene

Styrene is one of the easiest monomers to polymerize and this led to early discovery and commercialization of polystyrene (PS). Solid polystyrene was probably first prepared in 1845 by heating the monomer in air. At first, the reaction was considered to be an oxidation until Staudinger first proposed the long-chain structure of polymer molecules [42]. The Dow Chemical Company had a major effort in development of a commercial process for polystyrene in the 1930's leading to the can process documented by Boyer [43].

PS is one of the most widely used thermoplastic materials ranking behind polyolefins and PVC. Due to its brittle characteristics, the main development

directions were aimed at copolymerization of styrene with polar comonomers such as methacrylates or maleic anhydride and as impact modified with different rubbers or styrene-butadiene block copolymers, which will be discussed later. It is a linear polyethylene chain with laterally attached phenyl rings, being responsible for the enhanced glass transition temperature and high refractive index. Polystyrene has two different structures according to the side of the chain on which the phenyl groups are attached. Syndiotactic polystyrene has phenyls groups that are attached to the alternating sides of the polymer chain whereas atactic polystyrene has no order. Their chemical structures are shown in Figure 2.8. Stiffness, brilliance, gloss and hardness are the main characteristics of this material [44, 45].
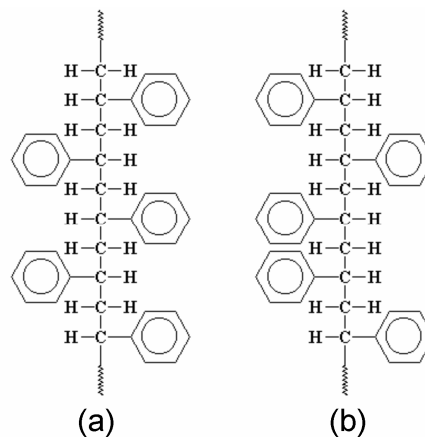
Figure 2.8 Chemical structure of (a) Syndiotactic PS (b) Atactic PS

Commercial polystyrene is an amorphous material with a molecular weight between 100,000 and 400,000. At temperatures sufficiently below glass transition temperature (T_g) and at low deformations, the material obeys Hooke's law of elasticity under external stress. Above its T_g, polystyrene is a viscoelastic melt. It is called viscoelastic, because the polymeric material displays both a viscous and an elastic response to shear stress, depending on the rate and the temperature of the test. Also, there are two main factors that influence the viscous and the elastic

behavior of the product, namely molecular weight and molecular weight distribution [46].

The applications of polystyrene include many areas such as, audio/video cassette packs, beakers, transparent food packing, shower cabinets, lamp covers, toys, electronics, furniture and construction insulations [45].

2.3.1 Polymerization of Styrene

Styrene is able to polymerize under free radical, anionic, cationic and metal catalyzed conditions. This is due to low polarity of the styrene molecule and to the resonance stabilization of the growing polystyrene species in the transition state.

In the polymerization of styrene, it is assumed that upon heating styrene forms a Dies–Alder intermediate product which isomerizes to phenyltetralin or transfers a hydrogen atom to a further styrene molecule forming two radicals in a solvent medium, and diffusion of the radicals from solvent medium lead to subsequent polymerization to polystyrene. The polymerization reaction is terminated by disproportionation or recombination to cyclic dimmers and trimers, with the ratio depending mainly on the temperature [47]. Polymerization steps are schematically shown in Figure 2.9.
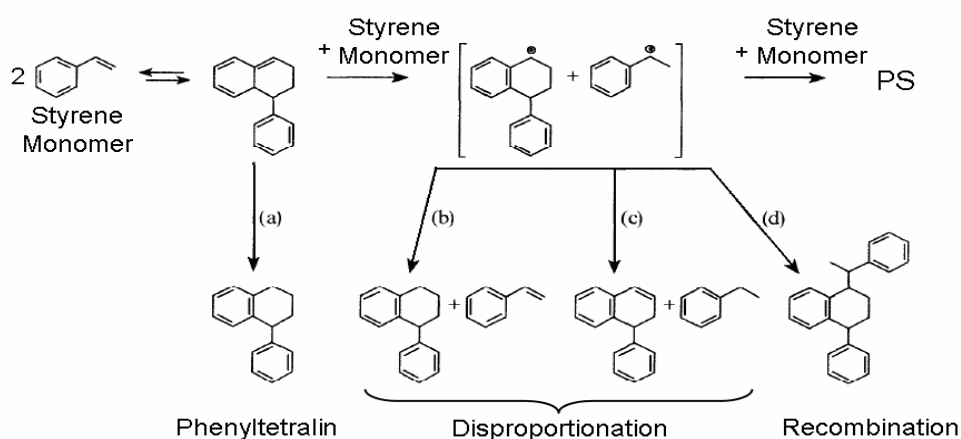
Figure 2.9 Polymerization of styrene [46]

19

In addition to the thermal initiation, the use of peroxides and azo components is a common and well established method to start the chain reaction. These materials increase the rate of the polymerization and grafting efficiency.

2.4 Impact Modification of Polystyrene

One of the most important weaknesses of polystyrene is its poor impact resistance. At high impact and deformation rates, this material tries to withstand the external stress by forming crazes to dissipate the impact energy to a broader area. Those crazes are the precursors for cracks and the reason for the formation of them lies in the insufficient segment mobility of the molecular chain. To overcome this drawback, polymer matrix is blended with different types of rubbery materials.

Rubber modified polystyrene exhibits higher toughness than polystyrene by preventing crazes from developing into cracks. The rubber particles constitute the dispersed phase in the polymer matrix. Generally, small dispersed particles enhance the stress concentration while larger ones stop the growth of cracks. In order to establish this mechanism, a well defined adhesion of the rubber particles to the matrix is required [48, 49]. Rubber particles dissipate impact energy by transforming it into deformation of themselves, eventually by the formation of voids in the rubber phase itself. Difference between the formation of crazes after mechanical impact for brittle materials and rubber toughened materials is shown in Figure 2.10. When the toughened material is subjected to uni-axial stress the localized stress nearby a rubber particle is magnified by the local stress concentration effect of the particle. The matrix will yield locally in response to this localized stress field, thus avoiding a brittle failure of the material [46].
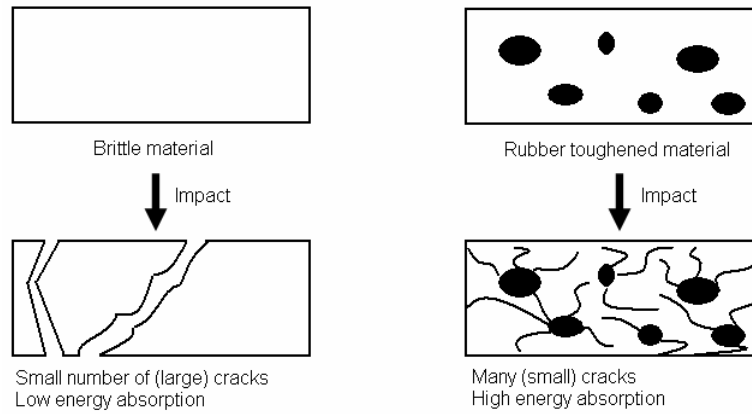
Figure 2.10 Craze formation after mechanical impact [46].

The improvement in the toughness of the brittle styrenic polymers can be seen in several commercialized systems. Thus, the glassy and brittle polystyrene is transformed into high impact polystyrene (HIPS), which is used as an engineering material successfully.

2.4.1 High Impact Polystyrene (HIPS)

High impact polystyrene, which is referred as HIPS, is an elastomer modified polystyrene thermoplastic. This versatile product can be found in many compositions for applications in the automotive, appliance, power tool, furniture, housewares, telecommunication, electronic, computer, medical, packing, and recreation markets.

In the process of HIPS, polybutadiene (PB) phase is dissolved in monomer styrene followed by the free radical polymerization. Thus, some of the growing styrene polymer chains graft on to the polybutadiene rubber (Figure 2.11). Polystyrene homopolymer is preferred for its clarity, rigidity and dimensional stability. In addition to these properties HIPS is valued for its high impact strength compared to polystyrene. However, HIPS has some disadvantages such as poor high-temperature properties, poor oxygen barrier properties, relatively low ultraviolet light stability and low chemical resistance [50]. PS and PB homopolymers do not

21

mix and PB branches form little globs. But these little globs are always tied to the PS phase and act to absorb energy when the polymer gets hit with something [51].
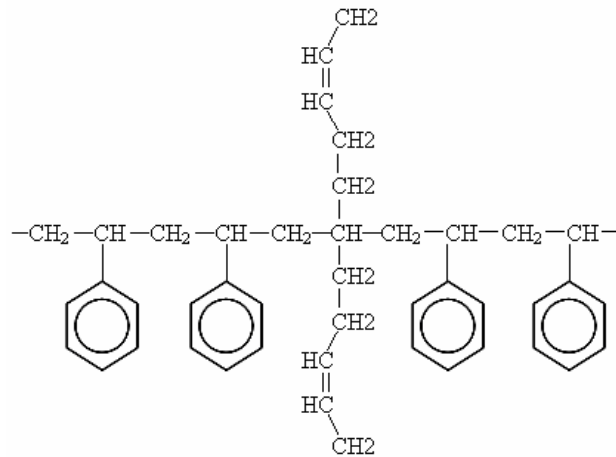
Figure 2.11 Chemical structure of HIPS [51]

The tensile strength of HIPS increases with decreasing temperature and increasing strain rate. This is an expected characteristic of a rubber toughened system. On the other hand, elongation at break value decreases as the temperature drops and the deformation rate increases. Temperature has a significantly greater effect on the mechanical properties of HIPS when compared with the effect of deformation rate.

2.4.2 Styrene Block Copolymers as Impact Modifiers

For the impact modification of polystyrene, mostly block copolymers, which are compatible with the polymer matrix, are used. Compatibility is directly related with the ability of the rubber phase to disperse itself uniformly to reduce interfacial tension and to improve adhesion [52]. There are several types of block copolymers used for impact modification, but commercially available styrene-rubber-styrene

block copolymers, in which the outer styrene blocks serve to anchor the middle rubber block, are preferred.

Styrenic block copolymers have useful properties because of their ability to form distinct styrene (hard phase) and diene (rubber phase) domains, with well defined morphologies. To achieve this, requires an unusual degree of control over the polymerization, which must yield discrete blocks of a uniform and controlled size. Most styrene containing block copolymers are manufactured using anionic polymerization chemistry. However, the most important disadvantage of this method is; it is the costly polymerization chemistry because of the stringent requirements for monomer and solvent purity.

Theoretically, butadiene rubber block is useful to prepare block copolymers. However, degradation and crosslinking of this phase at high processing temperatures, about 300˚C for PS, is an expected result. In order to prevent this, butadiene block is hydrogenated to give SEBS polymer. Using these SEBS block copolymers, impact strength can be increased with a high molecular weight product [46]. The reason for better impact modification with increasing molecular weight of the block copolymer depends on the molecular weight of the rubber block and the rubber particle size in the PS matrix. As the molecular weight of rubber block increases, the impact strength increases, and with increasing viscosity the size of the dispersed particles increases leading to higher impact strength.

2.5 Morphology Development

The morphology development during melt blending of partially or completely immiscible polymers involves processes such as, fluid drops stretching into threads, break-up of the threads into smaller droplets and coalescence of the droplets into larger ones. The type of the morphology depends on the material characteristics of the constituent polymers, their volume fractions and mixing conditions [52].

There are three basic morphologies for binary blends; dispersed, stratified and co-continuous morphologies. The dispersed morphology is formed by the breaking up of the minor phase during melt mixing. The size and the shape of the dispersed

23

phase are determined by the interfacial tension, rheological properties, volume fractions of the components, melt viscosity and the complex strain field in the mixer [53].

According to the general criteria for phase inversion, the phase with the lower viscosity tends to be the continuous phase because of its tendency to flow around the higher viscosity phase. Also, the phase with larger volume fraction tends to be the continuous phase [54]. The constitution of inversion from dispersed morphology to co-continuous morphology can be defined by percolation theory. According to this theory, at low concentration of the minor phase, there occurs a dispersion of particles in the continuous phase. A gradual change in the structure, from dispersed to fully co-continuous morphology takes place at high minor phase loadings. The concentration ratio that the continuous morphology can be seen is referred as the "phase inversion point".

Phase inversion is an adaptation of a system to an increase in the fraction of the minor phase which generates a maximum interfacial area leading to continuous structure. In a co-continuous morphology, each blend components takes its part in the load sharing and it is important for compatibilizing the immiscible pairs.

This continuous morphology can exist over a range of compositions, depending on the blending conditions [55]. Beyond this range the phase network of the matrix component starts to breakdown until finally this component becomes the dispersed phase. This is because, as the concentration of the minor phase increases, particles become close enough to behave as if they were connected. The further addition of minor phase material extends the network continuity until the minor phase is continuous throughout the sample.

Several empirical relations have been proposed in literature by giving the volume fractions which co-continuity can be formed as a function of the viscosity ratio. Some of the relations that were employed in this study are given in equations below.

Jordhamo et. al. [56] suggested a linear expression as shown in Equation 2.1.

$$\frac{\eta_1}{\eta_2} = \frac{\phi_1}{\phi_2}$$

(2.1)

where, the symbols η and Φ represent the melt viscosity and volume fractions of the pure components respectively.

Chen and Su [57] proposed another model which is limited to low shear rates.

$$\frac{\phi_{hv}}{\phi_{lv}} = 1.2 \left(\frac{\eta_{hv}}{\eta_{lv}} \right)^{0.3}$$

(2.2)

In this model *hv* and *lv* terms define high- and low- viscosity phases.

Chen and Su modified Equation 2.2 and defined a new model [58].

$$\frac{\phi_{hv}}{\phi_{lv}} = \left(\frac{\eta_{hv}}{\eta_{lv}} \right)^{0.3}$$

(2.3)

Another model, which was proved by Jordhamo, was defined by Paul and Barlow [59].

$$\frac{\phi_1}{\phi_2} = \frac{\eta_1(\dot{\gamma})}{\eta_2(\dot{\gamma})}$$

(2.4)

Where, $\dot{\gamma}$ is shear rate.

The model proposed by Metelkin and Blekht [60] gives the following relation.

$$\phi_1 = \left[1 + \frac{\eta_1}{\eta_2} \left(1 + 2.25 \log\left(\frac{\eta_1}{\eta_2} \right) + 1.81 \left(\log\left(\frac{\eta_1}{\eta_2} \right) \right)^2 \right) \right]^{-1}$$

(2.5)

2.6 Polymer Processing Methods

To obtain desired size and shaped finished products, polymers are subjected to different processing methods. In this study, nanocomposites were prepared by extrusion and samples for mechanical tests were produced by injection molding.

2.6.1 Extrusion

The dictionary meaning of the extrusion is the act of pushing or squeezing out by applying pressure. Extrusion process is used to produce plastic products such as plastic film, sheet, profiles and mostly pellets. Extrusion is not only an adding or mixing process but also a shaping process [61]. The feed of the extrusion process is mostly in solid state and subjected to melting, mixing and pressurization in the extruder [7].

During the extrusion process, volatiles such as solvents, water, or trapped air can easily be removed. The normal form of the product from extrusion process is thin rods that are chopped into pellets. In addition to the long, thin rods that are chopped into pellets, other common extruded shapes include; pipes, sheets, fibers, coatings on wire and cable, coatings on paper, etc.

Thermoplastics are the most common plastics that are extruded. However, some thermosets can also be extruded, provided the temperature of the extruder is kept below the temperature that initiates the cure [62].

2.6.1.1 Continuous Screw Extruders

Screw extrusion machines consist of a screw of special form rotating in a heated barrel or cylinder. In absolute terms, probably the most referenced number for extruder specification is the L/D ratio (barrel length/barrel diameter) as this defines many of the operating characteristics of the extruder for all types. The L/D ratio is a major factor in the effectiveness of the extruder and of the types of material that it can process. For most extruder types, the L/D ratio has increased as technology has advanced. The limitation to high L/D ratios is the torque available from the

motor (longer screws mean higher friction) and the capacity of the thrust bearings of the extruder [63].

In the extrusion process in screw extruder, the polymer is fed to the cavity between the screw section and extruder barrel from the feed hopper. The barrel and screw are zoned into between 3 and 7 sections which are individually heated and cooled depending on the material and process parameters. As the screw rotates the material is dragged forward, compressed and heated. Then, the molten polymer is transmitted to the die section in a viscous state to form the basic shape of the desired product. The extruded polymer is still soft and flexible as it leaves the die. Thus, it is controlled by sizing devices, cooling devices and fixtures to shape it into its final configuration [63, 64]. Schematic drawing of extrusion line for continuous screw extruders is shown in Figure 2.12.
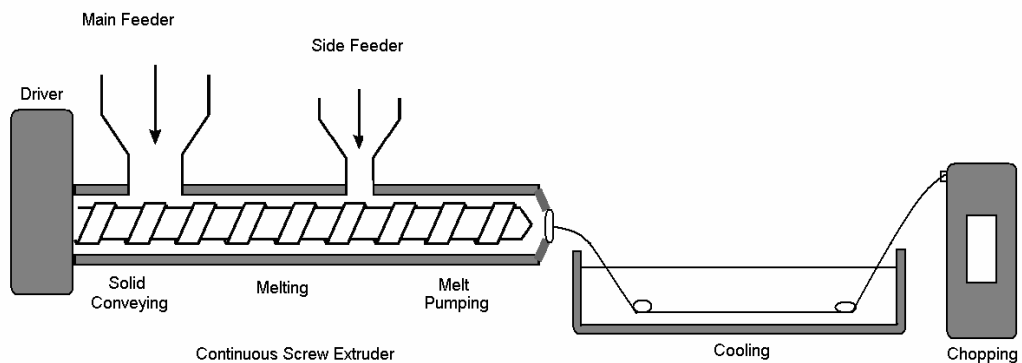
Figure 2.12 Extrusion line for continuous screw extrusion

2.6.1.2   Basic Continuous Screw Extruder Types

Continuous screw extruders can be classified in two main groups; singe screw and multiple screw extruders. Among multiple screw extruders the most commonly used type is the twin screw extruders.

Twin Screw Extruder:

Today, the twin screw extruders are more advanced, offering many advantages to the modern processor. As more companies see these advantages, the trend is toward twin screw extruders. Some of their advantages are good mixing, good heat transfer rate and large melting capacity. These types of extruders have more positive pumping action when compared to single-screw extruders and can therefore be used more effectively in high-output situations. This feature of twin-screw machines has led to their use in some applications which volume is critically important [65].

Different screw configurations are possible for twin-screw extruders; these are non-intermeshing twin screws and intermeshing twin screws. When the distance between the flights is large, the design is called non-intermeshing. This type of measure relieves the enforced pumping effect to some extent and allows backflow. In the intermeshing design, the relative motion of the flight of one screw inside the channel of the other acts as a paddle that pushes the material from screw to screw and from flight to flight.

While non-intermeshing twin screws are offered only with counter-rotation, intermeshing screws can be employed in a co-rotating or counter-rotating pattern [61]. In co-rotating pattern, the screws rotate in the same direction. This type of extruder support high contact with the extruder barrel, which improves the efficiency of the thermal heating, and provides better mixing compared to other processes. The path also ensures that most of the resin will be subjected to the same amount of shear as it passes between the screws and the barrel. In the counter-rotating patterns pumping is more efficient when compared to co-rotating screw systems. However; total shear applied to the material is low in this systems and makes co-rotating screw pattern more preferential [66, 67]. Figure 2.13 shows these two patterns of a twin screw extruder.
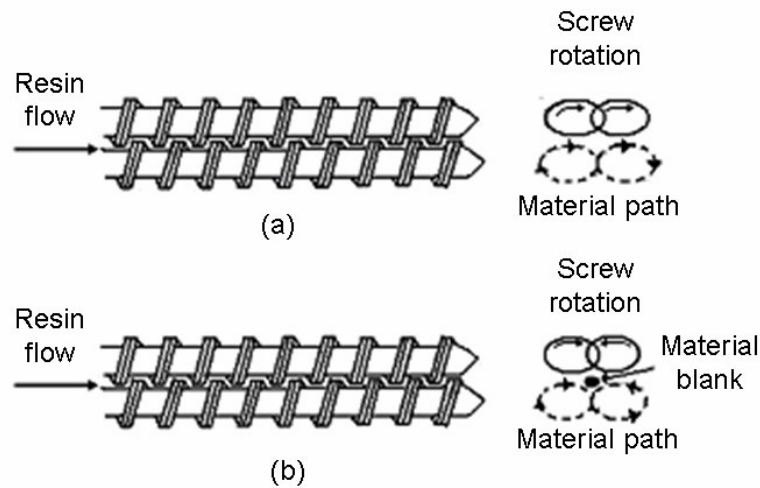
Figure 2.13 Screw Patterns of an Intermeshing Twin Screw Extruder

2.6.2 Injection Molding

During the injection molding processing, discrete parts that can have complex and variable cross sections as well as a range of surface textures and characteristics are produced under high pressure [61].

The process is a simple cycling operation which includes three steps; filling, packing and cooling. Firstly, polymer melt is pushed forward through a nozzle to a cooled cavity of a closed mold which gives the shape to the plastic. After waiting for a sufficient time for the plastic part to solidify, the mold opens and the part is removed. The pressure exerted on the polymer melt by the screw section is kept constant during the filling step. In the packing step, the pressure builds up and it is maintained very high during the cooling stage to minimize shrinkage and shape changes [68]. The temperature of the melt is controlled by the temperature control system of the injection unit, but it may also be affected by the injection speed and by the level of back pressure, and it should be kept above the T_m of the polymer. On the contrary, the thermoplastic must be cooled under pressure below T_g and T_m before the opening of the mold followed by part ejection [69].

29

Polymer Characterization

In order to determine the properties of the newly developed materials and the applications for which the materials can be used, some analyses are required. During this study, morphological, rheological, mechanical and thermal analyses are performed on the prepared samples.

2.6.3   Morphological Characterization

By the help of morphological analysis, such as X-ray diffraction, scanning electron microscopy and transmission electron microscopy, surface and interfacial properties of the nanocomposites can be understood. In this study, X-ray diffraction and transmission electron microscopy analyses were used to investigate the dispersion state of the clay particles and scanning electron microscopy was used to observe the coalescence of elastomeric phase in the polymer matrix.

2.6.3.1   X-Ray Diffraction (XRD)

Arrangement of atoms or molecules within a crystal is determined by X-ray diffraction in which a beam of X-rays is scattered from the electrons within the crystal. A diffraction pattern which varies with scattering angle is produced by the X-rays scattered from different electrons that interfere with each other [70]. The energetic X-rays can penetrate deep into the materials and provide information about the bulk structure.

X-rays are generally produced by either X-ray tubes, which is the primary x-ray source used in laboratory X-ray instruments, or synchrotron. In an X-ray tube, X-rays are generated when a focused electron beam that is accelerated across a high voltage field bombards a stationary or rotating solid target. As electrons collide with atoms in the target, some photons from the incident beam will be deflected away from the direction where they originally travel. If the wavelength of these scattered x-rays does not change, the process is called elastic scattering in that only momentum is transferred in the scattering process. On the other hand, in the inelastic scattering process, X-rays transfer some of their energy to the electrons

and the scattered x-rays will have different wavelength than the incident X-rays [71].

The peaks in an X-ray diffraction pattern are directly related to the atomic distances. Figure 2.14 shows the two scattering planes of atoms, which may be either due to two consecutive clay layers or other crystallographic planes of the layers themselves that are separated by the interplanar spacing.
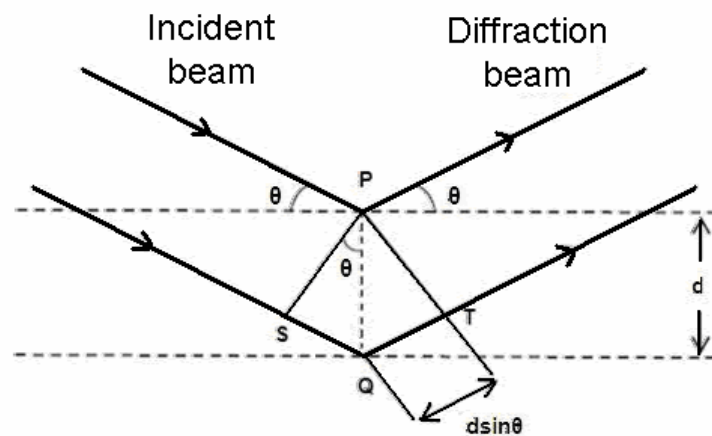
Figure 2.14 Diffraction of X-rays by planes of atoms [3]

For a given set of lattice plane with an inter-plane distance of d (Å), the condition for a diffraction (peak) to occur can be simply written as the following equation, which is the Bragg's law:

$$n.\lambda = 2.d.\sin\theta \tag{2.6}$$

In the equation, λ (Å) is the wavelength of the x-ray, θ (˚) is the scattering angle, and n is an integer representing the order of the diffraction peak [72]. X-ray diffraction techniques can be categorized in two main groups; wide-angle X-ray scattering (WAXS) and small-angle scattering (SAXS). WAXS is a technique which concentrates on scattering angles larger than 5˚ while SAXS probes structure in

the nanometer to micrometer range by measuring scattering intensity at scattering angles close to 0°. The information obtained from scattering at low angles (SAXS) is used for investigation of fibrillar and lamellar structures and detection of cavities whereas wide angle X-ray scattering (WAXS) detects the changes in crystallinity and orientation by which spatial arrangement of atoms is described [73].

2.6.3.2 Scanning Electron Microscopy (SEM)

By using optical light microscopy, some of the fine and small structure elements can be examined. Scanning electron microscopy (SEM) is a method for high-resolution imaging of surfaces. While light microscope uses visible light, SEM uses electrons to form images. When these two microscopes are compared, SEM has many advantages. It has a large depth of field, which allows a large amount of the sample to be in focus at one time, and produces images of high resolution, which means that closely spaced features can be examined at a high magnification. Also, preparation of the samples is relatively easy, since SEM only requires the sample to be conductive. In order to make the surface conductive, the surface of the specimen is coated with a gold-platinum including solution with a sputter coater under vacuum [74, 75].

In the scanning electron microscopy, an incident electron beam is scanned across the sample's surface, and the resulting electrons emitted from the sample are collected to form an image of the surface. Imaging is typically obtained using secondary electrons for the best resolution of fine surface topographical features. Alternatively, imaging with backscattered electrons gives contrast based on atomic number to resolve microscopic composition variations, as well as, topographical information [76].

2.6.3.3 Transmission Electron Microscopy (TEM)

Among the microscopy techniques, TEM is often used with thin materials (less than 100 nm thick) in which different regions within the sample absorb electrons differently. With this technique, objects to the order of a few angstroms (10^{-10} m) can be seen and details in the cell or different materials down to near atomic levels can be studied [75].

The electrons that travel through vacuum in the column of microscope are emitted by a light source at the top of the microscope. In the TEM analysis, electromagnetic lenses are used to focus the elements into very thin beam, instead of glass lenses that focus the light in the microscope. The electron beam then travels through the specimen to be studied. Depending on the density of the material present, some of the electrons are scattered and disappear from the beam. At the bottom of the microscope, the unscattered electrons hit a fluorescent screen, which gives rise to a shadow image of the specimen with its different parts displayed in varied darkness according to their density. The image can be studied directly by the operator or photographed with a camera [77]. Figure 2.15 shows the schematic representation of TEM.
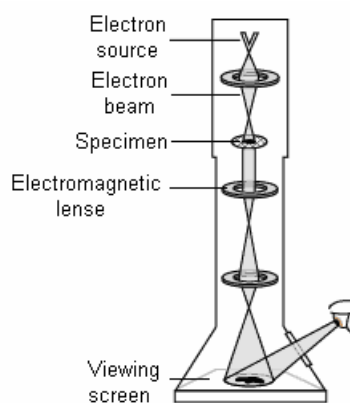
Figure 2.15 Schematic representation of TEM [77]

2.6.4 Rheological Characterization

The final morphological structure and mechanical properties of polymeric composites are directly related with the flow characteristics of the materials. To obtain the apparent and true viscosities of the base materials, capillary viscometer was used. For further analysis of the effect of nanoparticles, MFI test was performed.

33

2.6.4.1 Capillary Viscometry

The viscosity of Newtonian fluids can be measured by using capillary viscometer. This method measures the time taken for a defined quantity of fluid to flow through a capillary with known diameter and length. It consists of a very small, cylindrical tube and a liquid or viscous melt is forced through the capillary by imposing a pressure drop. The very small diameter of the tube, the very large length to diameter ratio minimizes entrance and exit effects and ensures a fully developed velocity profile [78].

For all fluids, the shear stress at the tube wall (τ_{wall}) is shown as below:

$$\tau_{wall} = \frac{\Delta P.R_c}{2.L_c} \tag{2.7}$$

In which ΔP is pressure drop across the capillary tube, R_c is the inside capillary tube radius and L_c is capillary tube length.

For a laminar, incompressible, Newtonian fluid the apparent shear rate (Γ) at the tube wall is defined by the relation:

$$\Gamma = \frac{4.Q}{\pi.R_c^{3}} \tag{2.8}$$

where, Q is volumetric flow rate.

To get viscosity, the slope of the plot τ_{wall} versus Γ is used, since the following relation is true for Newtonian fluids:

$$\tau_{wall} = \mu.\Gamma \tag{2.9}$$

For Non-Newtonian fluids the equations mentioned above need Rabinowitsch correction. The shear rate is converted into true shear rate (γ_{wall}) by using the following equations:

$$-\dot{\gamma}_{wall} = \Gamma.\left[\frac{3n+1}{4n}\right]$$

(eqn 2.10)

Where, the integer n can be found by the following equation, which indicates the slope of the logarithmic plot of apparent sear rate versus shear stress.

$$\frac{1}{n} = \frac{d\ln\Gamma}{d\ln\tau_{wall}}$$

(eqn 2.11)

2.6.4.2 Melt Flow Index (MFI)

Melt flow index is a measure of the ease of flow of the melt of a thermoplastic. It is inversely proportional to the melt viscosity of the material and defined as the mass of material in grams flowing in 10 minutes through a capillary of specific diameter and length. During the test, pressure is applied by standard alternative gravimetric weights for a prescribed temperature [70].

The material is packed properly inside the capillary and a piston is introduced which acts as an equipment that causes the extrusion of the molten polymer. Then, the sample is preheated for a specified amount of time, and after the preheating, a specified weight is introduced onto the piston. Finally, owing to the weight, shear is exerted on the molten polymer and the polymer melt starts flowing immediately through the die. A sample of the melt is taken after desired period of time and it is weighed accurately.

2.6.5 Mechanical Characterization

For most applications, mechanical properties of the materials are the most important of all physical and chemical properties. There are many ways of achieving the mechanical properties by using standardized testing techniques. Establishment and publication of these standards are often coordinated by professional societies. In the United States, the most active organization is the American Society for Testing and Materials. Strength, hardness, ductility and stiffness are some of the important mechanical properties, and in this study, they are determined by tensile, and impact tests.

35

2.6.5.1 Tensile Test

The aim of the tensile test is to obtain the force required to fracture a specimen and the extent to which the specimen elongates. According to the tensile test standards, the specimens are generally in the shape of rectangular or dogbone, and the ends of the specimen are clamped into the jaws of the testing machine. As the jaws are separated by the application of a known force, the specimen elongates and breaks when the load is higher than the force that the specimen can resists. Drawing of a tensile testing machine is shown in Figure 2.16.
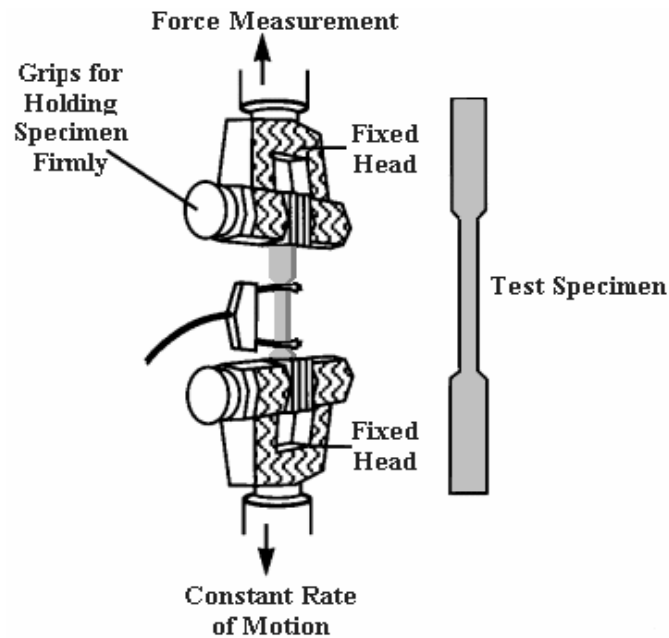
Figure 2.16 Tensile testing machine [73]

Tensile test gives an instantaneous load F (N) versus elongation (mm) chart which is converted into engineering stress σ (MPa) and engineering strain ε (mm/mm) by using the initial gauge length, which is the length of the center section, and initial cross sectional area A_0. The engineering stress and strain are defined by the following equations.

$$\sigma = \frac{F}{A_0} \tag{2.12}$$

$$\varepsilon = \frac{L_i - L_0}{L_0} \tag{2.13}$$

Tensile strength σ_m is the maximum tensile stress that the material can develop. The tensile modulus E (MPa) is the ratio of the stress to the strain where the relationship between stress and strain is linear and it can be defined by Hooke's law [79]:

$$\sigma = E.\varepsilon \tag{2.14}$$

A typical drawing of stress versus strain curve is shown in Figure 2.17. In Figure 2.17.a, the height of the curve when the sample breaks is the tensile strength and the tensile modulus is the initial slope of this curve. On the contrary, in Figure 2.17.b, the height of the curve at yield point gives the tensile strength.
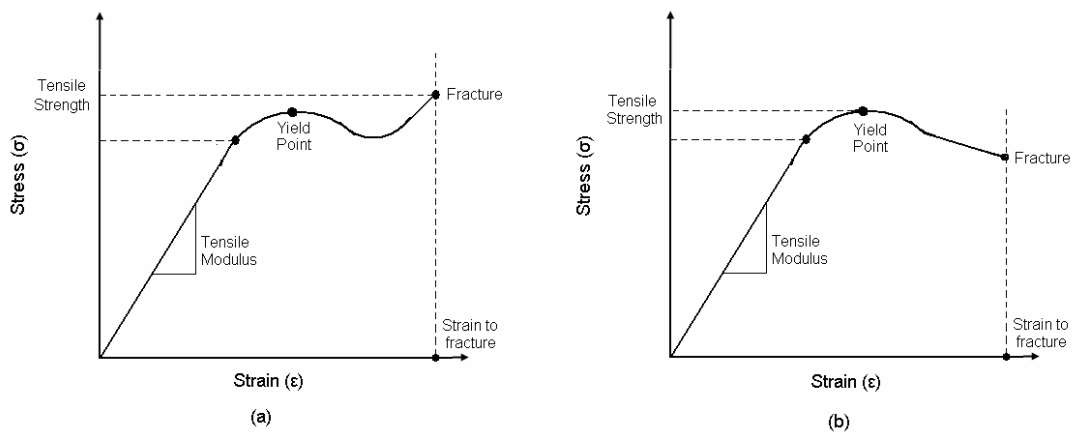
Figure 2.17 Stress strain curves: (a) Tensile strength at fracture; (b) Tensile strength at yield.

There are several types of stress-strain curves which represent the different material properties. Some of them are shown in Figure 2.18.

Soft and weak   Hard and brittle   Soft and tough

Hard and strong   Hard and tough
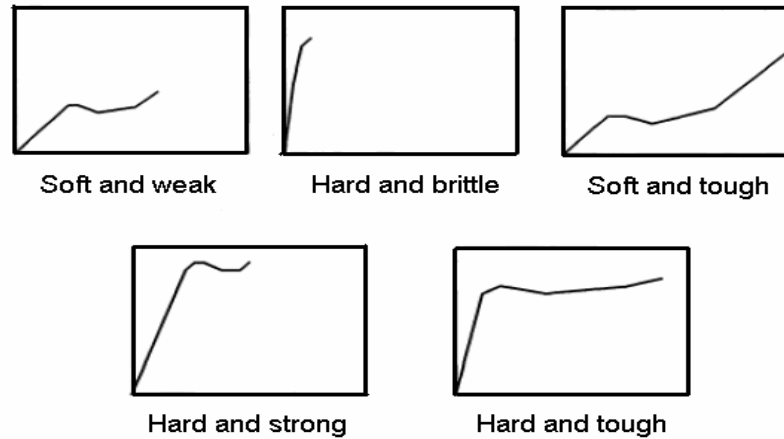
Figure 2.18 Different types of stress-strain curves

2.6.5.2 Impact Test

The ability of a component to withstand a sudden impact is an important issue. By using standardized techniques, it is straightforward to obtain results that allow the comparison of one type of polymer with another. Impact test is a high strain rate test that determines the amount of energy absorbed by a material during fracture [73]. This absorbed energy is a measure of the toughness of a material and used to study the temperature dependent ductile / brittle transition.

There are several types of impact test types as can be seen from Figure 2.19. In the Charpy test, a specimen is held at each end and it is stroke by a hammer with one or two knife edges, which gives a three or four-point impulsive bending respectively. The diagram of standard Charpy impact test is shown in Figure 2.20. In the Izod test, the specimen is held vertical at one end and stroke at the other. For either test, a notch can be cut in the sample at the point where it is to break and the sample is placed in the tester with the notch pointing away [75].

38
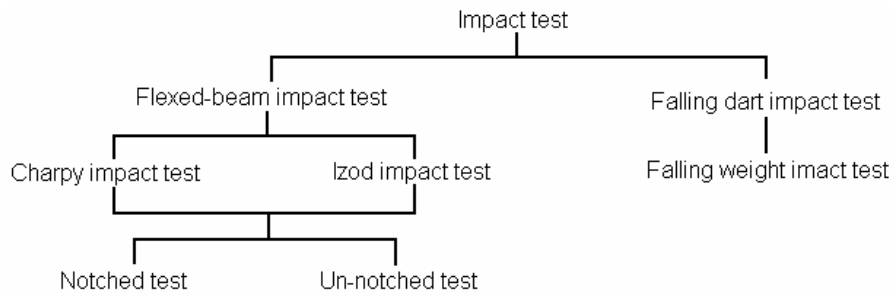
Figure 2.19 Types of impact tests [75]
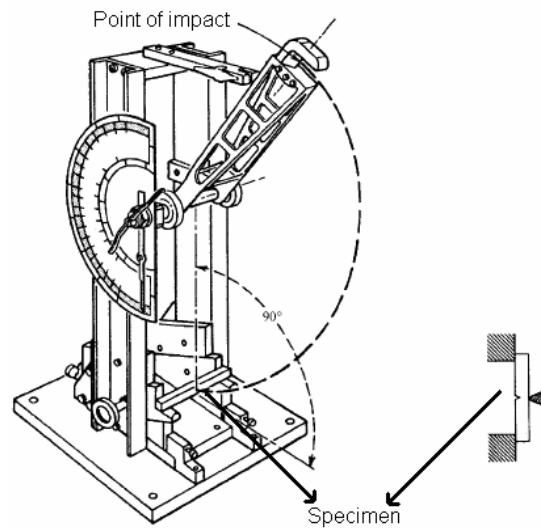
Figure 2.20 Charpy impact test [75]

2.6.6 Thermal Characterization

There are various kinds of analytical techniques to monitor the physical or chemical change of a sample when its temperature is increased or decreased. Thermo-gravimetry (TGA), differential thermal analysis (DTA), and differential scanning calorimetry (DSC) are the three principal thermo-analytical methods. For this work, T_g of the nanocomposites was studied with DSC analysis.

2.6.6.1 Differential Scanning Calorimetry (DSC)

The difference in the amount of heat required to increase the temperature of a sample and reference (empty aluminum pan) are measured as a function of temperature in DSC analysis. It is a thermo-analytical technique in which both the sample and reference are maintained at nearly the same temperature throughout the experiment.

When the sample undergoes a physical transformation such as phase transition, more (or less) heat, depending on whether the process is endothermic (or exothermic), will need to flow to it than the reference, to maintain both at the same temperature. The difference of the heat flow between the sample and reference is sent to an output device which results in a plot of the differential heat flow as a function of temperature (DSC curve). If there is no thermodynamic change, DSC curve shows a flat or very shallow base line on the plot. However, an exothermic or endothermic process within the sample results in a peak.

There are two types of DSC instruments currently used; 'heat flux' and 'power compensation' instruments (see Figure 2.21). In a heat flux calorimeter, heat is transferred to the sample and reference through a disk made of the alloy constantan, while in power compensated calorimeters, separate heaters are used for the sample and reference [70].
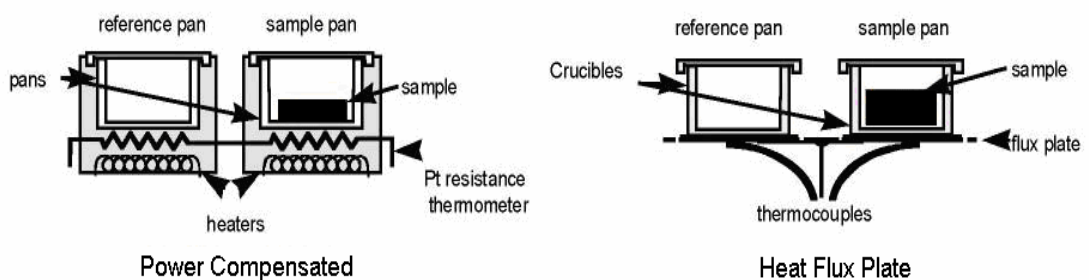
Figure 2.21 Types of Differential Scanning Calorimeters

DSC Curve:

In a DSC curve there are mainly three important points; Glass Transition Temperature, Crystallization Temperature and melting Temperature. They can be shown in a DSC curve as can be seen from Figure 2.22.

When the polymer is heated, the plot shifts downward suddenly. This happens because the polymer has just gone through the glass transition. Because there is a change in heat capacity, but there is no latent heat involved with the glass transition, the glass transition is called a second order transition, whereas transitions like melting and crystallization, which do have latent heats, are called first order transitions. Above the glass transition, the polymers have a lot of mobility and when they reach the right temperature, they gain enough energy to move into very ordered arrangements, which is called crystals. When polymers fall into these crystalline arrangements, they give off heat which results in an upward peak on the DSC curve. The temperature at the highest point is usually considered to be the polymer's crystallization temperature, or T_c. If polymer is kept heating another thermal transition is reached which is called melting. When the polymer reaches to its melting temperature, or T_m, the chains come out of their ordered arrangements, and begin to move around freely. When the polymer crystals melt, they must absorb heat in order to do so. This results in an extra heat flow which is showed as a large dip in DSC plot [80].
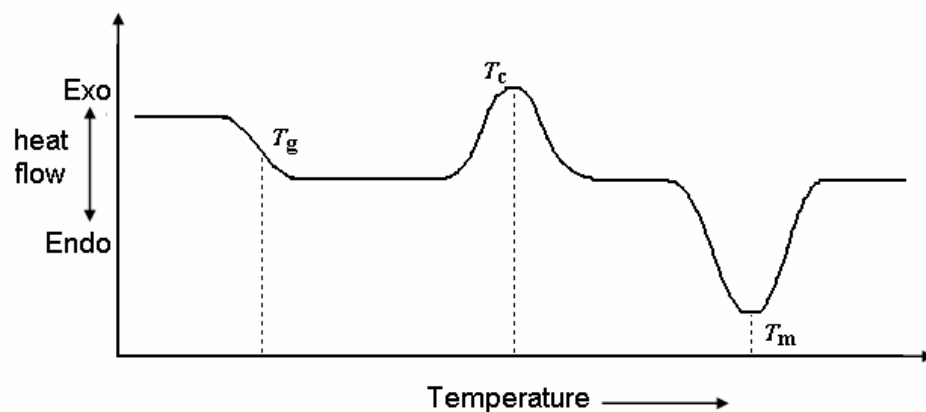
Figure 2.22 An example of DSC Plot

2.7 Previous Studies

Özden [67] studied three different types of nanocomposite preparation methods; melt intercalation, in-situ polymerization and masterbatch method which is a combination of melt intercalation and in-situ methods. Mechanical properties of the PS/organoclay nanocomposites were improved up to certain clay content for all the three methods, but decreased for high clay loadings. Among these three methods, the highest increase in the layer spacing of the organoclay was achieved for in-situ polymerization at low clay contents. Also, the best improvement in mechanical properties including tensile, impact strength and Young's modulus was obtained for the nanocomposites prepared with this method.

Xie et. al. [81] investigated the effects of the alkyl chain length that were used for the organic modification of MMT. For the preparation of the PS-MMT nanocomposites, suspension free radical polymerization was used. They concluded that as the chain length increases the glass transition temperature of the PS nanocomposites increases. According to XRD and TEM results, exfoliated nanocomposites were obtained and for thermal stability and mechanical properties 5 wt% and 7.5 wt% clay contents gave the best improvements respectively.

Park et. al. [82] processed PS/organoclay nanocomposites in the presence of poly(styrene-co-vinyloxazolin) (OPS). They found out that the arrangement of the organic modifier between the clay layers affects the dispersion of layers. Lateral bilayer type arrangement results in exfoliated structures, whereas intercalated structures are obtained with paraffinic monolayer type arrangement. Owing to the greater dispersion of the clay layers, the exfoliated nanocomposites showed a faster crystallization rate leading a lower degree of crystallinity and better mechanical properties than intercalated nanocomposites.

Tanoue et. al. [83] showed that the dispersion of silicate layer for PS/organoclay nanocomposites are tremendously affected by the screw rotation speed, namely the degree of shear. Poly(styrene-co-vinyloxazolin) (OPS) was used as an additional material which enhanced the mechanical properties. It was demonstrated that as the screw rotation increases the distance between the clay

platelets increases for PS/OPS/organoclay ternary systems and fully exfoliated structures were obtained for 70 – 100 rpm speeds.

Zhang et. al. [84] used γ-ray radiation polymerization technique for PS/MMT nanocomposite preparation. The insertion of PS chains between the silicate layers was observed by XRD and TEM analyses, and increasing glass transition temperature for those intercalated nanocomposites was observed by DSC analyses. In addition, no change was observed in the distance between the sheets with increasing organoclay content.

Chang et. al. [85] indicated that the microstructure is important for morphology and mechanical properties of high impact polystyrene, elastomer and filler ($Mg(OH)_2$) ternary composites. They used poly[styrene-b-(ethylene-co-butylene)-b-styrene] (SEBS) as elastomer and separation of elastomer and filler was observed. When maleinated SEBS (SEBS-g-MA) was used, encapsulation of the filler by elastomer was observed which resulted in lower elongation, modulus and impact strength compared to composites with separate dispersion structure. Thus, it is concluded that extensive plastic deformation and cavitation resulted from filler–matrix debonding were main toughening mechanisms for such composites.

Li et. al. [86] found that SEBS-g-MA is beneficial for the dispersion of polyamide 1212 (PA 1212) in PS matrix, owing to reaction between them. The un-compatibilized blends were observed to be unstable toward coalescence during melt processing leading poor mechanical properties. The phase structure was varied with increasing SEBS-g-MA content in the blend. Firstly, sheet structures were formed, and then a co-continuous phase with core-shell structure was obtained. In addition to core-shell structure, the increase in SEBS-g-MA content retarded the crystallization of PA 1212. The co-continuous phase and the reduced crystallinity lead to an apparent increase in impact strength.

Bruzaud et. al. [87] made a comparison between two cationic surfactants that are used for the organic modification of MMT. During the preparation of PS/organophilic nanocomposites, in-situ polymerization was used and three different protocols were tried. Partially exfoliated and intercalated materials were obtained for all cases. But, the thermal properties, especially thermal

decomposition temperature, of the nanocomposites containing alkylphosphonium ion surfactant in its organoclay were found to be greater compared to pure PS and the nanocomposites prepared with organoclay modified with alkyl ammonium.

Gelfer et. al. [88] demonstrated that due to the higher compatibility of organoclay with PMMA than PS matrix, the organoclay concentrated on PMMA phase and at the interphase in PS/PMMA blends. Since PS and PMMA are immiscible polymers, they form separated phases, however, with the addition of organoclay it was found that the average domain size reduces drastically which is the indication of the compatibilization effect of the organoclay. This compatibility is attributed to the interaction between the polymer matrix and the surfactant, rather than the interaction between polymer matrix and clay surface.

Jose et. al. [89] prepared polyamide 12 (PA12) blends by using two different elastomers: SEBS and SEBS-g-MA. Compounding was carried out in a twin screw extruder. Interfacial reactions between PA12 and the grafted part of the SEBS-g-MA provided a better dispersion of the elastomeric phase in the polymer matrix and brought a better impact strength to the blend. In addition to impact strength, tensile and elongation properties were improved for the blends containing SEBS-g-MA.

Karayannididis et al. [90] investigated the effect of the functionalized block copolymer SEBS-g-MA on the rubber toughening of glass fiber reinforced PA 66. Increased resistance to crack propagation and hence toughness was obtained with the incorporation of SEBS-g-MA into PA 66 matrix. Toughening was influenced by the size of cavitation and the extent of reaction between PA 66 and SEBS-g-MA.

Aphiwantrakul et. al. [91] compared two clays that have different cation exchange capacities: Bentonite H and Wyoming. For the nanocomposites containing Wyoming, liquid-like phase was obtained while both solid-like and liquid-like phases were found for nanocomposites prepared with bentonite H. Liquid-like phase led to low surface coverage, and exfoliated structures were observed. However, for solid-like phase, with high surface coverage, intercalated nanocomposites were found.

Ramsteiner et. al. [92] reported morphological and mechanical characterization of syndiotactic PS/SEBS blends prepared in an extruder. With respect to neat PS, they found a remarkable increase in toughness. A fine dispersion and good adhesion of the rubber at the interface induced by the compatibilizing effect of SEBS were evidenced by TEM, and it was considered as a prerequisite to increase toughness. In addition to fine dispersion, the orientation induced by the injection process and reduced crystallinity by rapid cooling were shown to be the other factors for this improvement.

Joseph et. al. [53] used SEM and dissolution techniques to determine the co-continuity level of PS and polybutadiene (PB) blends. Between 40 and 60 wt% PS content in the blends, a co-continuous morphology was observed and beyond 50 wt% phase inversion occurred. These results that were found experimentally compared with some theoretical phase inversion models depending on the viscosity ratio of the blend components. However, it was concluded that theoretical and experimental results are not in accordance with each other.

Uthirakumar et. al. [93] examined the effect of polymerization type on the dispersion of clay layer in HIPS/MMT nanocomposites. Nanocomposites were prepared by in-situ polymerization of styrene in the presence of polybutadiene using anchored cationic radical initiator–MMT hybrid. With bulk polymerization, the exfoliation process remained incomplete, whereas solution polymerization led to efficient exfoliation due to low extra-gallery viscosity, and the mechanical properties of these exfoliated nanocomposites exhibited a significant improvement.

CHAPTER 3

EXPERIMENTAL

3.1 Materials

3.1.1 Polymer Matrix

The polystyrene matrix with a trade name of Lacqrene® 1960N was purchased from TOTAL Petrochemicals. It was supplied in the form of pellets in 25kg polyethylene bags. Properties of Lacqrene® 1960N given by the supplier are in Table 3.1.

Table 3.1 Properties of polystyrene (Lacqrene® 1960N) [94]

Property	Method	Unit	Value
Rheological			
Density	ISO 1183	g/cm³	1.05
Melt flow index (200°C-5kg)	ISO 1133 H	g/10min	30
Thermal			
Vicat softening point 10N (T° increase = 50°C/h)	ISO 306A50	°C	105
Vicat softening point 50N (T° increase = 50°C/h)	ISO 306B50	°C	101
HDT unannealed under 1.8 MPa	ISO 75-2A	°C	84
HDT annealed under 1.8 MPa	ISO 75-2A	°C	96

Table 3.1 (cont'd) Properties of polystyrene (Lacqrene® 1960N)

Mechanical			
Unnotched Charpy impact strength	ISO 179/1eU	kJ/m²	6
Tensile strength at break	ISO 527-2	MPa	35
Elongation at break	ISO 527-2	%	2.5
Tensile modulus	ISO 527-2	MPa	3200
Flexural modulus	ISO 178	MPa	2900
Hardness	ISO 2039-2		L 70
Electrical			
Dielectric strength	---	kV/mm	135
Surface resistivity	ISO IEC 93	Ohms	$> 10^{14}$
Miscellaneous			
Mold shrinkage	---	%	0.4-0.7
Water absorption	ISO 62	%	< 0.1

3.1.2 Impact Modifier

Two different types of elastomers were used as impact modifiers. The first one is poly[styrene-b-(ethylene-co-butylene)-b-styrene] a clear linear triblock copolymer grafted with maleic anhydride (SEBS-g-MA) containing 13% polystyrene. It has a trade name Kraton® FG1924X. Its chemical structure and sale specifications are given in Figure 3.1 and Table 3.2 respectively. The second elastomer, poly(ethylene-b-butyl acrylate-b-glycidyl methacrylate) triblock copolymer (E-BA-GMA) with a trade name DuPont ™ Elvaloy® PTW was purchased from DuPont. Its chemical structure is shown in Figure 3.2 and properties are given in Table 3.3.
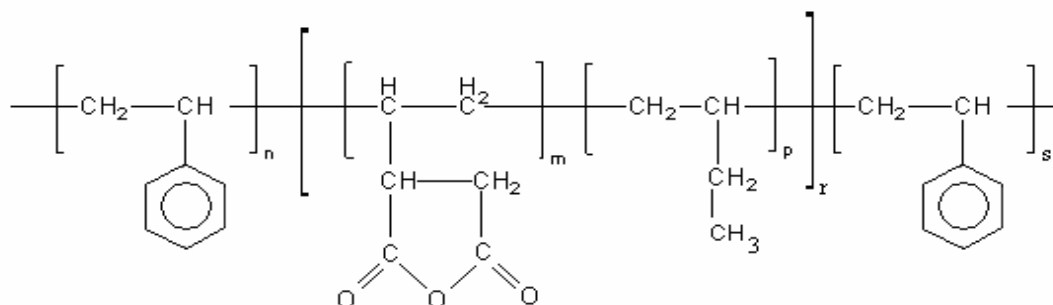
Figure 3.1 Chemical structure of SEBS-g-MA

Table 3.2 Properties of SEBS-g-MA (Kraton® FG1924X) [95]

Property	Method	Unit	Value
Content			
Maleic Anhydride content (free)	Othr Ametek	Wt%	0.3 max.
Maleic Anhydride content (bound)	BAM 1026	Wt%	0.7-1.3
Dust content (Talc)	BAM 908	Wt%	0.15 min
Water	BAM 1024	ppmw	500 max.
Styrene/Rubber ratio		%	13/87
Thermal			
Melting point		˚C	120-140
Vicat softening point		˚C	-55
Rheological			
Solution viscosity		cps	19,000
Melt flow index (230˚C-5kg)		g/10min	40
Specific gravity		g/cm^3	0.9
Mechanical			
Hardness		A	49
Tensile strength at break		MPa	23
Elongation at break		%	750
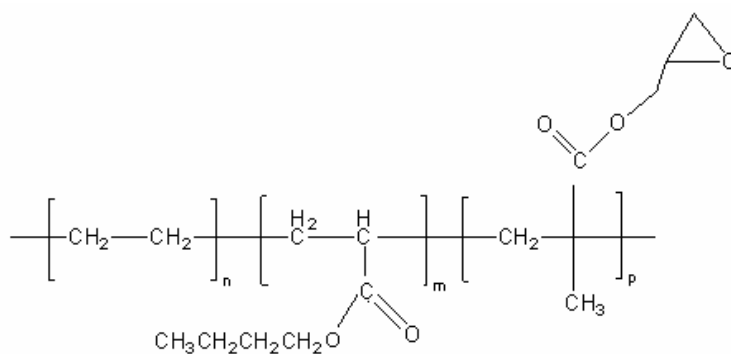
Figure 3.2 Chemical structure of E-BA-GMA

Table 3.3 Properties of E-BA-GMA (Elvaloy® PTW) [96]

Property	Method	Unit	Value
Thermal			
Melting point	ASTM D3418	˚C	72
Vicat softening point	ASTM D3418	˚C	-55
Rheological			
Density	ASTM D792	g/cm^3	0.94
Melt flow index (190°C-2.16kg)	ASTM D1238	g/10min	12
Mechanical			
Hardness	ASTM D2240	A	73
Tensile strength at break	ASTM D638	MPa	23
Elongation at break	ASTM D638	%	750

3.1.3 Organoclays

Three different types of organically modified clays, with trade names Cloisite® 30B, Cloisite® 15A and Cloisite® 25A, were used in this study. They were purchased from Southern Clay Products (USA). Due to the nature of organic modifier, surface hydrophobicities are different from one organoclay to another. They are arranged according to their hydrophobicity in Figure 3.3. Cloisite® 15A is the most hydrophobic one and the least hydrophobic organoclay is Cloisite® 30B. The physical properties of organoclays, Cloisite® 30B, 15A and 25A, are shown in Table 3.4.
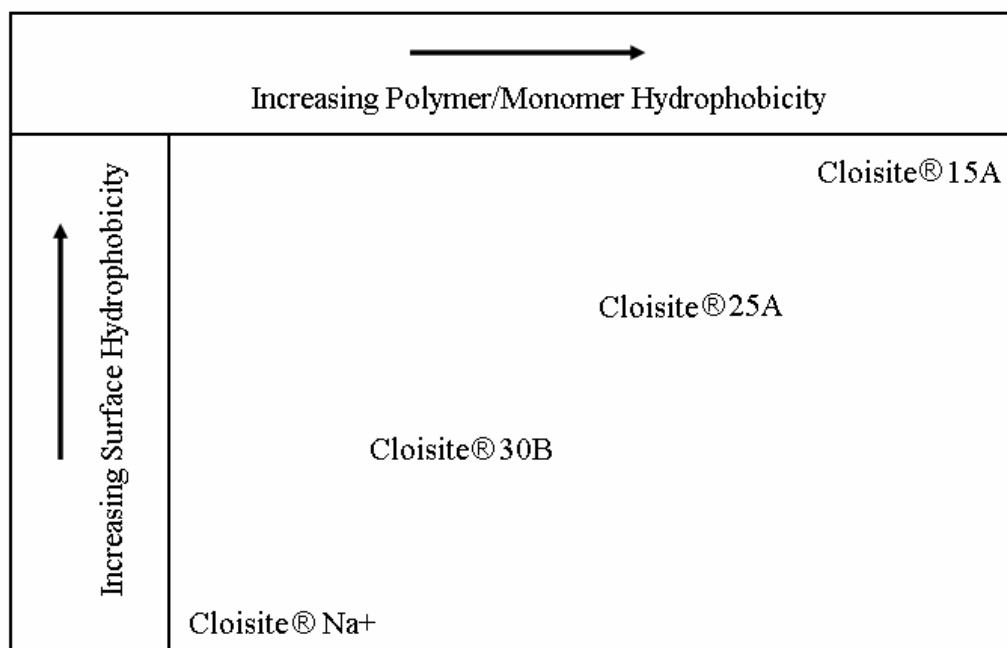
Figure 3.3 Clay selection chart based on polymer/monomer chemistry [97]

Table 3.4 Properties of organoclays [97]

Property	Cloisite® 30B	Cloisite® 15A	Cloisite® 25A
Modifier concentration (CEC meq/100gclay)	90	125	95
Moisture (%)	<2	<2	<2
Weight loss on ignition (%)	30	43	34
d-spacing (Å)	18.5	31.5	18.6
Dry particle size (μ, by volume)	10% <2 50% <6 90% <13	10% <2 50% <6 90% <13	10% <2 50% <6 90% <13
Color	Off white	Off white	Off white
Specific gravity (g/cc)	1.98	1.66	1.87
Loose bulk (lbs/ft^3)	14.25	10.79	12.08
Packed bulk (lbs/ft^3)	22.71	18.64	20.48

Quaternary ammonium salt cation and anion of the organic modifier of Cloisite® 30B are methyl, tallow, bis-2-hydroxyethyl quaternary ammonium (MT2EtOH) and chloride, respectively. Almost 65 % of the carbon chains have 18 carbons, 30 % has 16 carbons and 5 % has 14 carbons in the tallow structure. Figure 3.4 shows the chemical structure of the organic modifier.
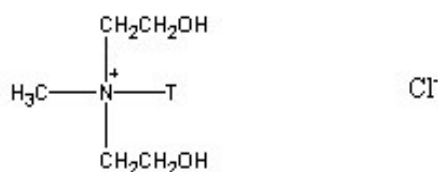
Figure 3.4 Chemical structure of the organic modifier of Cloisite® 30B

Organic modifier of Cloisite® 15A contains dimethyl, dehydrogenated tallow, quaternary ammonium cation (2M2HT) with chloride anion. The hydrogenated tallow is predominantly composed of chains with 18 carbons (~65 %), and to a lesser degree chains with 16 carbons (~30 %) and 14 carbons (~5 %). Chemical structure of the organic modifier of Cloisite® 15A is given in Figure 3.5.
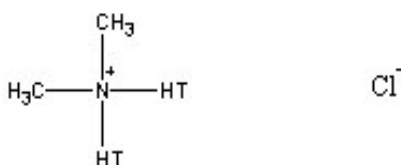
Figure 3.5 Chemical structure of the organic modifier of Cloisite® 15A

Dimethyl, dehydrogenated tallow, 2-ethylhexyl quaternary ammonium cation (2MHTL8) with methyl sulfate anion constitutes the chemical structure of the organic modifier of Cloisite® 25A, where hydrogenated tallow contains chains mostly with 18 carbons (~65 %), to a lesser degree chains with 16 carbons (~30 %) and 14 carbons (~5 %). Chemical structure of the organic modifier of Cloisite® 25A can be seen from Figure 3.6.
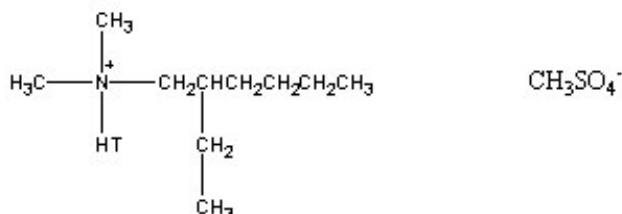
Figure 3.6 Chemical structure of the organic modifier of Cloisite® 25A

3.2 Nanocomposite Preparation

3.2.1   Melt Blending

Polystyrene based nanocomposites were prepared by melt blending in a co-rotating, intermeshing Thermoprism TSE 16 TC twin screw extruder (L = 384 mm D = 16 mm). Figure 3.7 shows the drawing of extruder used in this study. During the experiments, the screw speed and the feed rate were kept at 300 rpm and 25 g/min respectively and the temperature profile was set to 200-200-200-200-200˚C from the main hopper to the die.

In addition to ternary PS/elastomer/organoclay nanocomposites, PS/organoclay, elastomer/organoclay nanocomposites and PS/elastomer blends were prepared for comparison purposes. All nanocomposites and blends were extruded twice to increase the effect of shear intensity on the organoclay dispersion and to achieve the desired compositions.   Prior to processing, polystyrene, organically modified montmorillonites, elastomers and extruded samples were dried under vacuum. Drying conditions are given in Table 3.5.
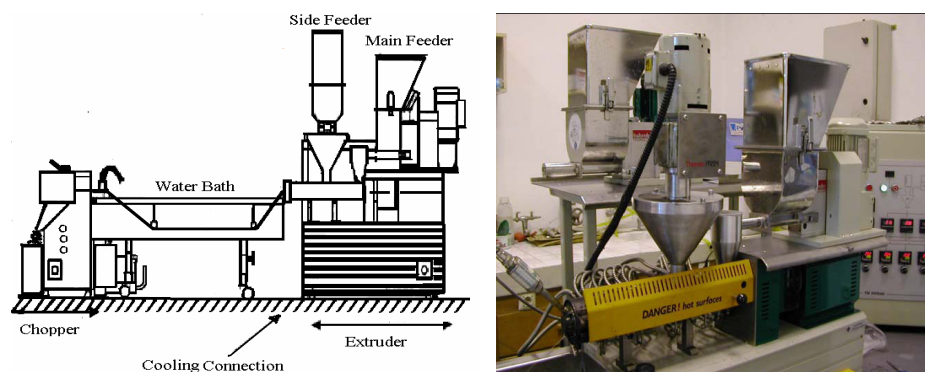
Figure 3.7 Thermoprism TSE 16 TC twin screw extruder

Table 3.5 Drying conditions

Composition	Temperature / Time
Before 1st run extrusion	
PS	80˚C / 4 hr
Organoclays	80˚C / 12 hr
Elastomers	40˚C / 4 hr
Before 2nd run extrusion	
PS	80˚C / 4 hr
PS + Elastomer	80˚C / 4 hr
PS + Organoclay	80˚C / 12 hr
Elastomer + Organoclay	80˚C / 12 hr
PS + Elastomer + Organoclay	80˚C / 12 hr
Before injection molding	
PS	80˚C / 4 hr
PS + Elastomer	80˚C / 4 hr
PS + Organoclay	80˚C / 12 hr
Elastomer + Organoclay	80˚C / 12 hr
PS + Elastomer + Organoclay	80˚C / 12 hr

3.2.2 Injection Molding

After the second extrusion run, the specimens were injection molded by DSM Xplore laboratory scale micro injection molding equipment. The photograph of this equipment can be seen in Figure 3.8. It consists of a mold on the left hand side and a pressure cylinder on the right hand side, where a nozzle is connected to the mold. The maximum pressure that this machine can reach is 16 bars.

Figure 3.8 DSM Xplore injection molding machine

Before molding the samples, the pellets were put into the cylinder with a spoon. After waiting three minutes for the material to melt, the melt was injected into the mold with a maximum pressure of 13 bars. In each molding operation, two specimens were obtained, one of which had the shape of a dogbone, whereas the other one is the sample of the impact test with rectangular shape. During the molding process, the melt and mold temperatures were set to 200 and 30˚C for all samples, except for the elastomer/organoclay nanocomposites. For these binary nanocomposites, the mold temperature was set to 20˚C to be able to obtain regular sample shapes.

3.3 Experimental Procedure

In the first extrusion run, the masterbatch PS/elastomer blend was fed from the main feeder while side feeder was used to feed the organoclay. The extruded rod was cut into pellets by the help of a chopper. However, for SEBS-g-MA/organoclay nanocomposites, the chopper could not cut the rod that came out of the extruder die due to the highly elastic characteristic of the rod. Thus, the rods were later frozen in liquid N_2 and ground into small pellets by the help of a hammer as shown in Figure 3.9. In the second extrusion run, PS/organoclay,

55

PS/elastomer/organoclay nanocomposites were diluted with pure PS, while elastomer/organoclay nanocomposites were diluted with pure elastomer to achieve the desired organoclay compositions. Generalized flowchart of experimental procedure is given Figure 3.10.
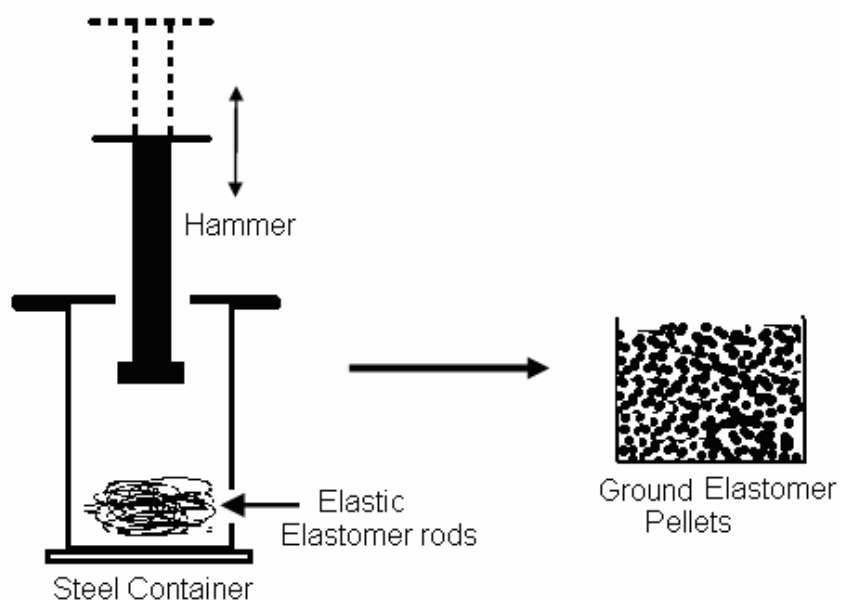
Figure 3.9 Elastomer grinding process

```
                    ┌─────────────────┐
                    │  Drying of raw  │
                    │   materials     │
                    └────────┬────────┘
                             │
                    ┌────────▼────────────┐
                    │  Simultaneous melt  │
                    │ blending of raw     │
                    │ materials in the    │
                    │ 1st extrusion run   │
                    └──┬───────────────┬──┘
                       │               │
          ┌────────────▼──┐       ┌────▼─────────────┐
          │ PS + Elastomer│       │ Organoclay from  │
          │ from main     │       │ side feeder      │
          │ feeder        │       └────┬─────────────┘
          └────────────┬──┘            │
                       └───────┬───────┘
                    ┌──────────▼──────┐
                    │ Drying of       │
                    │ extruded        │
                    │ materials       │
                    └────────┬────────┘
                             │
                    ┌────────▼────────┐
                    │ Dilution with   │
                    │ pure PS or      │
                    │ elastomer in    │
                    │ the 2nd         │
                    │ extrusion run   │
                    └────────┬────────┘
                             │
                    ┌────────▼────────┐
                    │ Drying of       │
                    │ extruded        │
                    │ materials       │
                    └────────┬────────┘
                             │
                    ┌────────▼────────┐
                    │ Injection       │
                    │ molding         │
                    └────────┬────────┘
                             │
                    ┌────────▼────────┐
                    │ Characterization│
                    │ experiments     │
                    └────────┬────────┘
```

Drying of raw materials

Simultaneous melt blending of raw materials in the 1st extrusion run

PS + Elastomer from main feeder

Organoclay from side feeder

Drying of extruded materials

Dilution with pure PS or elastomer in the 2nd extrusion run

Drying of extruded materials

Injection molding

Characterization experiments

Morphological analyses	Rheological analyses	Mechanical analyses	Thermal analyses
* XRD	* Capillary visc.	* Tensile	* DSC
* SEM	* MFI	* Impact	

Figure 3.10 Flowchart of experimental procedure

To investigate effect of the elastomer and organoclay content on the properties of nanocomposites several compositions are prepared as shown in Table 3.6.

Table 3.6 Composition of the samples

No.	Composition	Concentration (wt%)		
		Polystyrene	Elastomer	O-clay
Raw materials				
1	PS	100	---	---
2	SEBS-g-MA	---	100	---
3	E-BA-GMA	---	100	---
PS / Elastomer blends				
4	PS + SEBS-g-MA	95	5	---
5	PS + SEBS-g-MA	85	15	---
6	PS + SEBS-g-MA	80	20	---
7	PS + SEBS-g-MA	70	30	---
8	PS + SEBS-g-MA	60	40	---
9	PS + E-BA-GMA	95	5	---
10	PS + E-BA-GMA	85	15	---
11	PS + E-BA-GMA	80	20	---
12	PS + E-BA-GMA	70	30	---
13	PS + E-BA-GMA	60	40	---
PS / Organoclay nanocomposites				
14	PS + 30B	99	---	1
15	PS + 30B	98	---	2
16	PS + 15A	99	---	1
17	PS + 15A	98	---	2
18	PS + 25A	99	---	1
19	PS + 25A	98	---	2
Elastomer / Organoclay nanocomposites				
20	SEBS-g-MA + 30B	---	99	1
21	SEBS-g-MA + 30B	---	98	2
22	SEBS-g-MA + 15A	---	99	1
23	SEBS-g-MA + 15A	---	98	2
24	SEBS-g-MA + 25A	---	99	1
25	SEBS-g-MA + 25A	---	98	2
26	E-BA-GMA + 30B	---	99	1
27	E-BA-GMA + 30B	---	98	2
28	E-BA-GMA + 15A	---	99	1
29	E-BA-GMA + 15A	---	98	2
30	E-BA-GMA + 25A	---	99	1
31	E-BA-GMA + 25A	---	98	2

Table 3.6 (cont'd) Composition of the samples

	PS / 5 wt% Elastomer / Organoclay nanocomposites			
32	PS + SEBS-g-MA + 30B	94	5	1
33	PS + SEBS-g-MA + 30B	93	5	2
34	PS + SEBS-g-MA + 15A	94	5	1
35	PS + SEBS-g-MA + 15A	93	5	2
36	PS + SEBS-g-MA + 25A	94	5	1
37	PS + SEBS-g-MA + 25A	93	5	2
38	PS + E-BA-GMA + 30B	94	5	1
39	PS + E-BA-GMA + 30B	93	5	2
40	PS + E-BA-GMA + 15A	94	5	1
41	PS + E-BA-GMA + 15A	93	5	2
42	PS + E-BA-GMA + 25A	94	5	1
43	PS + E-BA-GMA + 25A	93	5	2
	PS / 15 wt% Elastomer / Organoclay nanocomposites			
44	PS + SEBS-g-MA + 30B	84	15	1
45	PS + SEBS-g-MA + 30B	83	15	2
46	PS + SEBS-g-MA + 15A	84	15	1
47	PS + SEBS-g-MA + 15A	83	15	2
48	PS + SEBS-g-MA + 25A	84	15	1
49	PS + SEBS-g-MA + 25A	83	15	2
	PS / 20 wt% Elastomer / Organoclay nanocomposites			
50	PS + SEBS-g-MA + 30B	79	20	1
51	PS + SEBS-g-MA + 30B	78	20	2
52	PS + SEBS-g-MA + 15A	79	20	1
53	PS + SEBS-g-MA + 15A	78	20	2
54	PS + SEBS-g-MA + 25A	79	20	1
55	PS + SEBS-g-MA + 25A	78	20	2
	PS / 30 wt% Elastomer / Organoclay nanocomposites			
56	PS + SEBS-g-MA + 30B	69	30	1
57	PS + SEBS-g-MA + 30B	68	30	2
58	PS + SEBS-g-MA + 15A	69	30	1
59	PS + SEBS-g-MA + 15A	68	30	2
60	PS + SEBS-g-MA + 25A	69	30	1
61	PS + SEBS-g-MA + 25A	68	30	2
	PS / 40 wt% Elastomer / Organoclay nanocomposites			
62	PS + SEBS-g-MA + 30B	59	40	1
63	PS + SEBS-g-MA + 30B	58	40	2
64	PS + SEBS-g-MA + 15A	59	40	1
65	PS + SEBS-g-MA + 15A	58	40	2
66	PS + SEBS-g-MA + 25A	59	40	1
67	PS + SEBS-g-MA + 25A	58	40	2

3.4 Characterization Experiments

The effects of component concentrations, elastomer type and organoclay type on the final properties of the nanocomposites were examined with some characterization experiments. Morphology of the nanocomposites was investigated by XRD, SEM and TEM analyses. Capillary viscometry and MFI tests were carried out to investigate the flow characteristics. Mechanical behavior of the nanocomposites was evaluated by measuring impact strength and tensile properties (tensile strength, Young's modulus, elongation at break). Finally, glass transition temperature of the nanocomposites was studied with DSC analysis.

3.4.1 Morphological Analyses

3.4.1.1 X-Ray Diffraction

RIGAKU D/MAX 2200/PC X-Ray diffractometer that generates a voltage of 40kV and current 40 mA from Cu Kα radiation source (λ = 1.5418) was used to analyze the nanocomposites. The diffraction angle 2θ was scanned from 1˚ to 10˚ with scanning rate of 1˚/min and a step size of 0.01˚. To calculate the distance between the silicate layers Bragg' law, which is given in Equation 2.6, was used.

3.4.1.2 Scanning Electron Microscopy

In order to examine the failure mechanism and elastomer dispersion, the impact–fracture surface of the nanocomposites were scanned by a low voltage Scanning Electron Microscope (JEOL JSM-6400). The elastomeric phase in binary blends and ternary nanocomposites was dissolved by using n-Heptane as solvent. The etching process was achieved at room temperature in an ultrasonic bath. The surfaces of the samples were kept in n-Heptane until deterioration occurs. SEM photographs of the impact-fractured surfaces were taken at x250 and x3500 magnifications.

3.4.1.3 Transmission Electron Microscopy

For TEM analysis ultra sections of 70 nm in thickness were cryogenically cut with a diamond polymer knife at a temperature of -100˚C for PS/organoclay binary and PS/elastomer/organoclay ternary nanocomposites and at -120˚C for the elastomer/organoclay binary nanocomposite. These samples were examined by a Phillips CM200 Transmission Electron Microscope at an acceleration rate of 120 kV in DSM Research Laboratory. All samples are trimmed parallel to the molding direction.

3.4.2 Rheological Analyses

3.4.2.1 Capillary Viscometry

The apparent shear viscosity of the raw materials PS, SEBS-g-MA and E-BA-GMA were found by using LCR Series capillary rheometer. The experiments were performed at 200˚C and at shear rate from 1.37 to 412 (1/s). The dimensions of the die are; 30.48 mm capillary length, 0.762 mm capillary diameter.

3.4.2.2 Melt Flow Index

Melt flow index tests were carried out according to the procedure identified in ISO 1333 standards. The temperature was set to 200˚C and 2.16kg load was used. The amount of polymer melt flowing through the die of the capillary in 10 minutes was obtained. For each sample at least five measurements were done to get a more accurate result.

3.4.3 Mechanical Tests

Tensile and impact tests were conducted at room temperature and the properties were obtained on at least five samples to calculate the standard deviation.

3.4.3.1 Tensile Test

Tensile tests were performed by using Lloyd LR 30K Universal Testing machine according to ISO 527 [98]. The photograph of the testing machine is shown in Figure 3.11. During the test, the specimen was placed in the grips of the testing machine, taking care that it was properly aligned and the grips were tightened evenly and firmly enough to prevent the slippage of the specimen. Tensile strength (MPa), Young's modulus (MPa) and percent elongation at break (%) were determined from the stress-strain curves.

However, for elastomer containing nanocomposites, tests were applied according to ISO 37 [99] standards because of their high elongation values.

The shape and dimensions of the specimens are given in Figure 3.12 and Table 3.7 respectively. For SEBS-g-MA/organoclay nanocomposites smaller dimensions were obtained due to the shrinkage of the polymer melt in the mold and during the cooling processes and their dimensions are given in Table 3.7.

Figure 3.11 Lloyd LR 30K Universal Testing Machine
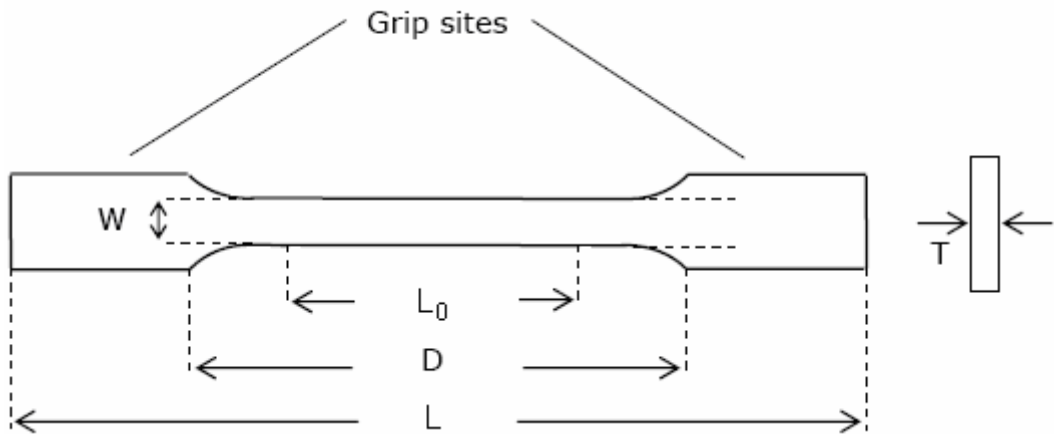
Figure 3.12 Tensile test specimen

Table 3.7 Dimensions of the tensile test specimens

Definition	Dimensions (mm)	Shrunk dimensions (mm)
L-Overall length	75	60
D-Distance between grips	50	40
L_0-Gauge length	30	25
W- Narrow section width	5	5
T-Thickness	2.1	2.1

The crosshead speed was applied as 3 mm/min, based on the gauge length of 30mm and strain rate of $0.1 min^{-1}$. On the other hand, for SEBS-g-MA/organoclay binary nanocomposites gauge length and crosshead speed were set to 25 mm and 25 mm/min respectively whereas for E-BA-GMA/organoclay binary nanocomposites these values were 30 mm and 30 mm/min.

3.4.3.2 Impact Test

Ceast Resil Impactor was used to perform the un-notched charpy impact test on samples with dimensions of 80x10x4 mm according to ISO 179 [100]. Its configuration is shown in Figure 3.13. All of the tests were performed at room temperature and the results are the averages of five tests carried out for all the compositions.

Figure 3.13 Ceast Resil Impactor

3.4.4 Thermal Analysis

3.4.4.1 Differential Scanning Calorimetry

The glass transition temperature measurements of the samples were carried out under nitrogen atmosphere by using DSC-60 Shimadzu differential scanning calorimeter. They were heated from 30°C to 350°C with a heating rate of 20°C/min. Samples about 3 mg were cut from dry tensile bars and placed in aluminum DSC pans. Changes in T_g values were examined for each composition to see the effect of clay content and type of the method used for composite preparation. Polystyrene is an amorphous polymer and no crystallinity was detected.

CHAPTER 4

RESULTS AND DISCUSSION

4.1 Morphological Analyses

4.1.1 X-Ray Diffraction

To analyze the dispersion state of an organoclay in the polymer matrix and the interlayer spacing of the silicate layers XRD is a useful technique. The patterns obtained from the analysis are used for the characterization of the structure of nanocomposites by using the 2theta peak, which is used for the calculation of the distance between the silicate layers with Bragg's law. The intercalation of polymer chains between the silicate layers results in an increase in the interlayer spacing. For those intercalated structures, the characteristic peak tends to shift to a lower angle due to the expansion of the basal spacing [101]. Although the layer spacing increases, there still exists an attractive force between the layers to stack them in an ordered structure. Change in intensity and the shape of the basal reflections is another evidence that specifies the intercalation of polymer chains [25].

On the contrary, no peak can be observed in the XRD pattern of exfoliated polymer nanocomposites owing to fully dispersed clay platelets in the matrix [6]. The absence of a diffraction peak may indicate an exfoliated or delaminated structures, however, it should not be used as the only evidence for the formation of an exfoliated structure. Due to the low concentration of the organoclay, X-ray beams may hit to a non-uniformly dispersed region of the sample and Bragg's reflection may be eliminated demonstrating exfoliation or it may remain unchanged as in conventional structures. The features of the local microstructures from TEM give useful detail to the overall picture that is drawn from the XRD results [102]. Thus, XRD and TEM analyses are regarded complementary to each other for the

65

material characterization of polymer/clay nanocomposites. Besides the exfoliated and intercalated structures, intermediate structures may also be defined that displays both of these two morphologies.

One of the most important reasons that results in exfoliated structures is the interaction between the clay surface and the polymer. Also, increasing viscosity and other shear elements like screw configuration and screw speed cause delamination of the layers. As a consequence, the clay platelets may be dispersed uniformly in the polymer matrix rather than be agglomerated as tactoids.

The XRD diffraction pattern of the organoclays, Cloisite® 30B, 15A and 25A, used in this study and pattern of each combinations are shown in Appendix A separately. The basal spacing values of all the compositions are shown in Table 4.1. The basal spacing of the organoclays 30B, 15A and 25A are found as 18.1Å, 31.5 Å / 12.4Å and 18.7Å respectively.

Table 4.1 XRD results of all compositions

Composition	1st Peak		2nd Peak	
	2theta (˚)	d_{001} (Å)	2theta (˚)	D_{002} (Å)
Organoclays				
Cloisite® 30B	4.88	18.1	---	---
Cloisite® 15A	2.80	31.5	7.10	12.4
Cloisite® 25A	4.72	18.7	---	---
PS / Organoclay nanocomposites				
PS + 30B (1%)	6.14	14.4	---	---
PS + 30B (2%)	6.00	14.7	---	---
PS + 15A (1%)	2.88	30.6	5.65	15.6
PS + 15A (2%)	2.87	30.7	5.56	15.9
PS + 25A (1%)	3.47	25.3	5.64	15.7
PS + 25A (2%)	3.28	26.9	5.62	15.7
Elastomer / Organoclay nanocomposites				
S* + 30B (1%)	6.34	13.9	---	---
S + 30B (2%)	6.28	14.1	---	---
S + 15A (1%)	---	---	---	---
S + 15A (2%)	---	---	---	---
S + 25A (1%)	---	---	---	---
S + 25A (2%)	---	---	---	---

Table 4.1 (cont'd) XRD Results of all compositions

Composition	1st Peak		2nd Peak	
	2theta (°)	d_{001} (Å)	2theta (°)	D_{002} (Å)
E* + 30B (1%)	6.32	13.4	---	---
E + 30B (2%)	6.29	14.0	---	---
E + 15A (1%)	4.56	19.4	---	---
E + 15A (2%)	4.59	19.2	---	---
E + 25A (1%)	5.03	17.5	---	---
E + 25A (2%)	5.10	17.3	---	---
PS / 5 wt% Elastomer / Organoclay nanocomposites				
PS + S (5%) + 30B (1%)	6.16	14.3	---	---
PS + S (5%) + 30B (2%)	6.23	14.2	---	---
PS + S (5%) + 15A (1%)	2.8	31.5	---	---
PS + S (5%) + 15A (2%)	2.6	33.9	4.97	17.8
PS + S (5%) + 25A (1%)	---	---	---	---
PS + S (5%) + 25A (2%)	---	---	---	---
PS + E (5%) + 30B (1%)	6.25	14.1	---	---
PS + E (5%) + 30B (2%)	6.19	14.3	---	---
PS + E (5%) + 15A (1%)	2.49	35.4	4.74	18.6
PS + E (5%) + 15A (2%)	2.49	35.4	4.78	18.5
PS + E (5%) + 25A (1%)	2.58	34.2	5.17	17.1
PS + E (5%) + 25A (2%)	2.77	31.9	5.32	16.6
PS / 15 wt% Elastomer / Organoclay nanocomposites				
PS + S (15%) + 30B (1%)	6.17	14.3	---	---
PS + S (15%) + 30B (2%)	6.05	14.6	---	---
PS + S (15%) + 15A (1%)	---	---	---	---
PS + S (15%) + 15A (2%)	---	---	---	---
PS + S (15%) + 25A (1%)	---	---	---	---
PS + S (15%) + 25A (2%)	---	---	---	---
PS / 20 wt% Elastomer / Organoclay nanocomposites				
PS + S (20%) + 30B (1%)	6.17	14.3	---	---
PS + S (20%) + 30B (2%)	6.17	14.3	---	---
PS + S (20%) + 15A (1%)	---	---	---	---
PS + S (20%) + 15A (2%)	---	---	---	---
PS + S (20%) + 25A (1%)	---	---	---	---
PS + S (20%) + 25A (2%)	2.30	38.4	---	---
PS / 30 wt% Elastomer / Organoclay nanocomposites				
PS + S (30%) + 30B (1%)	6.17	14.3	---	---
PS + S (30%) + 30B (2%)	6.11	14.5	---	---
PS + S (30%) + 15A (1%)	2.56	34.5	---	---
PS + S (30%) + 15A (2%)	2.67	33.1	---	---
PS + S (30%) + 25A (1%)	---	---	---	---
PS + S (30%) + 25A (2%)	3.36	26.3	---	---

Table 4.1 (cont'd) XRD Results of all compositions

Composition	1st Peak		2nd Peak	
	2theta (°)	d_{001} (Å)	2theta (°)	d_{002} (Å)
PS / 40 wt% Elastomer / Organoclay nanocomposites				
PS + S (40%) + 30B (1%)	6.05	14.6	---	---
PS + S (40%) + 30B (2%)	6.21	14.2	---	---
PS + S (40%) + 15A (1%)	2.19	40.3	---	---
PS + S (40%) + 15A (2%)	3.04	29.0	---	---
PS + S (40%) + 25A (1%)	---	---	---	---
PS + S (40%) + 25A (2%)	---	---	---	---

*S and E capital letters refer to elastomers SEBS-g-MA and E-BA-GMA respectively

Figures 4.1 – 4.2 show the XRD patterns of nanocomposites containing Cloisite® 30B and 5wt% elastomer. In order to obtain exfoliated or intercalated structures, it is important to have a good interaction between the clay surface and polymer matrix. However, for non-polar polymers like polystyrene such structures are difficult to obtain. Due to this reason, a compatibilizer, that is interactive with both the polymer matrix and the organic modifier of the clay, should be used. For the binary nanocomposites of PS / Cloisite® 30B, no improvement was observed in the basal spacing of the silicate layers. Due to –OH groups on its organic modifier, Cloisite® 30B has the highest hydrophilic surface among the organoclays used in this study. Thus, its poor dispersion in the highly non-polar PS matrix is an expected result.

The intercalation of polymer matrix into van der Waals gallery of the organoclay was tried to achieve by adding an elastomeric phase to the PS/organoclay binary nanocomposites. The elastomeric materials SEBS-g-MA and E-BA-GMA contain functional groups of maleic anhydride and glycidyl methacrylate respectively. Maleic anhydride increases adhesion onto polar substances and allows the creation of chemical bonds. Especially, chemical reaction occurs between the hydroxyl groups of the surface of the organoclay and maleic anhydride. Also, glycidyl methacrylate reacts with hydroxyl groups because of the epoxy group that it contains. Thus, it can be stated that the functional groups of the elastomers may interact with the modifier of the Cloisite® 30B. However, the ethylene-butylene and

68

butyl-acrylate blocks of the elastomers are incompatible with the layer surface and may repel the clay layer during intercalation process [103]. The binding forces between the clay and polymer matrix are very effective in the separation of clay platelets. Due to the lack of such an interaction between the clay and the polymer matrix, the platelets remain as tactoids without the penetration of polymer chains between them.

When the effect of elastomer type and organoclay content on the dispersion of layers is investigated, no difference can be observed in ternary nanocomposites with Cloisite® 30B. In addition, as can be seen from Figures 4.1 and 4.2, the basal spacing of the organoclay Cloisite® 30B collapse slightly for both types of elastomers. The interaction between the functional groups of the elastomeric materials and the hydroxyl groups on the clay surface may be weakened by heat treatment due to the decomposition of the organic modifier, so that some portion of the polymer chains may exude from the clay gallery, leading to a reduction in interlayer spacing [83].
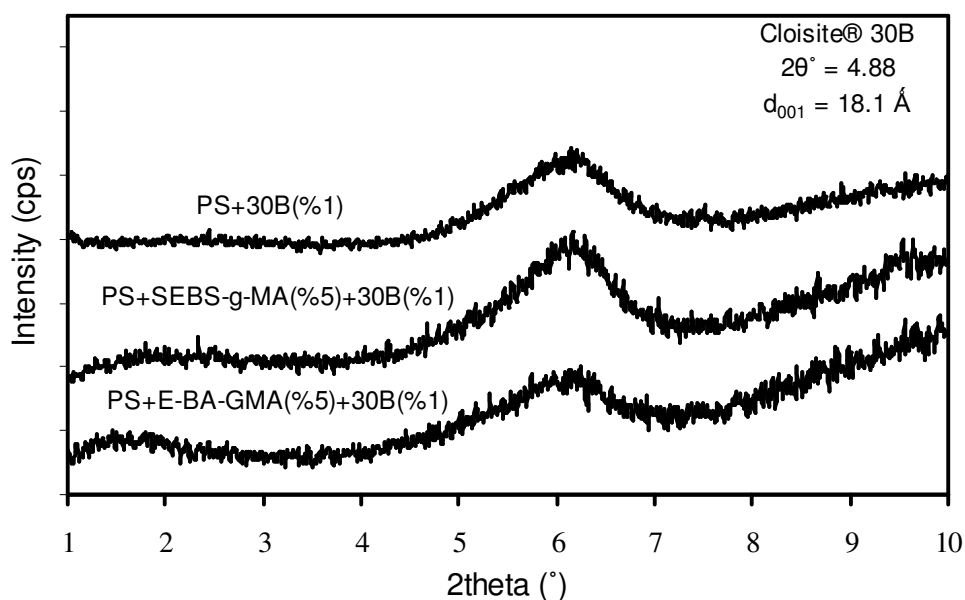
Figure 4.1 XRD pattern of nanocomposites containing 1wt% Cloisite® 30B and 5wt% Elastomer
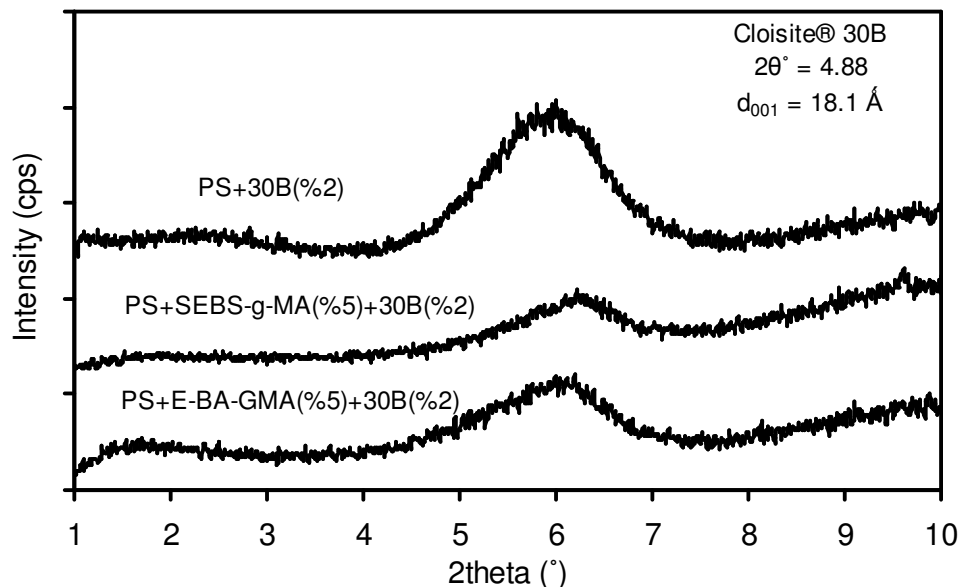
Figure 4.2 XRD pattern of nanocomposites containing 2wt% Cloisite® 30B and 5wt% Elastomer

XRD patterns of binary elastomer/Cloisite® 30B nanocomposites are given in Figure 4.3. The diffraction peak of the Elastomer/Cloisite® 30B binary nanocomposites prepared with E-BA-GMA or SEBS-g-MA shifts to right, indicating a collapse in the basal spacing. Cloisite® 30B is a highly polar organoclay and this organoclay proposed to be the most compatible with polar elastomers compared to other clays used in this study. However, XRD analysis does not reveal this phenomenon. Thus, it can be said that due to this great attraction between polar materials, the silicate layers remain as tactoids. As a consequence, these elastomeric materials do not exfoliate the silicate layers; they even do not get inserted between the layers.

The secondary peaks in the patterns come from the elastomeric materials used as the matrix. For E-BA-GMA this peak occurs approximately at $2\theta°=2.2$ and for SEBS-g-MA it has a value of approximately $2\theta°=9.5$ (See Appendix A for the XRD patterns of pure SEBS-g-MA and E-BA-GMA, Figure A.58 and A.59).
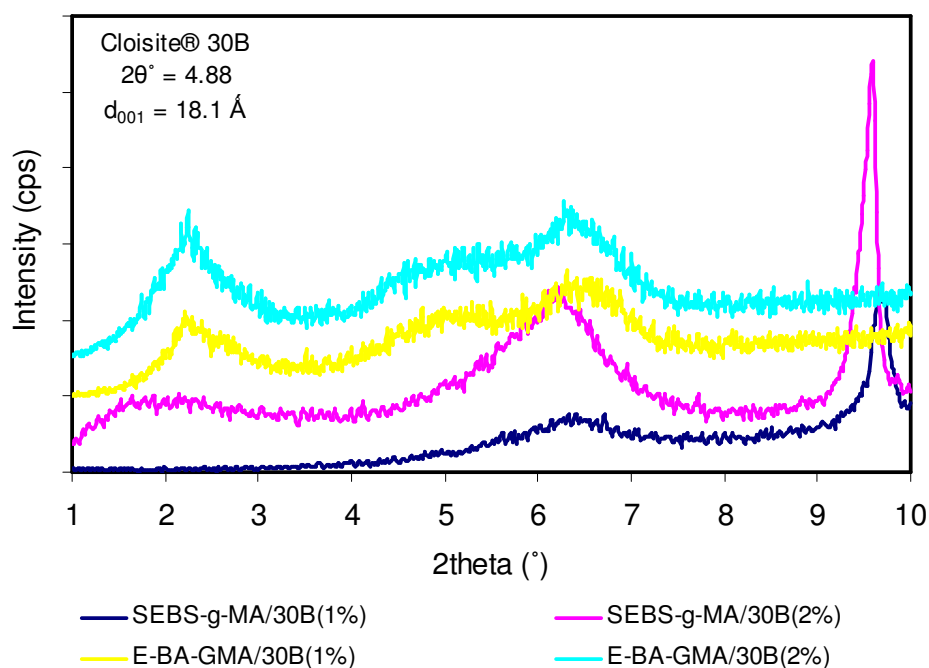
Figure 4.3 XRD pattern of binary nanocomposites containing Cloisite® 30B and Elastomer

XRD patterns of nanocomposites containing Cloisite® 15A and 5wt% elastomer are shown in Figures 4.4 and 4.5. XRD diffractogram of Cloisite® 15A organoclay powder shows two diffraction peaks (See Appendix A). Because the intensity of the first peak is larger than that of the second peak, it is possible to judge the first peak as it is due to d_{001} and that the second one is due to d_{002}. Therefore, d_{001} estimated by Bragg's law is the d-spacing between clay platelets. If a second 2θ value of approximately twice the first 2θ exists, it is interpreted as resulting from the second silicate layer [104, 105]. For Cloisite® 15A, the second silicate layer is not the reason for the second peak. According to Southern Clay Products, where the organoclays are purchased from, the d_{002} spacing of Cloisite® 15A in powder form is equal to the d_{001} spacing of unmodified MMT, Cloisite® Na⁺. Thus, this second peak corresponds to clay in which the inorganic cations of the smectite clay were not fully replaced by the organic ions.

For the interlayer spacing of the PS/Cloisite® 15A binary nanocomposites no intercalation was observed, whereas the second peak shifted to the left due to insertion of the PS chains between unmodified layers. Cloisite® 15A has the most hydrophobic surface among the organoclays used for this study due lack of polar groups on its modifier; and this absence of functional groups in the organic modifier makes dispersive forces more effective in the exfoliation of the organoclay. Also, its relatively high initial d-spacing makes dispersion of silicate layers easier due to reduced platelet-platelet attraction, and diffusion of polymer chains inside the silicate layers is less hindered owing to increased spacing. Thus, the attraction between non-polar PS and Cloisite® 15A and the dispersion of Cloisite® 15A is expected to be the highest compared to other organoclay types used for this study. However, besides the attraction between polymer-organoclay, other factors such as, organoclay stability and surfactant packing density are important factors on which dispersion of layers is highly dependent. Other than these factors, shear intensity in the extruder may delaminate the clay layers, but it is just valid when the chemical bonding between the silicate layers is not strong enough.

It is obvious that organoclay 15A has no chance to make hydrogen bonding with the functional group of the elastomeric materials. However, when the ternary nanocomposites are considered, it can be seen that; the addition of elastomeric phase increases the d-spacings calculated both from the first peak and the second peak. As will be proved later, in ternary nanocomposites the clay particles reside both in elastomeric phase and at the interface between PS and elastomer instead of the PS matrix. Due to increase in viscosity with the addition of elastomeric phase, especially SEBS-g-MA, the shear intensity applied to clay platelets during the extrusion increases. Thus, the clay agglomerates that stay at the contact area of PS and elastomeric phase exhibit intercalated structures.

The XRD patterns of ternary nanocomposites prepared with SEBS-g-MA shows broader peaks indicating larger interlayer spacings. So, it can be said that the elastomer SEBS-g-MA acts as a better compatibilizer for PS/Cloisite® 15A nanocomposites.
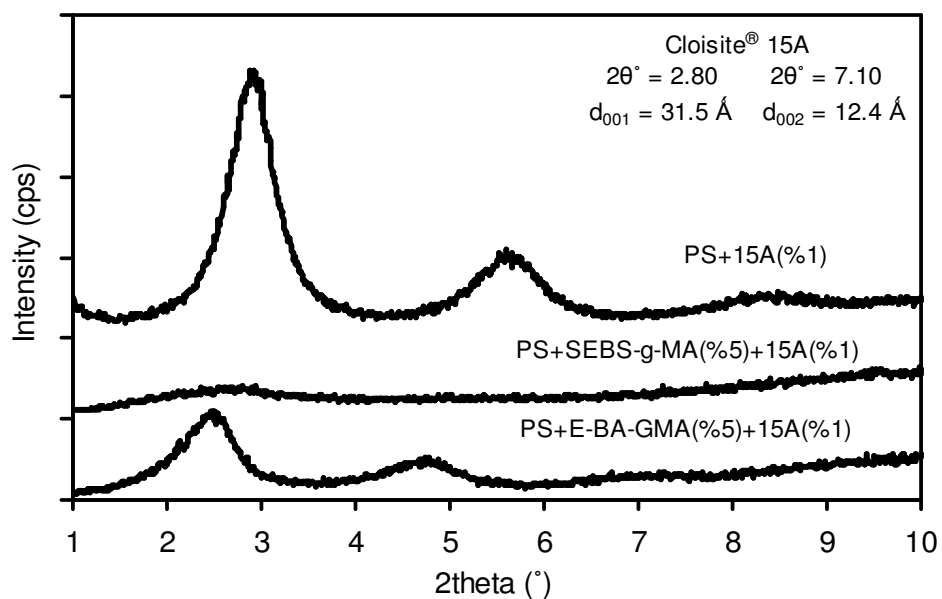
Figure 4.4 XRD pattern of nanocomposites containing 1wt% Cloisite[®] 15A and 5wt% Elastomer
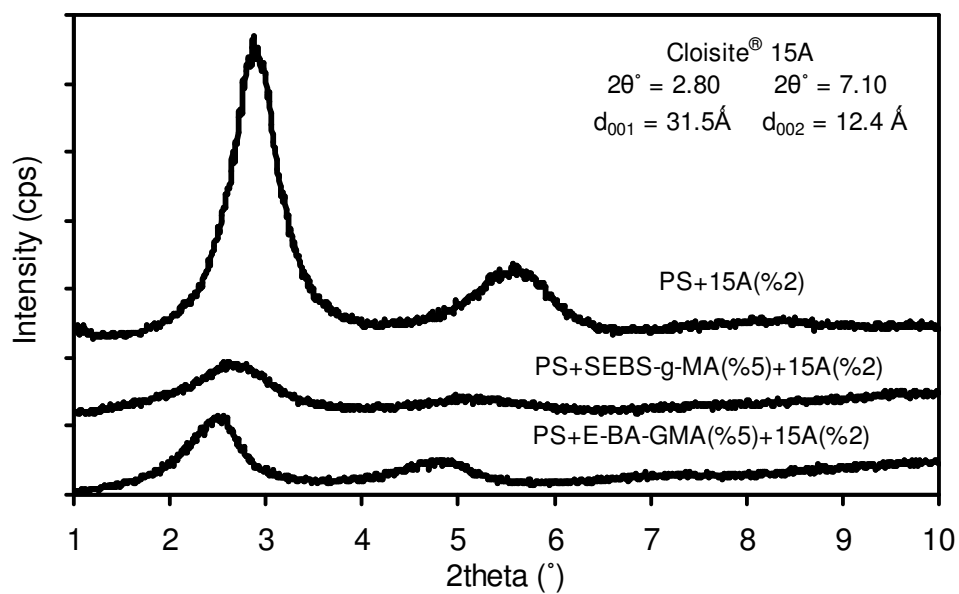
Figure 4.5 XRD pattern of nanocomposites containing 2wt% Cloisite[®] 15A and 5wt% Elastomer

In addition, in the nanocomposites containing smaller amount of Cloisite® 15A, i.e. 1wt%, both diffraction peaks disappear totally. The reason for better dispersion of organoclay layers in nanocomposite containing 1wt% Cloisite® 15A is that, as the amount of clay loading increases the probability of local ordering of clay platelets increases and clay particles remain as agglomerates which restrict the motion of polymer molecules between the layers [67, 106].

In Figure 4.6 XRD patterns of binary elastomer/Cloisite® 15A nanocomposites can be seen. Cloisite® 15A gets exfoliated in the elastomer SEBS-g-MA, whereas, in the E-BA-GMA/Cloisite® 15A binary nanocomposites no change can be observed in the basal spacing. This may be due to the higher viscosity of SEBS-g-MA compared to E-BA-GMA that leads to greater shear stress during melt blending. This phenomenon will be discussed later. As mentioned before the peaks at 2θ = 2.2 and 9.5 are due to E-BA-GMA and SEBS-g-MA, respectively.
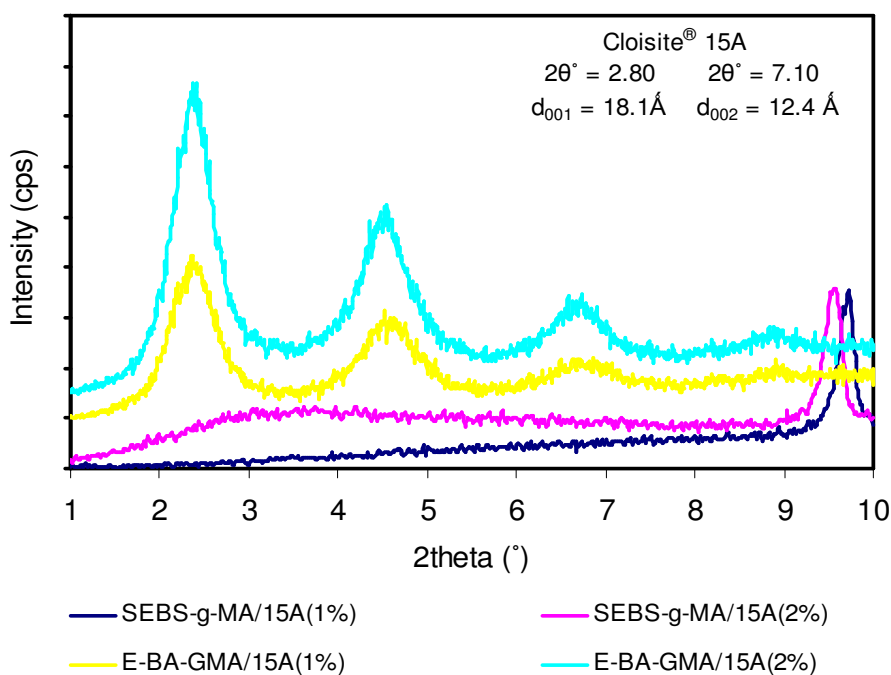
Figure 4.6 XRD pattern of binary nanocomposites containing Cloisite® 15A and Elastomer

Among the nanocomposites used in this study, Cloisite® 25A shows the best dispersion. Figures 4.7 and 4.8 show the XRD diffractograms of ternary nanocomposites, containing Cloisite® 25A and 5wt% elastomer. As can be seen from the patterns of PS/Cloisite® 25A nanocomposites, the clay layers remained as tactoids with intercalated polymer chains between the layers. Although Cloisite® 25A has no secondary peak in its pure powder form (See Appendix A) a second peak appears in the XRD diffractometer of binary PS/organoclay and ternary nanocomposites. When calculated with Bragg's law, these peaks have a d-spacing value of approximately twice that of the first characteristic peak. Thus, it can be said that the second peak is due to the second silicate layer.

Especially, for the ternary nanocomposites containing SEBS-g-MA and Cloisite® 25A, no diffraction peak is observed showing exfoliated structures both for 1 and 2wt% clay loadings. A better dispersion was expected for nanocomposites containing Cloisite® 15A due to its lower polar characteristics compared to Cloisite® 25A. However, Cloisite® 15A has two long aliphatic tails and these tails limit the access of polymer chains to the clay surface. Because of these alkyl chains, the interaction between the polymer chain and organoclay platelet could not overcome the interaction between the organoclay platelets. Thus, alkylammonium compound consisting of one alkyl tail is more effective than the quaternary cation having two alkyl tails in forming exfoliated nanocomposites [107].
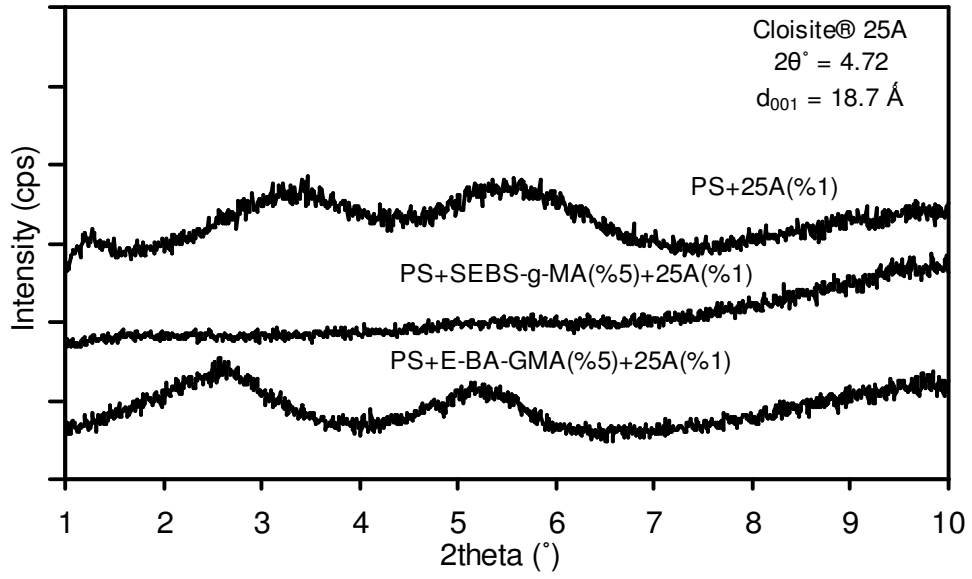
Figure 4.7 XRD pattern of nanocomposites containing 1wt% Cloisite® 25A and 5wt% Elastomer
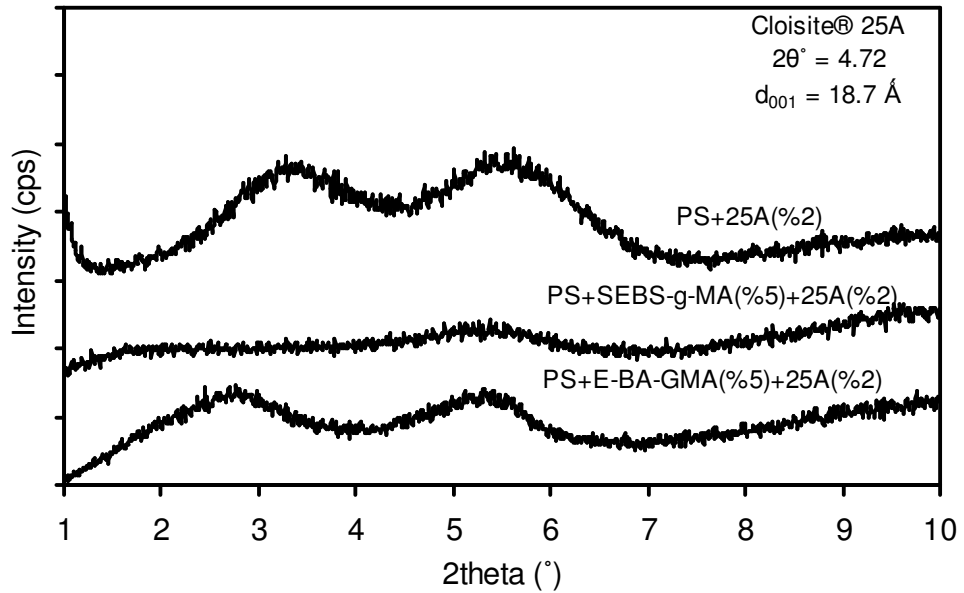
Figure 4.8 XRD pattern of nanocomposites containing 2wt% Cloisite® 25A and 5wt% Elastomer

In Figure 4.9 XRD patterns of binary elastomer/Cloisite® 25A nanocomposites are shown. The same characteristics that were found for the elastomer/Cloisite® 15A binary nanocomposites were obtained. In the elastomer SEBS-g-MA, organoclay platelets are completely separated from each other, whereas E-BA-GMA results in conventional composites. Compared to the viscosity of the E-BA-GMA, SEBS-g-MA has higher viscosity that provides greater shear stress on the clay platelets during extrusion and the better dispersion in ternary nanocomposites containing SEBS-g-MA can be attributed to the higher viscosity. This difference between the viscosities of the two elastomers was observed with both capillary viscometer and MFI tests, and will be sown in the following sections. Thus, as mentioned before, not only chemical compatibility between the polymer matrix and organoclay, and the chemistry of the clay treatment are important factors in intercalation/exfoliation mechanisms, but also the shear intensity in the extruder is a crucial factor.
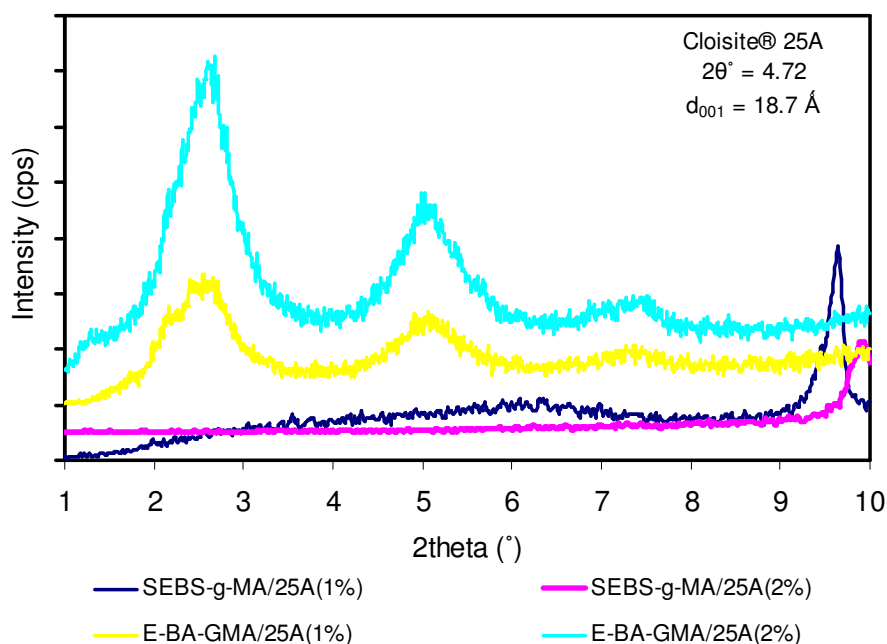
Figure 4.9 XRD pattern of binary nanocomposites containing Cloisite® 25A and Elastomer

Up to this stage of this study, it was seen that SEBS-g-MA is a better compatibilizer for PS based nanocomposites compared to E-BA-GMA. Shortly before, it was explained that this better compatibilization effect is a result of the higher viscosity of SEBS-g-MA. In addition to the viscosity effect, this finer dispersion in SEBS-g-MA containing nanocomposites may be due to the higher phase compatibility between SEBS part of the elastomer and PS arising from the solubility of polystyrene end block of SEBS with the amorphous polystyrene matrix. Owing to this reason, it was decided to use only SEBS-g-MA as the elastomer, and in order to see the effect of the elastomer concentration on the nanocomposites, the elastomer content was increased. Thus, besides ternary nanocomposites containing 5wt% elastomer, nanocomposites with 15, 20, 30 and 40wt% SEBS-g-MA content were prepared in the second part of the study.

Figures 4.10-4.11 show XRD patterns of nanocomposites containing Cloisite® 30B with increasing SEBS-g-MA content. As can be seen from the patterns, increasing Cloisite® 30B content has no significant effect on the degree of dispersion of clay particles. As in the case of 5wt% elastomer containing nanocomposites, the diffraction peak does not shift to lower angles. However, the peak becomes broader with increasing SEBS-g-MA content.
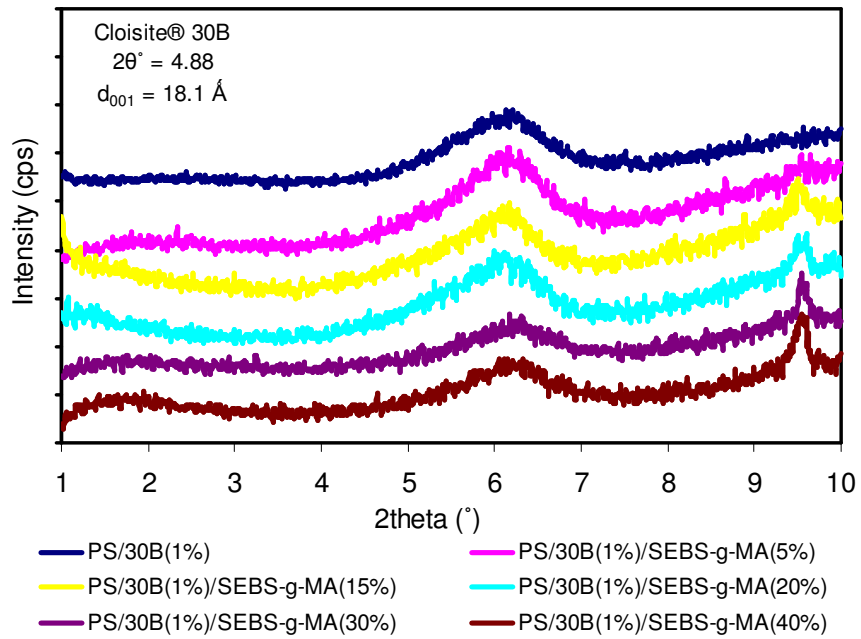
Figure 4.10 XRD pattern of nanocomposites containing 1wt% Cloisite® 30B and SEBS-g-MA
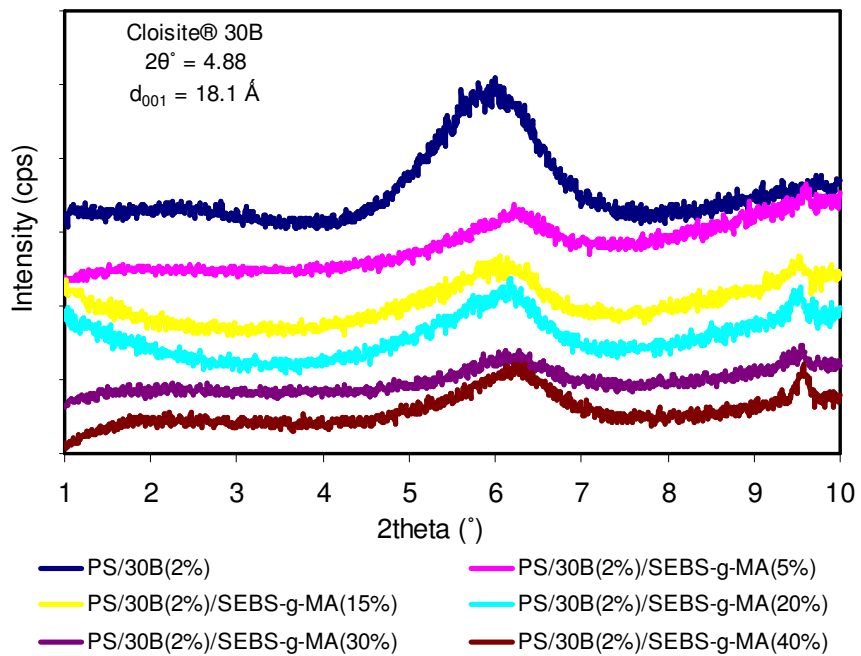
Figure 4.11 XRD pattern of nanocomposites containing 2wt% Cloisite® 30B and SEBS-g-MA

The effects of increasing SEBS-g-MA content on the dispersion of Cloisite® 15A platelets can be seen from Figures 4.12 and 4.13. As the amount of elastomeric material increases, the clay layers that shelter the elastomeric phase between their layers get enlarged and become dispersed. Specifically, the nanocomposites containing 15 and 20wt% elastomeric phase show exfoliated structures due to the optimum elastomer content that provides better interaction with the polymer matrix and enhances mechanical properties in a desired way. This phenomenon will be discussed later in SEM analysis and mechanical properties.

When the XRD diffraction patterns of nanocomposites containing Cloisite® 25A with increasing SEBS-g-MA content are considered, it can be said that further addition of elastomeric material does not affect exfoliated structure in a negative way. As can be seen from Figures 4.14 and 4.15, all of the patterns represent no diffraction peaks indicating exfoliated structures.
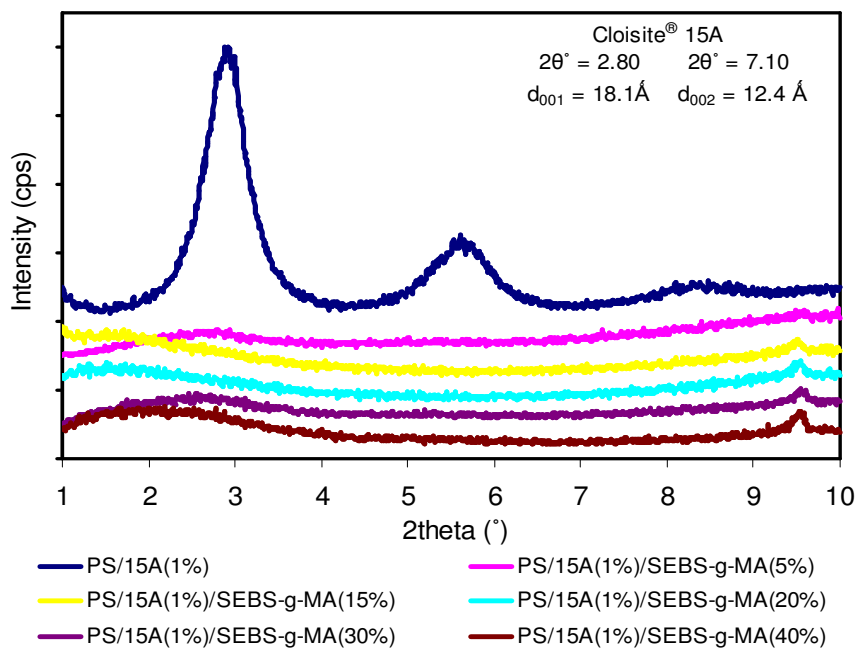
Figure 4.12 XRD pattern of nanocomposites containing 1wt% Cloisite® 15A and SEBS-g-MA
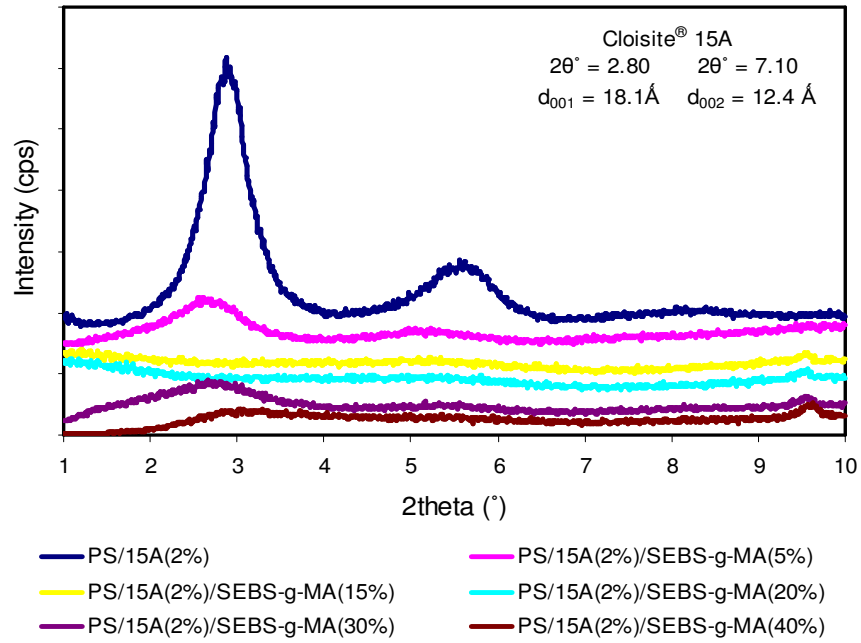
Figure 4.13 XRD pattern of nanocomposites containing 2wt% Cloisite[®] 15A and SEBS-g-MA
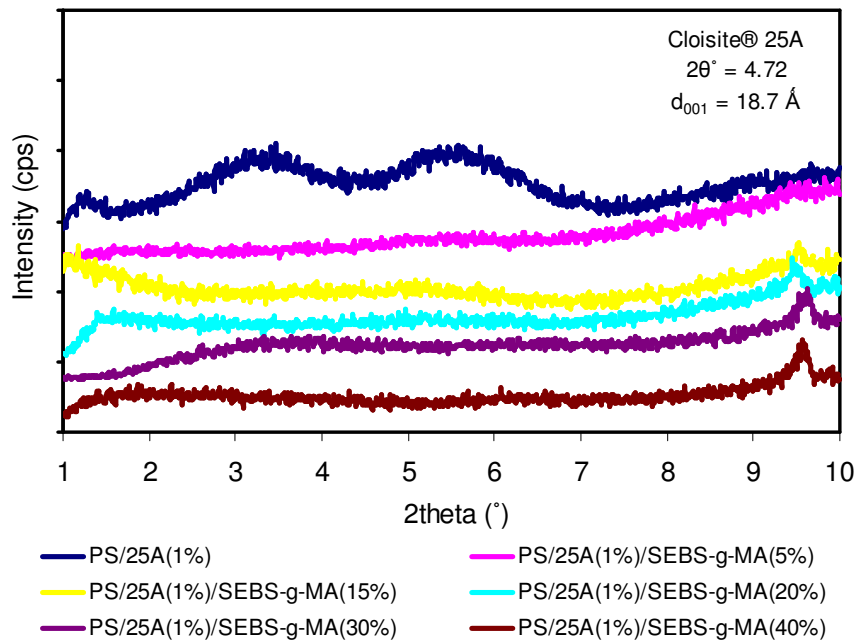
Figure 4.14 XRD pattern of nanocomposites containing 1wt% Cloisite[®] 25A and SEBS-g-MA
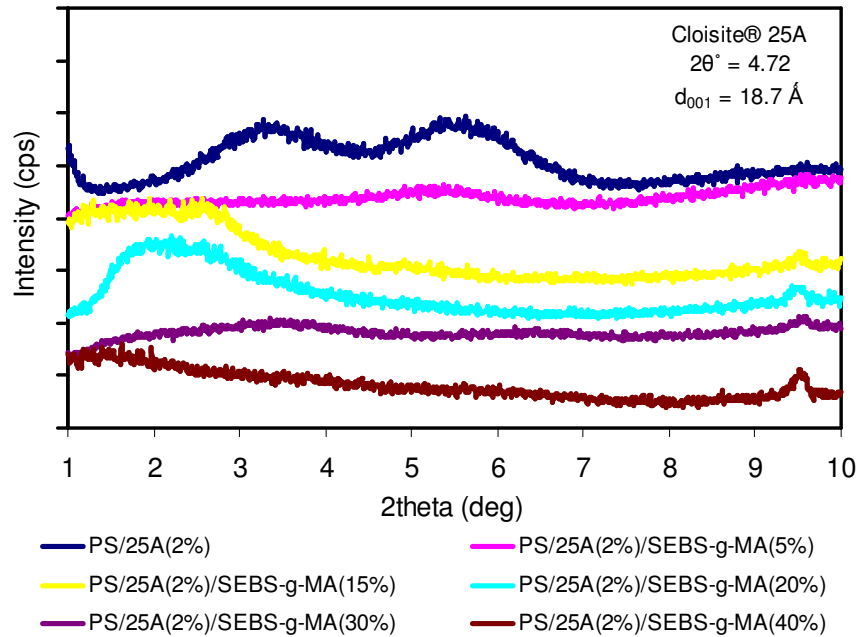
Figure 4.15 XRD pattern of nanocomposites containing 2wt% Cloisite$^{®}$ 25A and SEBS-g-MA

4.1.2 Scanning Electron Microscopy

Modification with rubbery block copolymers is one of the ways of improving the toughness of brittle polymers and it is directly related with the dispersion of the rubber phase in the polymer matrix. In order to examine the elastomeric particle size and their distribution, SEM analysis can be used. Failure mechanism is another property that can be investigated with SEM. For the SEM analysis of this study photographs with x250 and x3500 magnification were taken.

Before taking SEM photographs, the fractured surface of the samples were etched with n-Heptane, at room temperature, to remove the elastomeric phase. The average size of the dispersed phase was analyzed by using ImageJ software program. Approximately 50-100 domains were analyzed to get an accurate dimension. Average domain size (average diameter) was calculated by using Equations 4.1 and 4.2 where A_i and n_i represents the area and the number of domains that has an area of A_i, respectively.

$$\overline{A} = \frac{\sum n_i . A_i}{\sum n_i} \qquad (4.1)$$

$$\overline{d} = \sqrt{\frac{\overline{A} \times 4}{\pi}} \qquad (4.2)$$

The average domain size calculated for samples are illustrated in Table 4.2. Figure 4.16 shows the SEM micrograph of pure PS. Since PS is a brittle polymer it exhibits straight crack propagation lines rather than tortuous lines. These straight lines enhance further growth and make it easier to fracture with only a small amount of energy [108].
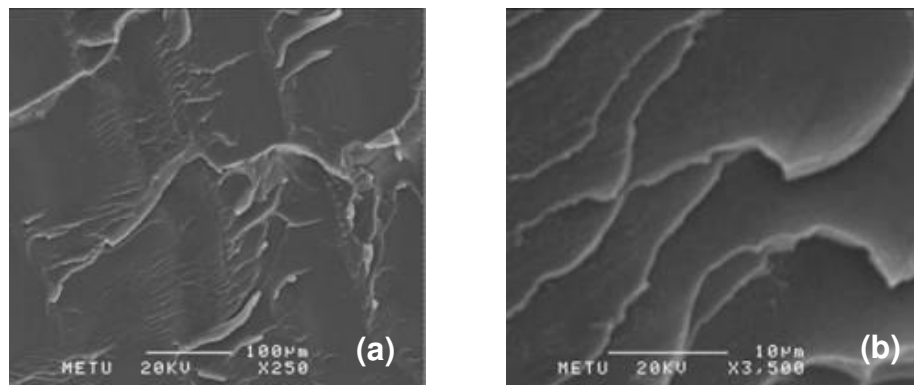
Figure 4.16 SEM micrographs of PS with (a)x250 (b)x3500 magnifications

Table 4.2 Average domain size for all samples

Composition	d_{av} (nm)
PS / SEBS-g-MA blends	
PS + SEBS-g-MA (5%)	225
PS + SEBS-g-MA (15%)	475
PS + SEBS-g-MA (20%)	589
PS + SEBS-g-MA (30%)	638
PS + SEBS-g-MA (40%)	Co-continuous
PS / E-BA-GMA blends	
PS + E-BA-GMA (5%)	176
PS + E-BA-GMA (15%)	391
PS + E-BA-GMA (20%)	454
PS + E-BA-GMA (30%)	666
PS + E-BA-GMA (40%)	Co-continuous
PS / 5 wt% Elastomer / Organoclay nanocomposites	
PS + SEBS-g-MA (5%) + 30B (1%)	495
PS + SEBS-g-MA (5%) + 30B (2%)	449
PS + SEBS-g-MA (5%) + 15A (1%)	499
PS + SEBS-g-MA (5%) + 15A (2%)	485
PS + SEBS-g-MA (5%) + 25A (1%)	512
PS + SEBS-g-MA (5%) + 25A (2%)	495
PS / 15 wt% Elastomer / Organoclay nanocomposites	
PS + SEBS-g-MA (15%) + 30B (1%)	540
PS + SEBS-g-MA (15%) + 30B (2%)	583
PS + SEBS-g-MA (15%) + 15A (1%)	608
PS + SEBS-g-MA (15%) + 15A (2%)	539
PS + SEBS-g-MA (15%) + 25A (1%)	552
PS + SEBS-g-MA (15%) + 25A (2%)	619
PS / 20 wt% Elastomer / Organoclay nanocomposites	
PS + SEBS-g-MA (20%) + 30B (1%)	631
PS + SEBS-g-MA (20%) + 30B (2%)	736
PS + SEBS-g-MA (20%) + 15A (1%)	744
PS + SEBS-g-MA (20%) + 15A (2%)	702
PS + SEBS-g-MA (20%) + 25A (1%)	691
PS + SEBS-g-MA (20%) + 25A (2%)	674
PS / 30 wt% Elastomer / Organoclay nanocomposites	
Co-continuous	
PS / 40 wt% Elastomer / Organoclay nanocomposites	
Co-continuous	
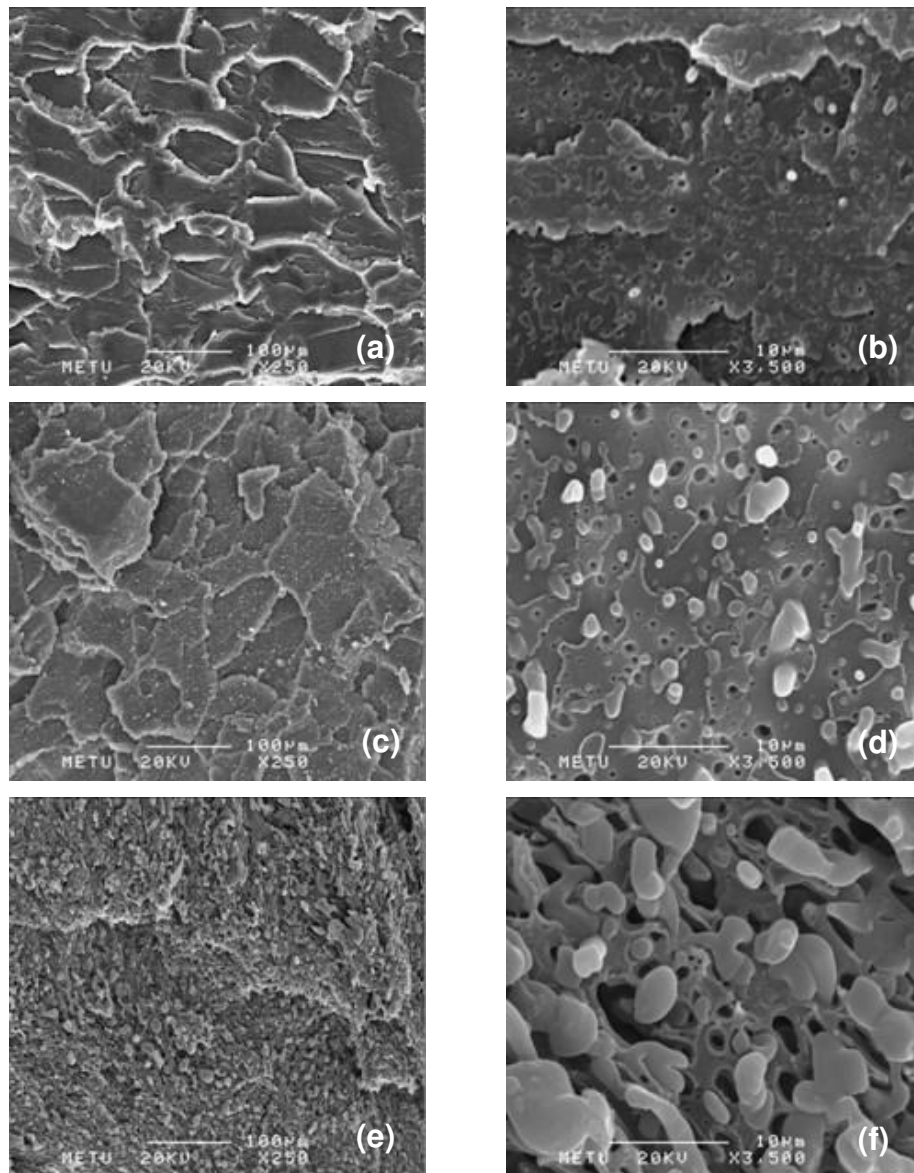
Figure 4.17 SEM micrographs of un-etched PS/SEBS-g-MA blends: (a) 5wt% (x250), (b) 5wt% (x3500); (c) 15wt% (x250); (d) 15wt% (x3500); (e) 40wt% (x250); (f) 40wt% (x3500) SEBS-g-MA

Since etching procedure annihilates the crack propagation lines, in Figure 4.17 the un-etched fracture surfaces of the PS/SEBS-g-MA polymer blends are shown to see the effects of elastomer addition on the fracture mechanism. By the addition of elastomer, the crack propagation lines become shorter and closer to each other and the number of cracks increase. As the amount of compatibilizer increases this process becomes more significant. Thus, featureless structure of the PS disappears, indicating an increased amount of energy dissipation during fracture. Also, the increasing roughness of a surface directly affects the toughness of a material. Mechanical results that will be discussed later verify this argument.

For the blend containing 40wt% SEBS-g-MA the crack lines become very dense, resulting in a considerable increase in the energy which is required to keep the cracks moving for failure of the material. However, as will be discussed later, this co-continuous structure decreases the tensile strength.

The morphology development of the blends during melt mixing comprise processes such as, fluid drops stretching into threads, break-up of the threads into smaller droplets and coalescence of the droplets into larger ones [52]. In most of the cases coalescence occurs, although small domains make the system more stable due to the larger surface area created. This is due to the cohesive forces between domains and interfacial mobility of the dispersed phase. Thus, during the coalescence process, that is a result of collision forces, the system becomes un-stabilized and in order to stabilize the blend systems, components of the mixture tend to create a phase structure with a minimum total free energy. Input of energy is required to form these new surfaces and interfaces. When the rate of coalescence and breakdown are balanced, the recombination of the domains is impeded and the equilibrium particle size is achieved [89].

In this study, elastomeric domains were observed when the fractured surfaces of the samples were etched with n-Heptane. The effects of both the increase in elastomer content and organoclay addition on the morphology are discussed by the help of the size of these domains.

The etched fracture surfaces of the PS/SEBS-g-MA binary blends are shown in Figures 4.18-4.22. An important aspect of the phase morphology is its microstructure. The microstructure of two phase blends may be formed from domains with different shape, size and distribution which are one of the key factors for achieving desired properties. Droplet matrix morphologies improve the impact properties, fibrillar morphologies result in better tensile properties, blends with lamellar structure enhance barrier properties and co-continuous morphologies show a combination of both components [55, 109].

The SEBS-g-MA domains in PS matrix form dispersed droplets. As the amount of the dispersed phase increases, the average domain size increases and the circular shape of the elastomeric domains become stretched and a less uniform domain distribution is observed. This is related with droplet coalescence during melt mixing, which results in broadening of the domains. Since SEBS-g-MA has a higher viscosity than PS matrix, its presence increases the viscosity of the blend and the shear stress applied on the platelets during extrusion. However, increasing viscosity prevents the elastomeric phase to disperse into small droplets because the shear stress that is applied on to the material becomes insufficient. So the coalescence rate increases. Another factor that leads to increase in the coalescence rate with increasing elastomer content may be attributed to the increase in the number of dispersed domains and therefore the probability of the domains to collide with each other [53, 89].

Average domain size and interdomain distance are important factors that affect the toughening of the materials. The final domain size is controlled by many factors such as; the melt viscosity, melt elasticity of the components, rheological properties, volume fractions of the components, shear stresses and rates, mobility of the interface and surface tension. Small inter-particle distance suppresses craze or crack growth and facilitate the overlap of the stress fields around the adjacent rubber articles. By this way, local shear yielding is promoted and high impact energies are absorbed [55, 110]. However, the size of the domain should not be too small or too big. When there is high adhesion owing to great compatibilization, ultra-fine domains of elastomers are formed and cause low impact strength values, because crack propagation lines progress without touching the elastomer domains. Larger elastomeric domains also influence the toughness negatively since they

form large regions that could not stop the crack propagation. As will be seen later on, the blends containing 15 and 20wt% SEBS-g-MA have the optimum average domain size resulting in higher impact strength without deteriorating the tensile strength values.

In this study, PS is the continuous phase according to the general criteria for phase inversion which states that, the phase with lower viscosity or higher volume fraction tends to be the continuous phase. With increasing elastomer content, the dispersed morphology turn from dispersed phase structure into a co-continuous structure. As can be seen from Figure 4.22, when the elastomer content is set to 40wt% the phase morphology becomes co-continuous leading to maximum interfacial contact area.

The concentration where the co-continuous phase morphology becomes observable is called "phase inversion" point. PS/SEBS-g-MA blends have a point of inversion between 30 and 40wt% content of the elastomeric phase. The point of phase inversion can also be found by using some theoretical models. The experimental observation of this study will be compared with the theoretical models in the next section.
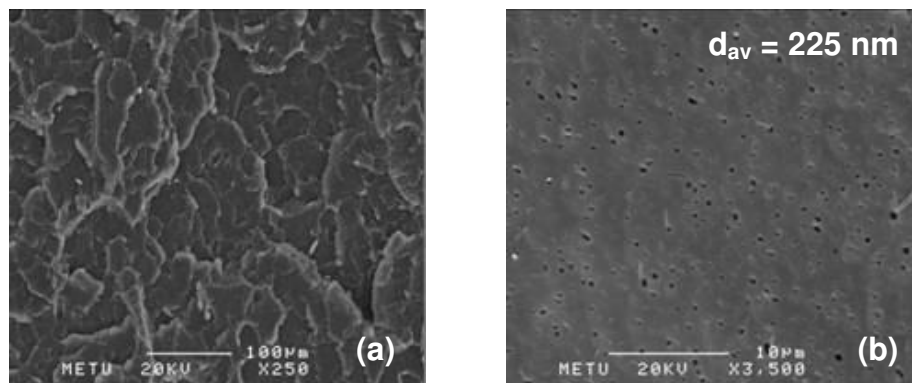
Figure 4.18 SEM micrograph of PS/SEBS-g-MA (5wt%) blend: (a)x250; (b)x3500
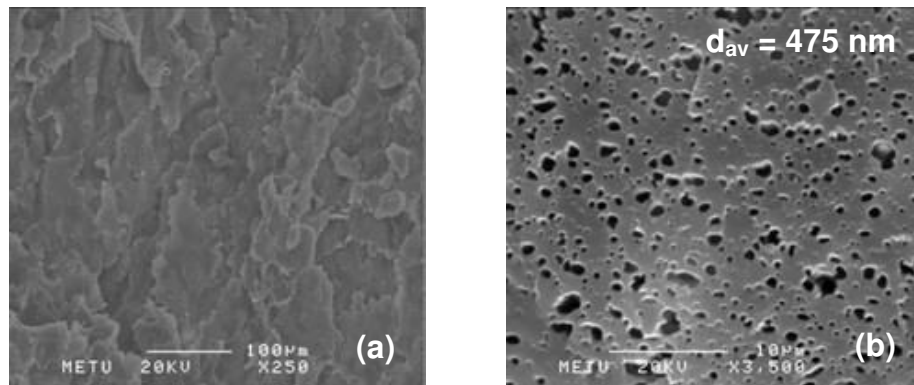
Figure 4.19 SEM micrograph of PS/SEBS-g-MA (15wt%) blend: (a)x250; (b)x3500
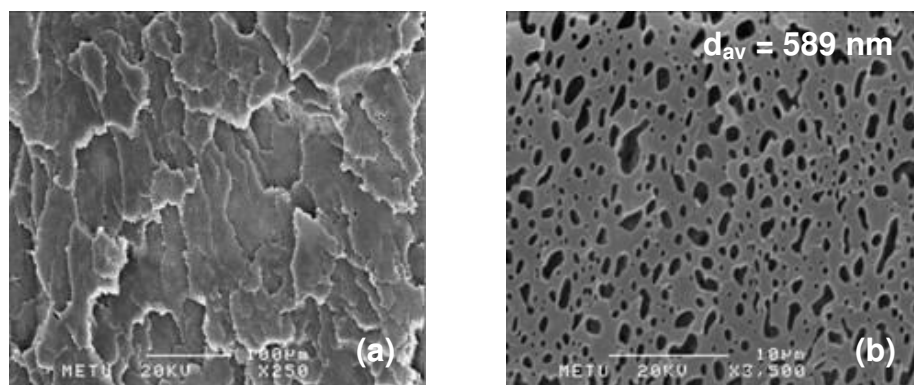
Figure 4.20 SEM micrograph of PS/SEBS-g-MA (20wt%) blend: (a)x250; (b)x3500
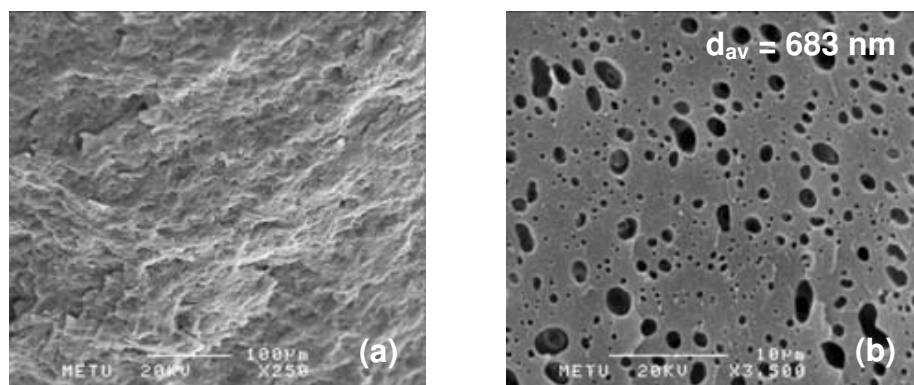
Figure 4.21 SEM micrograph of PS/SEBS-g-MA (30wt%) blend: (a)x250; (b)x3500
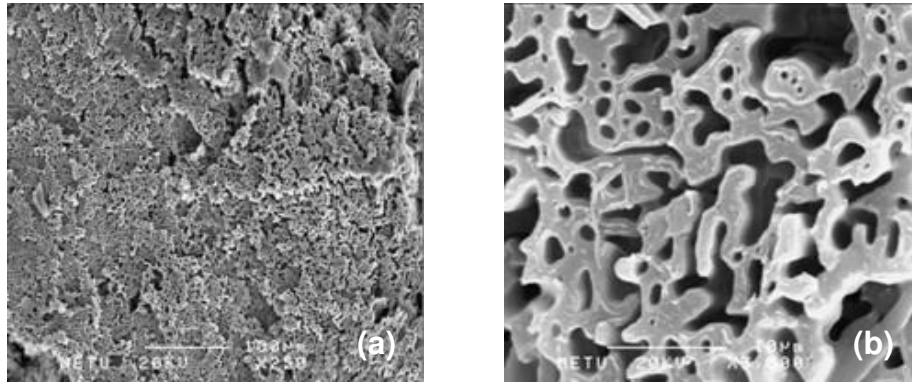
Figure 4.22 SEM micrograph of PS/SEBS-g-MA (40wt%) blend: (a)x250; (b)x3500

Figures 4.23-4.27 show the etched fracture surface of PS/E-BA-GMA blends. When the change in the size of the interdomain particles of these blends with increasing elastomer content are considered, the same trend that is observed for PS/SEBS-g-MA blends can be seen. As the elastomer content increases, the average domain size also increases. Since the viscosity of E-BA-GMA is lower than the viscosity of PS matrix, the discussion indicating that increasing viscosity leads to higher coalescence rate is not valid. On the contrary, it is thought that the probability of the domains to collide with each other may be increased owing to the increase in the number of dispersed domains. Also, the general phase inversion criteria which states that lower viscosity material forms the continuous phase in binary blends is not valid owing to the lower volume fraction of E-BA-GMA in the PS matrix.
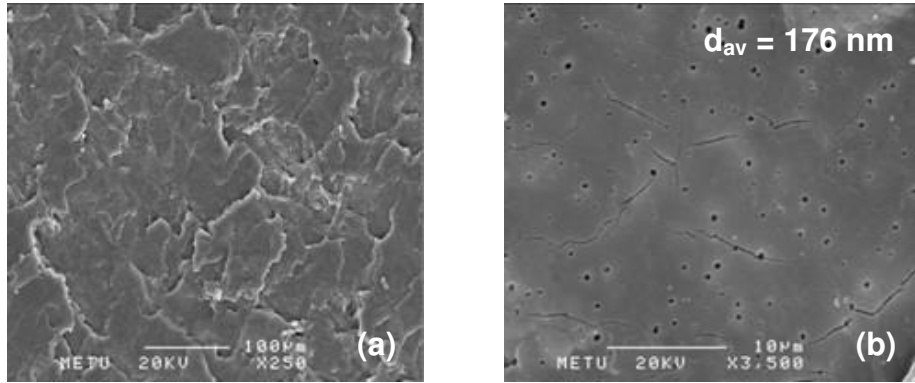
Figure 4.23 SEM micrograph of PS/E-BA-GMA (5wt%) blend: (a)x250; (b)x3500
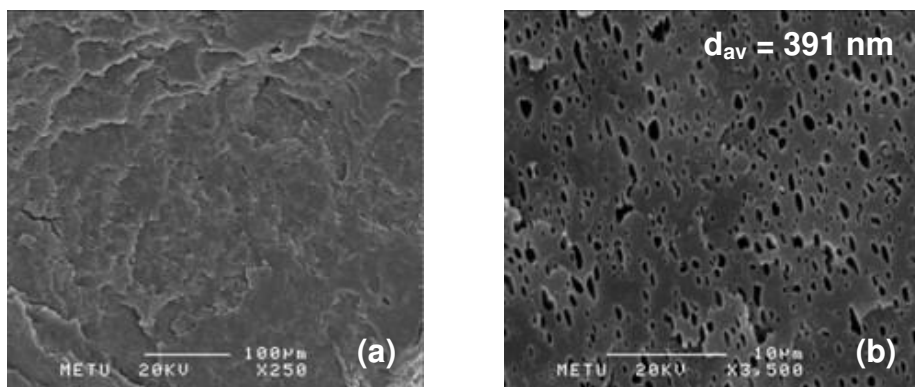
Figure 4.24 SEM micrograph of PS/E-BA-GMA (15wt%) blend: (a)x250; (b)x3500
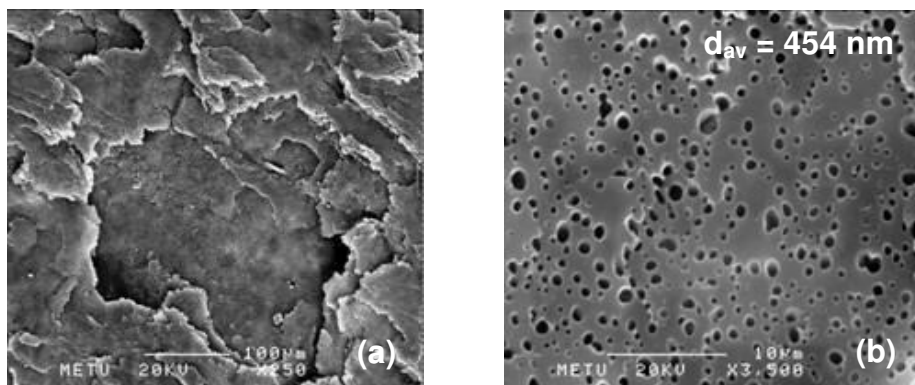
Figure 4.25 SEM micrograph of PS/E-BA-GMA (20wt%) blend: (a)x250; (b)x3500
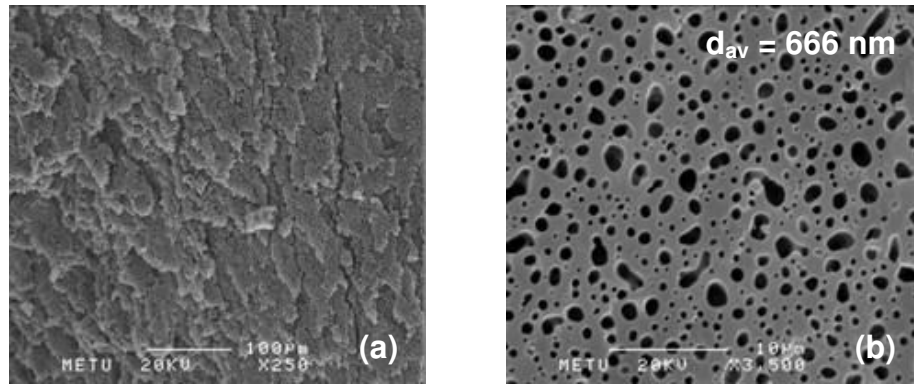
Figure 4.26 SEM micrograph of PS/E-BA-GMA (30wt%) blend: (a)x250; (b)x3500
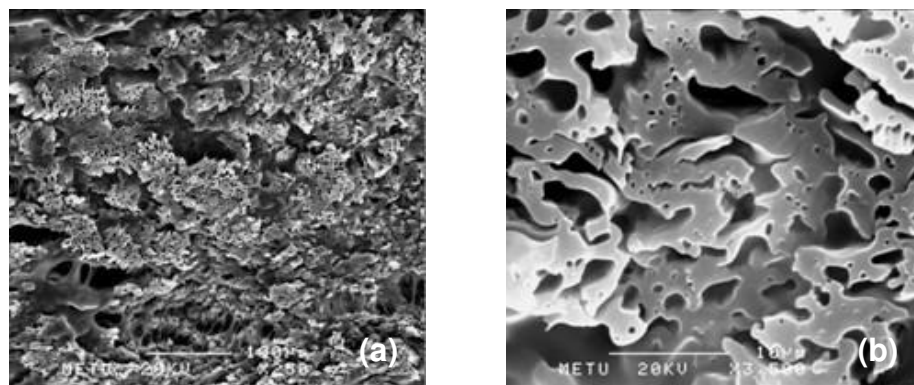
Figure 4.27 SEM micrograph of PS/E-BA-GMA (40wt%) blend: (a)x250; (b)x3500

Figures 4.28-4.29 show the etched fracture surface of the ternary nanocomposites containing 5wt% SEBS-g-MA for three types of organoclays. When compared with average domain size of the corresponding binary blend, which has an average diameter of 225 nm, the ternary nanocomposites show an increase in their average dispersed particle sizes. If the organoclay particles were dispersed in the PS matrix, the clay platelets would suppress the agglomeration of the elastomeric domains and cause a barrier effect that hinders the recombination of elastomeric domains [111]. However, for this case the average domain size increases with organoclay addition, no matter whether it is well dispersed or not, because the clay particles reside at the interphase between PS and elastomeric material. Thus, the interfacial tension is reduced and the domain sizes are enlarged. This is proved later by TEM studies.

For the ternary nanocomposites containing Cloisite® 25A, enlarged elastomeric domain sizes were expected due to the good dispersion of silicate layers that stay both inside the domains and at the interface between the elastomer and the matrix. However, for different types of organoclays, no significant difference in the size of the domains can be observed for the samples having the same organoclay and elastomer content. When the impact strengths of these nanocomposites are considered, it can be seen that the SEM observations are consistent with impact tests. The impact strength values of these samples are similar, in other words, toughness values of the nanocomposites are independent of the organoclay type. However, as will be mentioned later, the impact strength values are directly proportional with the elastomer content and depend on the type of elastomer.

The SEM micrograph of the ternary nanocomposites containing 5wt% E-BA-GMA could not be taken, because during the etching process, these samples fractured into small pieces due to poor interfacial adhesion between the matrix and E-BA-GMA in the presence of organoclay.

Another feature that is observed with the addition of organoclay is, the higher number of crack lines. In the case of well dispersed layered silicates, many shorter and closer, circular, nonlinear, cracks are formed simultaneously, and these nonlinear cracks tend to grow until they interfere with each other [67].
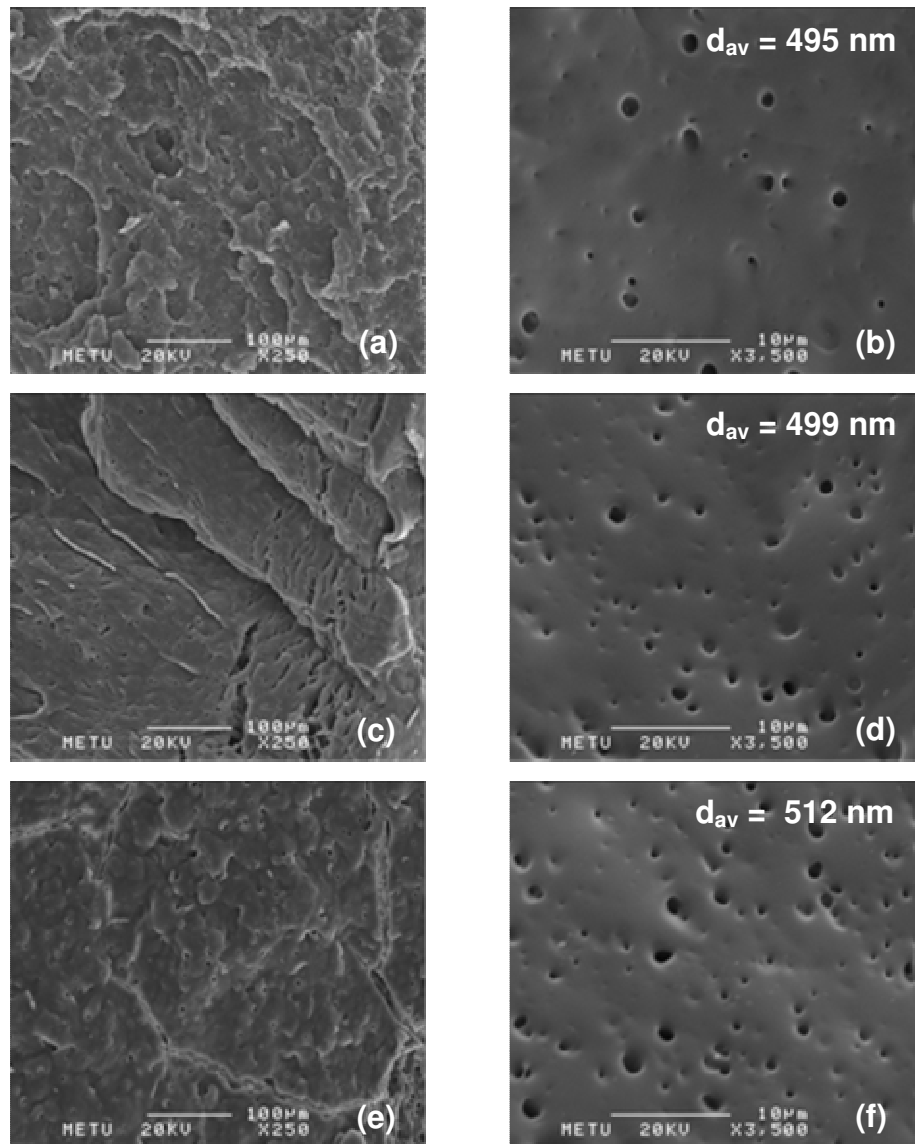
Figure 4.28 SEM micrograph of PS / SEBS-g-MA (5wt%) / Organoclay (1wt%) ternary nanocomposites: (a) Cloisite® 30B x250; (b) Cloisite® 30B x3500 (c) Cloisite® 15A x250; (d) Cloisite® 15A x3500; (e) Cloisite® 25A x250; (f) Cloisite® 25A x3500
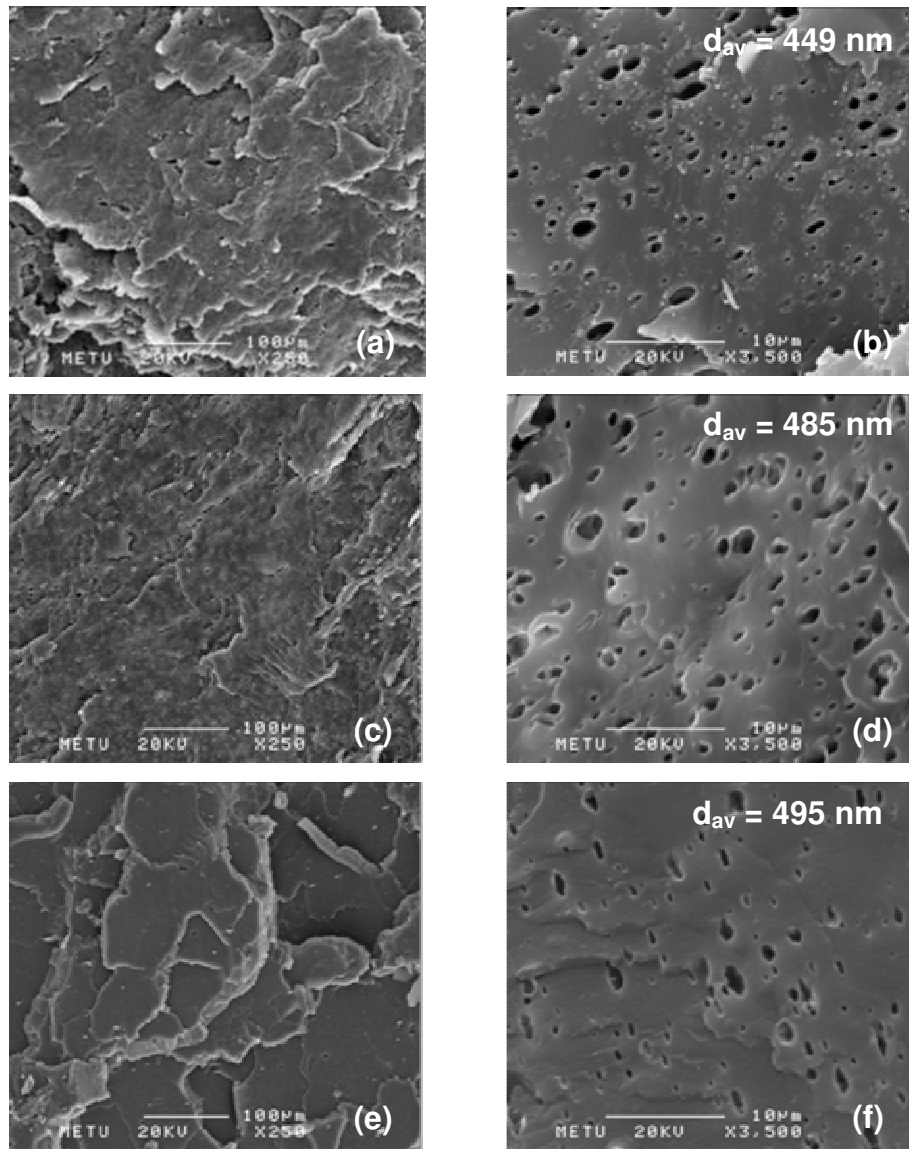
Figure 4.29 SEM micrograph of PS / SEBS-g-MA (5wt%) / Organoclay (2wt%) ternary nanocomposites: (a) Cloisite® 30B x250; (b) Cloisite® 30B x3500 (c) Cloisite® 15A x250; (d) Cloisite® 15A x3500; (e) Cloisite® 25A x250; (f) Cloisite® 25A x3500

The etched fracture surface of the ternary nanocomposites containing 15 and 20wt% SEBS-g-MA are shown in Figures 4.30-4.33. As in the case of 5wt% elastomer containing nanocomposites, the addition of organoclay makes the elastomeric domains larger.

When the SEM micrograph of nanocomposites containing 30 and 40wt% elastomer are considered (Figures 4.34-4.37) the interconnected structure of the minor component can be seen. The entire minor component incorporates into a single continuous phase network inside the PS component and a fully co-continuous morphology is observed. Since a co-continuous structure is observed at 30wt% elastomer content, it can be said that the phase inversion occurs between 20 and 30wt% elastomer content. According to these results, it is obvious that the phase inversion point shifts to lower dispersed phase content with the addition of organoclay. This is an indication of the dispersion of clay layers at the PS-elastomer interphase and also in the elastomer phase. Since clay particles lead to enlargement of the domains, the phase inversion occurs at lower elastomer content.

Co-continuous morphologies exhibit the characteristics of both of its constituents, and these constituents take their part in the load sharing. It is known that PS has a high tensile strength and a low impact strength value. On the other hand, the characteristics of elastomeric materials are totally opposite to those of PS. They can absorb high amounts of energy upon impact, however, their tensile strength and modulus values are considerably small. In this study, when the co-continuous morphologies are obtained at 30 and 40wt% elastomer loadings in ternary nanocomposites, high amount of increase was observed for the impact strength values. However, reduction in the tensile strength values is also significant.
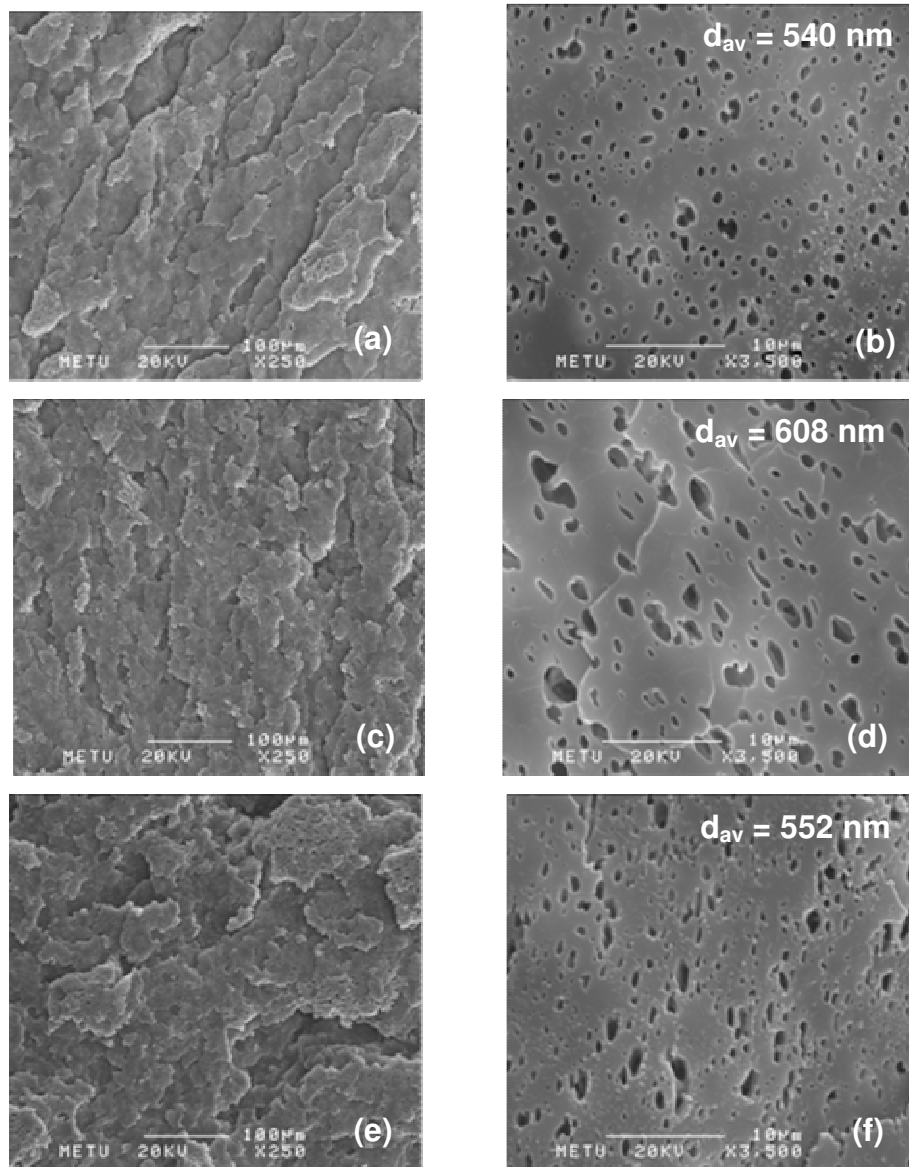
Figure 4.30 SEM micrograph of PS / SEBS-g-MA (15wt%) / Organoclay (1wt%) ternary nanocomposites: (a) Cloisite® 30B x250; (b) Cloisite® 30B x3500 (c) Cloisite® 15A x250; (d) Cloisite® 15A x3500; (e) Cloisite® 25A x250; (f) Cloisite® 25A x3500
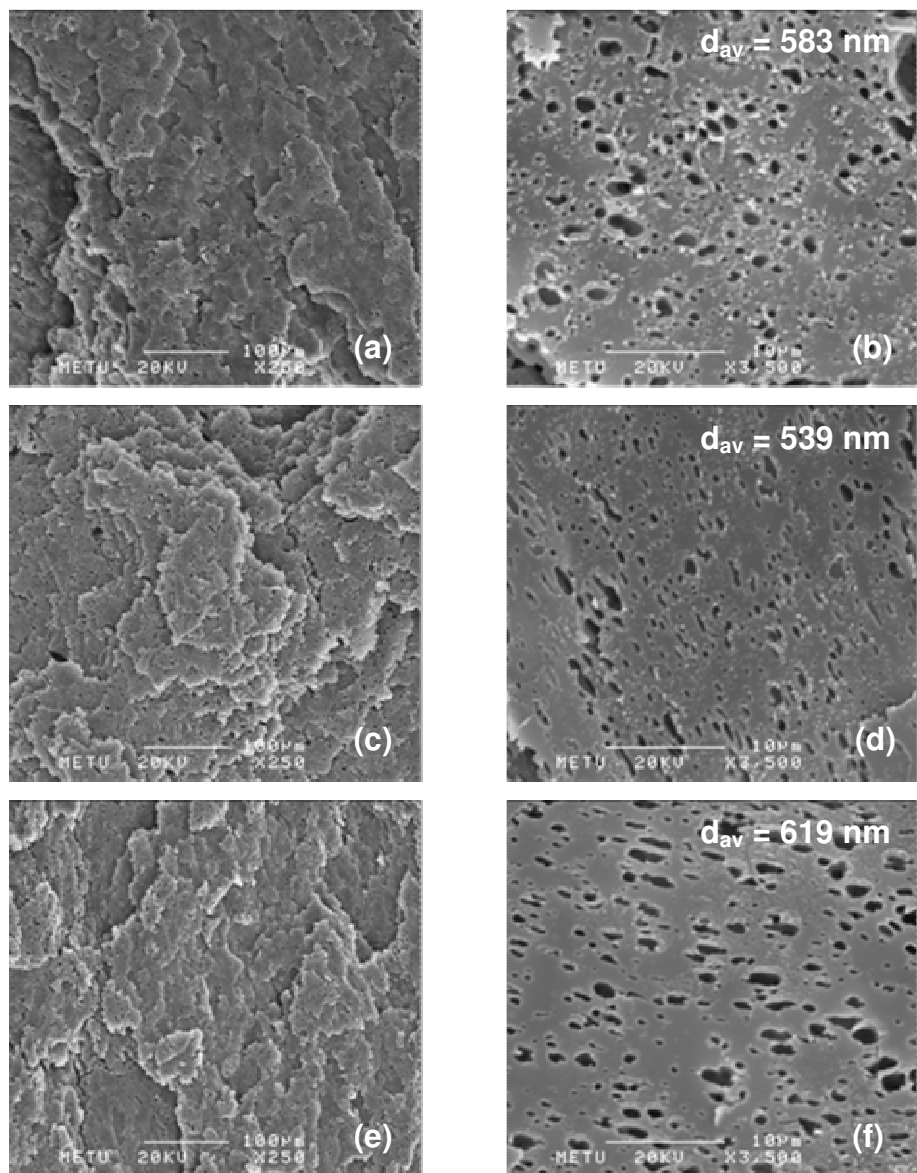
Figure 4.31 SEM micrograph of PS / SEBS-g-MA (15wt%) / Organoclay (2wt%) ternary nanocomposites: (a) Cloisite® 30B x250; (b) Cloisite® 30B x3500 (c) Cloisite® 15A x250; (d) Cloisite® 15A x3500; (e) Cloisite® 25A x250; (f) Cloisite® 25A x3500
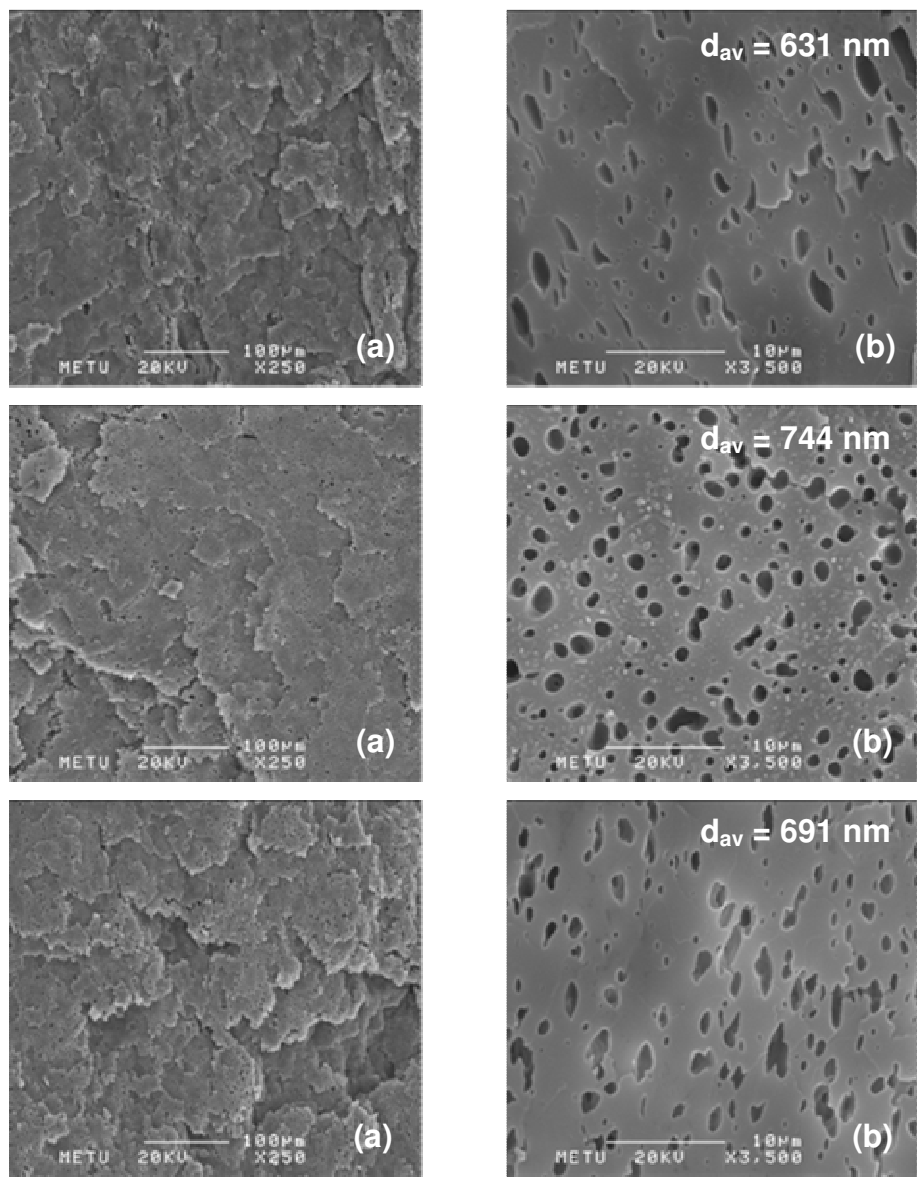
Figure 4.32 SEM micrograph of PS / SEBS-g-MA (20wt%) / Organoclay (1wt%) ternary nanocomposites: (a) Cloisite® 30B x250; (b) Cloisite® 30B x3500 (c) Cloisite® 15A x250; (d) Cloisite® 15A x3500; (e) Cloisite® 25A x250; (f) Cloisite® 25A x3500
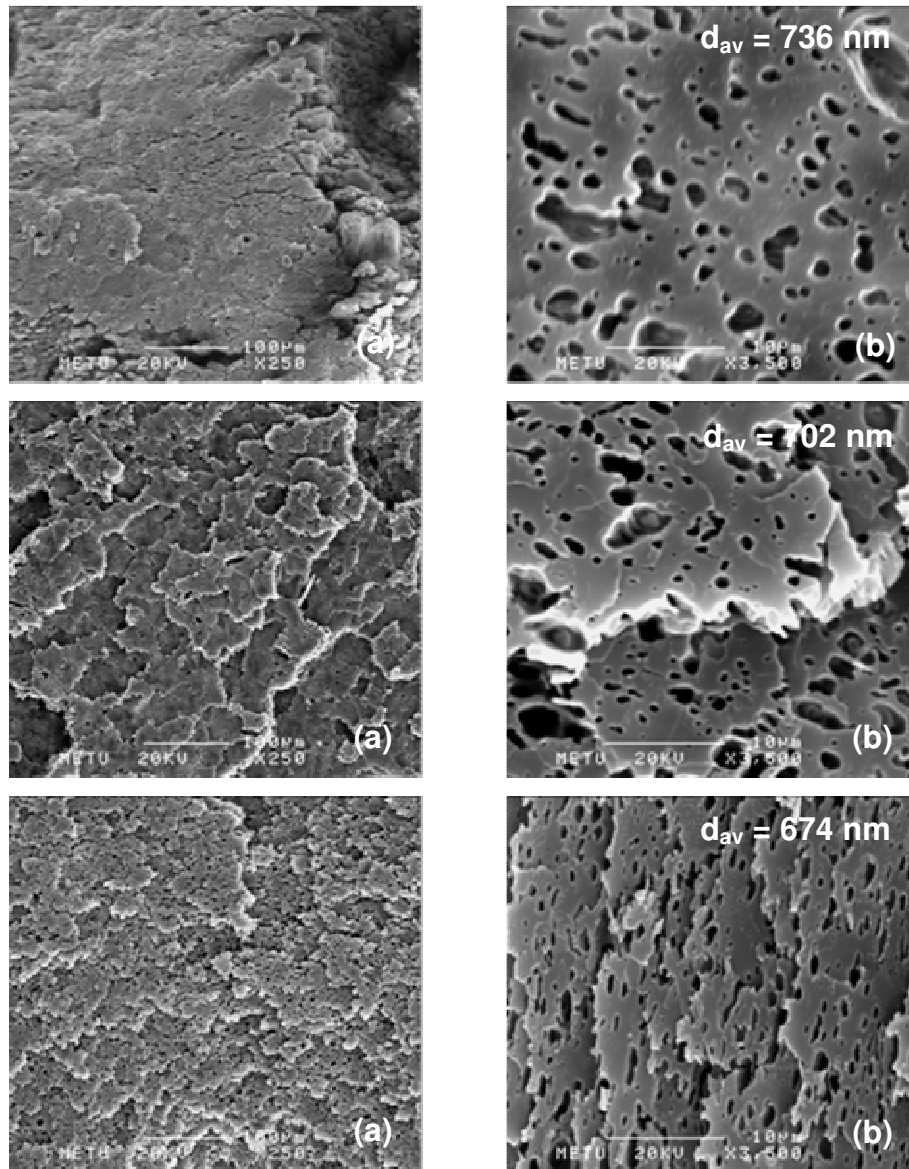
Figure 4.33 SEM micrograph of PS / SEBS-g-MA (20wt%) / Organoclay (2wt%) ternary nanocomposites: (a) Cloisite® 30B x250; (b) Cloisite® 30B x3500 (c) Cloisite® 15A x250; (d) Cloisite® 15A x3500; (e) Cloisite® 25A x250; (f) Cloisite® 25A x3500
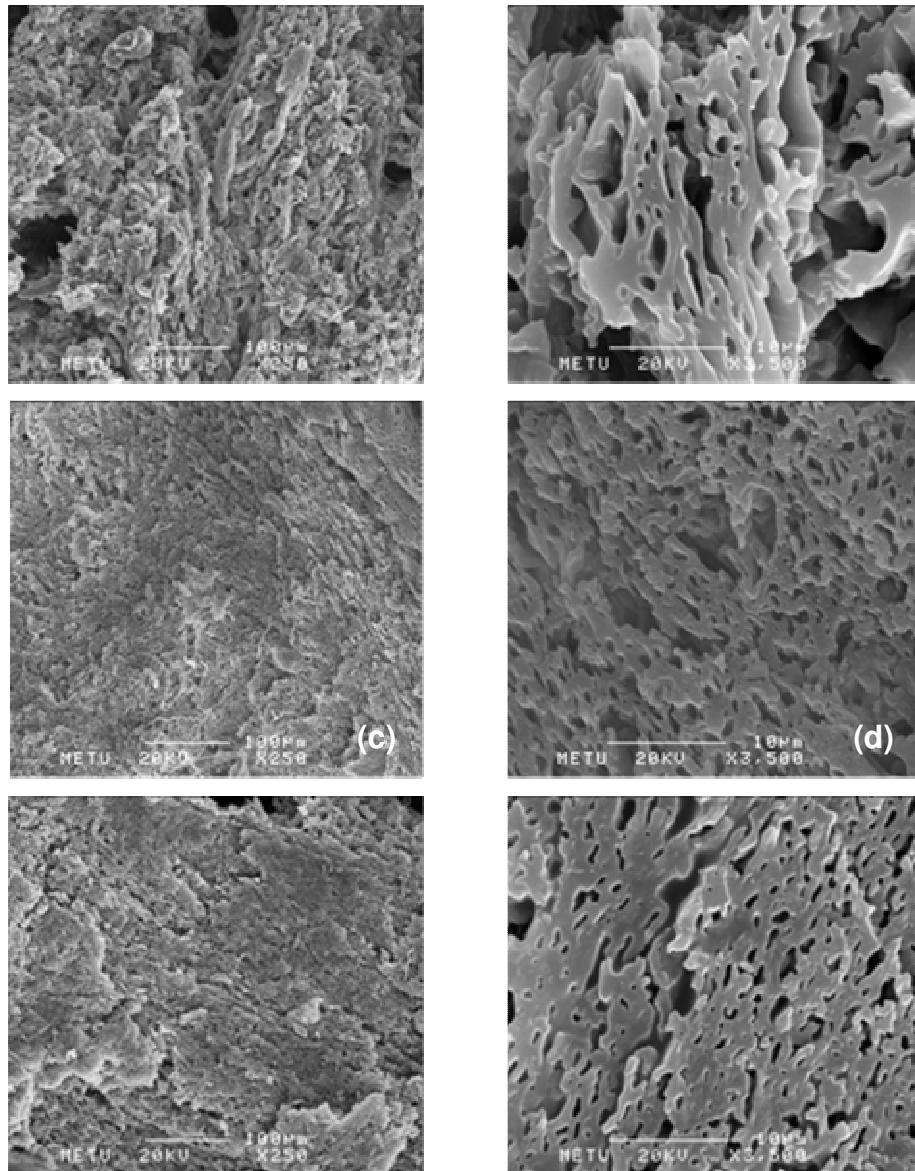
Figure 4.34 SEM micrograph of PS / SEBS-g-MA (30wt%) / Organoclay (1wt%) ternary nanocomposites: (a) Cloisite® 30B x250; (b) Cloisite® 30B x3500 (c) Cloisite® 15A x250; (d) Cloisite® 15A x3500; (e) Cloisite® 25A x250; (f) Cloisite® 25A x3500
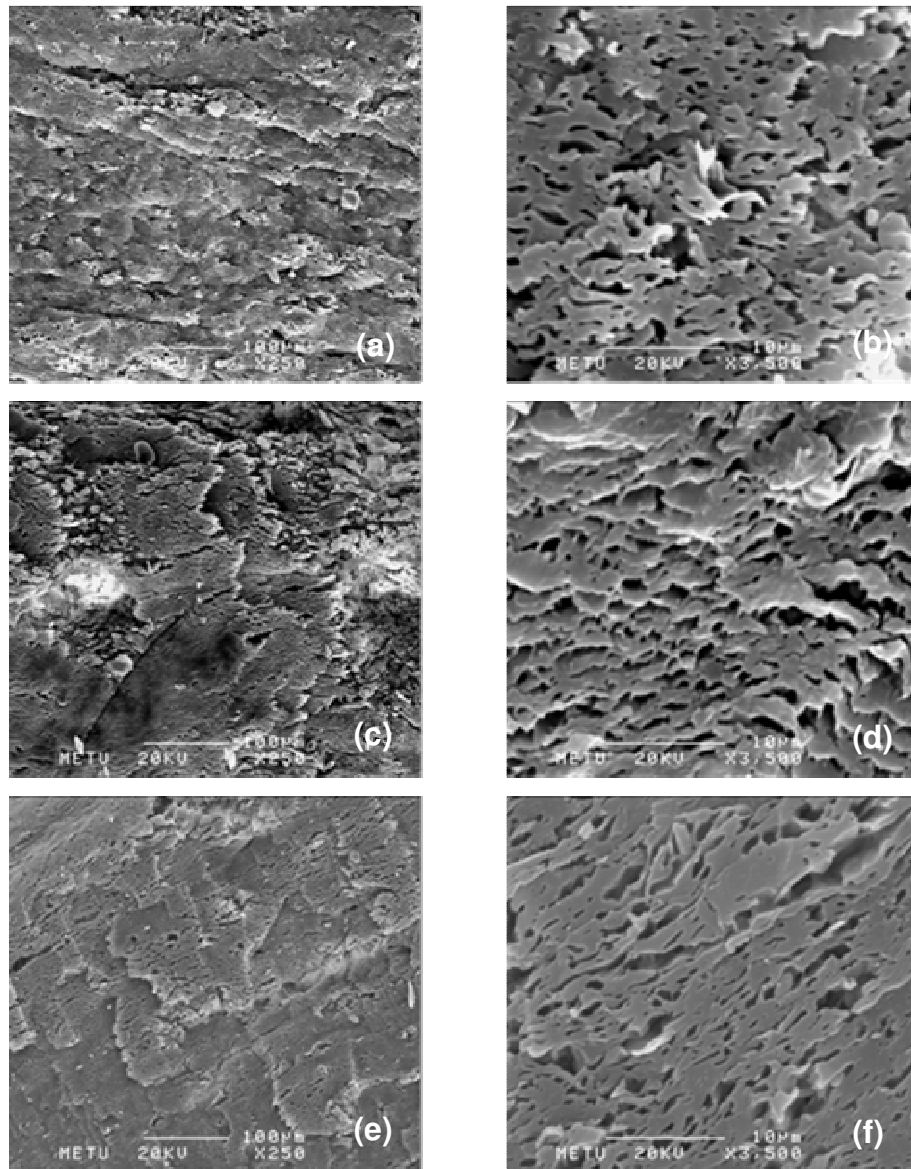
Figure 4.35 SEM micrograph of PS / SEBS-g-MA (30wt%) / Organoclay (2wt%) ternary nanocomposites: (a) Cloisite® 30B x250; (b) Cloisite® 30B x3500 (c) Cloisite® 15A x250; (d) Cloisite® 15A x3500; (e) Cloisite® 25A x250; (f) Cloisite® 25A x3500
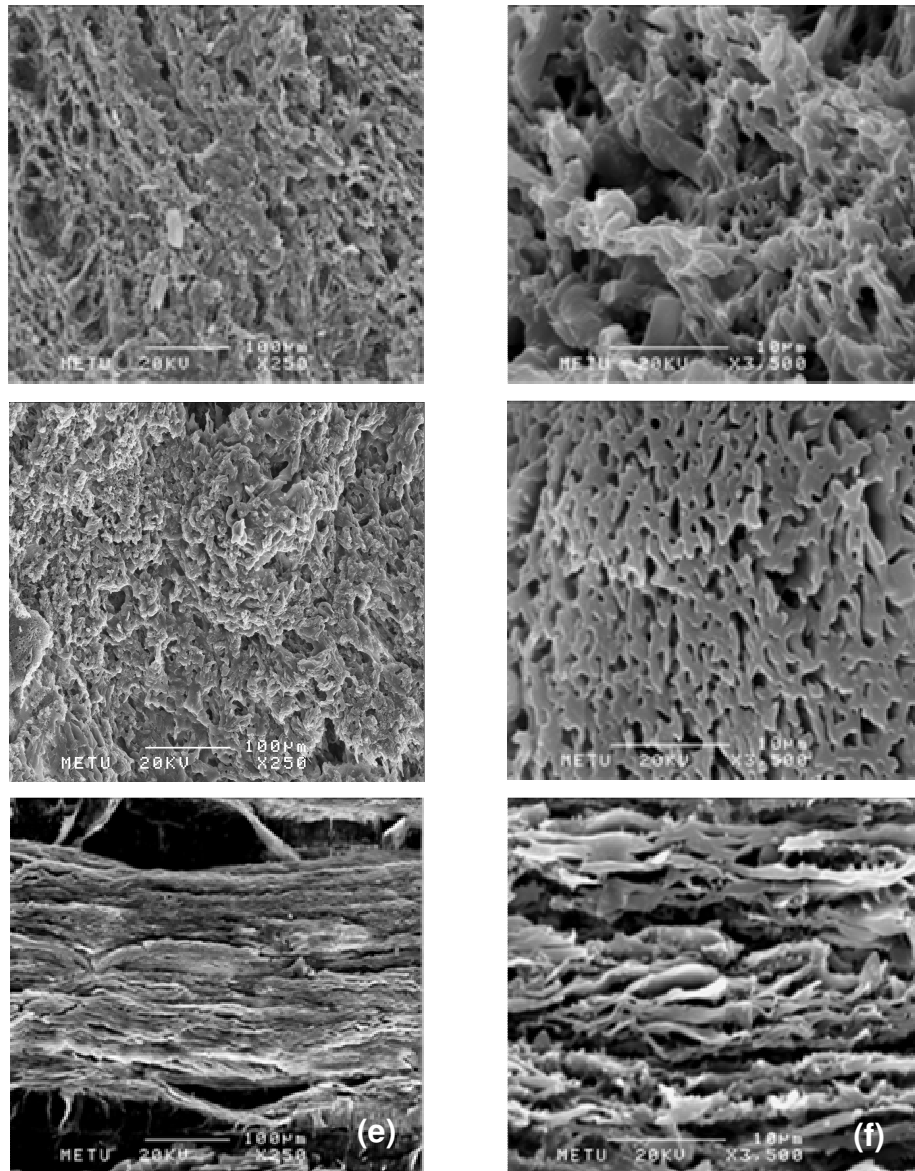
Figure 4.36 SEM micrograph of PS / SEBS-g-MA (40wt%) / Organoclay (1wt%) ternary nanocomposites: (a) Cloisite® 30B x250; (b) Cloisite® 30B x3500 (c) Cloisite® 15A x250; (d) Cloisite® 15A x3500; (e) Cloisite® 25A x250; (f) Cloisite® 25A x3500
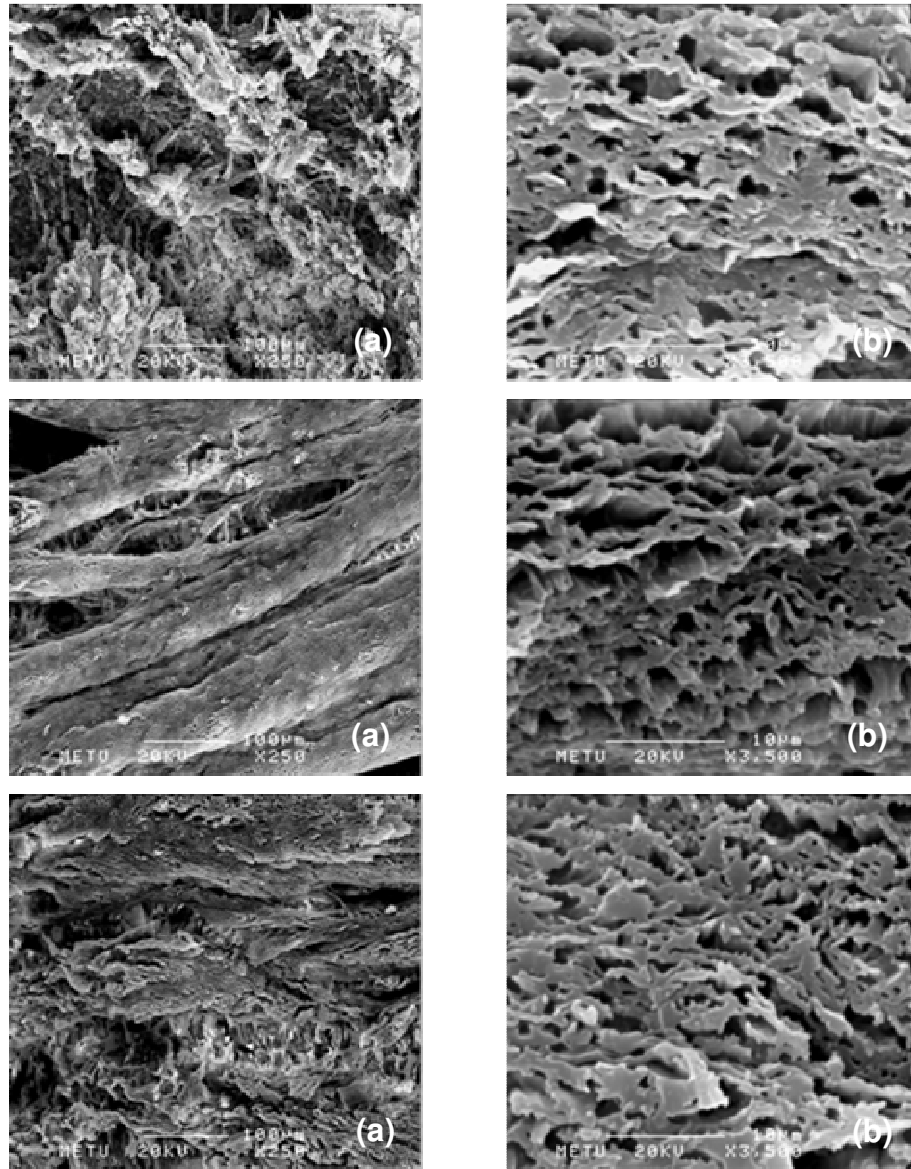
Figure 4.37 SEM micrograph of PS / SEBS-g-MA (40wt%) / Organoclay (2wt%) ternary nanocomposites: (a) Cloisite® 30B x250; (b) Cloisite® 30B x3500 (c) Cloisite® 15A x250; (d) Cloisite® 15A x3500; (e) Cloisite® 25A x250; (f) Cloisite® 25A x3500

4.1.3 Transmission Electron Microscopy

X-ray diffraction analysis was performed to investigate the dispersion of silicate layer within the polymer matrix. However, to validate the morphology of the nanocomposites, the internal nanometer scale structure should be observed with transmission electron microscopy (TEM), since it gives the distribution of the various phases, through direct visualization. In this study, not only the extent of dispersion of clay layers in nanocomposites was studied, but also the location of the clay particles was detected.

The visible black spots represent the clay agglomerates in TEM micrographs. For well dispersed structures, these spots appear as ribbons that indicate the delaminated layers of the filler. Moreover, the gray areas show the polymer matrix, whereas, elastomeric phases are observed as dispersed white regions. According to results obtained from XRD analysis and impact tests, it is concluded that, the clay particles are not finely dispersed in the presence of elastomeric material E-BA-GMA and the samples prepared with this material show no significant improvement in their impact strength values. Thus, it was decided to take TEM micrographs of only PS/elastomer/clay ternary nanocomposites, PS/clay binary nanocomposites and elastomer/clay binary nanocomposites prepared with SEBS-g-MA.

Figure 4.38 shows the TEM images of PS/Cloisite$^®$ 25A (2wt%) binary composite at different magnifications. In these images, clusters of clay platelets up to 1 µm are visible in the PS matrix. They show the sparse presence of primary particles of clay in the polymer matrix with closely stacked clay layers. This indicates that the clay layers are not exfoliated, but simply intercalated by polymer chains. This result is in accordance with the XRD result of PS/ Cloisite$^®$ 25A binary nanocomposite, which shows intercalation of polymer chains inside the clay galleries in the absence of a modifier. When, a compatibilizer is employed, the clay layers are dispersed more uniformly and they even delaminate depending on the type of the compatibilizer.
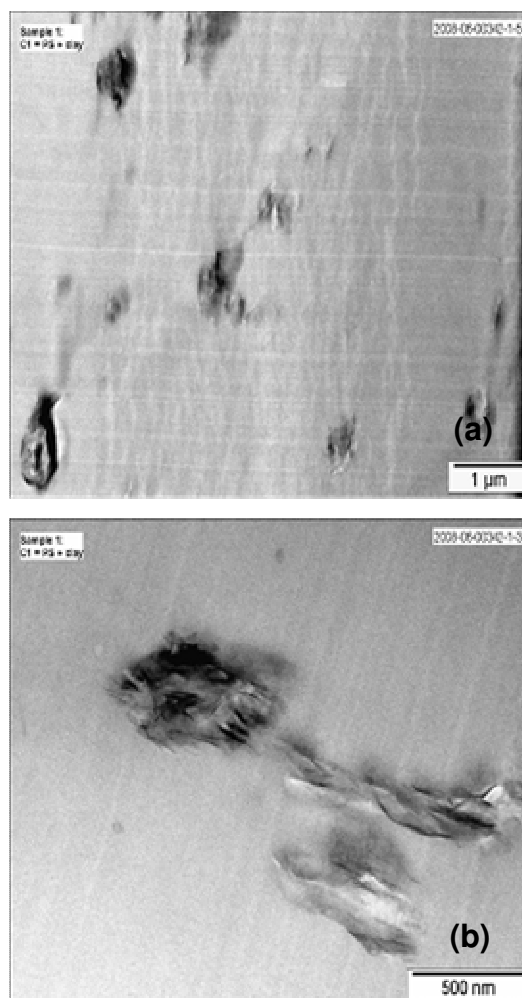
Figure 4.38 TEM micrograph of PS / Cloisite® 25A (2wt%) binary nanocomposites: (a)1μm scale; (b)500nm scale

Figures 4.39-4.41 display the TEM images of ternary nanocomposites containing PS/SEBS-g-MA (5wt%)/Cloisite® 25A (2wt%), PS/SEBS-g-MA/(15wt%)/Cloisite® 25A (2wt%) and PS/SEBS-g-MA (5wt%)/Cloisite® 30B (2wt%). The white droplets that are shown in the large magnification TEM images illustrate the elastomeric phase. Previously, it was suggested that the clay particles reside at the interphase between the PS and the elastomeric material. Thus, organoclay addition reduces the interfacial tension and leads to an increased elastomer domain size. As can be seen from the TEM images, the clay particles are localized both at the interphase between the PS and the elastomeric phase and inside the elastomeric phase.

Thus, the conclusion, which states that the addition of clay particles increases the elastomeric domain size, is true. From the SEM, analysis it was found that the domains were in droplet shape, but from the TEM analysis it is revealed that the shapes of these domains are mostly elliptical, owing to the direction of cutting.

In the nanocomposites containing Cloisite® 25A (Figures 4.39 and 4.40) mostly delaminated structures are visible. However, the nanocomposite containing higher amount of SEBS-g-MA (15wt%) shows a better dispersion of clay platelets in the elastomeric phase. These results are partially consistent with the XRD analysis. They are partially consistent, because from XRD analysis it was observed that both nanocomposites show almost the same degree of dispersion. But, the micrograph of the nanocomposites containing 5wt% SEBS-g-MA shows both intercalated and exfoliated structures, whereas, fully dispersion is noted by XRD for the nanocomposite containing 15wt% SEBS-g-MA. In other words, the state of dispersion was greatly enhanced as the compatibilizer to organoclay ratio was increased.

According to XRD analysis, Cloisite® 30B has the poorest dispersion in composite materials compared other organoclays used for this study. When the TEM image of the nanocomposite containing Cloisite® 30B and 5wt% SEBS-g-MA (Figure 4.41) is considered clay agglomerates are observed. It can be said that, even the addition of elastomeric material could not disperse the Cloisite® 30B particles, because, the layer surface of this organoclay is not only incompatible with PS matrix, but also with the elastomeric material SEBS-g-MA.
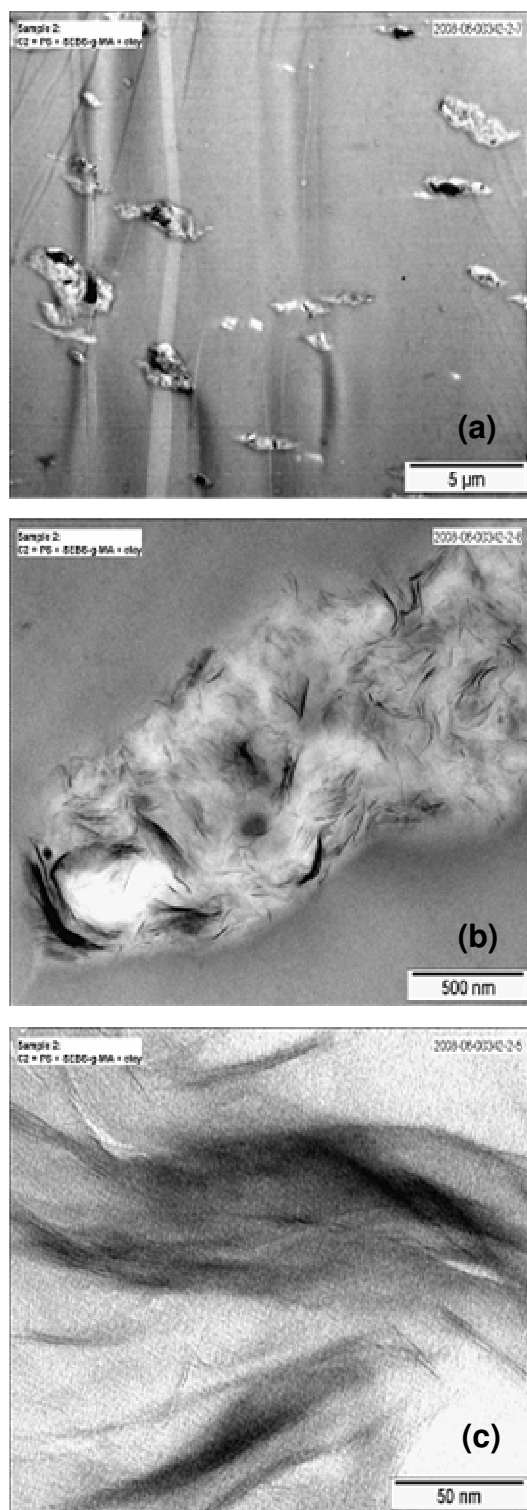
Figure 4.39 TEM micrograph of PS / SEBS-g-MA (5wt%) / Cloisite® 25A (2wt%) ternary nanocomposites: (a) 5 µm scale; (b) 500 nm scale (c) 20 nm scale
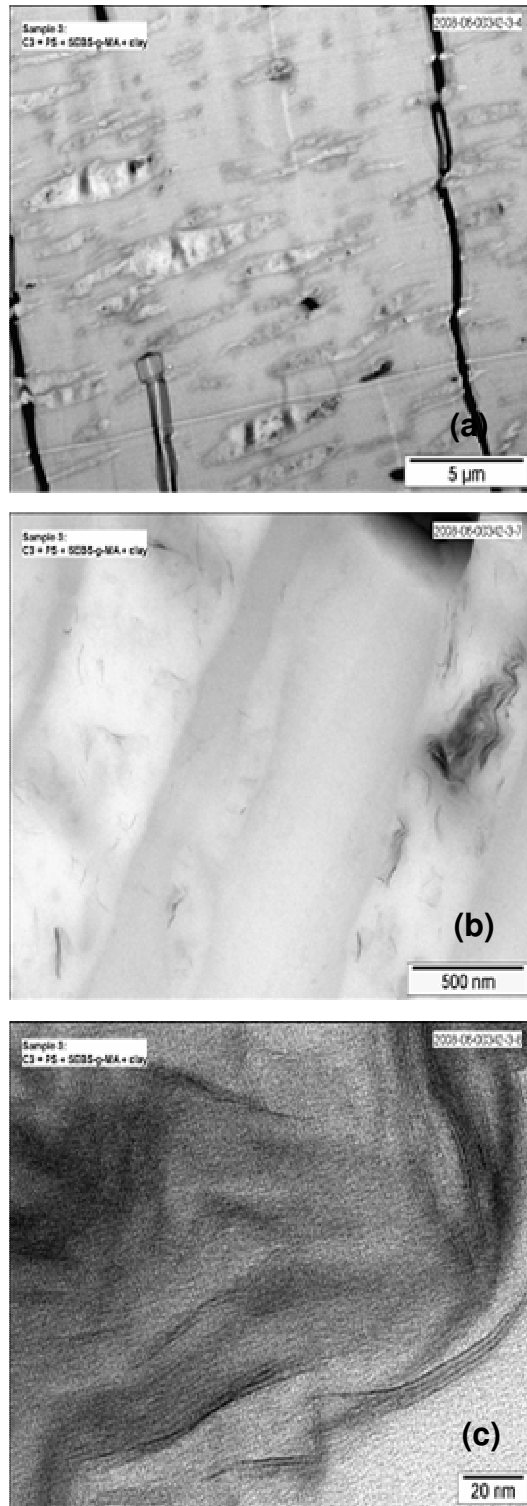
Figure 4.40 TEM micrograph of PS / SEBS-g-MA (15wt%) / Cloisite® 25A (2wt%) ternary nanocomposites: (a) 5 μm scale; (b) 500 nm scale (c) 20 nm scale
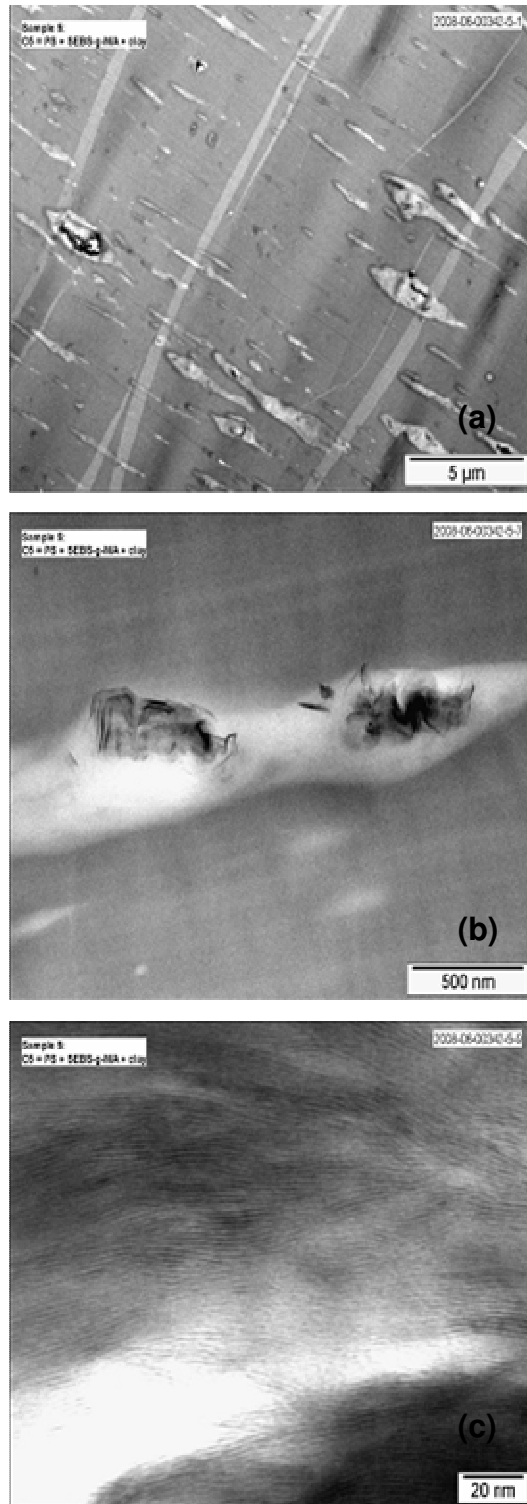
Figure 4.41 TEM micrograph of PS / SEBS-g-MA (5wt%) / Cloisite® 30B (2wt%) ternary nanocomposites: (a) 5 µm scale; (b) 500 nm scale (c) 20 nm scale

110

Figure 4.42 shows the TEM image of SEBS-g-MA/Cloisite® 25A binary nanocomposite. In consistence with XRD results fully exfoliated clay platelets exist in this nanocomposite. Compared with the ternary nanocomposites, elastomer/clay nanocomposite has a higher degree of dispersion. In ternary nanocomposites, encapsulation of clay particles in elastomer phase and the restricted dispersion of the elastomer phase in the polymer matrix may give rise to these observations.
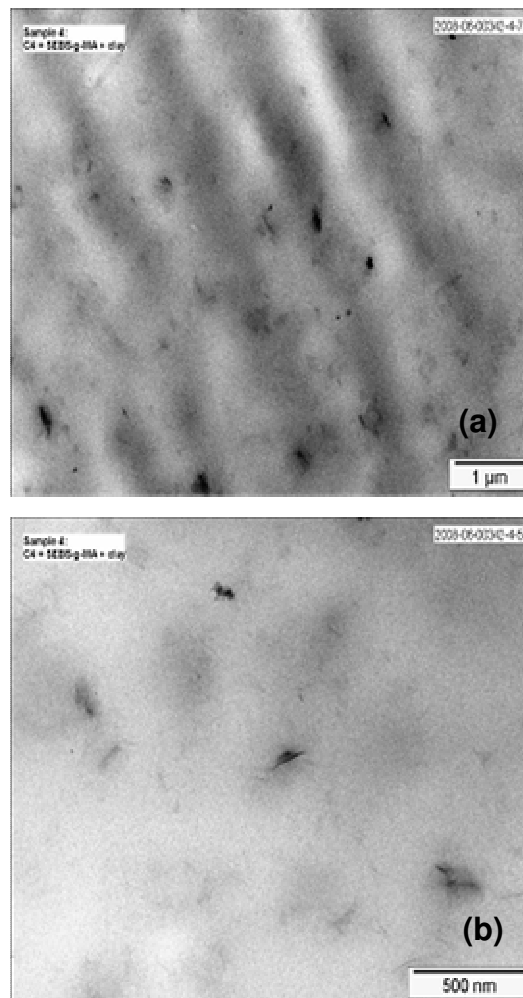
Figure 4.42 TEM micrograph of SEBS-g-MA / Cloisite® 25A (2wt%) binary nanocomposites: (a) 1 µm scale; (b) 500 nm scale

4.2 Rheological Analyses

4.2.1 Capillary Viscometry

For the component which occupies the most space in the mixture there is a tendency to act as a continuous phase. On the other hand, the component with the lower viscosity will tend to encapsulate the more viscous component since this reduces the rate of energy dissipation. So, regions in viscosity-composition space where both components will be the continuous phase can be expected. However, there is an intermediate zone where both components may form continuous phases resulting in a co-continuous structure [59]. To examine the phase inversion point, there are two main variables: the volume and viscosity ratios of the components.

In order to get the melt viscosity of the raw materials capillary viscometry was used. The apparent and Rabinowitsch corrected melt viscosity data of the raw materials at 200˚C are given in Figures 4.43 and 4.44, respectively and shown in Table 4.3. PS has a lower viscosity than SEBS-g-MA, whereas its viscosity is higher compared to elastomer E-BA-GMA. As can be seen from these figures, viscosity ration for PS/Elastomer blends does not change abruptly at high shear rates. Since, in extrusion process the shear rate is extremely high, the viscosity ratios at high shear rates were used for the determination of phase inversion point by theoretical models. They were calculated at shear rates between 87.13 and 412.29 s^{-1} and they were found as 0.535 and 4.17 for PS/SEBS-g-MA and PS/E-BA-GMA blends, respectively.
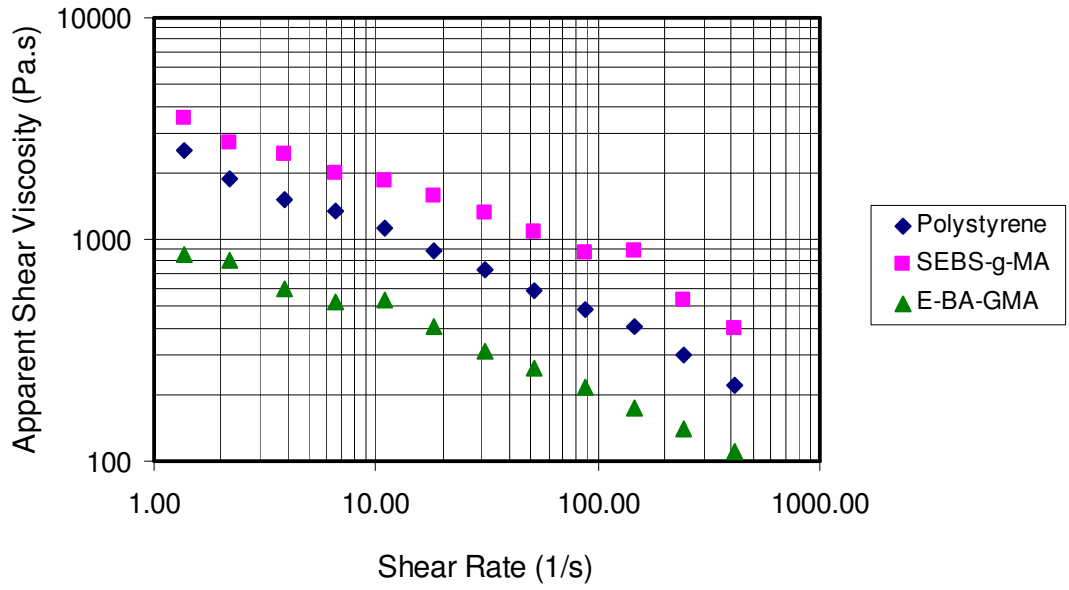
Figure 4.43 Apparent shear viscosity of the raw materials at 200˚C at different shear rates
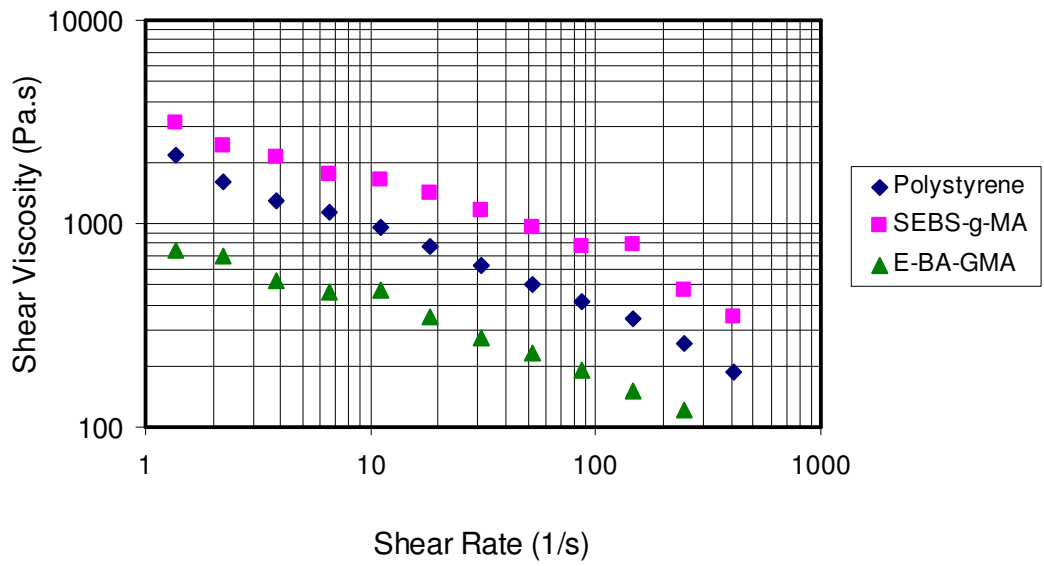
Figure 4.44 True shear viscosity of the raw materials at 200˚C at different rates

113

Table 4.3 The apparent and Rabinowitsch corrected melt viscosity data of raw materials at 200˚C

Shear Rate (1/s)	η_{PS} (Pa.s)		$\eta_{SEBS-g-MA}$ (Pa.s)		$\eta_{E-BA-GMA}$ (Pa.s)	
	App.	Correct.	App.	Correct.	App.	Correct.
412.29	219	187	396	350	110	97
245.45	303	259	537	475	140	122
146.23	403	344	889	786	173	152
87.13	485	414	873	772	215	189
51.95	586	500	1073	949	263	231
30.78	726	620	1311	1159	313	274
18.42	895	765	1579	1397	401	352
10.99	1127	963	1848	1634	537	471
6.60	1346	1150	1983	1754	524	459
3.85	1520	1299	2418	2139	594	521
2.20	1862	1591	2733	2417	798	699
1.37	2515	2148	3521	3114	851	746

By the SEM analysis, the phase inversion was found between 30 and 40wt% elastomer content for both PS/SEBS-g-MA and PS/E-BA-GMA blend. The prediction of phase inversion can be conducted with different models mentioned in the introduction part. The values of volume fractions at the point of phase inversion obtained for PS/SEBS-g-MA and PS/E-BA-GMA blends are indicated in Table 4.4 (Density of the materials are close to unity. Thus, the weight fraction was considered to be equal to the volume fraction).

Table 4.4 Prediction of the volume fraction value at phase inversion for PS/SEBS-g-MA and PS/E-BA-GMA blends

Model	$\Phi_{PS}/\Phi_{SEBS-g-MA}$	$\Phi_{PS}/\Phi_{E-BA-GMA}$
Jordhamo [56]	0.54	4.17
Chen and Su [57]	0.69	1.84
Modified Chen and Su [58]	0.83	1.53
Paul and Barlow [59]	0.54	4.17
Meltkin and Blekht [60]	3.45	0.078
Experimental	1.5- 2.33	1.5-2.33

The point of phase inversion for binary blends, suggested by these models, are not in agreement with morphological observations, except for the modified Chen and Su model applied to PS/E-BA-GMA blends. Since these models treat only viscosity and volume ratios they need some modifications, because other parameters such as, the non-Newtonian and elastic characteristics of the components, the nature of the flow field and interfacial tension should be taken into account to determine the point of phase inversion [59].

4.2.2 Melt Flow Index

To investigate the flow behavior of materials, melt flow index (MFI) test was performed. MFI value is inversely proportional to the viscosity and depends on the molecular weight, the presence of co-monomers, the degree of chain branching as well as heat transfer. In this study, the tests were performed under 2.16kg load at 200˚C. The MFI results of the samples prepared in this study are shown in Table 4.5. When the MFI value of pure PS is compared with the MFI of PS extruded twice, no significant change can be observed.

As expected from capillary viscometry analysis, PS has a higher MFI value indicating a lower viscosity than that of the elastomeric material SEBS-g-MA. On the other hand, the viscosity of E-BA-GMA is lower than that of the PS matrix. Thus, when the MFI values of the binary blends are considered, with the addition of

SEBS-g-MA the melt viscosity values decrease, whereas it increases by the incorporation of E-BA-GMA.

Pure PS and organoclay composites have similar MFI values. This is an expected result because clay particles generally act as fillers that increase the melt viscosity, if the silicate layers are totally dispersed or the polymer chains get inserted between the clay particles. Since for the PS/organoclay binary nanocomposites the dispersion of the platelets is not high, the increase in viscosity is very small.

Table 4.5 MFI results

Composition	Concentration		MFI (g/10min)	Standard deviation
	Elastomer (wt%)	O-clay (wt%)		
PS	---	---	19.2	0.12
PS (twice extruded)	---	---	19.3	0.27
SEBS-g-MA	100	---	4.77	0.09
E-BA-GMA	100	---	25.2	0.40
PS / Elastomer blends				
PS + SEBS-g-MA	5	---	18.9	0.43
PS + SEBS-g-MA	15	---	17.3	0.97
PS + SEBS-g-MA	20	---	14.5	0.31
PS + SEBS-g-MA	30	---	13.8	0.22
PS + SEBS-g-MA	40	---	11.7	0.14
PS + E-BA-GMA	5	---	19.5	0.13
PS + E-BA-GMA	15	---	20.1	0.14
PS + E-BA-GMA	20	---	21.3	0.19
PS + E-BA-GMA	30	---	22.6	0.24
PS + E-BA-GMA	40	---	23.2	0.32
PS / Organoclay nanocomposites				
PS + 30B	---	1	19.2	0.24
PS + 30B	---	2	19.1	0.12
PS + 15A	---	1	18.5	0.16
PS + 15A	---	2	18.7	0.16
PS + 25A	---	1	19.0	0.13
PS + 25A	---	2	18.5	0.27

Table 4.5 (cont'd) MFI results

Composition	Concentration		MFI (g/10min)	Standard deviation
	Elastomer (wt%)	O-clay (wt%)		
PS / 5 wt% Elastomer / Organoclay nanocomposites				
PS + SEBS-g-MA + 30B	5	1	18.5	0.36
PS + SEBS-g-MA + 30B	5	2	18.1	0.40
PS + SEBS-g-MA + 15A	5	1	17.3	0.23
PS + SEBS-g-MA + 15A	5	2	17.5	0.17
PS + SEBS-g-MA + 25A	5	1	17.4	0.21
PS + SEBS-g-MA + 25A	5	2	17.9	0.07
PS + E-BA-GMA + 30B	5	1	15.2	0.38
PS + E-BA-GMA + 30B	5	2	16.1	0.35
PS + E-BA-GMA + 15A	5	1	15.1	0.16
PS + E-BA-GMA + 15A	5	2	14.9	0.23
PS + E-BA-GMA + 25A	5	1	15.7	0.19
PS + E-BA-GMA + 25A	5	2	15.4	0.15
PS / 15 wt% Elastomer / Organoclay nanocomposites				
PS + SEBS-g-MA + 30B	15	1	14.0	0.12
PS + SEBS-g-MA + 30B	15	2	14.1	0.20
PS + SEBS-g-MA + 15A	15	1	13.0	0.09
PS + SEBS-g-MA + 15A	15	2	13.4	0.12
PS + SEBS-g-MA + 25A	15	1	13.7	0.26
PS + SEBS-g-MA + 25A	15	2	13.1	0.10
PS / 20 wt% Elastomer / Organoclay nanocomposites				
PS + SEBS-g-MA + 30B	20	1	12.1	0.08
PS + SEBS-g-MA + 30B	20	2	12.0	0.10
PS + SEBS-g-MA + 15A	20	1	11.3	0.23
PS + SEBS-g-MA + 15A	20	2	11.5	0.21
PS + SEBS-g-MA + 25A	20	1	11.3	0.14
PS + SEBS-g-MA + 25A	20	2	11.4	0.19
PS / 30 wt% Elastomer / Organoclay nanocomposites				
PS + SEBS-g-MA + 30B	30	1	9.22	0.39
PS + SEBS-g-MA + 30B	30	2	9.21	0.20
PS + SEBS-g-MA + 15A	30	1	8.32	0.21
PS + SEBS-g-MA + 15A	30	2	8.14	0.17
PS + SEBS-g-MA + 25A	30	1	8.15	0.36
PS + SEBS-g-MA + 25A	30	2	8.60	0.29
PS / 40 wt% Elastomer / Organoclay nanocomposites				
PS + SEBS-g-MA + 30B	40	1	8.40	0.24
PS + SEBS-g-MA + 30B	40	2	8.34	0.13
PS + SEBS-g-MA + 15A	40	1	7.91	0.23
PS + SEBS-g-MA + 15A	40	2	7.24	0.15
PS + SEBS-g-MA + 25A	40	1	7.20	0.14
PS + SEBS-g-MA + 25A	40	2	7.79	0.12

The viscosity of the polymer matrix is an important factor that affects the dispersion of organoclays, since intercalation and/or exfoliation require the diffusion of polymer chains into the silicate layers or peel away the top and bottom layers as promoted by the polymer adsorption and by the application of shear stress [112]. With increasing viscosity, the shear stress applied to the platelets increases and leads the separation of layers. For the ternary nanocomposites containing 5wt% SEBS-g-MA or 5wt% E-BA-GMA, the MFI values show a reduction compared to the MFI of respective PS/elastomer binary blends because the clays are thought to impart resistance to flow and hinder the flow of the melt polymer. Thus, it can be said that the presence of the elastomeric materials may provide better dispersion of clay platelets. Also, for the ternary nanocomposites containing 15, 20, 30 and 40wt% SEBS-g-MA, lower MFI values are obtained than those of PS/SEBS-g-MA binary blends. However, as can be seen from MFI values, the nanocomposites containing Cloisite$^®$ 15A and 25A have greater MFI values than the nanocomposites prepared with Cloisite$^®$ 30B due to poor dispersion of Cloisite® 30B, which was also proved with the XRD data.

4.3 Mechanical Analyses

To examine the mechanical properties of the materials tensile and impact tests were performed in this study. The mechanical results obtained for all compositions are given in Appendix B.

4.3.1 Tensile Test

Tensile tests were performed to obtain the response of the prepared nanocomposites to the applied force and the extent to which the specimens elongate before failure. Tensile strength, Young's modulus and elongation at break values were determined from the stress-strain curves. The tensile properties of the raw materials are shown in Table 4.6.

Table 4.6 Tensile properties of raw materials

Property	PS (ISO 527)	SEBS-g-MA (ISO 37)	E-BA-GMA (ISO 37)
Tensile strength (MPa)	34.1	5.1	5.6
Elongation at break (%)	2.1	882	274
Young's modulus (MPa)	1688	3.3	12.6

PS is commonly used for many commercial applications because of its excellent transparency and relative ease of processing. However, it fails in a brittle mode when subjected to small deformations due to its failure mechanism which enables crack formation rapidly under applied stress [113]. In order to overcome its brittleness, addition of elastomeric materials is an effective method. It acts as stress concentrator during the elongation. Thus, yielding or crazing occurs around the elastomeric domains and a higher amount of energy is absorbed [114]. But, further addition of impact modifier usually results in the reduction of the tensile strength and Young's modulus values. Thus, it is logical to use fillers which stiffen the material.

In this study, in addition to the ternary nanocomposites, PS/elastomer blends and PS/organoclay composites were also examined with tensile tests. Figures 4.45-4.47 show the tensile properties of PS/SEBS-g-MA and PS/E-BA-GMA blends with increasing elastomer content. Elastomeric materials, SEBS-g-MA and E-BA-GMA, have relatively lower tensile strength and tensile modulus values compared to pure PS. When they are melt-blended, elastomers create a dilution effect. So, with the addition of these elastomers, the tensile strength and tensile modulus values decrease. However, the elongation at break values increase as a result of the elastomeric characteristic of the rubber particles.

An important point for the preparation of ternary nanocomposites is the selection of proper elastomer. As can be seen from Figures 4.45-4.47, SEBS-g-MA containing blends have greater tensile strength, tensile modulus and elongation at break values compared to blends prepared with E-BA-GMA. The other important point is

the optimum elastomer content. Although the addition of elastomer decreases tensile strength and Young's modulus, 5wt% elastomer content show an enhancement in these properties, so it was decided to keep the elastomer content at 5wt%. However, as will be seen later, this amount of elastomer is not enough to obtain high impact strength values for the ternary nanocomposites. Also, E-BA-GMA does not create a good compatibilization effect between PS and organoclay as SEBS-g-MA does. Thus, in the second part of the study, the SEBS-g-MA content was increased up to 40wt%.
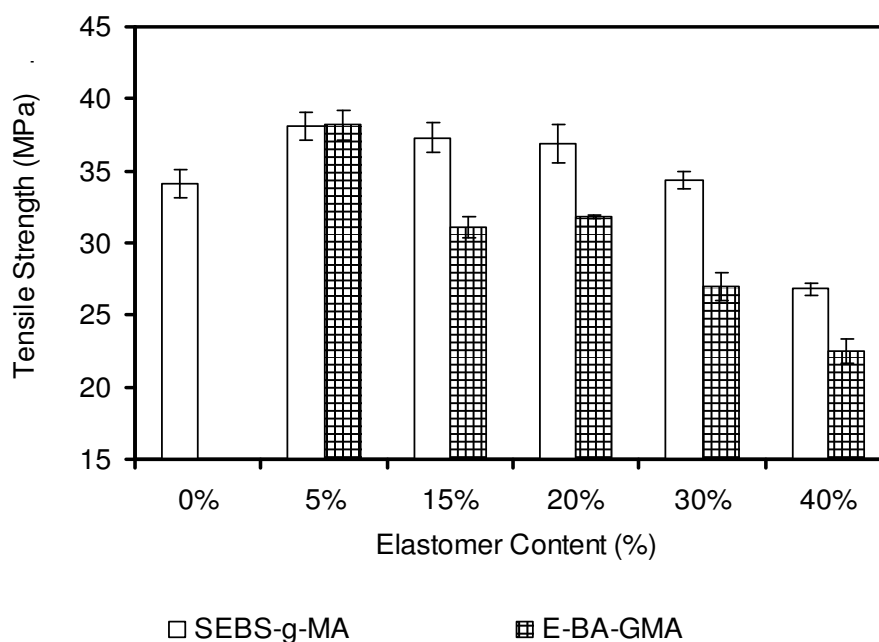
Figure 4.45 Tensile strength (MPa) of PS / elastomer binary blends
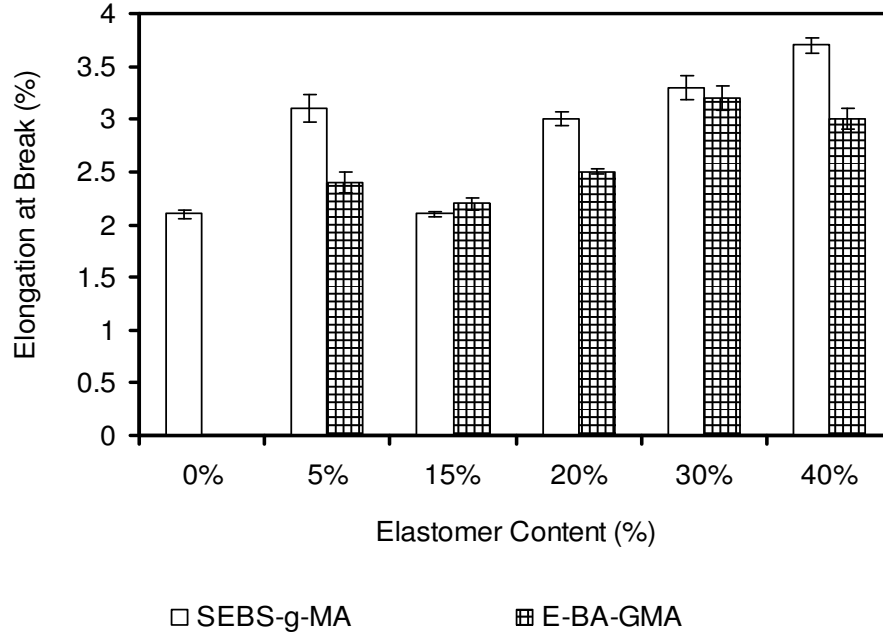
Figure 4.46 Elongation at break of (%) of PS / elastomer binary blends
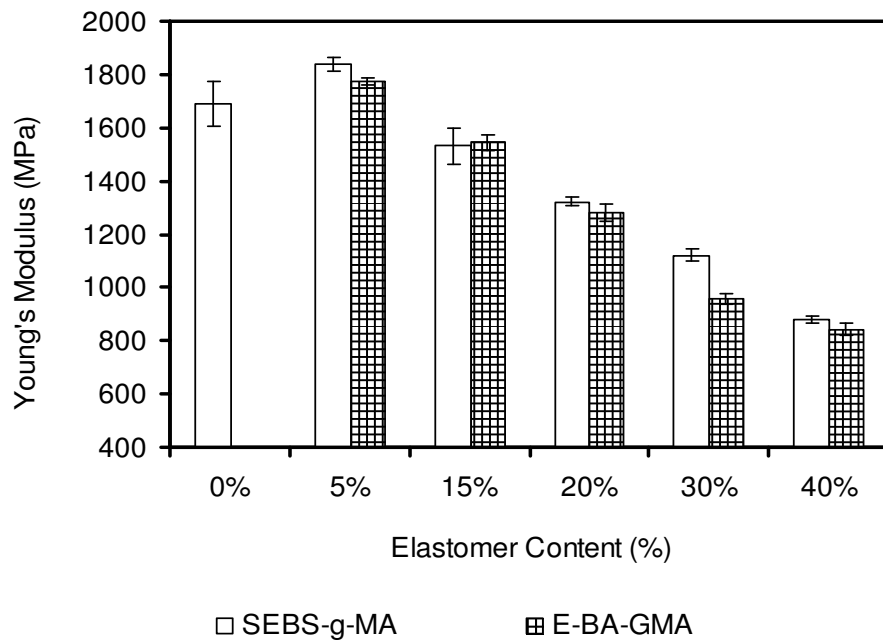
Figure 4.47 Young's modulus of (MPa) of PS / elastomer binary blends

Tensile test results of the binary elastomer/organoclay composites are given in Figures 4.48-4.50. Although from the XRD results, totally dispersed clay layers were observed for these binary composites, it can be seen that the clay particles affect the tensile strength in an adverse way for SEBS-g-MA/organoclay composites and cause an insignificant amount of increase for E-BA-GMA/organoclay composites prepared with Cloisite® 15A or 25A. It was expected that rigid fillers should contribute to the strength enhancement of the elastomeric materials; however, breakdown of the elastomeric structure may lead to reduction in tensile strength.

As expected, the elongation at break values of the elastomeric materials are reduced with organoclay addition, especially, in SEBS-g-MA composites. Nearly the same behavior obtained for tensile strength values was obtained for the Young's modulus values. For all the compositions containing Cloisite® 15A and 25A, small enhancement occurred.
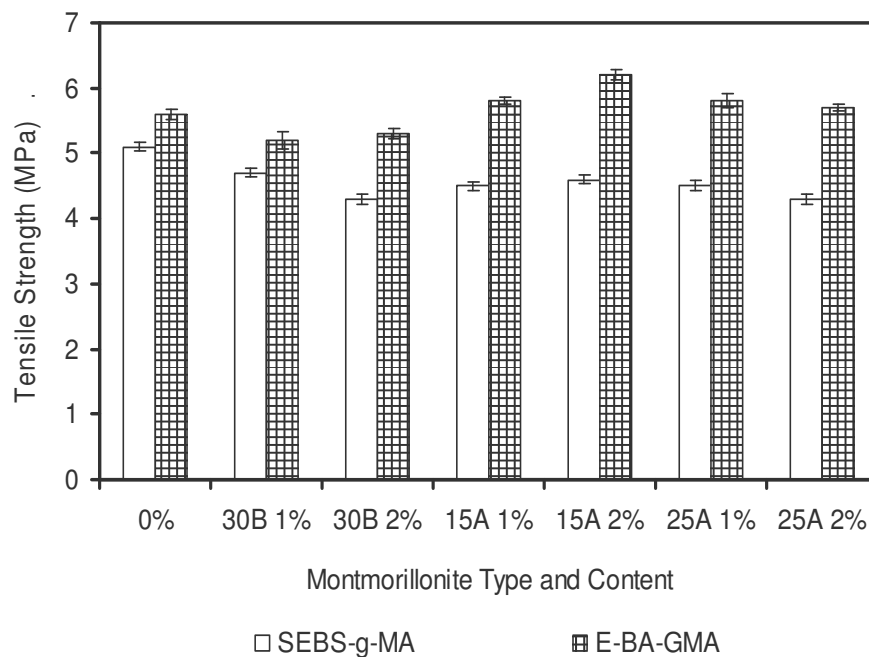
Figure 4.48 Tensile strength (MPa) of elastomer / organoclay composites
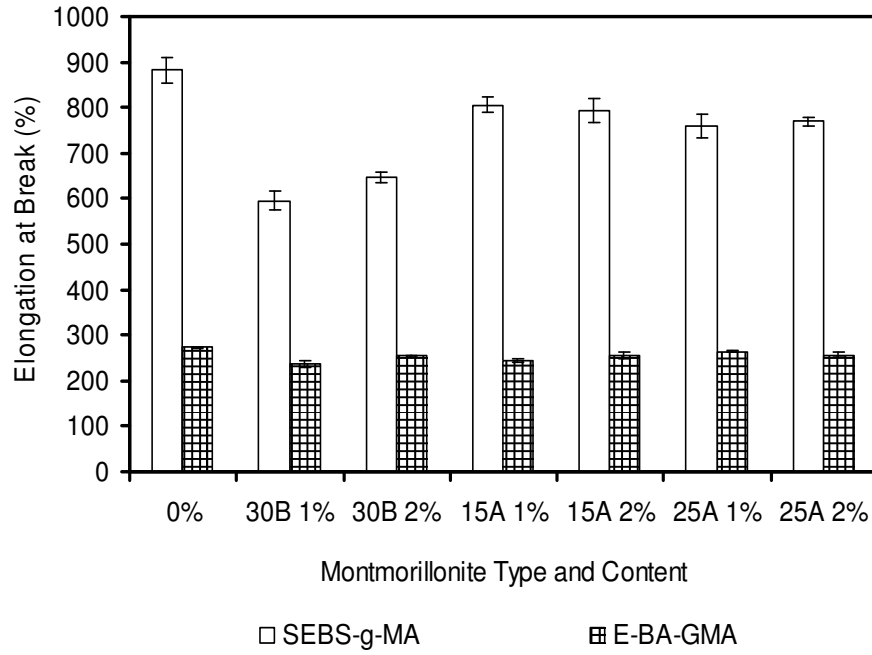
Figure 4.49 Elongation at break (%) of elastomer / organoclay composites
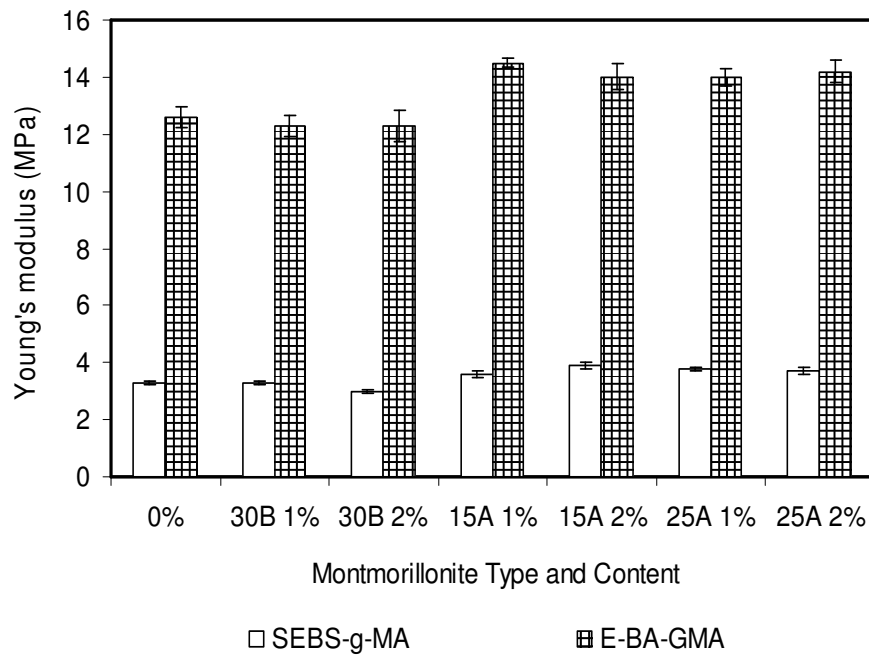
Figure 4.50 Young's modulus (MPa) of elastomer / organoclay composites

Tensile properties of the ternary nanocomposites containing 5wt% elastomer are shown and compared with PS/elastomer binary blends and PS/organoclay binary composites in Figures 4.51-4.53. It is a general fact that organoclay stiffens the polymer matrix due to its high aspect ratio which creates large contact area, and this contributes to the reinforcement effect [115]. Especially, if silicate layers are dispersed well, the matrix generally yields enhanced tensile strength and Young's modulus. However, a drastic reduction in the elongation at break value is commonly observed in thermoplastics associated with the clay addition, because silicate particles can not be strained by external stresses. Thus, rigid fillers in a rigid polymer generally decrease the elongation values of a polymer [116].

In this study, the PS/organoclay binary nanocomposites showed little or no improvement in their stiffness and strength in comparison to pure PS, due to the poor dispersion of organoclay in the matrix. Although reduction in tensile strength and modulus values are expected with the addition of elastomer, the reverse effect was observed for ternary nanocomposites; an increase in the tensile strength and no reduction in the Young's modulus were obtained. This result can be attributed to the better dispersion of clay particles in the presence of elastomeric phase as supported with the XRD results. Also, the increase in the elongation at break value is a specific result. Among all the nanocomposites, the best improvement in the tensile strength and elongation at break values were obtained for the ternary nanocomposites containing 2wt% Cloisite® 25A and 5wt% SEBS-g-MA. The improvements were 26% and 105% in tensile strength and elongation values respectively. The results obtained up to this point show that the compatibility between elastomer SEBS-g-MA and PS is effective and separated clay particles which enhance the tensile properties of the polymer matrix are observed. However, the elongation at break values obtained are still very low compared to high impact polystyrene.
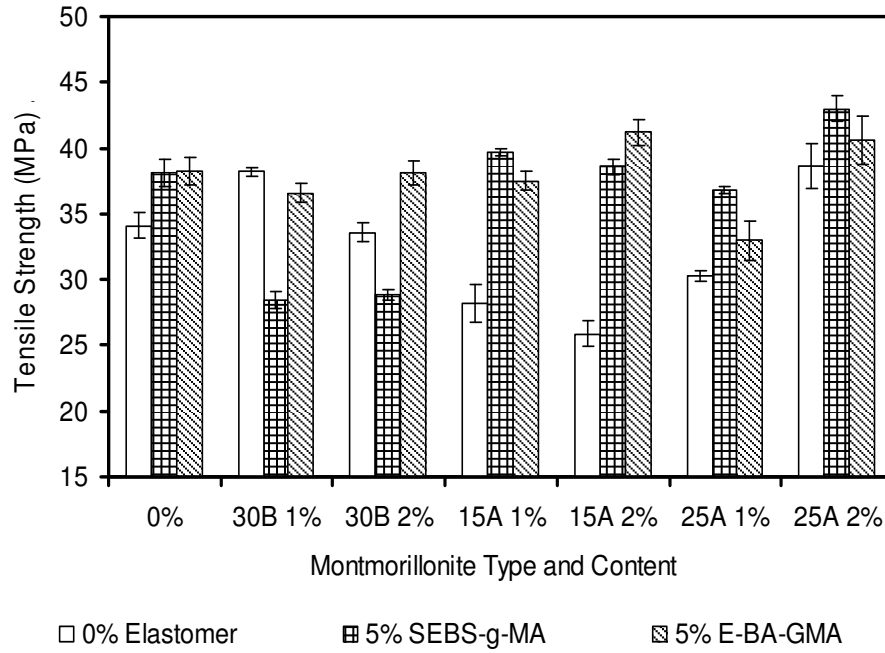
Figure 4.51 Tensile strength (MPa) of PS / elastomer (5wt%) / organoclay ternary nanocomposites
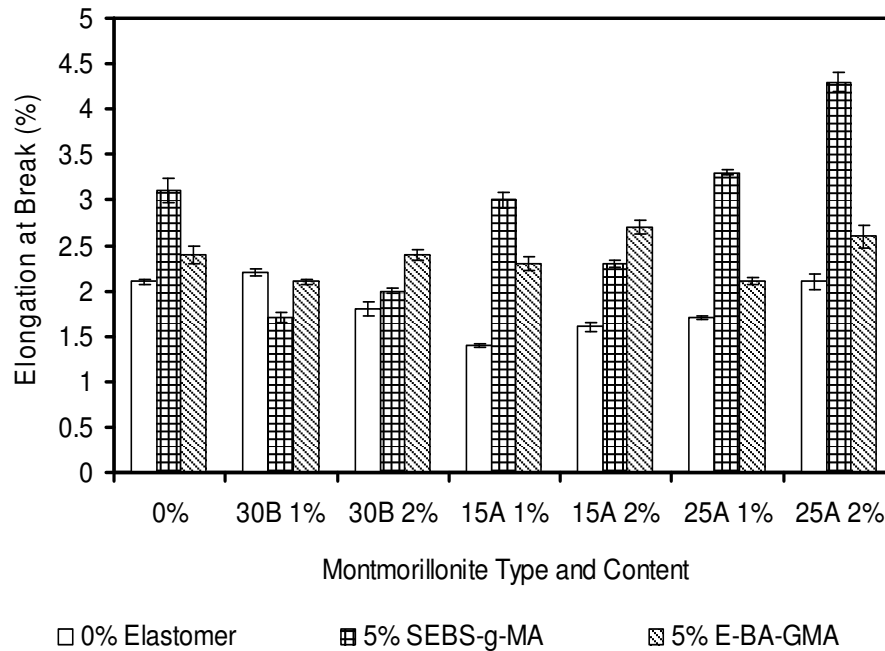
Figure 4.52 Elongation at break (%) of PS / elastomer (5wt%) / organoclay ternary nanocomposites
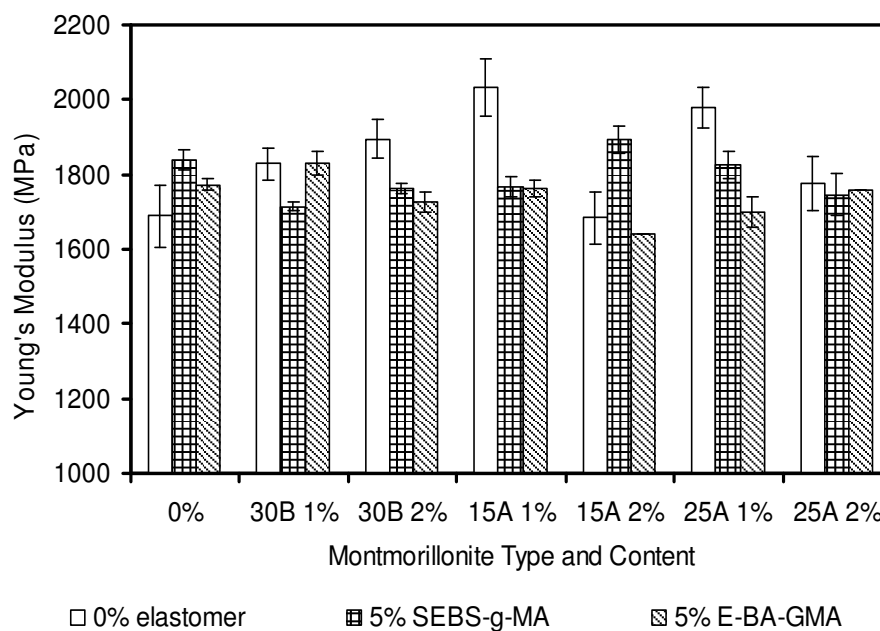
Figure 4.53 Young's modulus (MPa) of PS / elastomer (5wt%) / organoclay ternary nanocomposites

The effect of increasing SEBS-g-MA content on the tensile strength values of ternary nanocomposites are shown in Figures 4.54-4.56. The general trend obtained for the tensile strength of these nanocomposites is the increase of the tensile strength value up to a certain SEBS-g-MA content: 15 and 20wt% SEBS-g-MA. The PS/SEBS-g-MA (15 or 20wt%) blends show increase in their tensile strength from 34.1MPa, for pure PS, to 37.3MPa and 36.9MPa for 15 and 20wt% SEBS-g-MA respectively. After this optimum content, the tensile strength values decrease due to high amount of SEBS-g-MA. At 30 and 40wt% elastomer contents the tensile strength shows a drastic reduction. Among the nanocomposites prepared with the optimum elastomer content, the highest improvement in tensile strength values were obtained for the nanocomposites containing Cloisite[®] 25A and 15A based on the morphological analysis results described earlier. All of these nanocomposites are either intercalated or exfoliated. Approximately, 18-23% increases in tensile strength can be seen for these nanocomposites.

In fact, in nanocomposites containing Cloisite[®] 30B, tensile strength was also improved although its dispersion in polymer is too poor to enhance the tensile properties. Mechanical properties depend on orientation of clay tactoids, beside the dispersion of clay particles and clay loading. Misaligned fillers, which are perpendicular to applied load, lead to a mechanism where stress at the interface transforms from a shear mode to a tensile mode which generates a higher concentration of stress in the matrix and less tension in the filler particles. Thus, improvement in tensile strength values may be attributed to the flow induced clay orientation during injection molding.
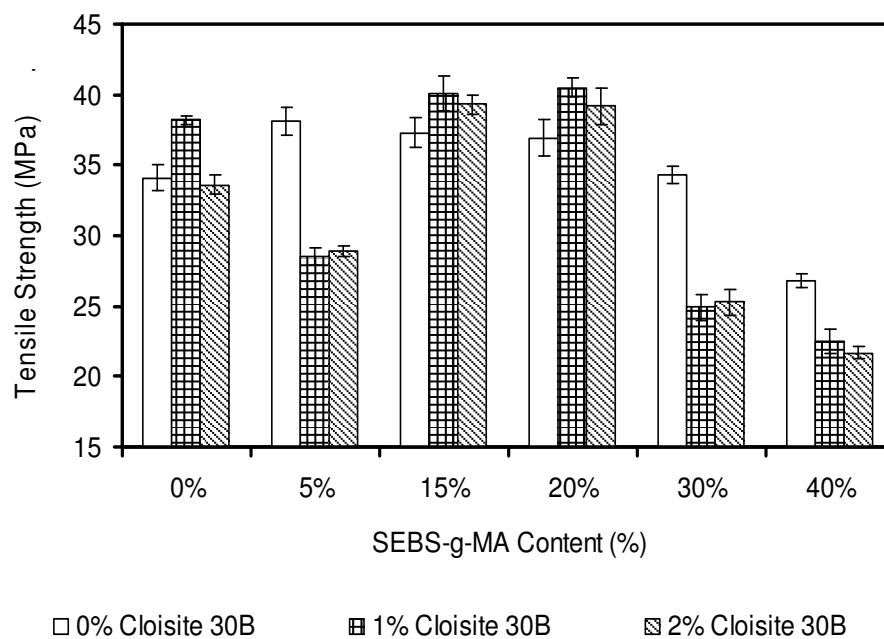
Figure 4.54 Tensile strength (MPa) of PS / elastomer / Cloisite[®] 30B ternary nanocomposites
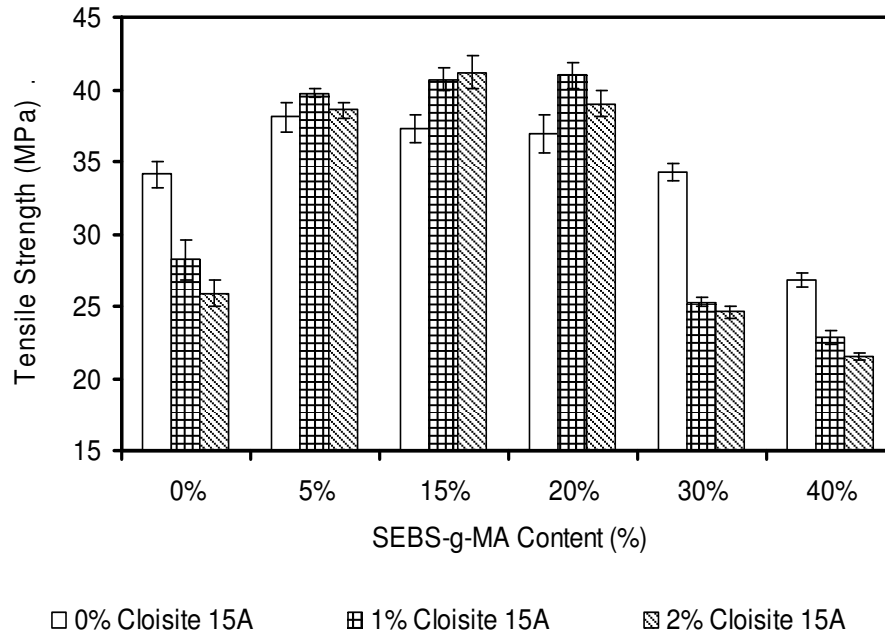
Figure 4.55 Tensile strength (MPa) of PS / elastomer / Cloisite® 15A ternary nanocomposites
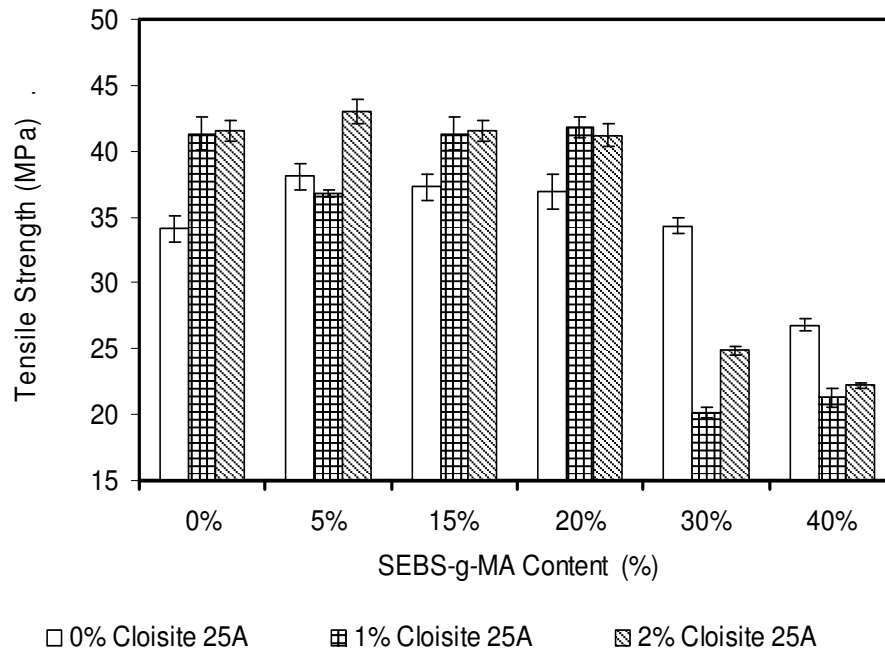
Figure 4.56 Tensile strength (MPa) of PS / elastomer / Cloisite® 25A ternary nanocomposites

Elongation at break values of the ternary nanocomposites with increasing SEBS-g-MA content can be seen in Figures 4.57-4.59 for three different types of organoclays. As the elastomer content increases, the elongation at break value increases for all organoclay types. For nanocomposites containing 30 and 40wt% SEBS-g-MA, the elongation at break values are significantly greater than those of nanocomposites containing lower amounts of SEBS-g-MA. However, for these nanocomposites containing large amounts of SEBS-g-MA, the tensile strength values are approximately half of the tensile strength value of the nanocomposites containing 15 to 20wt% elastomer. Thus, it can be said that the elastomer content should be chosen according to the application where the material will be used. If the application requires high tensile strength values, low elastomer content, 15 or 20wt%, can be used. Among the organoclays used in this study the best improvement in elongation at break values were observed in the presence of Cloisite® 25A due to the exfoliated structures it creates.
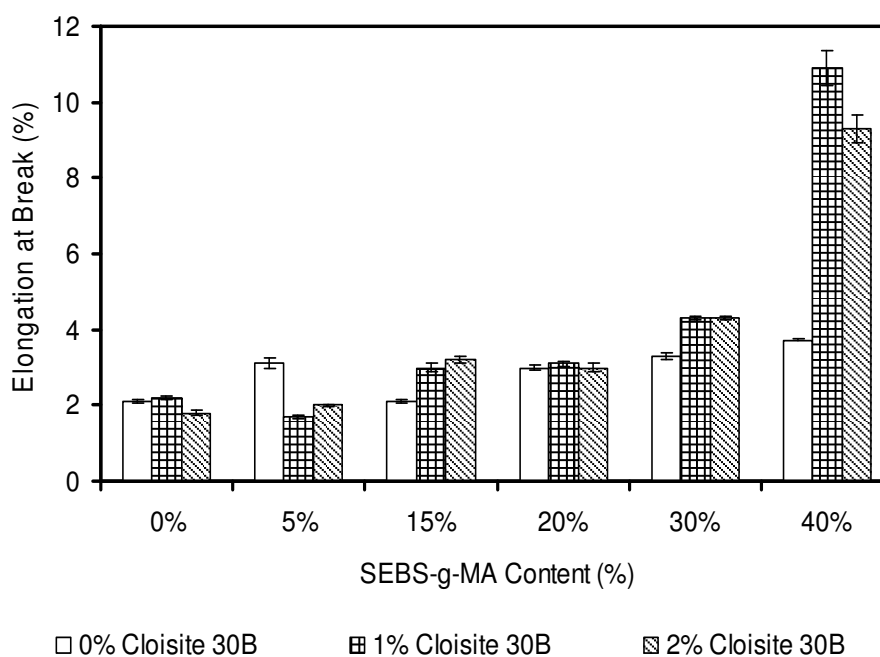
Figure 4.57 Elongation at break (%) of PS / elastomer / Cloisite® 30B ternary nanocomposites
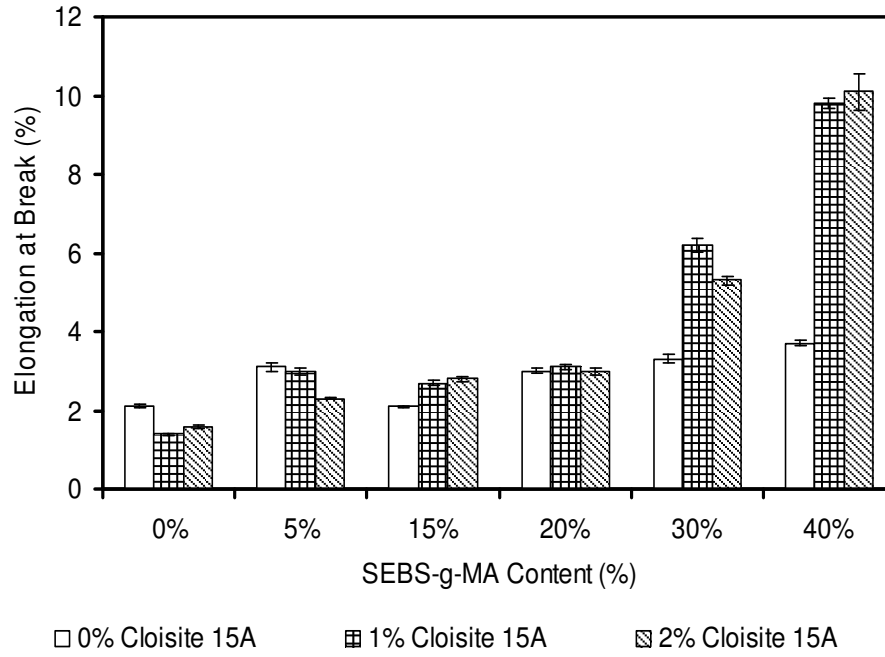
Figure 4.58 Elongation at break (%) of PS / elastomer / Cloisite® 15A ternary nanocomposites
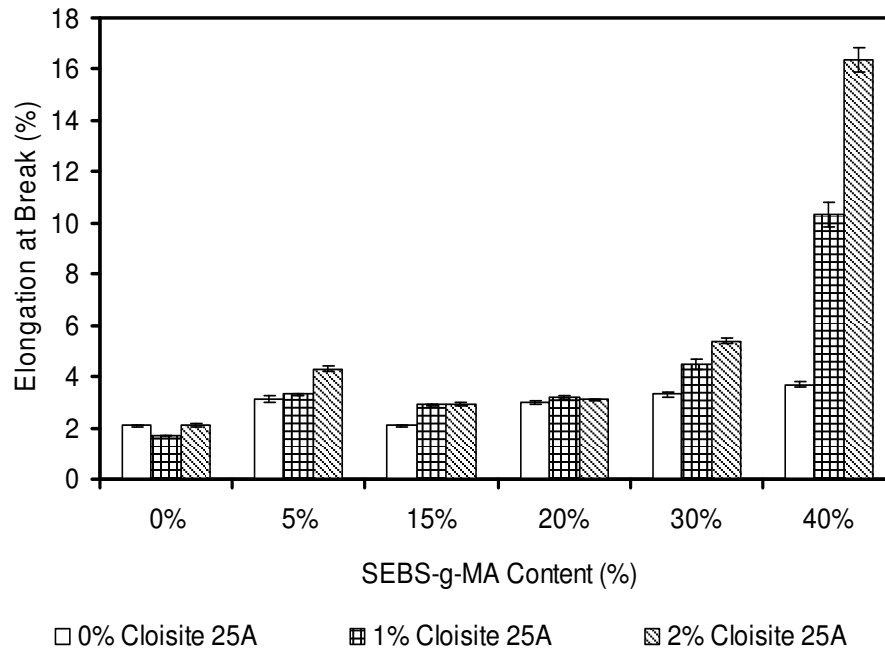
Figure 4.59 Elongation at break (%) of PS / elastomer / Cloisite® 25A ternary nanocomposites

130

When the effect of increasing SEBS-g-MA content on the Young's modulus values are considered, the same behavior that was observed for tensile strength values can be seen (Figure 4.60-4.62). The nanocomposites containing 15 and 20wt% SEBS-g-MA do not show an intense reduction, whereas, the nanocomposites containing 30 and 40wt% elastomeric material do. The negative effect of elastomer on modulus values is compensated by organoclay particles.
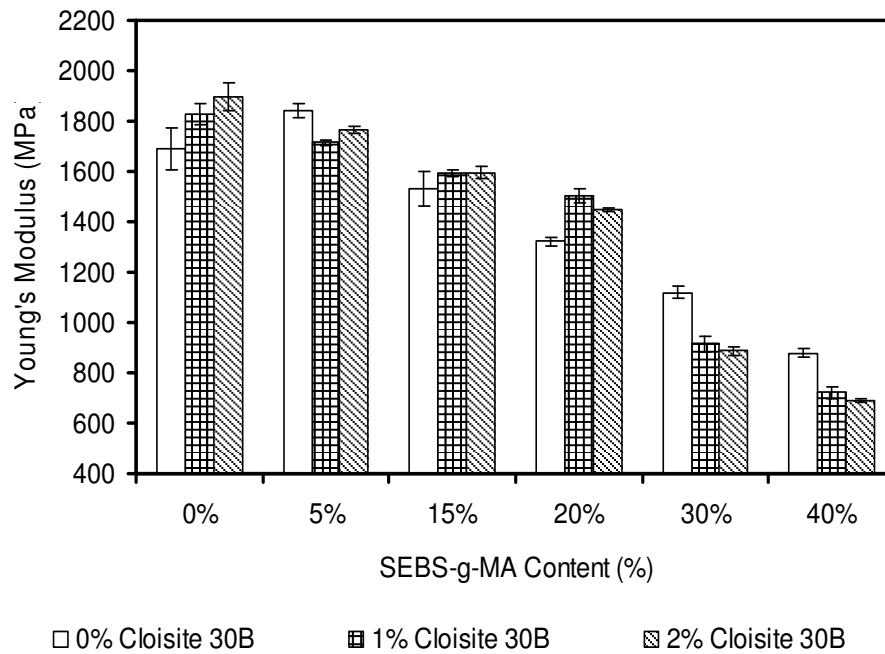
Figure 4.60 Young's modulus (MPa) of PS / elastomer / Cloisite$^{®}$ 30B ternary nanocomposites
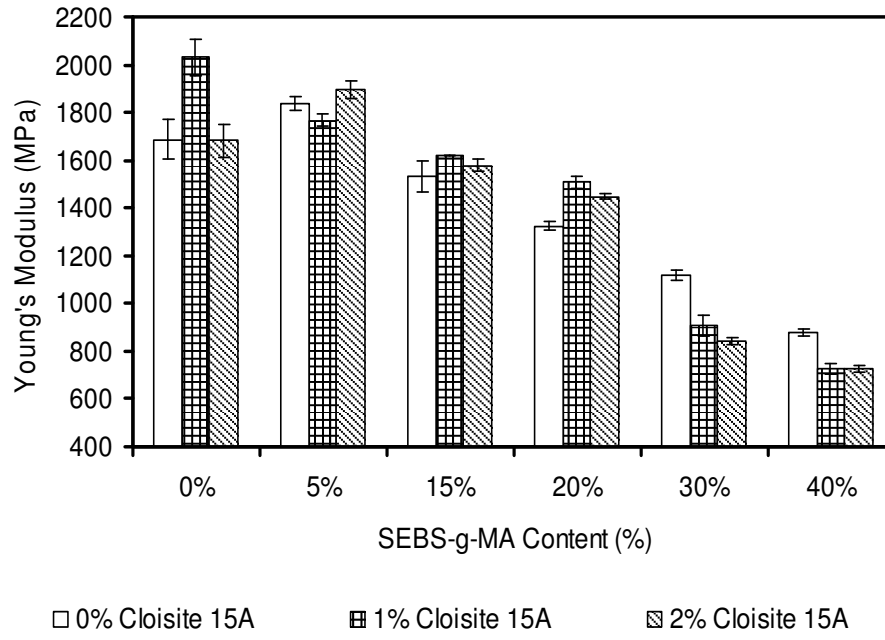
Figure 4.61 Young's modulus (MPa) of PS / elastomer / Cloisite$^®$ 15A ternary nanocomposites
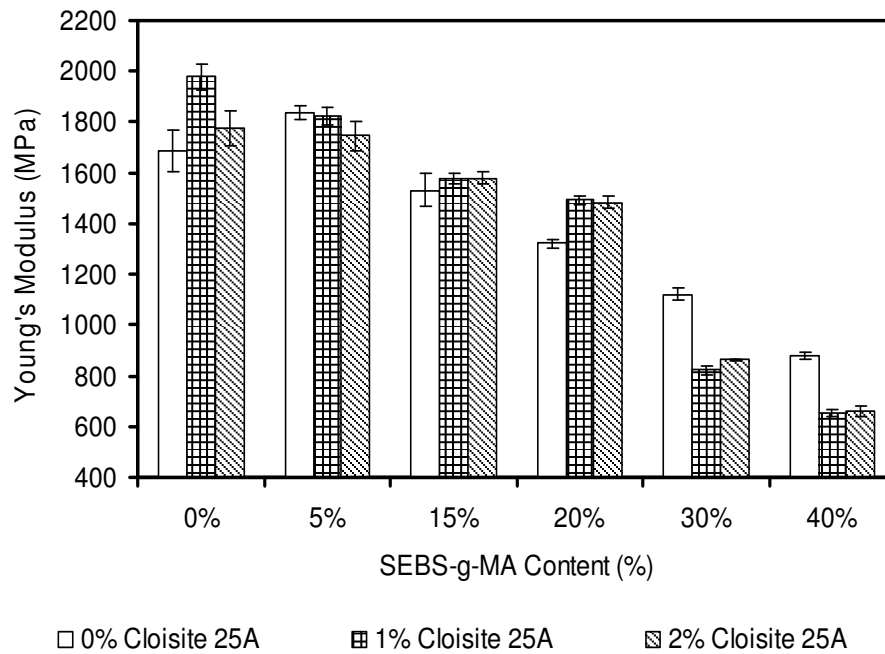
Figure 4.62 Young's modulus (MPa) of PS / elastomer / Cloisite$^®$ 25A ternary nanocomposites

In this study, increasing organoclay concentration from 1wt% to 2wt% does not affect the tensile properties significantly. However, it is a general fact that the stiffness of the nanocomposites increases with increasing clay content at the expenses of their impact strength and tensile ductility until an optimum organoclay concentration is reached [117]. After this optimum content, further addition of organoclay hinders the separation of clay platelets, and clay particles are found as tactoids in the polymer matrix and the tensile properties can not be improved.

4.3.2 Impact Test

Un-notched charpy impact tests were applied to investigate the toughness of the nanocomposites and blends prepared in this study. PS is a stiff material, whereas its brittleness renders its use in many applications. Thus it is important to increase its energy absorbance when it gets hit with something. In industry high impact polystyrene is produced to overcome this main disadvantage of PS. But, the HIPS processing is inconvenient for large capacity productions due to styrene polymerization step in the presence of polybutadiene. The main characteristic of HIPS is that, the PB particles are dispersed in the polymer matrix and dissipate impact energy by transforming the energy into deformation of themselves [46].

Another effective way to improve the impact strength of PS is to melt blend it with block co-polymers. These co-polymers should be compatible with the matrix and disperse themselves uniformly to reduce the interfacial tension and to improve the adhesion [52]. The effectiveness of block co-polymers in the improvement of impact strength is directly related with the size of the dispersed elastomeric domains in the polymer matrix. As the domain size increases the impact strength increases owing to lower stress concentration effect of the domains. The size of the domains mainly depends on some properties such as mobility of the interface, melt viscosity, shear stress and surface tension. Higher shear stress and melt viscosity lead to finer elastomeric domains due to the effectiveness in uniform dispersion. However, the domain size should not be too enormous to obtain high toughness, because large domains form large cavities that could not stop the crack propagation.

As can be seen from the SEM images the elastomeric materials melt blended with PS matrix form droplets. The droplet morphology improves the impact strength [55]. The impact strength values of the PS/SEBS-g-MA and PS/E-BA-GMA blends are shown in Figure 4.63. The impact strength of the PS/SEBS-g-MA binary blends increases with elastomer content, whereas the blends containing E-BA-GMA do not display such an increase due to lower compatibility between PS and E-BA-GMA. This is one of the most important reasons to eliminate E-BA-GMA as the elastomer and investigate the effect of increasing SEBS-g-MA content on the properties of ternary nanocomposites.
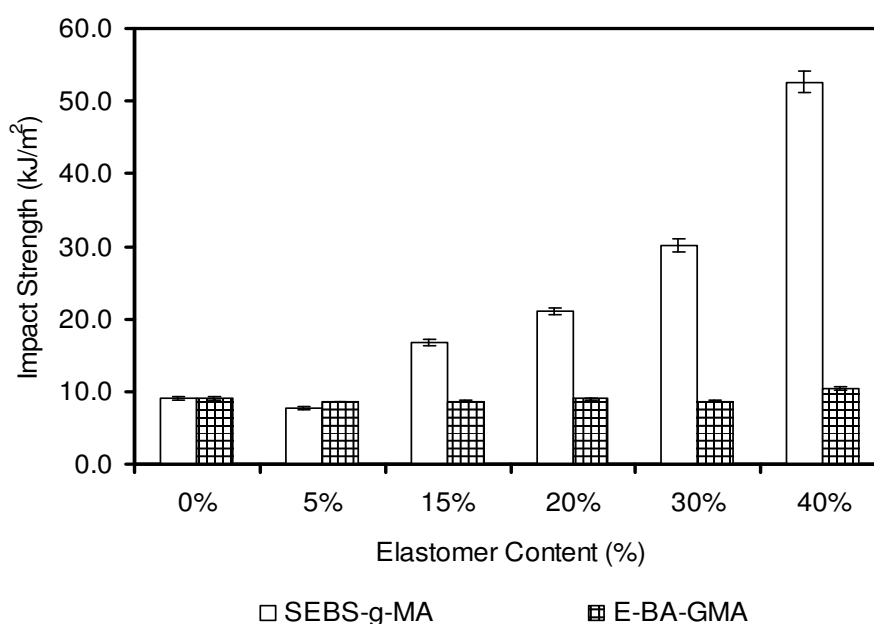
Figure 4.63 Impact strength (kJ/m^2) of PS / elastomer binary blends

As mentioned in the discussion of tensile properties, organoclay addition makes the PS matrix stiffer by decreasing the molecular mobility of the polymer chains due to the interaction between the matrix and clay surface, and the toughness of the rigid polymer matrix decreases. Thus, the elastomeric material has two important functions: to act as an impact modifier by compensating the reduced

134

impact strength with organoclay addition and to increase the compatibility between organoclay and the polymer matrix to aid the penetration of polymer chains between the silicate layers. Figure 4.64 shows the impact strength of nanocomposites containing 5wt% elastomer and different types of organoclays. Usually, exfoliated organoclays hinder the coalescence of the elastomeric domains by acting as barriers. However, in this study, it was observed that the addition of organoclays increases the average domain size and this was attributed to the dispersion of clay particles at the interface between PS and elastomer phase. Thus, the ternary nanocomposites show higher impact strength values compared to PS/elastomer binary blends. With different organoclay types, no significant difference can be observed in ternary nanocomposites containing 5wt% elastomer. Nearly all of them show approximately 9% increase in their impact strength value. However, this enhancement is relatively small compared to the impact strength of HIPS materials, which generally possess 20-30kJ/m^2 impact strength [85]. Thus, it was decided to increase the elastomer content, especially SEBS-g-MA content due to the tensile and morphological properties that were analyzed previously.
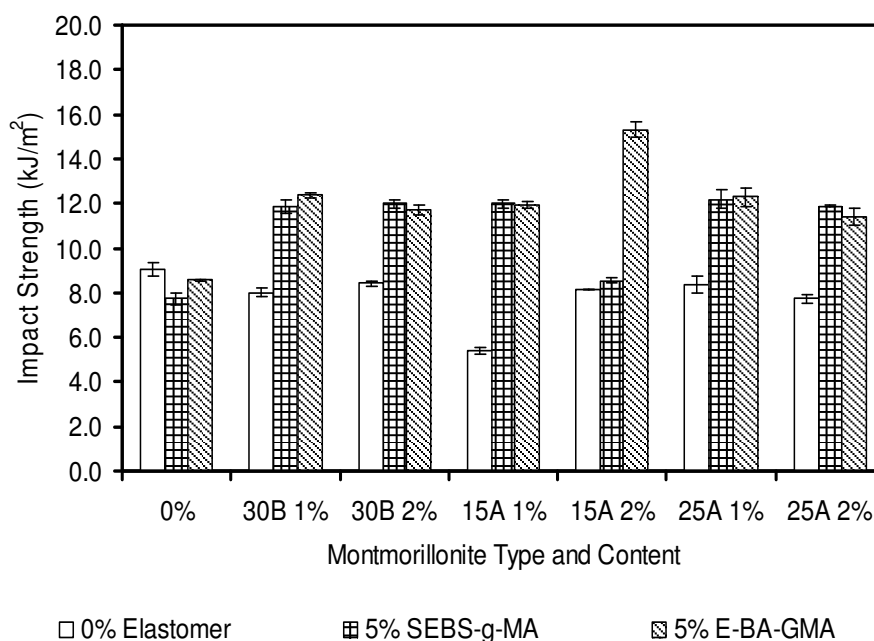
Figure 4.64 Impact strength (kJ/m^2) of PS / elastomer (5wt%) / organoclay ternary nanocomposites

135

Impact strength values of the ternary nanocomposites containing SEBS-g-MA and three different organoclays are shown in Figures 4.65-4.67. Effect of increasing SEBS-g-MA content on the impact strength is investigated and it is seen that as the elastomer content increases the toughness of the nanocomposite increases. However, a drastic reduction is obtained for the nanocomposites containing 30wt% SEBS-g-MA. This may be due to the large droplets that represent the starting point of co-continuous structure, which form large cavities under the applied impact. As the elastomer content increases to 40wt% the inversion of the morphologic structure from dispersed droplet type to co-continuous type occurs and the impact strength increases significantly. From the results obtained up to now, it can be specified that the nanocomposites containing 15 and 20wt% SEBS-g-MA have the optimum average domain size that results in better impact strength values without deteriorating tensile properties. Also, from Figures 4.65-4.67 it is obvious that the best improvement in the impact strength values are obtained for nanocomposites prepared with Cloisite® 25A.
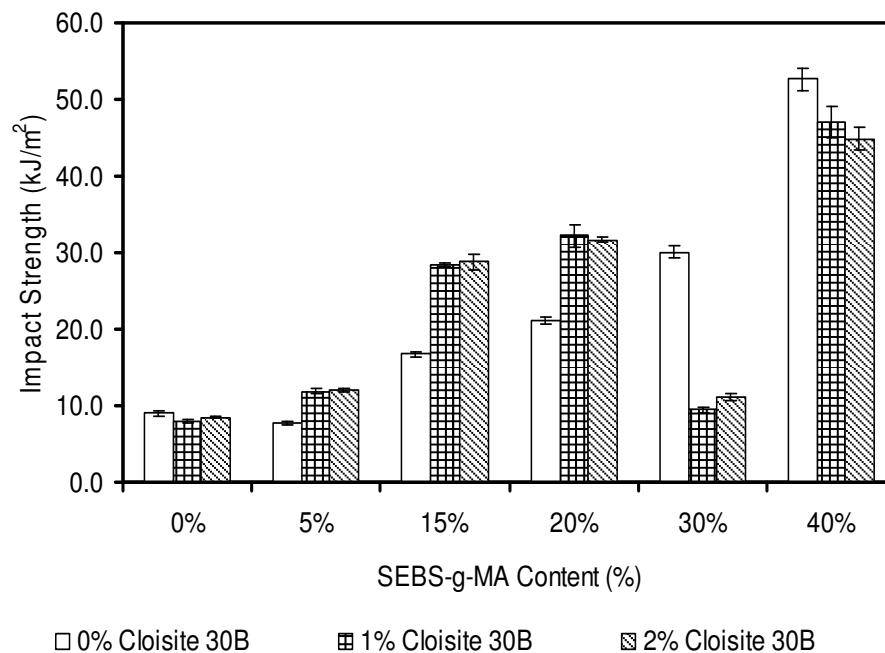
Figure 4.65 Impact strength (kJ/m^2) of PS / elastomer / Cloisite® 30B ternary nanocomposites
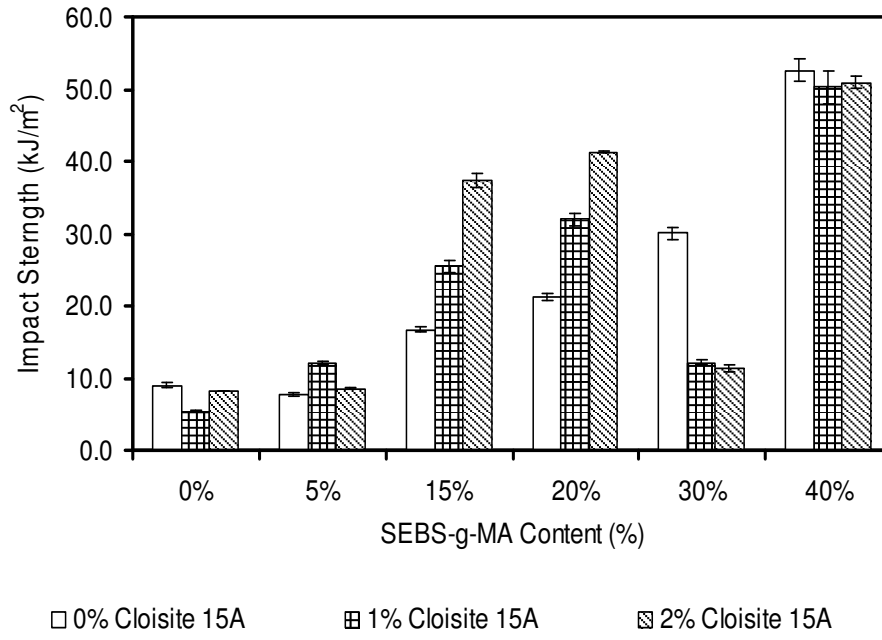
Figure 4.66 Impact strength (kJ/m^2) of PS / elastomer / Cloisite$^®$ 15A ternary nanocomposites
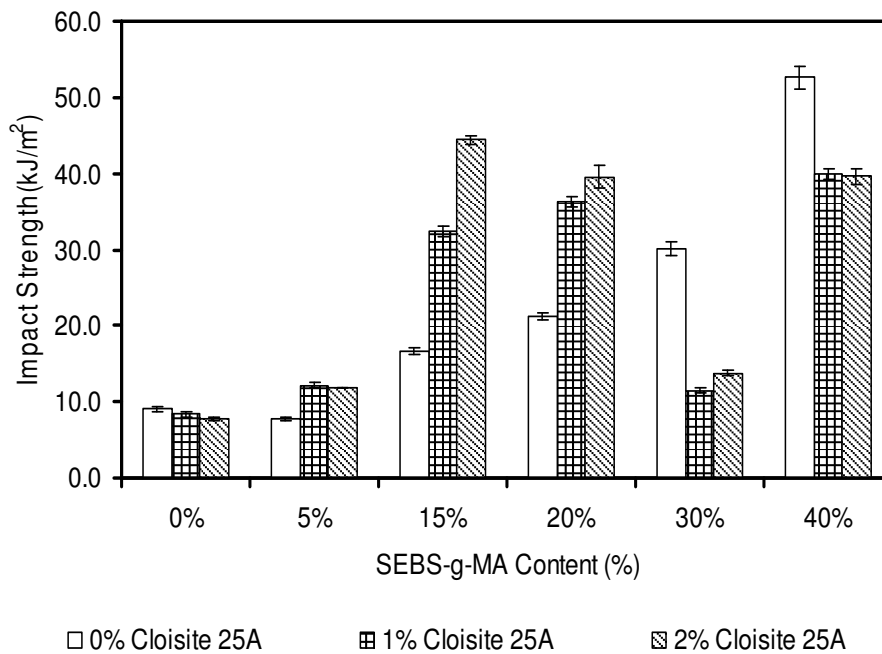
Figure 4.67 Impact strength (kJ/m^2) of PS / elastomer / Cloisite$^®$ 25A ternary nanocomposites

4.4 Thermal Analyses

4.4.1 Differential Scanning Calorimetry

In order to investigate the thermal properties of nanocomposites and blends in terms of their glass transition temperature, T_g, values, Differential Scanning Calorimetry analysis was performed. The obtained T_g values on the 1st run are shown in Table 4.7, and corresponding DSC thermograms are given in Appendix C. The experiments were conducted with 20˚C/min rate to increase the sensitivity and observe the glass transition temperature more clearly.

Above the glass transition temperature, the segmental motion of the polymer chains becomes significant [79]. Based on this definition, exfoliated or intercalated clay layers may prevent the segmental motion leading to higher glass transition temperature. However, in the binary PS / organoclay and ternary nanocomposites no significant variations are observed in the glass transition temperature. Thus, it can be said that glass transition temperature is found to be dependent neither on the organoclay content nor the elastomer content in the PS nanocomposites.

In addition, for high temperatures, approximately above 250˚C, the binary blends and ternary nanocomposites that contain high amounts of elastomer are found to have some fluctuations in their DSC thermogram. Firstly, it was thought that these fluctuations may be the result of thermal degradation of the composite and blends. However, 250˚C is a too low temperature to observe the degradation of a thermoplastic. So, it was concluded that crosslinking of elastomeric materials at high temperatures may cause these fluctuations. Also, with increasing elastomer content, it becomes difficult to observe the glass transition temperature.

Table 4.7 Glass transition temperature results

Composition	Concentration		T_g (˚C)
	Elastomer (wt%)	O-clay (wt%)	
PS	---	---	108.2
PS / Elastomer blends			
PS + SEBS-g-MA	5	---	104
PS + SEBS-g-MA	15	---	109.2
PS + SEBS-g-MA	20	---	109.4
PS + SEBS-g-MA	30	---	111.2
PS + SEBS-g-MA	40	---	110.0
PS + E-BA-GMA	5	---	108.5
PS + E-BA-GMA	15	---	111.0
PS + E-BA-GMA	20	---	110.4
PS + E-BA-GMA	30	---	109.5
PS + E-BA-GMA	40	---	109.2
PS / Organoclay nanocomposites			
PS + 30B	---	1	109.3
PS + 30B	---	2	109.2
PS + 15A	---	1	108.2
PS + 15A	---	2	108.4
PS + 25A	---	1	108.7
PS + 25A	---	2	108.9
PS / 5 wt% Elastomer / Organoclay nanocomposites			
PS + SEBS-g-MA + 30B	5	1	108.5
PS + SEBS-g-MA + 30B	5	2	107.8
PS + SEBS-g-MA + 15A	5	1	104.5
PS + SEBS-g-MA + 15A	5	2	108.2
PS + SEBS-g-MA + 25A	5	1	106.6
PS + SEBS-g-MA + 25A	5	2	105.4
PS + E-BA-GMA + 30B	5	1	108.2
PS + E-BA-GMA + 30B	5	2	107.9
PS + E-BA-GMA + 15A	5	1	109.8
PS + E-BA-GMA + 15A	5	2	109.4
PS + E-BA-GMA + 25A	5	1	109.2
PS + E-BA-GMA + 25A	5	2	110.9
PS / 15 wt% Elastomer / Organoclay nanocomposites			
PS + SEBS-g-MA + 30B	15	1	107.7
PS + SEBS-g-MA + 30B	15	2	107.6
PS + SEBS-g-MA + 15A	15	1	107.1
PS + SEBS-g-MA + 15A	15	2	108.4
PS + SEBS-g-MA + 25A	15	1	108.7
PS + SEBS-g-MA + 25A	15	2	108.0

Table 4.7 (cont'd) Glass transition temperature results

Composition	Concentration		T_g (˚C)
	Elastomer (wt%)	O-clay (wt%)	
PS / 20 wt% Elastomer / Organoclay nanocomposites			
PS + SEBS-g-MA + 30B	20	1	108.6
PS + SEBS-g-MA + 30B	20	2	107.7
PS + SEBS-g-MA + 15A	20	1	108.1
PS + SEBS-g-MA + 15A	20	2	108.6
PS + SEBS-g-MA + 25A	20	1	108.5
PS + SEBS-g-MA + 25A	20	2	107.5
PS / 30 wt% Elastomer / Organoclay nanocomposites			
PS + SEBS-g-MA + 30B	30	1	106.1
PS + SEBS-g-MA + 30B	30	2	107.8
PS + SEBS-g-MA + 15A	30	1	107.7
PS + SEBS-g-MA + 15A	30	2	106.4
PS + SEBS-g-MA + 25A	30	1	107.8
PS + SEBS-g-MA + 25A	30	2	Not observed
PS / 40 wt% Elastomer / Organoclay nanocomposites			
PS + SEBS-g-MA + 30B	40	1	109.1
PS + SEBS-g-MA + 30B	40	2	108.7
PS + SEBS-g-MA + 15A	40	1	107.3
PS + SEBS-g-MA + 15A	40	2	108.5
PS + SEBS-g-MA + 25A	40	1	108.8
PS + SEBS-g-MA + 25A	40	2	108.0

CHAPTER 5

CONCLUSIONS

Due to its brittle characteristics, PS needs impact modification. In most cases, styrene monomer is polymerized in the presence of polybutadiene, and this rubber phase forms little globs in the polymer matrix which inhibit crack formation. Due to the many disadvantages of this technique, impact modification of PS is still a growing research area. In this study, instead of polybutadiene, SEBS-g-MA or E-BA-GMA was used as the rubber phase and they were melt-blended in a co-rotating twin screw extruder. It is a well known fact that, addition of a rubber phase into a brittle polymer matrix leads to higher impact strength and elongation at break, whereas it reduces the tensile strength and modulus. In order to overcome this problem, organically modified montmorillonites, Cloisite® 30B, 15A and 25A, were used.

Initially, elastomer and organoclay contents were kept at 5wt% and 1-2wt% respectively. When the dispersion state of layers was investigated with XRD analysis, no improvement was observed in the basal spacing of binary and ternary nanocomposites containing Cloisite® 30B due to the highly hydrophilic surface of Cloisite® 30B. On the other hand, for the nanocomposites containing Cloisite® 15A, intercalated structures were obtained with the addition of 5wt% elastomer. In addition, Cloisite® 25A containing ternary nanocomposites, especially SEBS-g-MA containing ones, displayed exfoliated structures. The better compatibilizing effect of SEBS-g-MA was attributed to the higher viscosity of the SEBS-g-MA compared to the PS matrix. In addition, the higher compatibility between SEBS-g-MA and PS matrix is due to the solubility of polystyrene end block of SEBS with the PS matrix. Although a better dispersion was expected for nanocomposites containing Cloisite® 15A, the ones prepared with Cloisite® 25A showed exfoliated structures. This is

due to the two long aliphatic tails of Cloisite® 15A which limit the access of polymer chains to the clay surface.

The impact tests that are applied to 5wt% elastomer containing nanocomposites indicated that this amount of elastomer is not sufficient to improve the impact strength to a high level. Accordingly, it was decided to use only SEBS-g-MA and to increase its content up to 15-20-30 and 40wt%. As in the case of nanocomposites with 5wt% elastomer, the XRD peak does not shift to lower angles for nanocomposites containing Cloisite® 30B at higher elastomer contents. On the other hand, d-spacing of the Cloisite® 15A increased with increasing SEBS-g-MA content, up to 20wt% SEBS-g-MA. For the nanocomposites containing Cloisite® 25A, it was observed that further addition of elastomeric material does not affect exfoliated structure in a negative way.

According to SEM analysis, as the elastomer content increases, the crack propagation lines become shorter and closer to each other and the number of cracks increases. With the etching procedure with n-Heptane, the elastomeric phase was removed, and as expected droplet matrix morphology was observed. When the elastomeric domain sizes of PS/elastomer binary blends were investigated, increase in the average domain size with increasing elastomer content was obtained for both SEBS-g-MA and E-BA-GMA, due to the droplet coalescence during melt mixing. Another important point that was concluded from the SEM analysis was the point of phase inversion. For both elastomer types, the phase inversion point was found between 30 and 40wt% elastomer content. When some theoretical models were conducted to find the point of phase inversion, it was seen that these models are not in agreement with the morphological analysis, because some parameters such as non-Newtonian and elastic characteristics of the components, the nature of the flow field and interfacial tension should be considered besides the viscosity and volume ratios to determine the point of phase inversion.

SEM analysis of the ternary composites showed that the average domain size increases with organoclay addition, no matter whether it is well dispersed or not. This is attributed to accumulation of clay particles inside of the elastomer phase and at the interphase between the PS and elastomer phases, reducing the

interfacial tension and enlarging the domain sizes. With the organoclay addition, it is found that the point of phase inversion shifts to a lower elastomer content which is also an indication of the dispersion of organoclay particles at the PS-elastomer interphase and in the elastomer phase. The clay particles lead to enlargement of the domains and the phase inversion occurs at smaller elastomer content. Moreover, dispersion of the silicate layers observed by XRD and their location in the nanocomposites determined by SEM are confirmed with the TEM analysis.

By capillary viscometry, it is found that SEBS-g-MA has a higher viscosity compared to pure PS, whereas the viscosity of E-BA-GMA is smaller than that of PS and SEBS-g-MA. This result was supported by the MFI test. In binary PS/elastomer blends, it is seen that addition of SEBS-g-MA increases the viscosity of the blends, while addition of E-BA-GMA decreases the viscosity when it is blended with pure the PS. MFI results also indicated that incorporation of organoclay into the polymer matrix leads to an increase in the melt viscosity. The ternary nanocomposites showed higher viscosity values compared to their corresponding PS/organoclay composite counterparts. Increasing the viscosity affects the dispersion of silicate layers in a positive way due to the application of higher shear stress. In accordance with this theory, it was concluded that the nanocomposites containing Cloisite® 15A and 25A have higher viscosity compared to the ones containing Cloisite® 30B.

Tensile test results confirmed that SEBS-g-MA is a better compatibilizer compared to E-BA-GMA. When the ternary nanocomposites are considered, it was found that, the highest improvement in the tensile strength and elongation at break values were obtained for the ternary nanocomposites containing Cloisite® 25A and SEBS-g-MA. 26% and 105% increase in tensile strength and elongation at break values were obtained respectively. As the elastomer content increases, the tensile strength value increases up to 15 and 20wt% elastomer content. After this optimum content, at 30 and 40wt%, tensile strength showed a drastic reduction. As expected, elongation at break values increases with increasing elastomer content. Young's modulus values of the nanocomposites containing 15 and 20wt% SEBS-g-MA do not show high reduction, whereas, Young's modulus values of nanocomposites prepared with 30 and 40wt% elastomeric material do.

143

According to the impact test results, impact strength of the PS/SEBS-g-MA binary blends increases with the elastomer content, whereas for the PS/ E-BA-GMA blends no improvement was observed. The ternary nanocomposites prepared with 5wt% elastomer have higher impact strength values compared to PS/elastomer binary blends. However, with different organoclay types, no apparent difference can be observed. As the SEBS-g-MA content increases, the impact strength of the ternary nanocomposites increases, except for the ones containing 30wt% SEBS-g-MA. All of these results indicate that the nanocomposites containing 15 and 20wt% SEBS-g-MA have the optimum average domain size that results in high impact strength values without deteriorating the tensile properties. Also, the best improvement in the impact strength values were obtained for the nanocomposites prepared with Cloisite$^{®}$ 25A.

From the DSC analysis no significant variations are observed in the glass transition temperatures of the PS / organoclay and ternary nanocomposites.

REFERENCES

1. Hull, D., *An Introduction to Composite Materials* 1981, Cambridge: Cambridge University Press.

2. Akovali, G., *Handbook of Composite Fabrication*, ed. R.T. Ltd. 2001, UK: Shawburry.

3. Callister, J., and William D., *Materials Science and Engineering: An Introduction.* 6th ed. 2003, New York: John Wiley & Sons.

4. Rosen, S.L., *Fundamental Principles of Polymeric Materials.* 1982, New York: John Wiley &Sons.

5. Giannelis, E.P., *Polymer Layered Silicate Nanocomposites.* Advanced Materials, 1996. **8**: p. 29-35.

6. Tjong, S.C., *Structural and Mechanical Properties of Polymer Nanocomposites.* Materials Science and Engineering, 2006. **53**: p. 73-197.

7. Kroschwitz, J.I., *Encyclopedia of Polymer Science and Technology.* 3rd ed. 2003, Hoboken, N. J.: Wiley Interscience.

8. Huang, X., Lewis S., Brittain W. J., and Vaia R. A. , *Synthesis of Polycarbonate-Layered Silicate Nanocomposites via Cyclic Oligomers.* Macromolecules, 2000. **33**: p. 2000-2004.

9. Vaia, R.A., Ishii H., and Giannelis E. P., *Synthesis and Properties of Two-dimensional Nanostructures by Direct Intercalation of Polymer Melts in Layered Silicates.* Chemistry of Materials, 1993. **5**: p. 1694-1696.

10. Dennis, H.R., Hunter D.L., Chang D., Kim S., White J.L., Cho J.W., and Paul D.R., *Effect of Melt Processing Conditions On the Extent of Exfoliation in Organoclay-Based Nanocomposites* 2001. **42**: p. 9513-9522

11. Ray, S.S., Okamoto K., and Okamoto M., *Structure-Property Relationship in Biodegradable Poly(butylene succinate)/Layered Silicate Nanocomposites* Macromolecules, 2003. **36**: p. 2355-2367

12. Harper, C.A., *Handbook of Plastics, Elastomers & Composites.* 4th ed. 2002: McGraw-Hill.

13. Matthews, F.L., and Rowlings R.D., *Composite Materials, Engineering & Science.* 1994, London, New York: Chapman & Hall.

14. Daniel, I., and Ishai O., *Engineering Mechanics of Composite Materials*. 1994, New York: Oxford University Press.

15. Chawla, K., *Composite Materials Science and Engineering*. 2nd ed. 1998, New York: Springer - Verlag.

16. Sawyer, L.C., and Grubb D.T.,, *Polymer Microscopy*. 1987, New York: Chapman and Hall.

17. Chen B., Evans J.R., Greenwell H. C., Boulet P., Coveney P. V., Bowdenf A. A., and Whiting A. , *A Critical Appraisal of Polymer - Clay Nanocomposites.* Chemical Society Reviews, 2008. **37**: p. 568–594.

18. Zanetti, M., Lomakin S., and Camino G., *Polymer-Layered Silicate Nanocomposites.* Macromolecular Materials and Engineering, 2000. **279**: p. 1-9.

19. Luo, J., and Daniel I.M., *Characterization and Modeling of Mechanical Behavior of Polymer/Clay Nanocomposites.* Composites Science and Technology, 2003. **63**: p. 1607-1616.

20. Mark, J.E., *Ceramic Reinforced Polymers and Polymer-Modified Ceramics.* Polymer Engineering Science, 1996. **36**: p. 2905-2920.

21. Reynaud, E., Gauthier C., and Perez J. , *Nanophases In Polymers.* Revue De Metallurgie Cahiers D Informations Techniques, 1999. **96**: p. 169-176.

22. Werne, T., and Patten T.E. , *Preparation of Structurally Well Defined Polymer-Nanoparticle Hybrids With Controlled/Living Radical Polymerization.* Journal of the American Chemical Society 1999. **121**: p. 7409-7410.

23. Herron, N., and Thorn D.L., *Nanoparticles. Uses and Relationships to Molecular Clusters.* Advanced Materials, 1998. **10**: p. 1173-1184.

24. Favier, V., Canova G.R., Shrivastava S.C., and Cavaille J.Y., *Mechanical Percolation in Cellulose Whiskers Nanocomposites.* Polymer Engineering Science, 1997. **37**: p. 1732-1739.

25. Alexandre, M., and Dubois P., *Polymer-Layered Silicate Nanocomposites: Preparation, Properties, and Uses of a New Class of Materials,.* Materials Science and Engineering, 2000. **28**: p. 1-63.

26. Theng, B.K.G., *The Chemistry of Clay-Organic Reactions*. 1974, New York: John Wiley &Sons.

27. Ogawa, M., and Kuroda K., *Preparation of Inorganic-Organic Nanocomposites Through Intercalation of Organoammonium Ions into*

146

Layered Silicates. Bulletin of the Chemical Society of Japan 1997. **70**: p. 2593-2618.

28.   Giannelis, E.P., *Polymer-Layered Silicate Nanocomposites: Emerging Scientific and Commercial Opportunities.* Proceedings of 57th SPE Annual Technical Conference (ANTEC), 1999. **155**: p. 3966-3968.

29.   Pinnavaia, T.J., and Beall G.W.,, *Polymer-Clay Nanocomposites.* 2000, England: John Wiley & Sons.

30.   Moore, D.M., and Reynolds R.C., *X-ray Diffraction and the Identification and Analysis of Clay Analysis of Clay Minerals.* 1997, Oxford: Oxford University Press.

31.   Tjong, S.C., and Bao S.P., *Impact Fracture Toughness of Polyamide-6/Montmorillonite Nanocomposites Toughened With a Maleated Styrene/Ethylene Butylene/Styrene Elastomer* Journal of Polymer Science Part B Polymer Physics 2005. **43**: p. 585-595.

32.   Krishnamoorti, R., Vaia R.A, and Giannelis E.P., *Structure and Dynamics of Polymer-Layered Silicate Nanocomposites.* Chemistry of Materials, 1996. **8**: p. 1728-1734.

33.   Isık, F., *Nanocomposites Based On Blends Of Polyethylene*, *Chemical Engineering.* 2005, MS Thesis, Middle East Technical University: Ankara, Turkey.

34.   Lagaly, G., *Interaction of Alkylamines With Different Types of Layered Compounds.* Solid State Ionics 1986. **22**: p. 43-51.

35.   Lebaron, P.C., Wang Z., and Pinnavaia T., *Polymer-Layered Silicate Nanocomposites: An Overview.* Journal of Applied Clay Science, 1999. **15**: p. 11-29.

36.   Vaia, R.A., Teukolsky R.K., and Giannelis E.P. , *Interlayer Structure and Molecular Environment of Alkylammonium Layered Silicates.* Chemistry of Materials, 1994. **6**: p. 1017-1022.

37.   Ray, S.S., and Okamoto M. , *New Polylactide/Layered Silicate Nanocomposites;Melt Rheology and Foam Processing* Macromolecular Materials and Engineering, 2003. **288**: p. 936-944.

38.   Kornmann, X., *Synthesis and Characterization of Thermoset-Clay Nanocomposites*, in *Division of Polymer Engineering.* 2001, Luleå University of Technology: Luleå, Sweden.

39. Vaia, R.A., Jandt K.D., Kramer E.J., and Giannelis E.P., *Kinetics of Polymer Melt Intercalation.* Macromolecules, 1995. **28**: p. 8080-8085.

40. Vaia, R.A., and Giannelis E.P., *Lattice Model of Polymer Melt Intercalation In Organically-Modified Layered Silicates.* Macromolecules, 1997. **30**: p. 7990-7999.

41. Cho, J.W., and Paul D.R., *Nylon 6 Nanocomposites By Melt Compounding.* Polymer, 2001. **42**: p. 1083-1094.

42. Staudinger, H., *Über Polymerisation.* Berichte der Deutschen Chemischen Gesellschaft 1920. **53**: p. 1073-1085.

43. Boyer, R.F., *Anecdotal History of Styrene and Polystyrene* Journal of Macromolecular Science - Chemistry, 1981. **A15**: p. 1411 - 1434

44. Ullmann, F., *Ullmann's Encyclopedia of Industrial Chemistry.* 5th ed. Vol. A21. 1992, New York: Wiley-VCH

45. Ebewele, R.O., *Polymer Science and Technology.* 2000, USA: CRC Press LLC.

46. Scheirs, J., and Priddy D., *Modern Styrenic Polymers: Polystyrenes and Styrenic Copolymers.* 2003, New York: John Wiley & Sons.

47. Buzanowski, W.C., Graham J.D., Priddy D.B., and Shero E. , *Spontaneous Polymerization of Styrene in the Presence of Acid: Further Confirmation of the Mayo Mechanism* Polymer 1992. **33**: p. 3055-3059.

48. Bucknall, C.B., *Toughned Plastics.* 1977, London: Applied Science Publishers.

49. Kramer, E.J., and Krauch H.H., *Crazing in Polymers.* 1983, Berlin: Springer.

50. Moore, E.R., *Encyclopedia of Polymer Science and Engineering.* 1989, New York: John Wiley & Sons.

51. The University of Southern Mississippi, Polystyrene, *http://www.pslc.ws/mactest/styrene.htm.* Last visited on: December 2008.

52. Akkapeddi, M.K., *Reactive Polymer Blending.* 2001, USA: Hanser Gardner Publications.

53. Joseph, S., Rutkowska M., Jastrzêbska M., Janik H., Haponiuk J.T., and Thomas S., *Polystyrene/Polybutadiene Blends: An Analysis of the Phase Inversion Region and Cophase Continuity and a Comparison with Theoretical Predictions* Journal of Applied Polymer Science, 2003. **89**: p. 1007-1016.

54. Han, C.D., *Multiphase Flow in Polymer Processing*. 1981, London: Academic.

55. Wu, S., *Phase Structure and Adhesion in Polymer Blends: A Criterion for Rubber Toughening.* Polymer, 1985. **26**: p. 1855-1863

56. Jordhamo, G.M., Manson J.A., and Sperling L.H., *Phase Continuity and Inversion in Polymer Blends and Simultaneous Interpenetrating Networks.* Polymer Engineering and Science, 1986. **26**: p. 517-524.

57. Chen, T.H., and Su A.C., *Morphology of Poly(p-phenylene sulfide)polyethylene Blends.* Polymer, 1993. **34**: p. 4826-4831

58. Everaert, V., Aerts L., and G. Groeninckx, *Phase Morphology Development in Immiscible PP/(PS/PPE) Blends Influence of the Melt-Viscosity Ratio and Blend Composition.* Polymer, 1999. **40**: p. 6627-6644.

59. Paul, D.R., and Barlow J.W., *Polymer Blends (or Alloys).* Journal of Macromolecular Science Reviews in Macromolecular Chemistry, 1980. **18**: p. 109-168.

60. Metelkin, V.I., and Blekht V.S., *Formation of a Continuous Phase in Heterogeneous Polymer Mixtures.* Colloid J USSR, 1984. **46**: p. 425-429.

61. Strong, A.B., *Plastics, Materials & Processing*. 2000, New York: Prentice Hall.

62. Rauwendaal, C., *Polymer Extrusion*. 1990, New York: Hanser Gardner Publications.

63. Fisher, E.G., *Extrusion of Plastics.* 1976, New York: John Wiley & Sons.

64. *online.sfsu.edu/~jge/html/topofchachapter5.html.* SFSU-Extrusion, Last accessed: September 2008.

65. Hanser Gardner Publications, Technical Books for Industry, Science and Education,
https://www.hansergardner.com/plastic/.
Last visited on: December 2008.

66. Rubin, I.I., *Handbook of Plastic Materials and Technology*. 1990, New York: John Wiley & Sons.

67. Özden, G., *Synthesis and Characterization of Polystyrene Clay Nanocomposites*, *Chemical Engineering*. 2004, MS Thesis, Middle East Technical University: Ankara, Turkey.

68. Middleman, S., *Fundamentals of Polymer Processing*. 1977: McGraw- Hill.

69. Rodriguez, F., Cohen C., Ober C., and Archer A.L., *Principles of Polymer Systems*. 2003, New York: Taylor & Francis.

70. Billmeyer, F.W., *Textbook of Polymer Science*. 1984, New York: John Wiley & Sons.

71. University of California, Santa Barbara, Introduction to X-Ray Diffraction, *http://www.mrl.ucsb.edu/mrl/centralfacilities/xray/xray-basics/index.html.* Last visited on: December 2008.

72. Jens, A.N., and McMorrow D., *Elements of Modern X-ray Physics*. 2001, New York: John Wiley & Sons.

73. Seymour, R.B., *Polymer Chemistry: An Introduction*. 4th ed. 1996, New York: Marrel Dekker.

74. Iowa State University, SEM, *http://www.mse.iastate.edu/microscopy/whatsem.html.* Last visited on: December 2008.

75. Bower, D.I., *An Introduction to Polymer Physics*. 2002, USA: Cambridge University Press.

76. Materials Evalution and Engineering, Handbook of Analytical Methods, SEM, *http://www.mee-inc.com/sem.html.* Last visited on: December 2008.

77. Nobelprize.org, TEM, *http://nobelprize.org/educational_games/physics/microscopes/tem/ index.html.* Last visited on: December 2008.

78. Sperling, L.H., *Introduction to Physical Polymer Science*. 4th ed. 2006, New York: John Wiley & Sons.

79. Seymour, B.S., and Carraher C.E., *Structure and Property Relationships in Polymers*. 1984, New York: Plenum Press.

80. The University of Southern Mississippi, DSC, *http://www.pslc.ws/mactest/dsc.htm.* Last visited on: December 2008.

81. Xie, W., Hwu J. M., Jiang G.J., Buthelezi T.M., and Pan W.P., *A Study of the Effect of Surfactants on the Properties of Polystyrene-Montmorillonite Nanocomposites.* Polymer Engineering and Science, 2003. **43**: p. 214-222.

82.   Park, C.I., Choi W.M., Kim M.H., and Park O.O., *Thermal and Mechanical Properties of Syndiotactic Polystyrene/Organoclay Nanocomposites with Different Microstructures.* Journal of Polymer Science: Part B: Polymer Physics, 2004. **42**: p. 1685-1693.

83.   Tanoue, S., Hasook A., Itoh A., Yanou M., Iemoto Y., and Unryu T., *Effect of Screw Rotation Speed on the Properties of Polystyrene/Organoclay Nanocomposites Prepared by a Twin-Screw Extruder.* Journal of Applied Polymer Science, 2006. **101**: p. 1165–1173.

84.   Zhang, W.A., Shen X.F., Liu M.F., and Fang Y.E, *Synthesis and Thermal Properties of Polystyrene/Montmorillonite Nanocomposites by γ-Ray Radiation Polymerization.* Journal of Applied Polymer Science, 2003. **90**: p. 1692-1696.

85.   Chang, S., Xie T., and Yang G., *Morphology and Mechanical Properties of High-Impact Polystyrene/Elastomer/Magnesium Hydroxide Composites.* Journal of Applied Polymer Science, 2006. **102**: p. 5184-5190.

86.   Li, Y., Xie T., and Yang G., *Effects of Maleated Styrene–(Ethylene-co-Butene)–Styrene on the Morphology and Mechanical and Thermal Properties of Polystyrene/Polyamide 1212 Blends.* Journal of Applied Polymer Science, 2005. **95**: p. 1354-1360.

87.   Bruzaud, S., Grohens Y., Ilinca S., and Carpentier J.F., *Syndiotactic Polystyrene/Organoclay Nanocomposites: Synthesis via In Situ Coordination-Insertion Polymerization and Preliminary Characterization.* Macromolecular Materials and Engineering, 2005. **290**: p. 1106-1114.

88.   Gelfer, M.Y., Song H.H., Liu L., Hsiao B.S., Chu B., Rafailovich M., Si M., and Zaitsev V., *Effects of Organoclays on Morphology and Thermal and Rheological Properties of Polystyrene and Poly(methyl methacrylate) Blends.* Journal of Polymer Science Part B Polymer Physics, 2003. **41**: p. 44-54.

89.   Jose, S., Thomas S., Lievana E., and Karger-Kocsis J., *Morphology and Mechanical Properties of Polyamide 12 Blends with Styrene/Ethylene–Butylene/Styrene Rubbers with and without Maleation.* Journal of Applied Polymer Science, 2005. **95**: p. 1376-1387.

90.   Karayannidis, G.P., Bikiaris D.N., Papageorgiou G.Z., and Bakirtzis V. , *Rubber Toughening of Glass Fiber Reinforced Nylon-6,6 with*

Functionalized Block Copolymer SEBS-g-MA Advances in Polymer Technology, 2002. **21**: p. 153-163.

91. Aphiwantrakul, S., Srikhirin T., Triampo D., Putiworanat R., Limpanart S., Osotchan T., and Udomkichdecha W., *Role of the Cation-Exchange Capacity in the Formation of Polystyrene–Clay Nanocomposites by In Situ Intercalative Polymerization.* Journal of Applied Polymer Science, 2005. **95**: p. 785-789.

92. Ramsteiner, F., McKee G.E., Heckmann W., Oepen S., and Geprägs M., *Rubber Toughening of Syndiotactic Polystyrene and Poly/(styrene/diphenylethylene)* Polymer, 2000. **41**: p. 6635-6645

93. Uthirakumar, P., Hahn Y.B., Nahm K.S, and Lee Y.S., *Exfoliated High-Impact Polystyrene/MMT Nanocomposites Prepared Using Anchored Cationic Radical Initiator–MMT Hybrid.* European Polymer Journal, 2005. **41**: p. 1582-1588.

94. Total Petrochemicals, Lacqrene® 1960N, *http://www.totalpetrochemicals.com/en/index.asp.* Last visited on: December 2008.

95. Kraton, FG® 1924X, *http://www.kraton.com/Products/Kraton_FG/.* Last visited on: December 2008.

96. Dupont, Elvaloy® PTW, *http://www2.dupont.com/DuPont_Home/en_US/index.html.* Last visited on: December 2008.

97. Southern Clay Products, Cloisite® 30B, 15A and 25A, *www.nanoclay.com.* Last visited on: December 2008.

98. *Plastics: Determination of Tensile Properties & Test Conditions for Moulding and Extrusion Plastics.* ISO 527, International Organization for Standardization - Plastics.

99. *Rubber, Vulcanized or Thermoplastic: Determination of Tensile Stress-Strain Properties.* ISO 37, International Organization for Standardization - Plastics.

100. *Determination of Charpy Impact Properties.* ISO 179, International Organization for Standardization - Plastics.

101.   Brindley, G.W., and Brown G., *Crystal Structures of Clay Minerals and their X-Ray Identification*. 1980, London: Mineralogical Society.

102.   Vaia, R.A., Klaus D., Kramer E.J., and Giannelis E.P. Chem. Mater. 8 () 2628., *Microstructural Evolution of Melt Intercalated Polymer-Organically Modified Layered Silicates Nanocomposites* Chemistry of Materials 1996. **8**: p. 2628-2635

103.   Park, C.I., Park O.O., Lim J.G., and Kim H.J., *The Fabrcation of Syndiotactic Polystyrene/Organophilic Clay Nanocomposites and Their Properties* Polymer, 2001. **42**: p. 7465-7475.

104.   Isık, I., Yılmazer, U., Göknur, B., *Impact modified polyamide-6/organoclay nanocomposites: Processing and characterization* Polymer Composites, 2007. **29**: p. 133-141.

105.   Finnigan, B., Martin D., Halley P., Truss R., and Campell K., *Morphology and Properties of Thermoplastic Polyurethane Nanocomposites Incorporating Hydrophobic Layered Silicates.* Journal of Applied Polymer Science, 2005. **97**: p. 300-309.

106.   Tanoue, S., Utracki L.A., Garcia-Rejon A., Tatibouët J., Cole K.C., and Kamal M.R., *Melt Compounding of Different Grades of Polystyrene With Organoclay. Part 1: Compounding and Characterization.* Polymer Engineering and Science, 2004. **44**: p. 1046-1060.

107.   Fornes, T.D., Yoon P.J., and Paul D.R., *Polymer Matrix Degradation and Color Formation in Melt Processed Nylon 6/Clay Nanocomposites.* Polymer, 2003. **44**: p. 7545-7556

108.   Nielsen, L.E., *Mechanical Properties of Polymers*. 1962, New York: Reinhold.

109.   Verhoogt, H., Willems C.R.J., Dam Van J., and De Boer A.P. , *Blends of a Thermotropic LCP and a Thermoplastic Elastomer: II formation and stability of LCP fiber.* Polymer Engineering and Science, 1994. **34**: p. 453-460

110.   Wu, S., *Generalized Criterion For Rubber Toughening: The Critical Matrix Ligament Thickness.* Journal of Applied Polymer Science, 1988. **35**: p. 549-561.

111.   Mert, M., and Yilmazer, U., *Processing and properties of modified polyamide 66-organoclay nanocomposites.* Journal of Applied Polymer Science, 2008. **108**: p. 3890-3900.

112. Lee, K.M., and Han C.D., *Rheology of Organoclay Nanocomposites: Effects of Polymer Matrix/Organoclay Compatibility and the Gallery Distance of Organoclay,.* Macromolecules, 2003. **36**: p. 7165-7178.

113. Bottino, F.A., Fabbri E., Fragala I.L., Malandrino G., Orestano A., Pilati F., and Pollicino A., *Polystyrene-Clay Nanocomposites Prepared with Polymerizable Imidazolium Surfactants* Macromolecular Rapid Communications, 2003. **24**: p. 1079-1084

114. Kim, G.M., Michler G.H., Rösch J. and Mülhaupt R., *Micromechanical Deformation Processes in Toughened PP/PA/SEBS-g-MA Blends Prepared by Reactive processing.* Acta Polymerica, 1998. **49**: p. 88-95.

115. Hassan, A., Othman N., Wahit M.U., Wei L.J., Rahmat A.R., and Mohd Ishak Z.A. , *Maleic Anhydride Polyethylene Octene Elastomer Toughened Polyamide 6/Polypropylene Nanocomposites: Mechanical and Morphological Properties.* Macromolecular Symposia, 2006. **239**: p. 182-191

116. Nielsen, L., and Landel R., *Mechanical Properties of Polymers and Composites.* 2nd ed. 1993, USA: Marcel Dekker.

117. Park, J.H., and Jana S.C. , *The Relationship Between Nano- and Micro-Structures and Mechanical Properties in PMMA-Epoxy-Nanoclay Composites* Polymer, 2003. **44**: p. 2091-2100.

APPENDIX A

X-RAY DIFFRACTION PATTERNS
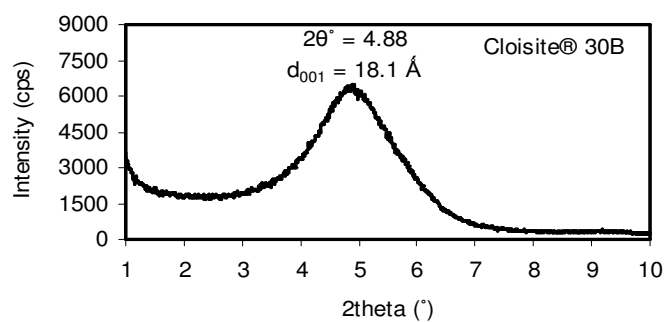
Figure A.1 XRD pattern of Cloisite® 30B
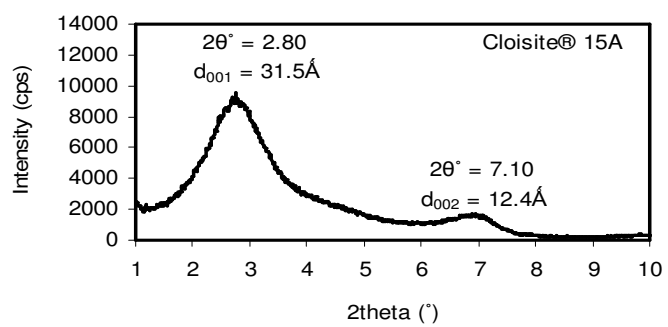
Figure A.2 XRD pattern of Cloisite® 15A
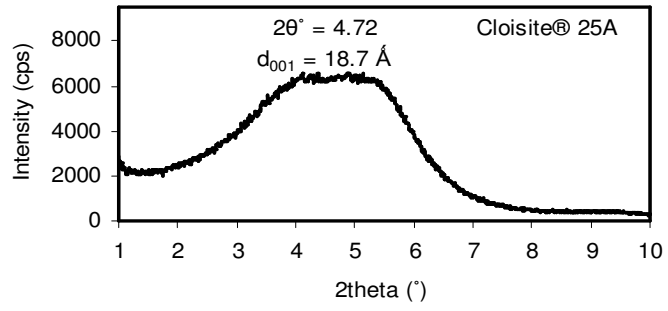
Figure A.3 XRD pattern of Cloisite® 25A
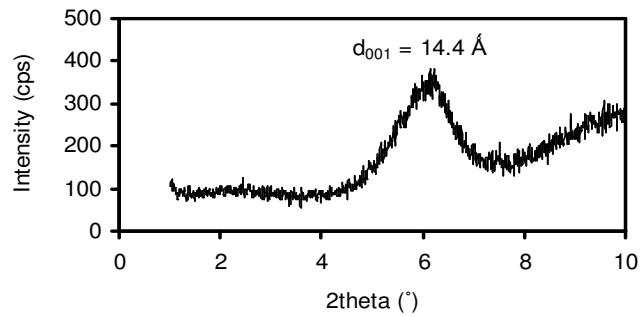
Figure A.4 XRD pattern of PS / Cloisite® 30B (1%) binary nanocomposite
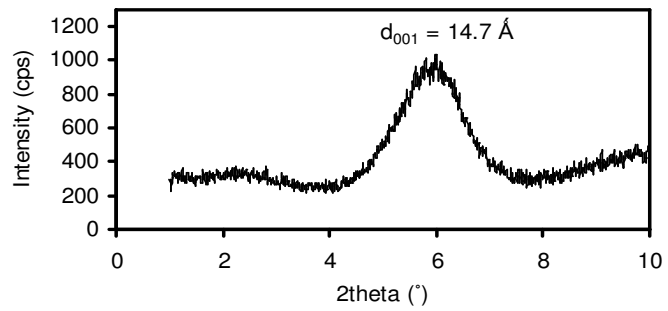
Figure A.5 XRD pattern of PS / Cloisite® 30B (2%) binary nanocomposite
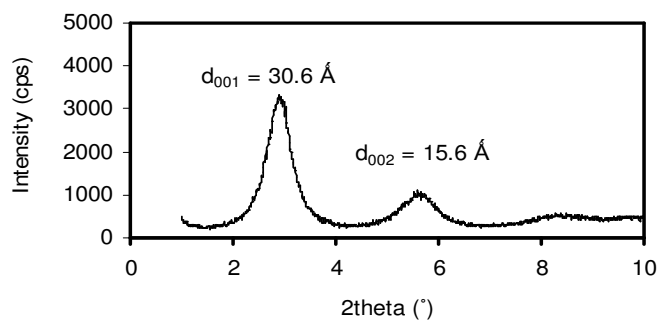
Figure A.6 XRD pattern of PS / Cloisite$^{®}$ 15A (1%) binary nanocomposite
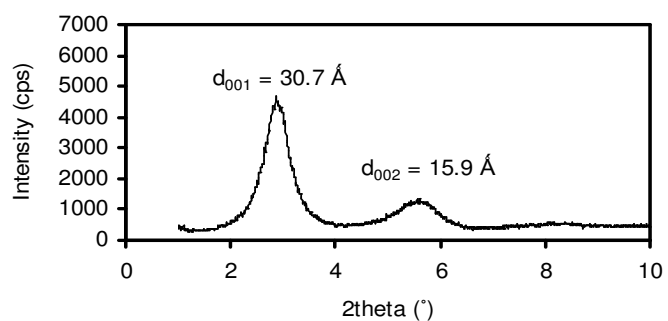
Figure A.7 XRD pattern of PS / Cloisite$^{®}$ 15A (2%) binary nanocomposite
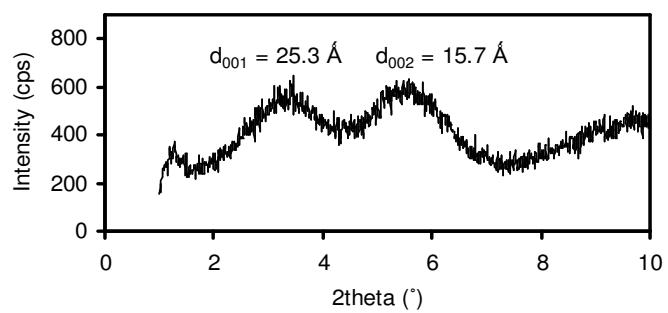
Figure A.8 XRD pattern of PS / Cloisite$^{®}$ 25A (1%) binary nanocomposite

157
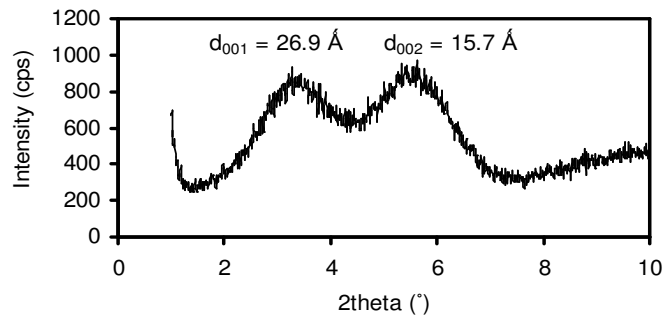
Figure A.9 XRD pattern of PS / Cloisite® 25A (2%) binary nanocomposite
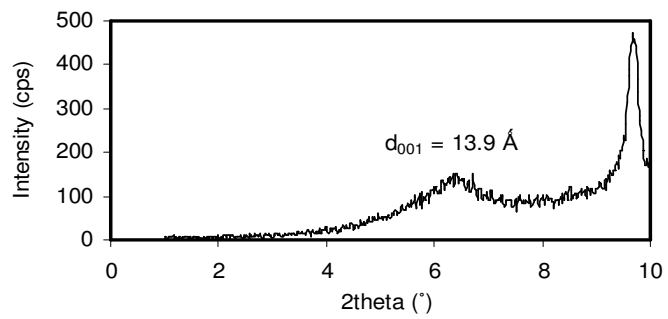
Figure A.10 XRD pattern of SEBS-g-MA / Cloisite® 30B (1%) binary nanocomposite
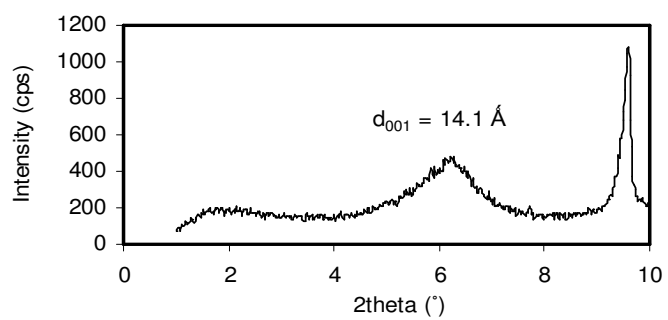
Figure A.11 XRD pattern of SEBS-g-MA / Cloisite® 30B (2%) binary nanocomposite
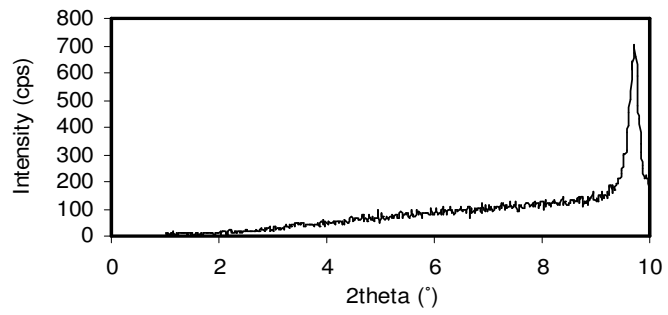
Figure A.12 XRD pattern of SEBS-g-MA / Cloisite® 15A (1%) binary nanocomposite
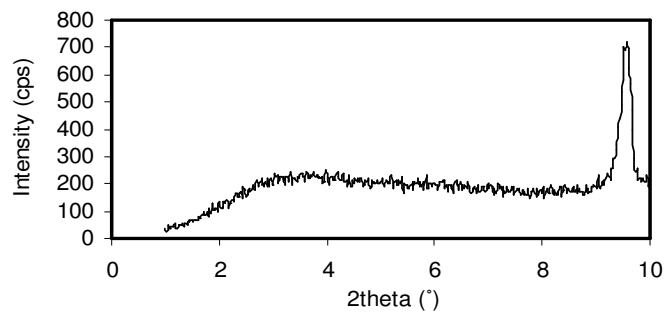
Figure A.13 XRD pattern of SEBS-g-MA / Cloisite® 15A (2%) binary nanocomposite
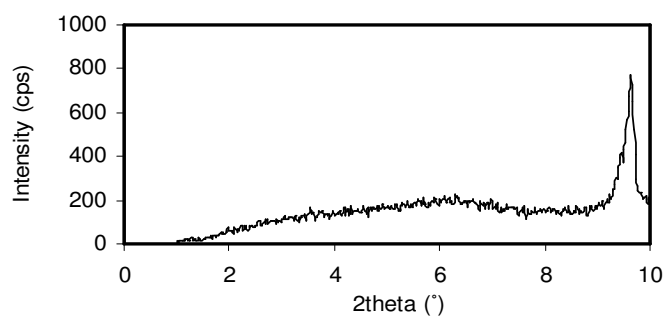
Figure A.14 XRD pattern of SEBS-g-MA / Cloisite® 25A (1%) binary nanocomposite

159
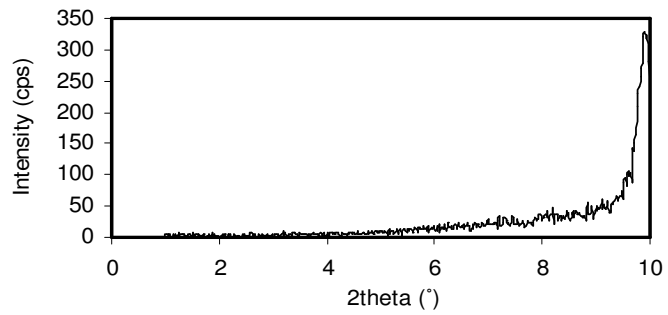
Figure A.15 XRD pattern of SEBS-g-MA / Cloisite® 25A (2%) binary nanocomposite
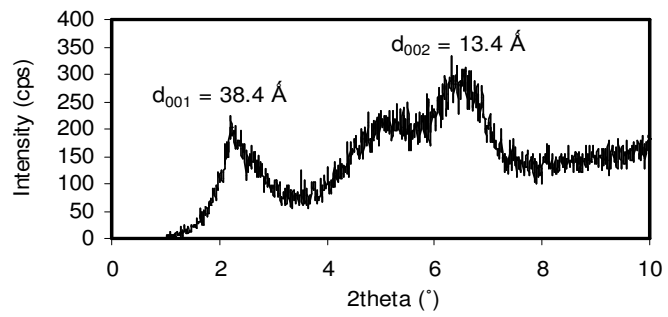
Figure A.16 XRD pattern of E-BA-GMA / Cloisite® 30B (1%) binary nanocomposite
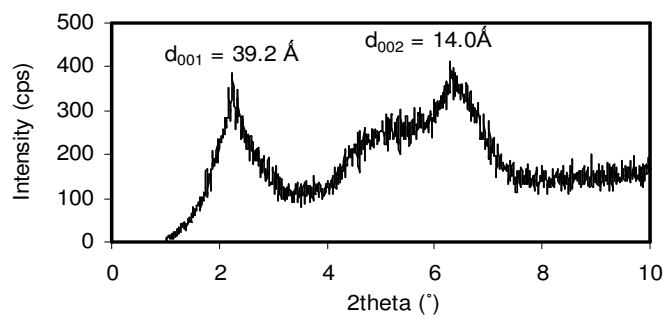
Figure A.17 XRD pattern of E-BA-GMA / Cloisite® 30B (2%) binary nanocomposite

160
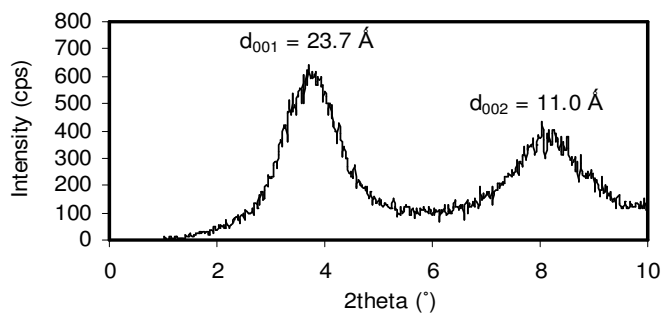
Figure A.18 XRD pattern of E-BA-GMA / Cloisite® 15A (1%) binary nanocomposite
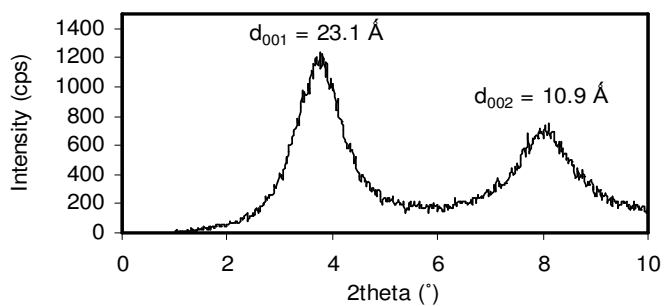
Figure A.19 XRD pattern of E-BA-GMA / Cloisite® 15A (2%) binary nanocomposite
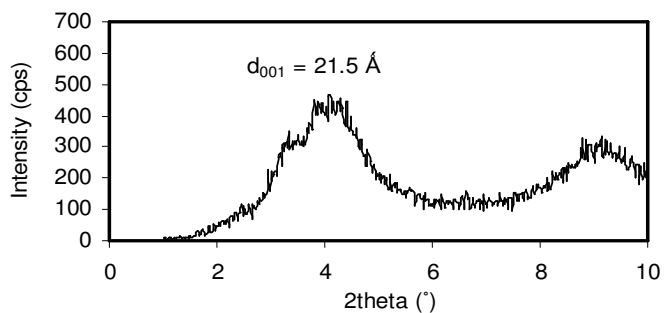
Figure A.20 XRD pattern of E-BA-GMA / Cloisite® 25A (1%) binary nanocomposite

161
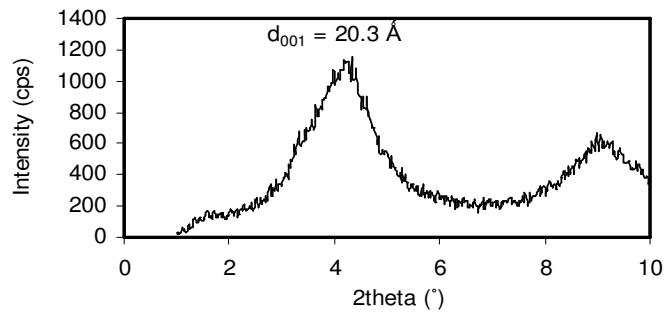
Figure A.21 XRD pattern of E-BA-GMA / Cloisite® 25A (2%) binary nanocomposite
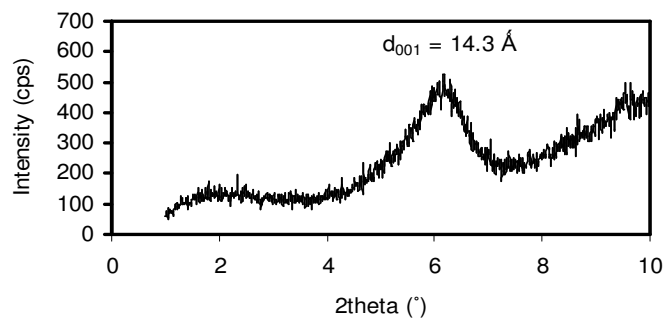
Figure A.22 XRD pattern of PS / SESB-g-MA (5%) / Cloisite® 30B (1%) ternary nanocomposite
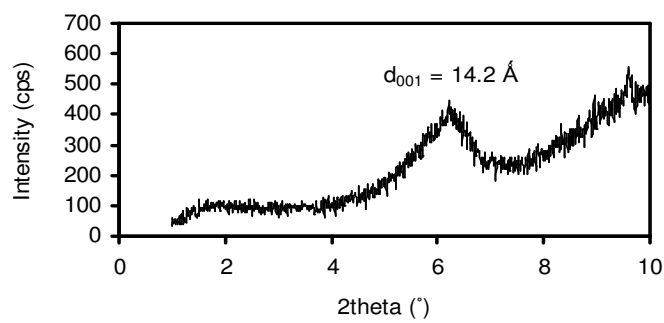
Figure A.23 XRD pattern of PS / SESB-g-MA (5%) / Cloisite® 30B (2%) ternary nanocomposite
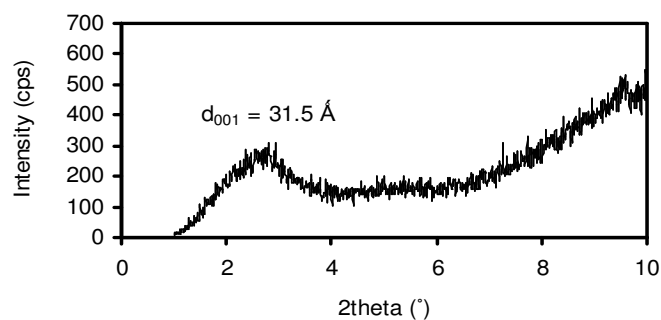
Figure A.24 XRD pattern of PS / SESB-g-MA (5%) / Cloisite® 15A (1%) ternary nanocomposite
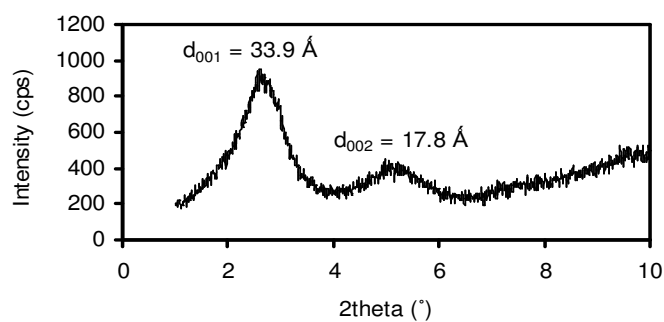
Figure A.25 XRD pattern of PS / SESB-g-MA (5%) / Cloisite® 15A (2%) ternary nanocomposite
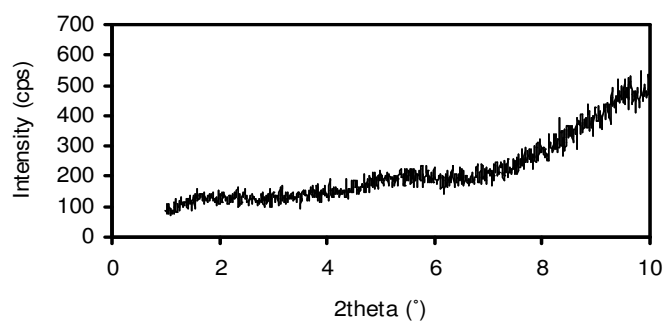
Figure A.26 XRD pattern of PS / SESB-g-MA (5%) / Cloisite® 25A (1%) ternary nanocomposite

163
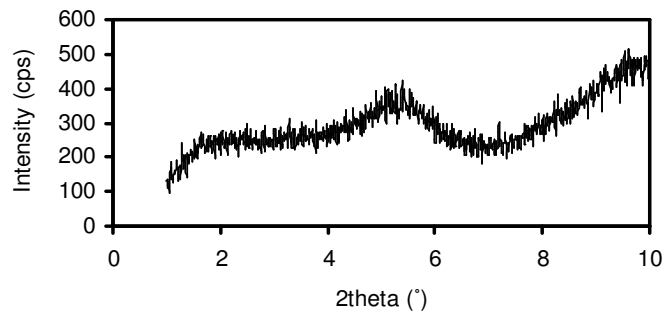
Figure A.27 XRD pattern of PS / SESB-g-MA (5%) / Cloisite[®] 25A (2%) ternary nanocomposite
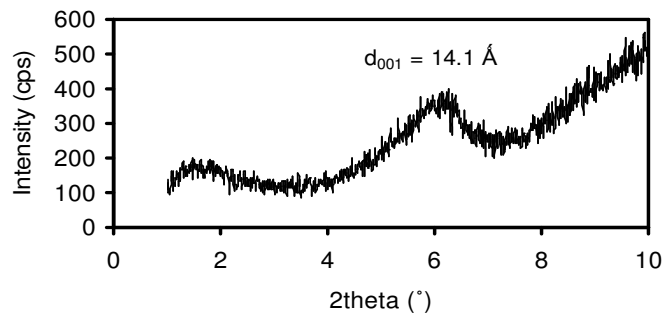
Figure A.28 XRD pattern of PS / E-BA-GMA (5%) / Cloisite[®] 30B (1%) ternary nanocomposite
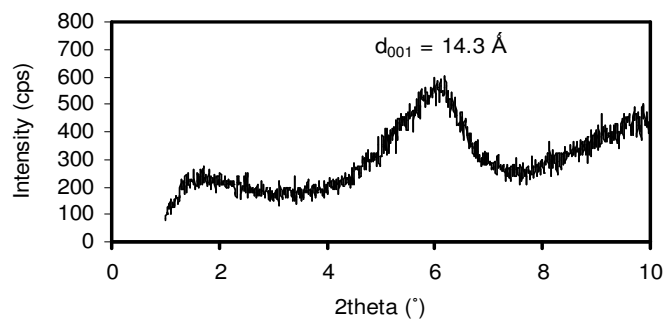
Figure A.29 XRD pattern of PS / E-BA-GMA (5%) / Cloisite[®] 30B (2%) ternary nanocomposite
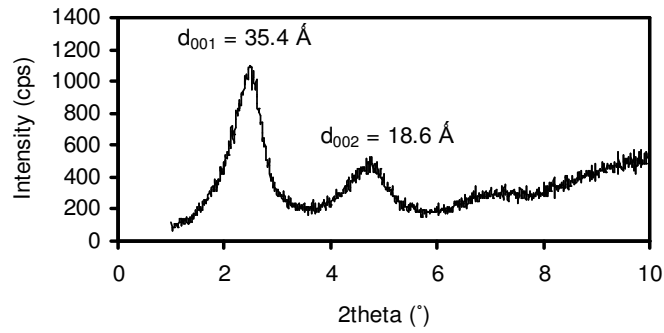
Figure A.30 XRD pattern of PS / E-BA-GMA (5%) / Cloisite® 15A (1%) ternary nanocomposite
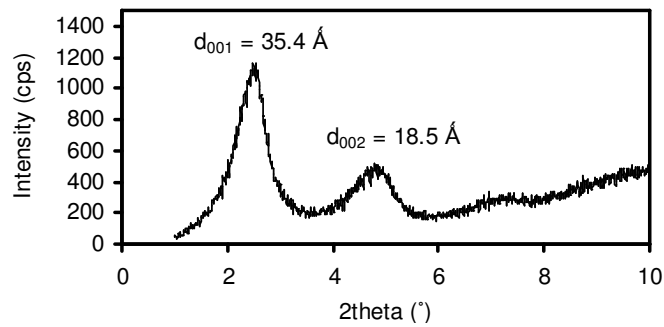
Figure A.31 XRD pattern of PS / E-BA-GMA (5%) / Cloisite® 15A (2%) ternary nanocomposite
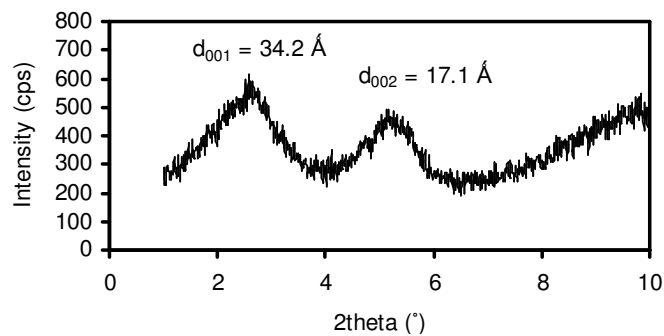
Figure A.32 XRD pattern of PS / E-BA-GMA (5%) / Cloisite® 25A (1%) ternary nanocomposite

165
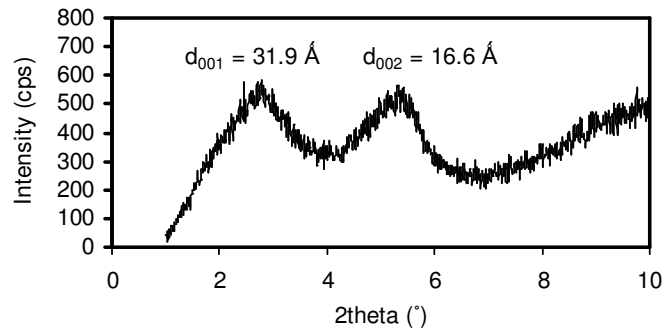
Figure A.33 XRD pattern of PS / E-BA-GMA (5%) / Cloisite® 25A (2%) ternary nanocomposite
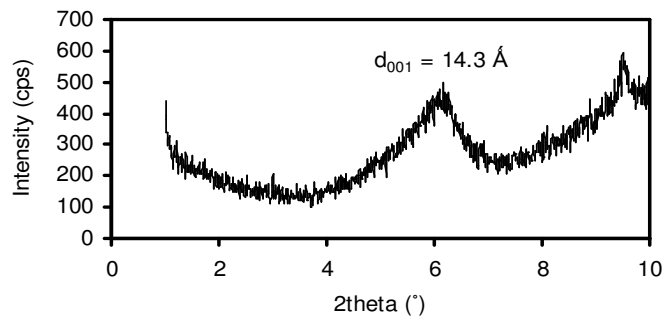
Figure A.34 XRD pattern of PS / SEBS-g-MA (15%) / Cloisite® 30B (1%) ternary nanocomposite
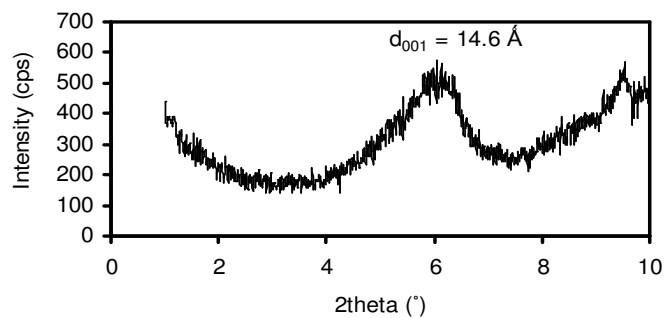
Figure A.35 XRD pattern of PS / SEBS-g-MA (15%) / Cloisite® 30B (2%) ternary nanocomposite
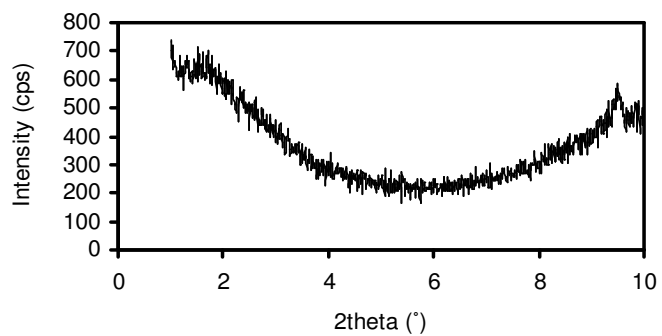
Figure A.36 XRD pattern of PS / SEBS-g-MA (15%) / Cloisite® 15A (1%) ternary nanocomposite
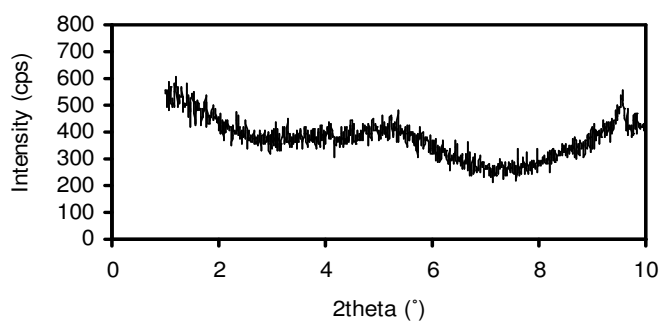
Figure A.37 XRD pattern of PS / SEBS-g-MA (15%) / Cloisite® 15A (2%) ternary nanocomposite
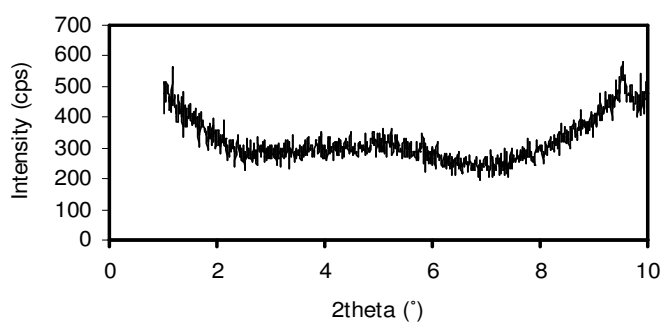
Figure A.38 XRD pattern of PS / SEBS-g-MA (15%) / Cloisite® 25A (1%) ternary nanocomposite
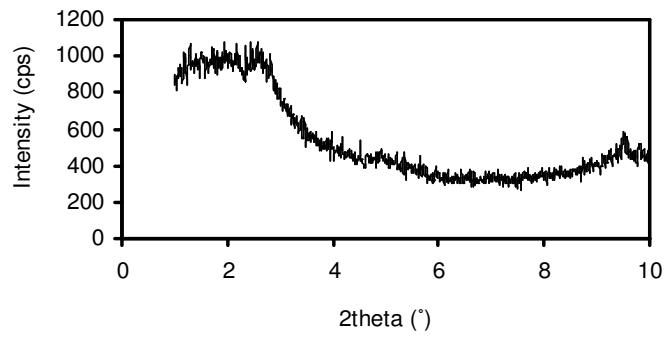
Figure A.39 XRD pattern of PS / SEBS-g-MA (15%) / Cloisite® 25A (2%) ternary nanocomposite
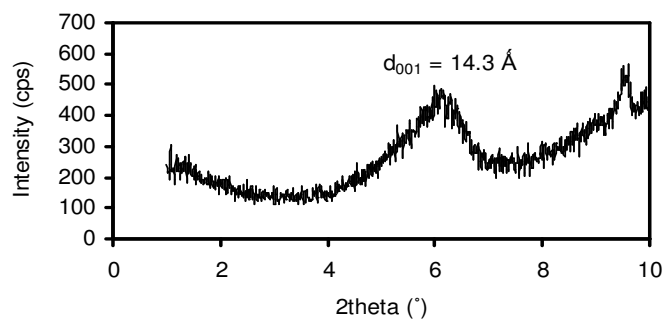
Figure A.40 XRD pattern of PS / SEBS-g-MA (20%) / Cloisite® 30B (1%) ternary nanocomposite
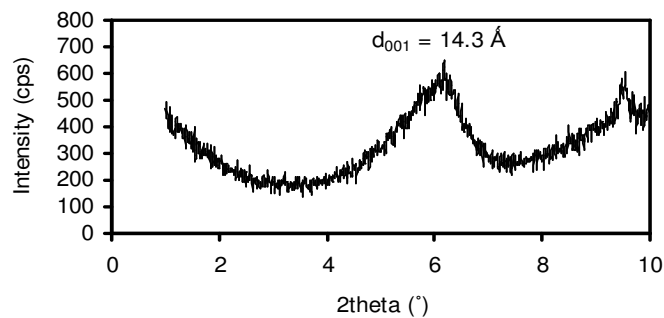
Figure A.41 XRD pattern of PS / SEBS-g-MA (20%) / Cloisite® 30B (2%) ternary nanocomposite
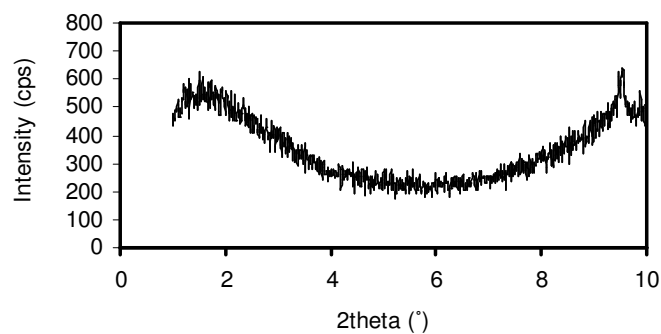
Figure A.42 XRD pattern of PS / SEBS-g-MA (20%) / Cloisite® 15A (1%) ternary nanocomposite
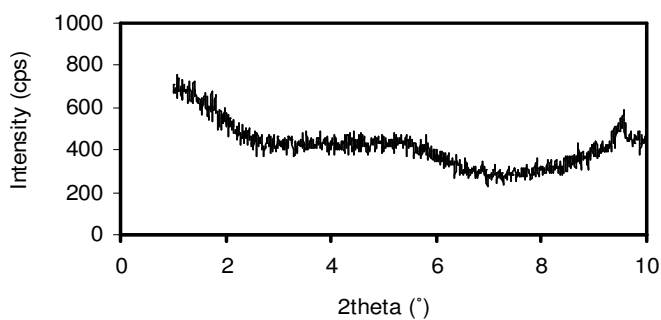
Figure A.43 XRD pattern of PS / SEBS-g-MA (20%) / Cloisite® 15A (2%) ternary nanocomposite
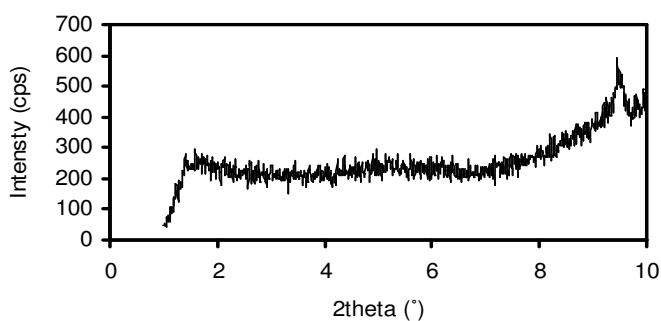
Figure A.44 XRD pattern of PS / SEBS-g-MA (20%) / Cloisite® 25A (1%) ternary nanocomposite
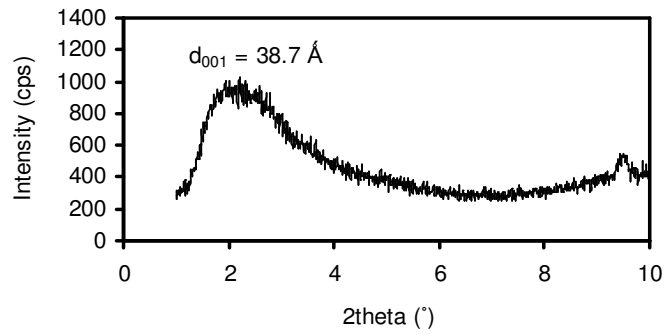
Figure A.45 XRD pattern of PS / SEBS-g-MA (20%) / Cloisite® 25A (2%) ternary nanocomposite
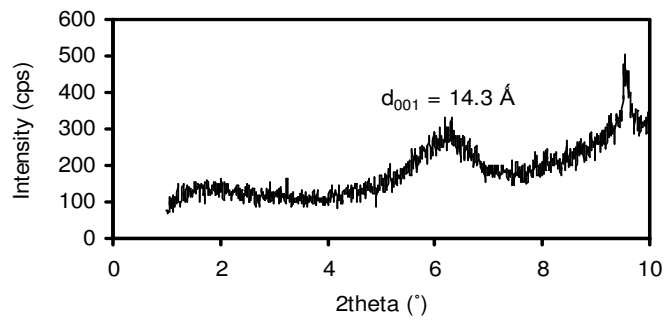
Figure A.46 XRD pattern of PS / SEBS-g-MA (30%) / Cloisite® 30B (1%) ternary nanocomposite
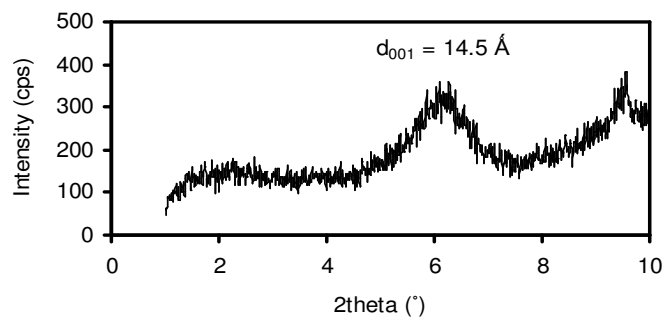
Figure A.47 XRD pattern of PS / SEBS-g-MA (30%) / Cloisite® 30B (2%) ternary nanocomposite
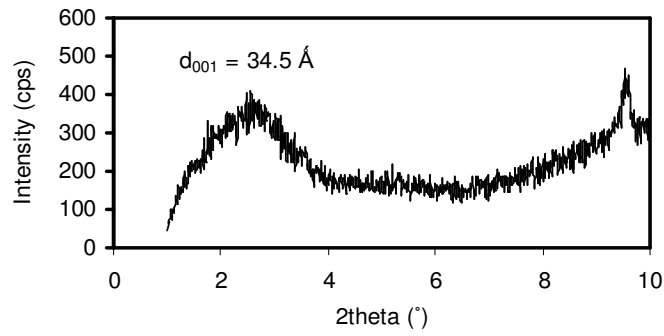
Figure A.48 XRD pattern of PS / SEBS-g-MA (30%) / Cloisite® 15A (1%) ternary nanocomposite
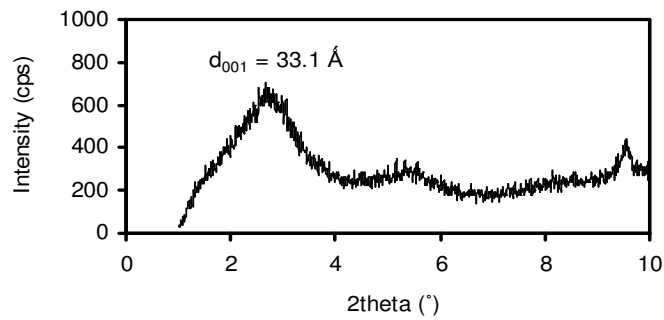
Figure A.49 XRD pattern of PS / SEBS-g-MA (30%) / Cloisite® 15A (2%) ternary nanocomposite
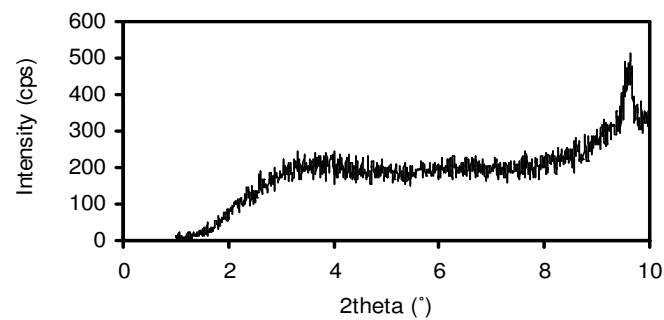
Figure A.50 XRD pattern of PS / SEBS-g-MA (30%) / Cloisite® 25A (1%) ternary nanocomposite
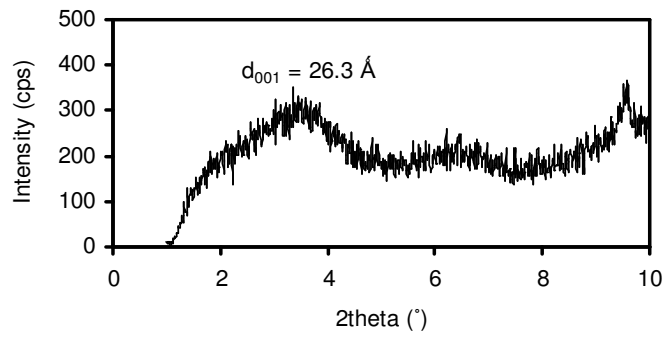
Figure A.51 XRD pattern of PS / SEBS-g-MA (30%) / Cloisite® 25A (2%) ternary nanocomposite
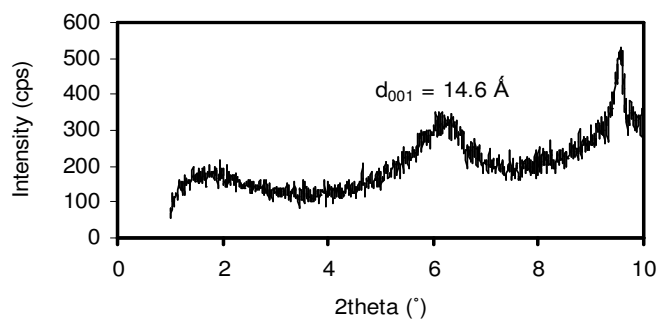
Figure A.52 XRD pattern of PS / SEBS-g-MA (40%) / Cloisite® 30B (1%) ternary nanocomposite
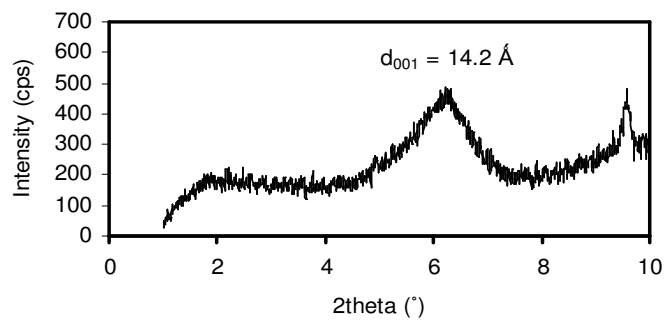
Figure A.53 XRD pattern of PS / SEBS-g-MA (40%) / Cloisite® 30B (2%) ternary nanocomposite
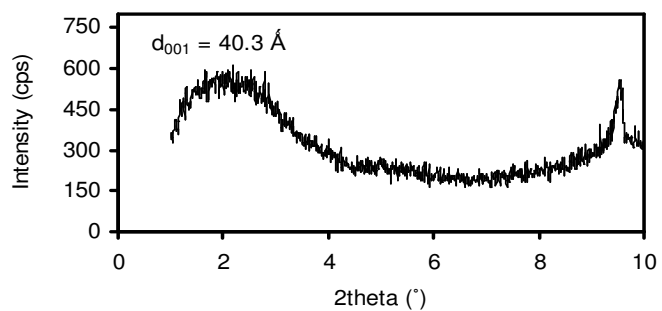
Figure A.54 XRD pattern of PS / SEBS-g-MA (40%) / Cloisite® 15A (1%) ternary nanocomposite
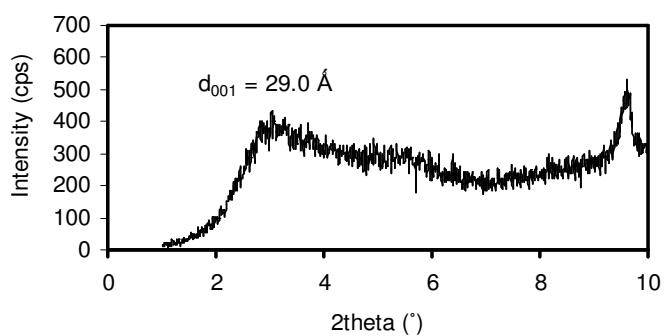
Figure A.55 XRD pattern of PS / SEBS-g-MA (40%) / Cloisite® 15A (2%) ternary nanocomposite
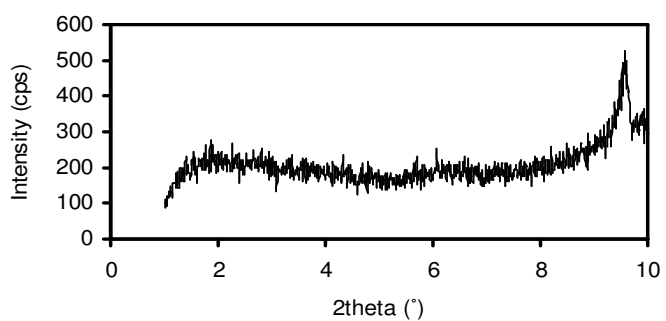
Figure A.56 XRD pattern of PS / SEBS-g-MA (40%) / Cloisite® 25A (1%) ternary nanocomposite
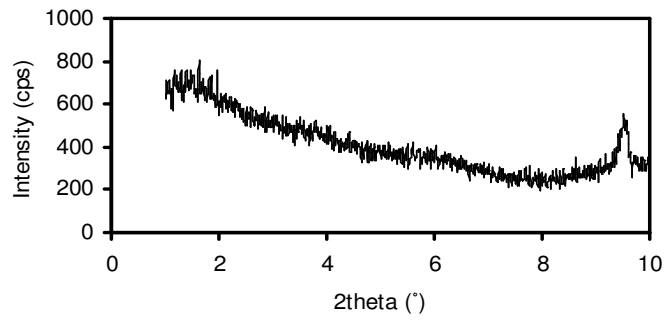
Figure A.57 XRD pattern of PS / SEBS-g-MA (40%) / Cloisite® 25A (2%) ternary nanocomposite
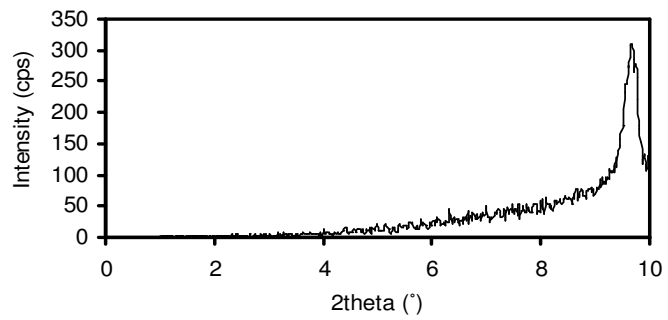
Figure A.58 XRD pattern of pure SEBS-g-MA
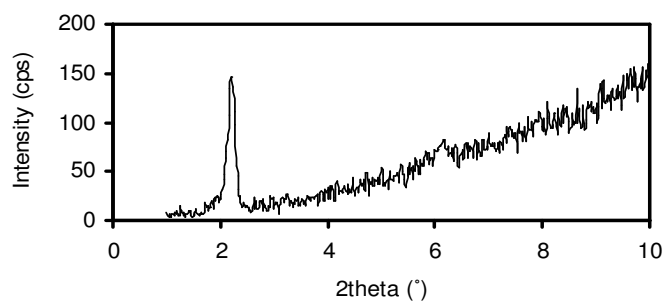
Figure A.59 XRD pattern of pure E-BA-GMA

APPENDIX B

MECHANICAL PROPERTIES

Table B.1 Tensile strength (MPa) of all compositions

Composition	Concentration		Tensile Strength (MPa)	Standard deviation
	Elastomer (wt%)	O-clay (wt%)		
PS	---	---	34.1	1.9
SEBS-g-MA	100	---	5.1	0.1
E-BA-GMA	100	---	5.6	0.2
PS / Elastomer blends				
PS + SEBS-g-MA	5	---	38.1	2
PS + SEBS-g-MA	15	---	37.3	2
PS + SEBS-g-MA	20	---	36.9	2.6
PS + SEBS-g-MA	30	---	34.3	1.2
PS + SEBS-g-MA	40	---	26.8	0.87
PS + E-BA-GMA	5	---	38.2	2.1
PS + E-BA-GMA	15	---	31.1	1.5
PS + E-BA-GMA	20	---	31.8	0.24
PS + E-BA-GMA	30	---	27	1.9
PS + E-BA-GMA	40	---	22.5	1.6
PS / Organoclay nanocomposites				
PS + 30B	---	1	38.2	0.6
PS + 30B	---	2	33.6	1.4
PS + 15A	---	1	28.2	2.8
PS + 15A	---	2	25.9	1.9
PS + 25A	---	1	30.3	0.8
PS + 25A	---	2	38.6	3.4
Elastomer / Organoclay nanocomposites				
SEBS-g-MA + 30B	99	1	4.7	0.14
SEBS-g-MA + 30B	98	2	4.3	0.17
SEBS-g-MA + 30B	99	1	4.5	0.14
SEBS-g-MA + 30B	98	2	4.6	0.15
SEBS-g-MA + 30B	99	1	4.5	0.15
SEBS-g-MA + 30B	98	2	4.3	0.17

Table B.1 (cont'd) Tensile strength (MPa) of all compositions

Composition	Concentration		Tensile Strength (MPa)	Standard deviation
	Elastomer (wt%)	O-clay (wt%)		
E-BA-GMA + 30B	99	1	5.2	0.26
E-BA-GMA + 30B	98	2	5.3	0.2
E-BA-GMA + 30B	99	1	5.8	0.1
E-BA-GMA + 30B	98	2	6.2	0.15
E-BA-GMA + 30B	99	1	5.8	0.21
E-BA-GMA + 30B	98	2	5.7	0.1
PS / 5 wt% Elastomer / Organoclay nanocomposites				
PS + SEBS-g-MA + 30B	5	1	28.5	1.3
PS + SEBS-g-MA + 30B	5	2	28.9	0.8
PS + SEBS-g-MA + 15A	5	1	39.7	0.6
PS + SEBS-g-MA + 15A	5	2	38.6	1.1
PS + SEBS-g-MA + 25A	5	1	36.8	0.59
PS + SEBS-g-MA + 25A	5	2	43	1.9
PS + E-BA-GMA + 30B	5	1	36.6	1.4
PS + E-BA-GMA + 30B	5	2	38.1	1.8
PS + E-BA-GMA + 15A	5	1	37.5	1.5
PS + E-BA-GMA + 15A	5	2	41.2	2
PS + E-BA-GMA + 25A	5	1	33	3
PS + E-BA-GMA + 25A	5	2	40.6	3.6
PS / 15 wt% Elastomer / Organoclay nanocomposites				
PS + SEBS-g-MA + 30B	15	1	42.1	2.4
PS + SEBS-g-MA + 30B	15	2	42	1.4
PS + SEBS-g-MA + 15A	15	1	40.7	1.6
PS + SEBS-g-MA + 15A	15	2	41.2	2.4
PS + SEBS-g-MA + 25A	15	1	41.3	2.5
PS + SEBS-g-MA + 25A	15	2	41.5	1.6
PS / 20 wt% Elastomer / Organoclay nanocomposites				
PS + SEBS-g-MA + 30B	20	1	40.5	1.3
PS + SEBS-g-MA + 30B	20	2	39.2	2.6
PS + SEBS-g-MA + 15A	20	1	41	1.8
PS + SEBS-g-MA + 15A	20	2	39	1.8
PS + SEBS-g-MA + 25A	20	1	41.8	1.6
PS + SEBS-g-MA + 25A	20	2	41.2	1.7
PS / 30 wt% Elastomer / Organoclay nanocomposites				
PS + SEBS-g-MA + 30B	30	1	24.9	1.9
PS + SEBS-g-MA + 30B	30	2	25.3	1.8
PS + SEBS-g-MA + 15A	30	1	25.3	0.5
PS + SEBS-g-MA + 15A	30	2	24.6	0.9
PS + SEBS-g-MA + 25A	30	1	20.2	0.8
PS + SEBS-g-MA + 25A	30	2	24.9	0.65

Table B.1 (cont'd) Tensile strength (MPa) of all compositions

Composition	Concentration		Tensile Strength (MPa)	Standard deviation
	Elastomer (wt%)	O-clay (wt%)		
PS / 40 wt% Elastomer / Organoclay nanocomposites				
PS + SEBS-g-MA + 30B	40	1	22.5	1.8
PS + SEBS-g-MA + 30B	40	2	21.7	0.79
PS + SEBS-g-MA + 15A	40	1	22.8	1
PS + SEBS-g-MA + 15A	40	2	21.5	0.47
PS + SEBS-g-MA + 25A	40	1	21.3	1.4
PS + SEBS-g-MA + 25A	40	2	22.2	0.31

Table B.2 Elongation at break (%) of all compositions

Composition	Concentration		Elongation at break (%)	Standard deviation
	Elastomer (wt%)	O-clay (wt%)		
PS	---	---	2.1	0.07
SEBS-g-MA	100	---	882	58
E-BA-GMA	100	---	274	3
PS / Elastomer blends				
PS + SEBS-g-MA	5	---	3.1	0.26
PS + SEBS-g-MA	15	---	2.1	0.06
PS + SEBS-g-MA	20	---	3	0.13
PS + SEBS-g-MA	30	---	3.3	0.22
PS + SEBS-g-MA	40	---	3.7	0.14
PS + E-BA-GMA	5	---	2.4	0.2
PS + E-BA-GMA	15	---	2.2	0.12
PS + E-BA-GMA	20	---	2.5	0.05
PS + E-BA-GMA	30	---	3.2	0.23
PS + E-BA-GMA	40	---	3	0.19
PS / Organoclay nanocomposites				
PS + 30B	---	1	2.2	0.08
PS + 30B	---	2	1.8	0.14
PS + 15A	---	1	1.4	0.05
PS + 15A	---	2	1.6	0.09
PS + 25A	---	1	1.7	0.03
PS + 25A	---	2	2.1	0.18
Elastomer / Organoclay nanocomposites				
SEBS-g-MA + 30B	99	1	595	43
SEBS-g-MA + 30B	98	2	647	24
SEBS-g-MA + 30B	99	1	805	33
SEBS-g-MA + 30B	98	2	794	53
SEBS-g-MA + 30B	99	1	760	55
SEBS-g-MA + 30B	98	2	770	20
E-BA-GMA + 30B	99	1	237	16
E-BA-GMA + 30B	98	2	254	7
E-BA-GMA + 30B	99	1	245	9
E-BA-GMA + 30B	98	2	256	13
E-BA-GMA + 30B	99	1	265	4
E-BA-GMA + 30B	98	2	257	11
PS / 5 wt% Elastomer / Organoclay nanocomposites				
PS + SEBS-g-MA + 30B	5	1	1.7	0.12
PS + SEBS-g-MA + 30B	5	2	2	0.06
PS + SEBS-g-MA + 15A	5	1	3	0.18
PS + SEBS-g-MA + 15A	5	2	2.3	0.07
PS + SEBS-g-MA + 25A	5	1	3.3	0.05
PS + SEBS-g-MA + 25A	5	2	4.3	0.2

Table B.2 (cont'd) Elongation at break (%) of all compositions

Composition	Concentration		Elongation at break (%)	Standard deviation
	Elastomer (wt%)	O-clay (wt%)		
PS + E-BA-GMA + 30B	5	1	2.1	0.06
PS + E-BA-GMA + 30B	5	2	2.4	0.12
PS + E-BA-GMA + 15A	5	1	2.3	0.14
PS + E-BA-GMA + 15A	5	2	2.7	0.16
PS + E-BA-GMA + 25A	5	1	2.1	0.08
PS + E-BA-GMA + 25A	5	2	2.6	0.25
PS / 15 wt% Elastomer / Organoclay nanocomposites				
PS + SEBS-g-MA + 30B	15	1	3	0.2
PS + SEBS-g-MA + 30B	15	2	3.2	0.16
PS + SEBS-g-MA + 15A	15	1	2.7	0.16
PS + SEBS-g-MA + 15A	15	2	2.8	0.12
PS + SEBS-g-MA + 25A	15	1	2.9	0.07
PS + SEBS-g-MA + 25A	15	2	2.9	0.11
PS / 20 wt% Elastomer / Organoclay nanocomposites				
PS + SEBS-g-MA + 30B	20	1	3.1	0.11
PS + SEBS-g-MA + 30B	20	2	3	0.22
PS + SEBS-g-MA + 15A	20	1	3.1	0.1
PS + SEBS-g-MA + 15A	20	2	3	0.16
PS + SEBS-g-MA + 25A	20	1	3.2	0.12
PS + SEBS-g-MA + 25A	20	2	3.1	0.06
PS / 30 wt% Elastomer / Organoclay nanocomposites				
PS + SEBS-g-MA + 30B	30	1	4.3	0.1
PS + SEBS-g-MA + 30B	30	2	4.3	0.06
PS + SEBS-g-MA + 15A	30	1	6.2	0.37
PS + SEBS-g-MA + 15A	30	2	5.3	0.25
PS + SEBS-g-MA + 25A	30	1	4.5	0.38
PS + SEBS-g-MA + 25A	30	2	5.4	0.22
PS / 40 wt% Elastomer / Organoclay nanocomposites				
PS + SEBS-g-MA + 30B	40	1	10.9	0.9
PS + SEBS-g-MA + 30B	40	2	9.3	0.76
PS + SEBS-g-MA + 15A	40	1	9.8	0.28
PS + SEBS-g-MA + 15A	40	2	10.1	0.93
PS + SEBS-g-MA + 25A	40	1	10.3	0.95
PS + SEBS-g-MA + 25A	40	2	16.4	0.95

Table B.3 Young's modulus (MPa) of all compositions

Composition	Concentration		Young's Modulus (MPa)	Standard deviation
	Elastomer (wt%)	O-clay (wt%)		
PS	---	---	1688	165
SEBS-g-MA	100	---	3.3	0.1
E-BA-GMA	100	---	12.6	0.77
PS / Elastomer blends				
PS + SEBS-g-MA	5	---	1839	56
PS + SEBS-g-MA	15	---	1532	133
PS + SEBS-g-MA	20	---	1323	34
PS + SEBS-g-MA	30	---	1120	47
PS + SEBS-g-MA	40	---	879	30
PS + E-BA-GMA	5	---	1773	29
PS + E-BA-GMA	15	---	1545	61
PS + E-BA-GMA	20	---	1284	65
PS + E-BA-GMA	30	---	955	41
PS + E-BA-GMA	40	---	843	43
PS / Organoclay nanocomposites				
PS + 30B	---	1	1829	85
PS + 30B	---	2	1895	107
PS + 15A	---	1	2032	152
PS + 15A	---	2	1684	137
PS + 25A	---	1	1979	105
PS + 25A	---	2	1776	143
Elastomer / Organoclay nanocomposites				
SEBS-g-MA + 30B	99	1	3.3	0.13
SEBS-g-MA + 30B	98	2	3	0.14
SEBS-g-MA + 30B	99	1	3.6	0.22
SEBS-g-MA + 30B	98	2	3.9	0.23
SEBS-g-MA + 30B	99	1	3.8	0.12
SEBS-g-MA + 30B	98	2	3.7	0.23
E-BA-GMA + 30B	99	1	12.3	0.7
E-BA-GMA + 30B	98	2	12.3	1.07
E-BA-GMA + 30B	99	1	14.5	0.27
E-BA-GMA + 30B	98	2	14	0.92
E-BA-GMA + 30B	99	1	14	0.57
E-BA-GMA + 30B	98	2	14.2	0.75
PS / 5 wt% Elastomer / Organoclay nanocomposites				
PS + SEBS-g-MA + 30B	5	1	1714	23
PS + SEBS-g-MA + 30B	5	2	1763	26
PS + SEBS-g-MA + 15A	5	1	1767	52
PS + SEBS-g-MA + 15A	5	2	1894	74
PS + SEBS-g-MA + 25A	5	1	1825	70
PS + SEBS-g-MA + 25A	5	2	1746	113

Table B.3 (cont'd) Young's modulus (MPa) of all compositions

Composition	Concentration		Young's Modulus (MPa)	Standard deviation
	Elastomer (wt%)	O-clay (wt%)		
PS + E-BA-GMA + 30B	5	1	1829	63
PS + E-BA-GMA + 30B	5	2	1725	54
PS + E-BA-GMA + 15A	5	1	1763	47
PS + E-BA-GMA + 15A	5	2	1641	0
PS + E-BA-GMA + 25A	5	1	1699	85
PS + E-BA-GMA + 25A	5	2	1756	0
PS / 15 wt% Elastomer / Organoclay nanocomposites				
PS + SEBS-g-MA + 30B	15	1	1593	24
PS + SEBS-g-MA + 30B	15	2	1594	48
PS + SEBS-g-MA + 15A	15	1	1620	0
PS + SEBS-g-MA + 15A	15	2	1579	51
PS + SEBS-g-MA + 25A	15	1	1577	42
PS + SEBS-g-MA + 25A	15	2	1547	36
PS / 20 wt% Elastomer / Organoclay nanocomposites				
PS + SEBS-g-MA + 30B	20	1	1502	59
PS + SEBS-g-MA + 30B	20	2	1448	19
PS + SEBS-g-MA + 15A	20	1	1509	53
PS + SEBS-g-MA + 15A	20	2	1448	19
PS + SEBS-g-MA + 25A	20	1	1492	34
PS + SEBS-g-MA + 25A	20	2	1483	45
PS / 30 wt% Elastomer / Organoclay nanocomposites				
PS + SEBS-g-MA + 30B	30	1	916	61
PS + SEBS-g-MA + 30B	30	2	887	31
PS + SEBS-g-MA + 15A	30	1	909	83
PS + SEBS-g-MA + 15A	30	2	844	28
PS + SEBS-g-MA + 25A	30	1	821	38
PS + SEBS-g-MA + 25A	30	2	862	13
PS / 40 wt% Elastomer / Organoclay nanocomposites				
PS + SEBS-g-MA + 30B	40	1	721	54
PS + SEBS-g-MA + 30B	40	2	691	13
PS + SEBS-g-MA + 15A	40	1	730	44
PS + SEBS-g-MA + 15A	40	2	728	25
PS + SEBS-g-MA + 25A	40	1	653	30
PS + SEBS-g-MA + 25A	40	2	661	42

Table B.4 Impact strength (kJ/mm^2) of all compositions

Composition	Concentration		Impact strength (kJ/mm^2)	Standard deviation
	Elastomer (wt%)	O-clay (wt%)		
PS	---	---	9.0	0.61
PS / Elastomer blends				
PS + SEBS-g-MA	5	---	7.7	0.50
PS + SEBS-g-MA	15	---	16.7	0.85
PS + SEBS-g-MA	20	---	21.2	0.89
PS + SEBS-g-MA	30	---	30.1	1.70
PS + SEBS-g-MA	40	---	52.6	3.00
PS + E-BA-GMA	5	---	8.6	0.12
PS + E-BA-GMA	15	---	8.7	0.27
PS + E-BA-GMA	20	---	9.0	0.25
PS + E-BA-GMA	30	---	8.7	0.28
PS + E-BA-GMA	40	---	10.4	0.33
PS / Organoclay nanocomposites				
PS + 30B	---	1	8.0	0.40
PS + 30B	---	2	8.4	0.23
PS + 15A	---	1	5.4	0.34
PS + 15A	---	2	8.1	0.00
PS + 25A	---	1	8.4	0.72
PS + 25A	---	2	7.7	0.37
PS / 5 wt% Elastomer / Organoclay nanocomposites				
PS + SEBS-g-MA + 30B	5	1	11.9	0.63
PS + SEBS-g-MA + 30B	5	2	12.0	0.36
PS + SEBS-g-MA + 15A	5	1	12.0	0.40
PS + SEBS-g-MA + 15A	5	2	8.5	0.22
PS + SEBS-g-MA + 25A	5	1	12.2	0.85
PS + SEBS-g-MA + 25A	5	2	11.9	0.13
PS + E-BA-GMA + 30B	5	1	12.4	0.19
PS + E-BA-GMA + 30B	5	2	11.7	0.42
PS + E-BA-GMA + 15A	5	1	11.9	0.23
PS + E-BA-GMA + 15A	5	2	15.3	0.71
PS + E-BA-GMA + 25A	5	1	12.3	0.82
PS + E-BA-GMA + 25A	5	2	11.4	0.70
PS / 15 wt% Elastomer / Organoclay nanocomposites				
PS + SEBS-g-MA + 30B	15	1	28.4	0.58
PS + SEBS-g-MA + 30B	15	2	28.8	2.00
PS + SEBS-g-MA + 15A	15	1	25.5	1.70
PS + SEBS-g-MA + 15A	15	2	37.3	1.80
PS + SEBS-g-MA + 25A	15	1	32.4	1.30
PS + SEBS-g-MA + 25A	15	2	44.4	1.20

Table B.4 (cont'd) Impact strength (kJ/mm^2) of all compositions

Composition	Concentration		Impact strength (kJ/mm^2)	Standard deviation
	Elastomer (wt%)	O-clay (wt%)		
PS / 20 wt% Elastomer / Organoclay nanocomposites				
PS + SEBS-g-MA + 30B	20	1	32.2	2.90
PS + SEBS-g-MA + 30B	20	2	31.7	0.68
PS + SEBS-g-MA + 15A	20	1	32.0	1.70
PS + SEBS-g-MA + 15A	20	2	41.3	0.37
PS + SEBS-g-MA + 25A	20	1	36.2	1.40
PS + SEBS-g-MA + 25A	20	2	39.5	3.00
PS / 30 wt% Elastomer / Organoclay nanocomposites				
PS + SEBS-g-MA + 30B	30	1	9.5	0.63
PS + SEBS-g-MA + 30B	30	2	11.2	0.98
PS + SEBS-g-MA + 15A	30	1	12.1	0.71
PS + SEBS-g-MA + 15A	30	2	11.4	0.92
PS + SEBS-g-MA + 25A	30	1	11.5	0.83
PS + SEBS-g-MA + 25A	30	2	13.8	0.48
PS / 40 wt% Elastomer / Organoclay nanocomposites				
PS + SEBS-g-MA + 30B	40	1	47.0	4.10
PS + SEBS-g-MA + 30B	40	2	44.8	3.00
PS + SEBS-g-MA + 15A	40	1	50.3	4.60
PS + SEBS-g-MA + 15A	40	2	50.9	1.70
PS + SEBS-g-MA + 25A	40	1	39.9	1.30
PS + SEBS-g-MA + 25A	40	2	39.6	2.00

APPENDIX C

DIFFERENTIAL SCANNING CALORIMETRY THERMOGRAMS
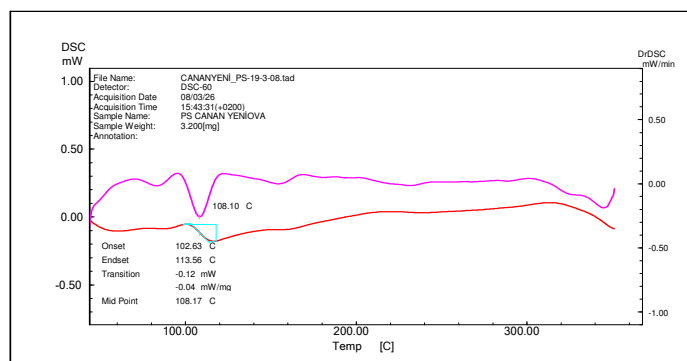
Figure C. 1 DSC thermogram of pure PS
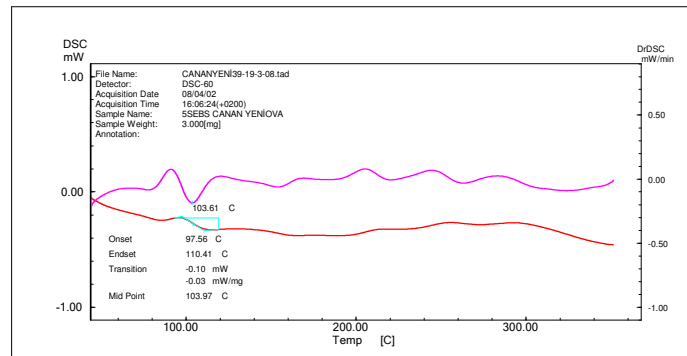
Figure C. 2 DSC thermogram of PS / SEBS-g-MA (5%) binary blend
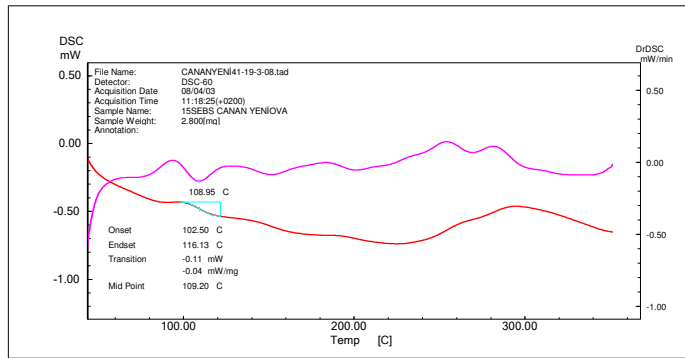
Figure C. 3 DSC thermogram of PS / SEBS-g-MA (15%) binary blend
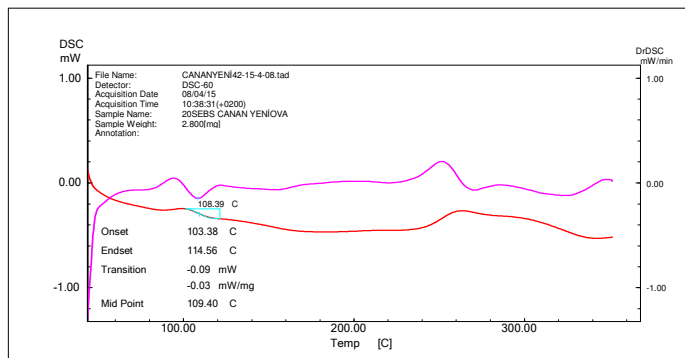
Figure C. 4 DSC thermogram of PS / SEBS-g-MA (20%) binary blend
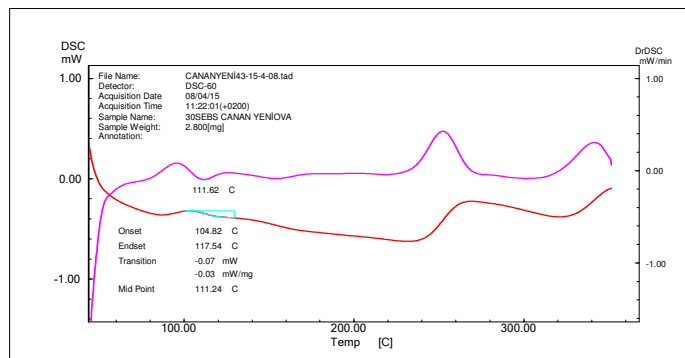
Figure C. 5 DSC thermogram of PS / SEBS-g-MA (30%) binary blend

185
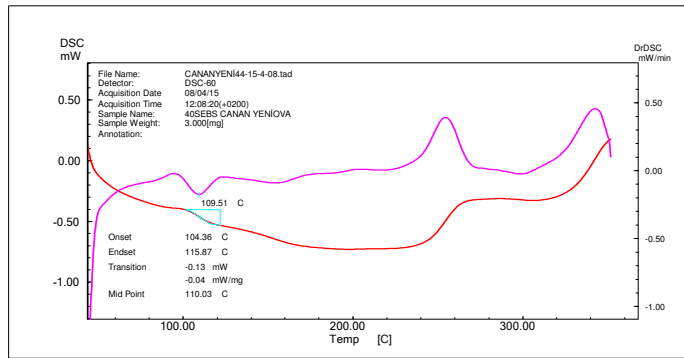
Figure C. 6 DSC thermogram of PS / SEBS-g-MA (40%) binary blend
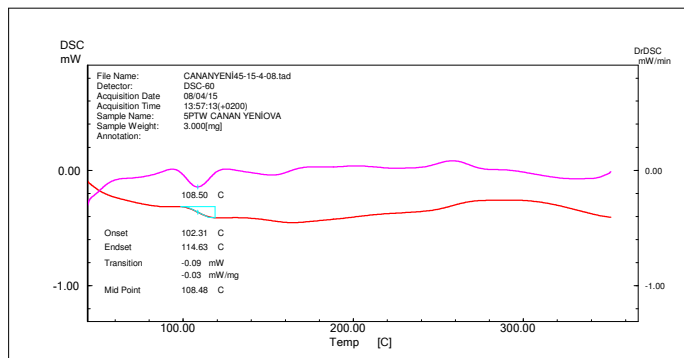
Figure C. 7 DSC thermogram of PS / E-BA-GMA (5%) binary blend
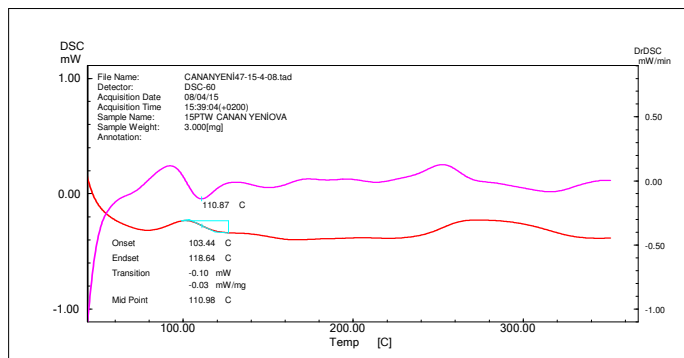
Figure C. 8 DSC thermogram of PS / E-BA-GMA (15%) binary blend

186
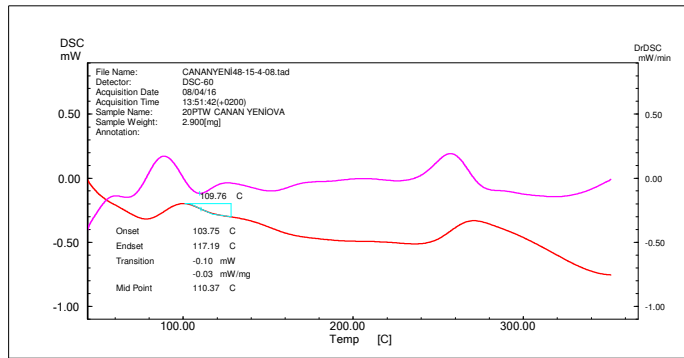
Figure C. 9 DSC thermogram of PS / E-BA-GMA (20%) binary blend
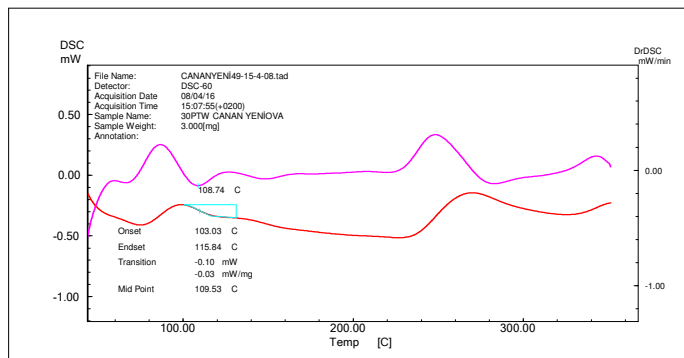
Figure C. 10 DSC thermogram of PS / E-BA-GMA (30%) binary blend
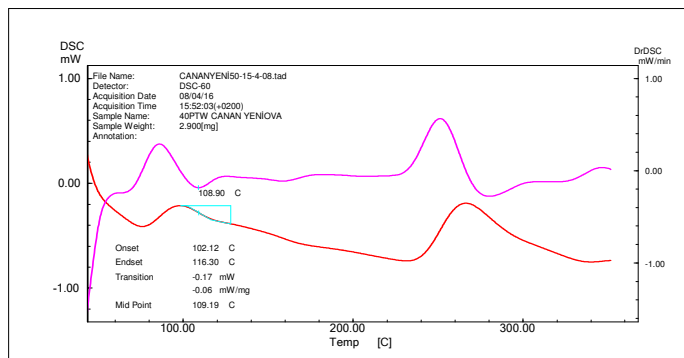
Figure C. 11 DSC thermogram of PS / E-BA-GMA (40%) binary blend
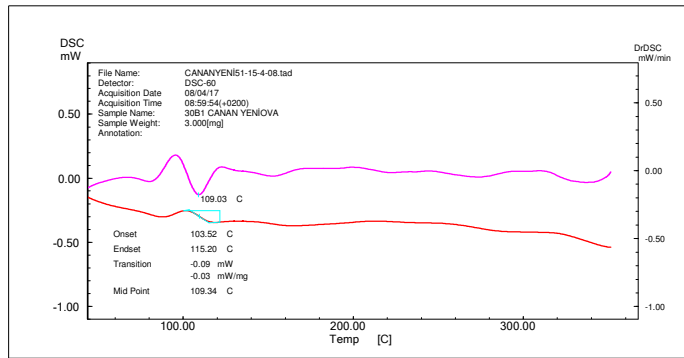
Figure C. 12 DSC thermogram of PS / Cloisite® 30B (1%) binary nanocomposite
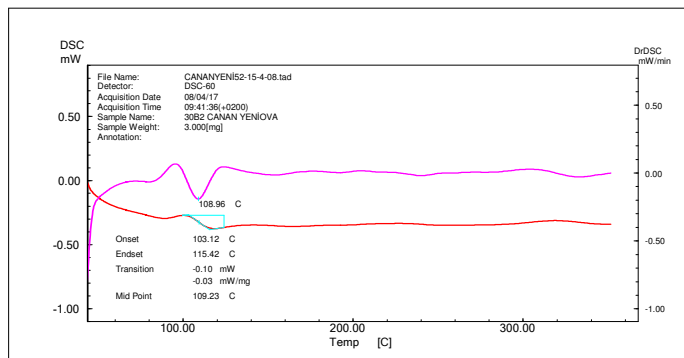
Figure C. 13 DSC thermogram of PS / Cloisite® 30B (2%) binary nanocomposite
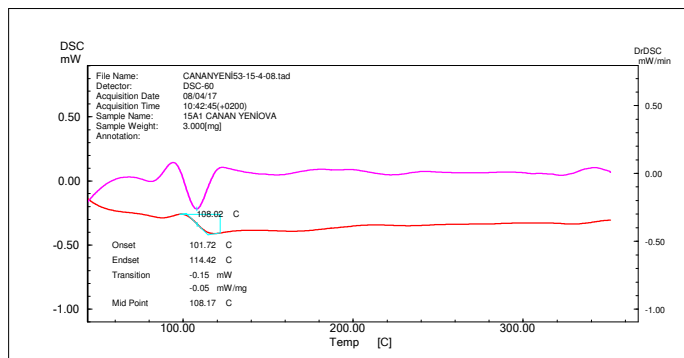
Figure C. 14 DSC thermogram of PS / Cloisite® 15A (1%) binary nanocomposite
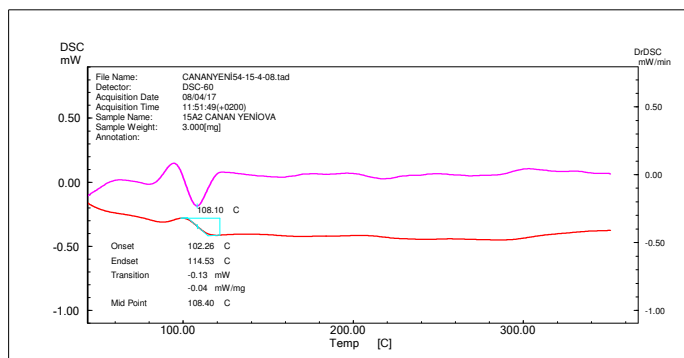
Figure C. 15 DSC thermogram of PS / Cloisite® 15A (2%) binary nanocomposite
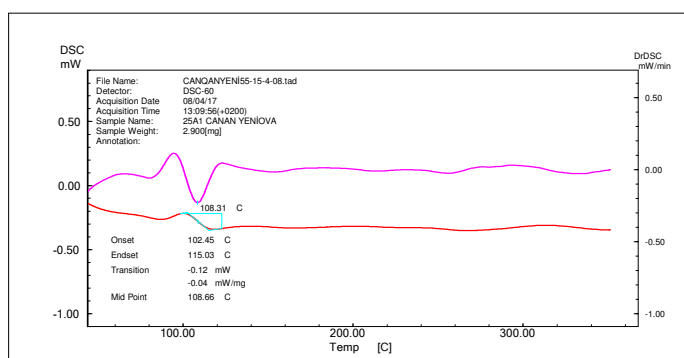
Figure C. 16 DSC thermogram of PS / Cloisite® 25A (1%) binary nanocomposite
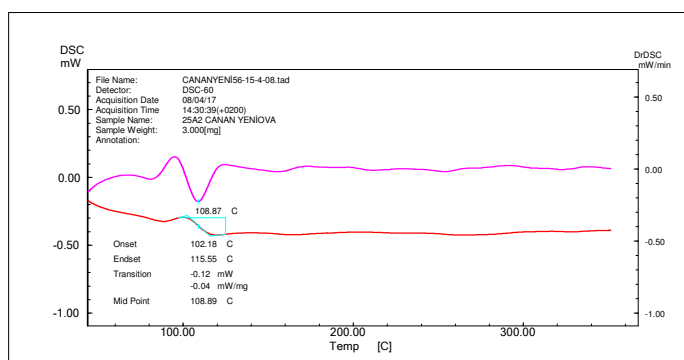
Figure C. 17 DSC thermogram of PS / Cloisite® 25A (2%) binary nanocomposite

189
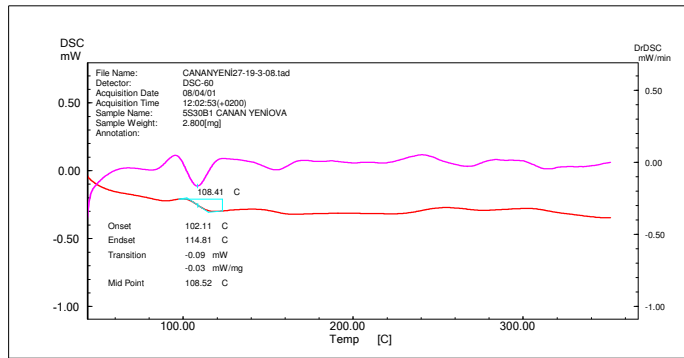
Figure C. 18 DSC thermogram of PS / SEBS-g-MA (5%) / Cloisite® 30B (1%) ternary nanocomposite
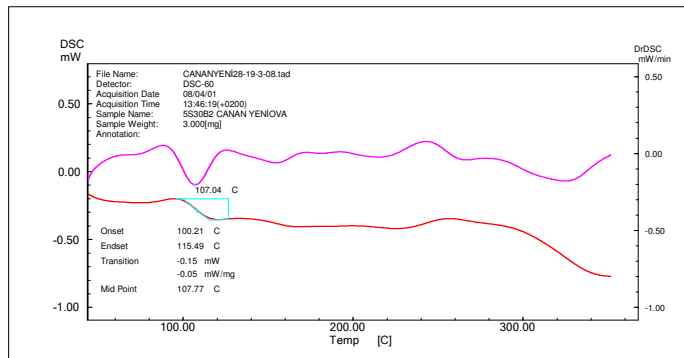
Figure C. 19 DSC thermogram of PS / SEBS-g-MA (5%) / Cloisite® 30B (2%) ternary nanocomposite
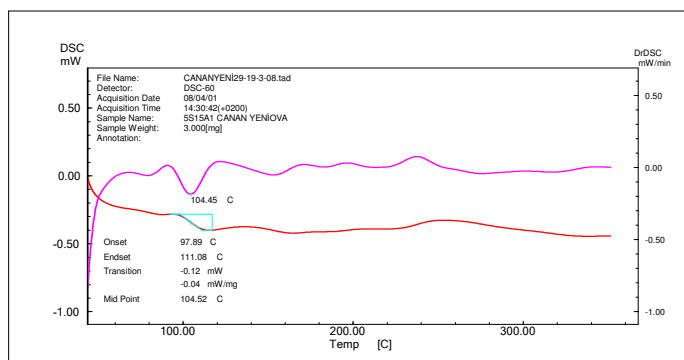
Figure C. 20 DSC thermogram of PS / SEBS-g-MA (5%) / Cloisite® 15A (1%) ternary nanocomposite
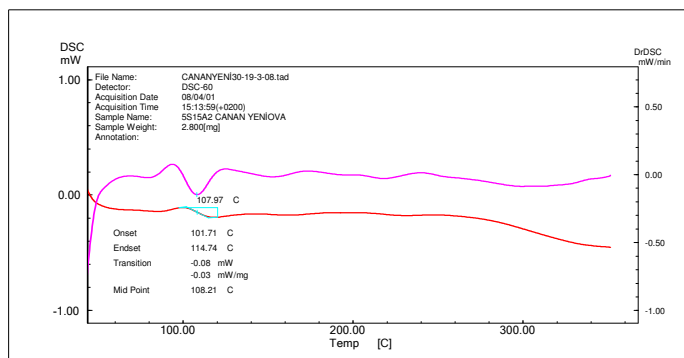
Figure C. 21 DSC thermogram of PS / SEBS-g-MA (5%) / Cloisite® 15A (2%) ternary nanocomposite
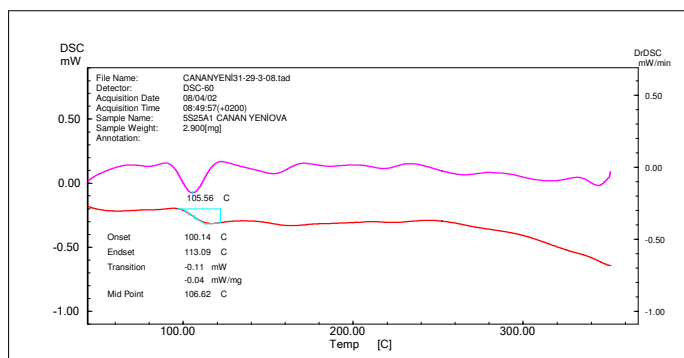
Figure C. 22 DSC thermogram of PS / SEBS-g-MA (5%) / Cloisite® 25A (1%) ternary nanocomposite
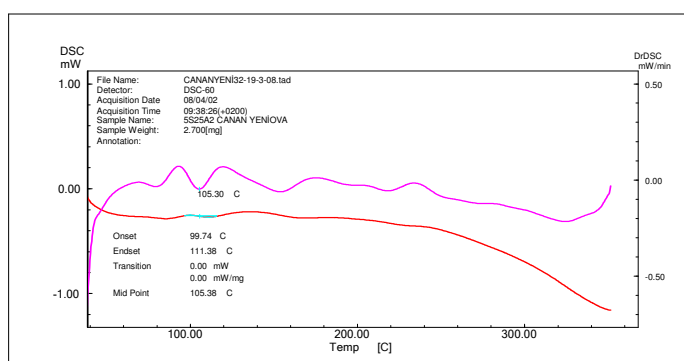
Figure C. 23 DSC thermogram of PS / SEBS-g-MA (5%) / Cloisite® 25A (2%) ternary nanocomposite
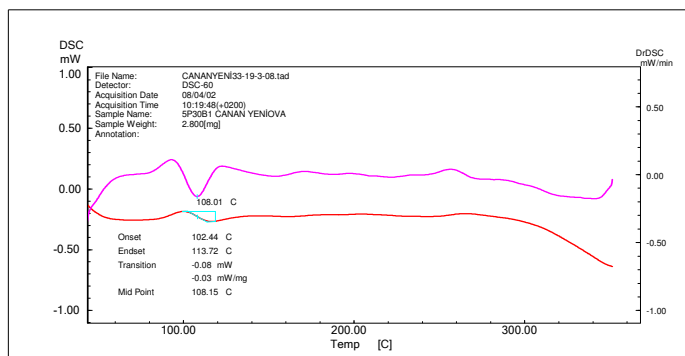
Figure C. 24 DSC thermogram of PS / E-BA-GMA (5%) / Cloisite® 30B (1%) ternary nanocomposite
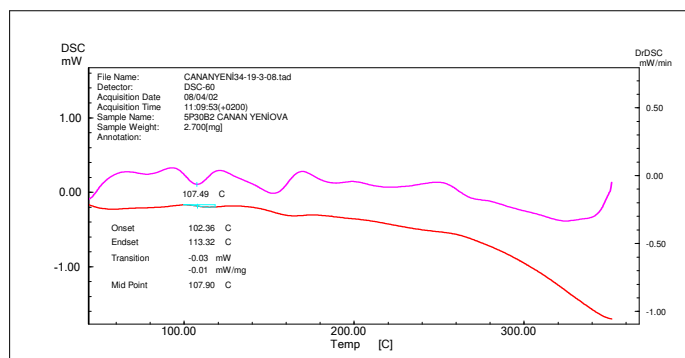
Figure C. 25 DSC thermogram of PS / E-BA-GMA (5%) / Cloisite® 30B (2%) ternary nanocomposite
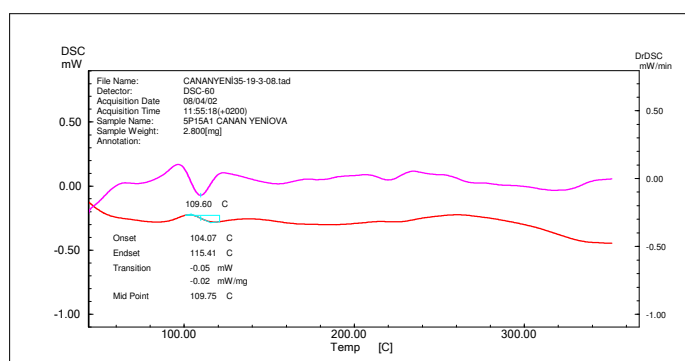
Figure C. 26 DSC thermogram of PS / E-BA-GMA (5%) / Cloisite® 15A (1%) ternary nanocomposite
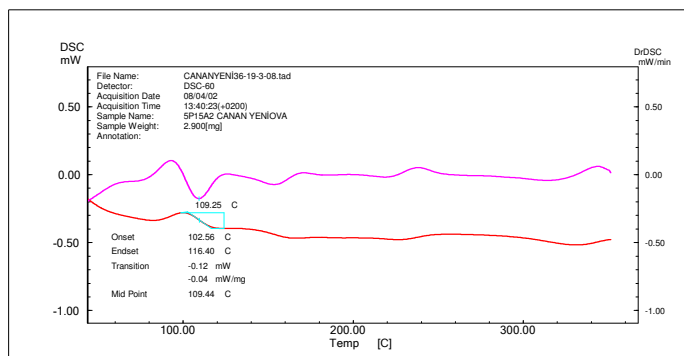
Figure C. 27 DSC thermogram of PS / E-BA-GMA (5%) / Cloisite® 15A (2%) ternary nanocomposite
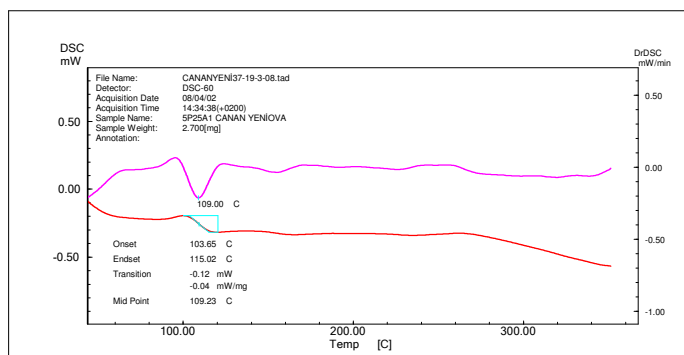
Figure C. 28 DSC thermogram of PS / E-BA-GMA (5%) / Cloisite® 25A (1%) ternary nanocomposite
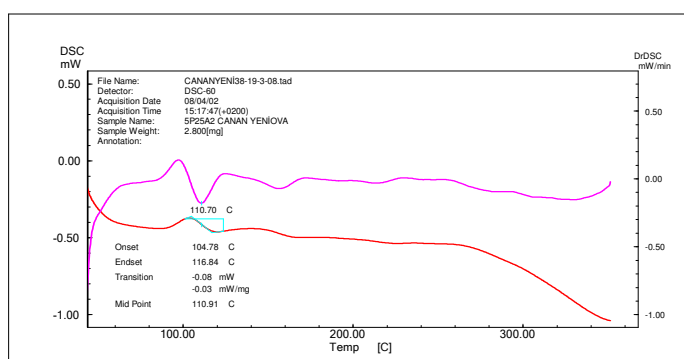
Figure C. 29 DSC thermogram of PS / E-BA-GMA (5%) / Cloisite® 25A (2%) ternary nanocomposite
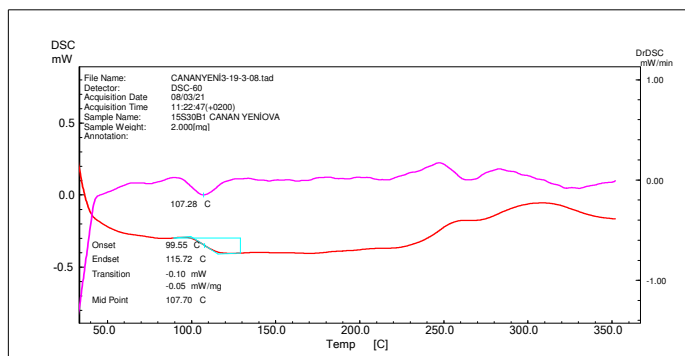
Figure C. 30 DSC thermogram of PS / SEBS-g-MA (15%) / Cloisite® 30B (1%) ternary nanocomposite
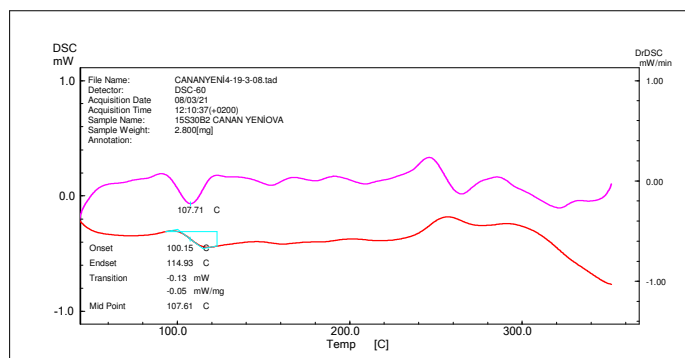
Figure C. 31 DSC thermogram of PS / SEBS-g-MA (15%) / Cloisite® 30B (2%) ternary nanocomposite
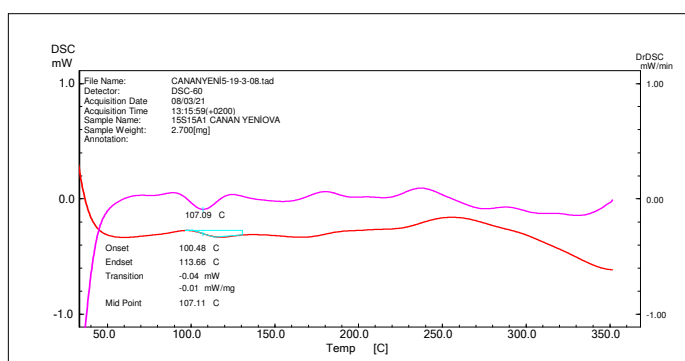
Figure C. 32 DSC thermogram of PS / SEBS-g-MA (15%) / Cloisite® 15A (1%) ternary nanocomposite
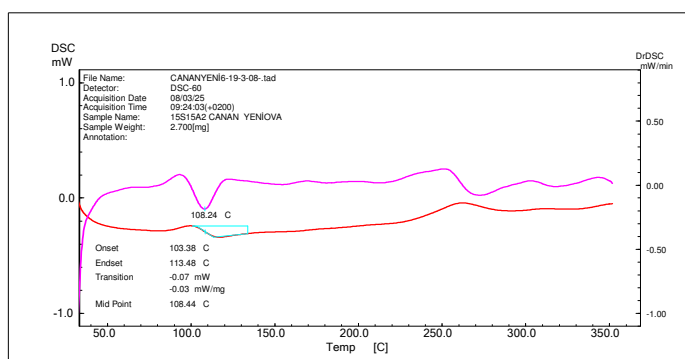
Figure C. 33 DSC thermogram of PS / SEBS-g-MA (15%) / Cloisite® 15A (2%) ternary nanocomposite
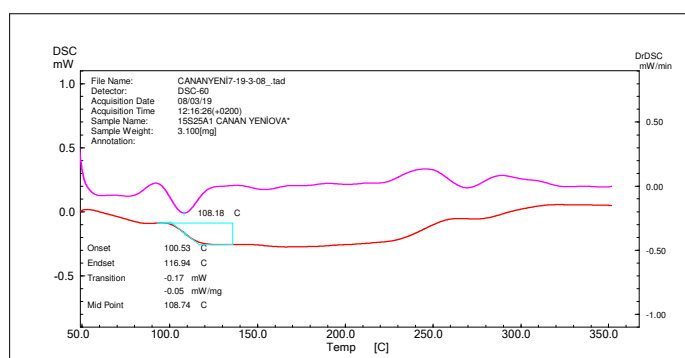
Figure C. 34 DSC thermogram of PS / SEBS-g-MA (15%) / Cloisite® 25A (1%) ternary nanocomposite
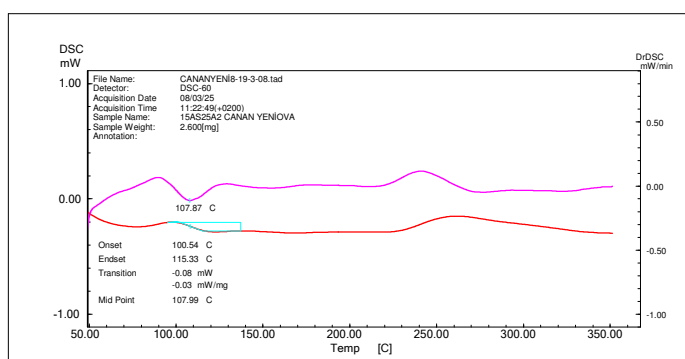
Figure C. 35 DSC thermogram of PS / SEBS-g-MA (15%) / Cloisite® 25A (2%) ternary nanocomposite

195
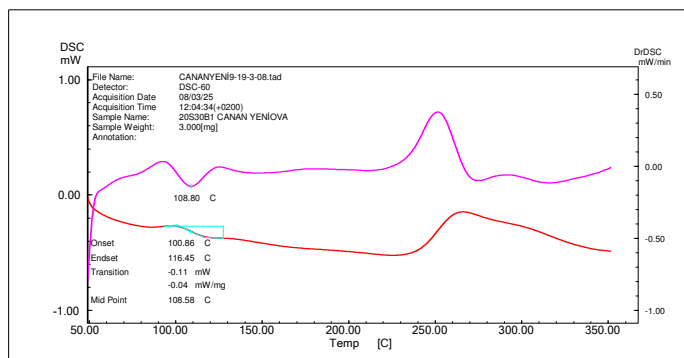
Figure C. 36 DSC thermogram of PS / SEBS-g-MA (20%) / Cloisite® 30B (1%) ternary nanocomposite
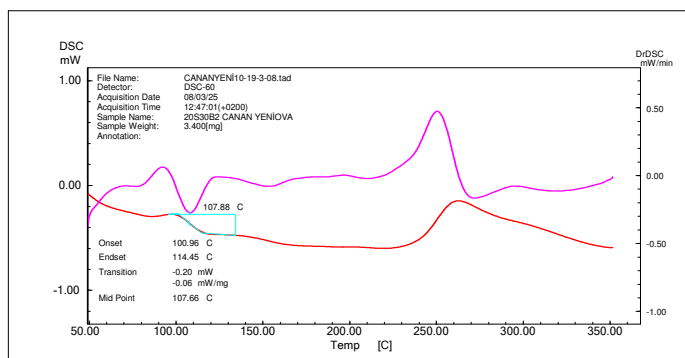
Figure C. 37 DSC thermogram of PS / SEBS-g-MA (20%) / Cloisite® 30B (2%) ternary nanocomposite
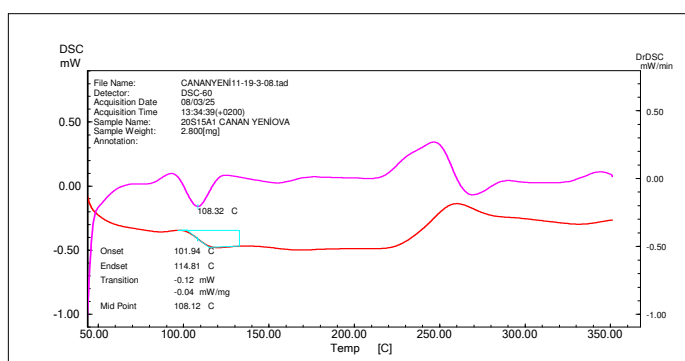
Figure C. 38 DSC thermogram of PS / SEBS-g-MA (20%) / Cloisite® 15A (1%) ternary nanocomposite
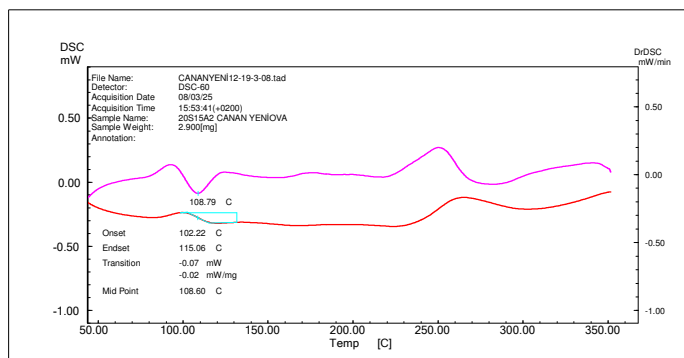
Figure C. 39 DSC thermogram of PS / SEBS-g-MA (20%) / Cloisite® 15A (2%) ternary nanocomposite
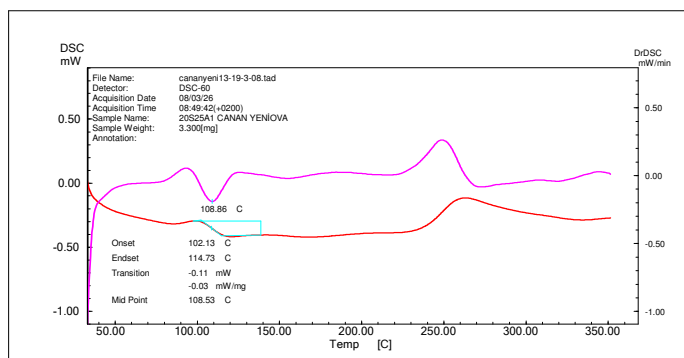
Figure C. 40 DSC thermogram of PS / SEBS-g-MA (20%) / Cloisite® 25A (1%) ternary nanocomposite
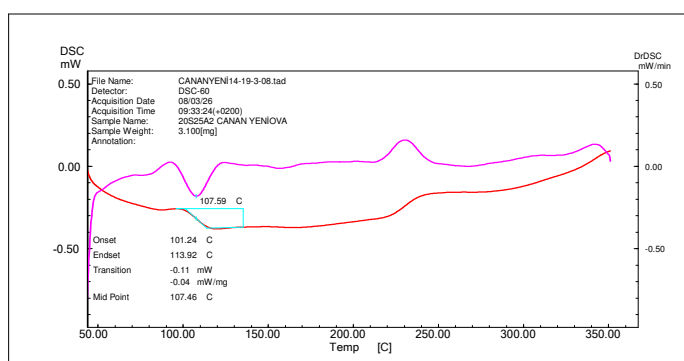
Figure C. 41 DSC thermogram of PS / SEBS-g-MA (20%) / Cloisite® 25A (2%) ternary nanocomposite

197
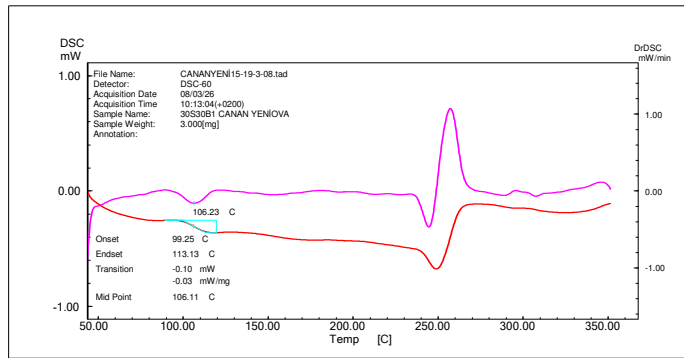
Figure C. 42 SC thermogram of PS / SEBS-g-MA (30%) / Cloisite® 30B (1%) ternary nanocomposite
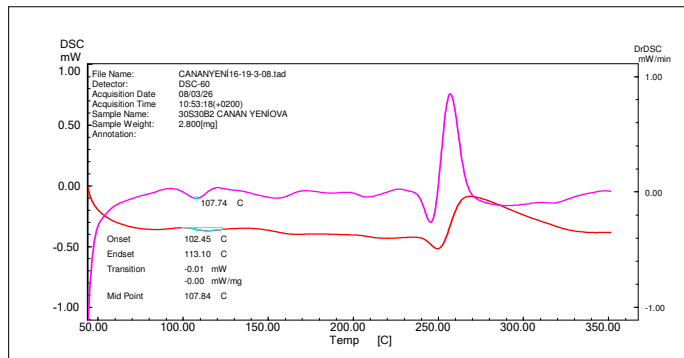
Figure C. 43 DSC thermogram of PS / SEBS-g-MA (30%) / Cloisite® 30B (2%) ternary nanocomposite
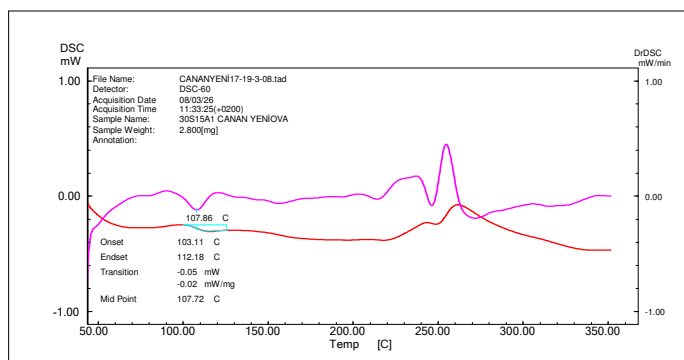
Figure C. 44 DSC thermogram of PS / SEBS-g-MA (30%) / Cloisite® 15A (1%) ternary nanocomposite
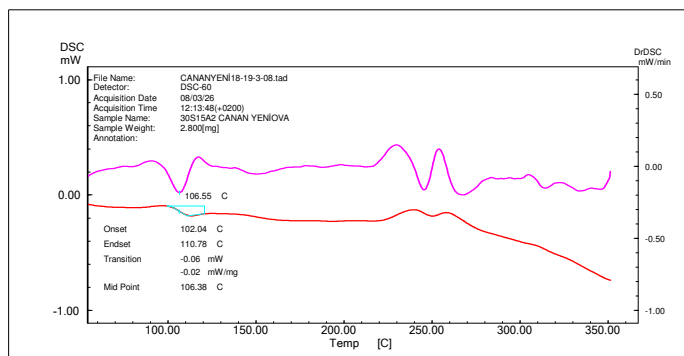
Figure C. 45 DSC thermogram of PS / SEBS-g-MA (30%) / Cloisite® 15A (2%) ternary nanocomposite
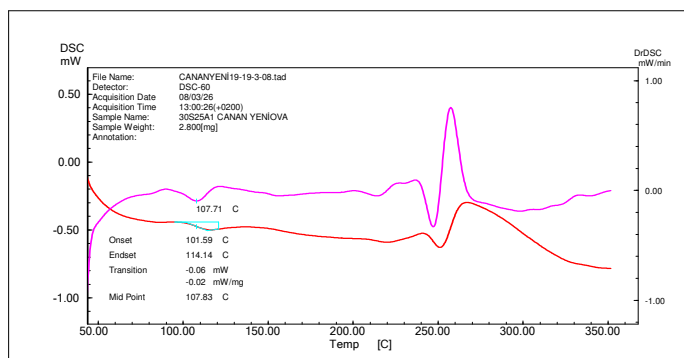
Figure C. 46 DSC thermogram of PS / SEBS-g-MA (30%) / Cloisite® 25A (1%) ternary nanocomposite
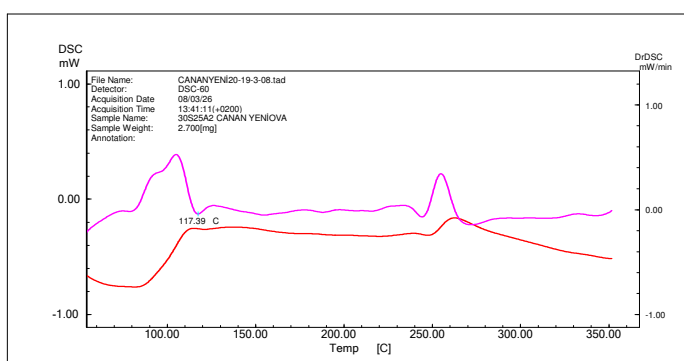
Figure C. 47 DSC thermogram of PS / SEBS-g-MA (30%) / Cloisite® 25A (2%) ternary nanocomposite
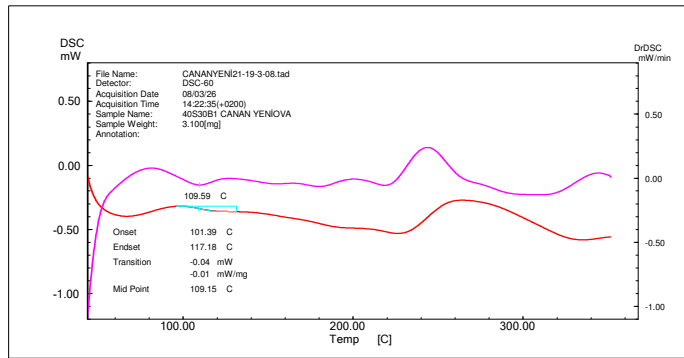
Figure C. 48 DSC thermogram of PS / SEBS-g-MA (40%) / Cloisite® 30B (1%) ternary nanocomposite
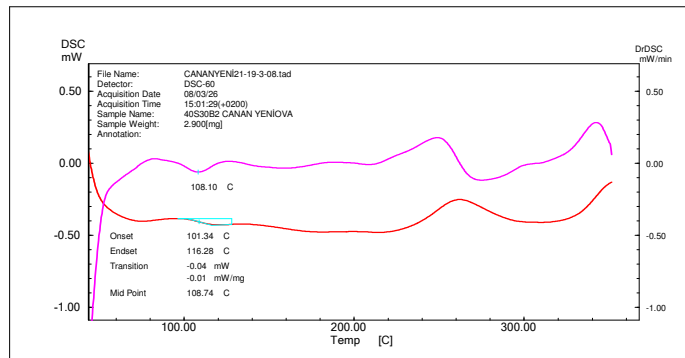
Figure C. 49 DSC thermogram of PS / SEBS-g-MA (40%) / Cloisite® 30B (2%) ternary nanocomposite
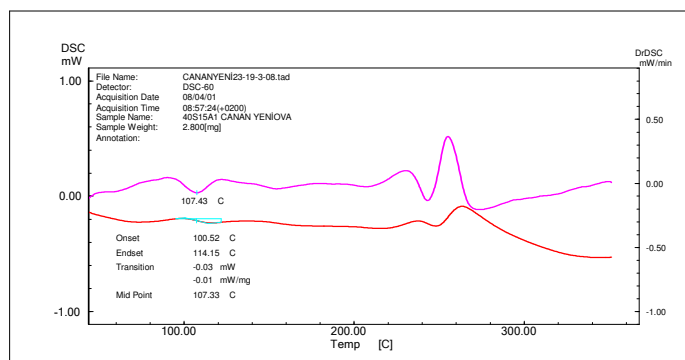
Figure C. 50 DSC thermogram of PS / SEBS-g-MA (40%) / Cloisite® 15A (1%) ternary nanocomposite

200
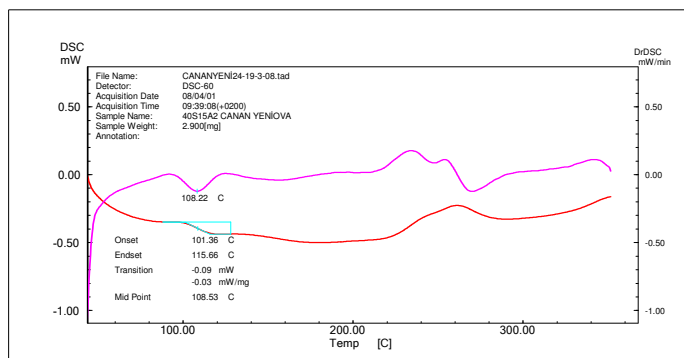
Figure C. 51 DSC thermogram of PS / SEBS-g-MA (40%) / Cloisite® 15A (2%) ternary nanocomposite
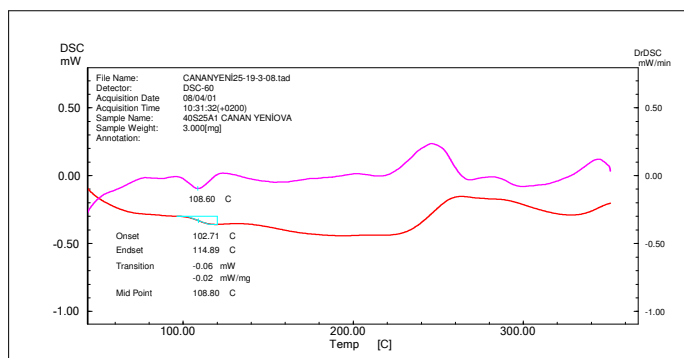
Figure C. 52 DSC thermogram of PS / SEBS-g-MA (40%) / Cloisite® 25A (1%) ternary nanocomposite
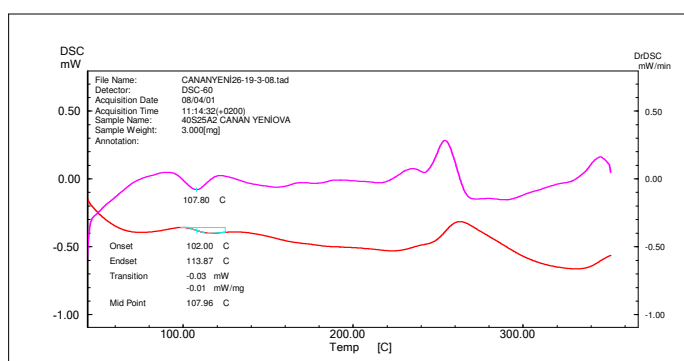
Figure C. 53 DSC thermogram of PS / SEBS-g-MA (40%) / Cloisite® 25A (2%) ternary nanocomposite

201